Influencing the photovoltaic properties and aggregation of diketopyrrolopyrrole based polymers via structural modification

Influencing the photovoltaic properties and aggregation of diketopyrrolopyrrole based polymers via structural modification

PROEFSCHRIFT

ter verkrijging van de graad van doctor aan de Technische Universiteit Eindhoven, op gezag van de rector magnificus prof.dr.ir. F.P.T. Baaijens, voor een commissie aangewezen door het College voor Promoties, in het openbaar te verdedigen op donderdag 17 oktober 2019 om 13:30 uur

door

Gaël Henri Louis Heintges

geboren te Sint-Truiden, België

Dit proefschrift is goedgekeurd door de promotoren en de samenstelling van de promotiecommissie is als volgt:

voorzitter:	prof. dr. ir. E. J. M. Hensen
1e promotor:	prof. dr. ir. R. A. J. Janssen
2e promotor:	prof. dr. W. Maes (Universiteit Hasselt)
leden:	prof. dr. P. J. Skabara (University of Glasgow)
	prof. dr. A. P. H. J. Schenning
	prof. dr. R. P. Sijbesma
	prof. dr. J. V. Manca (Universiteit Hasselt)

Het onderzoek of ontwerp dat in dit proefschrift wordt beschreven is uitgevoerd in overeenstemming met de TU/e Gedragscode Wetenschapsbeoefening.

Printing: Gildeprint, Enschede

A catalogue record is available from the Eindhoven University of Technology Library
ISBN: 978-90-386-4858-3

This work was supported by “Innovatie door Wetenschap en Technologie” (IWT).

Table of Contents

Chapter 1

Introduction

1.1 Introduction

Sustainable energy production is one of the major challenges for the coming decades, with the growing demand for energy projected to reach 27 TW by 2040.[1] Currently, a large part of the energy production is reliant on fossil fuels, which are becoming scarcer and have the problem of CO_2 emissions, which are linked to global climate change. To ensure a sustainable energy production, fossil fuels will have to be phased out over the coming time, and the switch will have to be made to renewable energy sources. Among these, solar energy is expected to play a large role due to its relative abundance.[2] Conversion of solar energy to power and fuels is therefore a fast growing technology.[3]

The photovoltaic effect was first reported in 1839 by Becquerel when he demonstrated that platinum covered by silver chloride in a liquid electrolyte could convert light to electrical power.[4] The research field of photovoltaics (PV) for energy production started, however, only in 1954, when Chapin fabricated the first silicon *p-n* junction and achieved a power conversion efficiency (PCE) of 6%.[5] Since then, steady advancements have led to crystalline silicon solar cells with efficiencies beyond 25%.[6] Due to the very high purity silicon required to make these cells, this technology was initially quite expensive, with the first commercial solar cells having a price of approximately $1500/Watt. Because of reduced production costs and technological developments, the price has now come down to $1-3/Watt, including the installation costs.[7] Hence, crystalline silicon is the dominant technology on the PV market today.[8]

Because of the historical high price of high purity silicon, other solar cell technologies have been developed. In addition to the low cost, most of these technologies are based on thin films and are therefore lightweight, increasing the potential areas of application. This represents an advantage over crystalline silicon cells, because silicon has an indirect band gap, requiring thick layers (200-300 μm) to absorb all the light. Thin film technologies can avoid this problem by employing direct band gap materials, such as amorphous silicon, cadmium telluride, gallium arsenide or CIGS (copper indium gallium (di)selenide). A recent thin film technology attracting much interest is based on solution processable hybrid organic metal halide perovskites, reaching PCEs up to 24.2%.[6,9] Due to their light weight and mechanical flexibility, these technologies can have a wide application range and promise to make a valuable contribution to the solar technology field. One

downside is, however, that they often rely on scarce or toxic materials, which can be mitigated by using organic materials.

1.2 Organic photovoltaics

Organic photovoltaics (OPV) are based on organic molecules or polymers having a conjugated double-bond structure, which forms a large π-conjugated structure with electrons being delocalized over large parts of these molecules. By changing the chemical structure of these molecules, their optoelectronic properties relevant to solar cell applications, such as the optical band gap and frontier energy levels, can easily be tweaked. Organic solar cells can therefore be based on a multitude of materials with a variety of optical band gaps, thus offering control over the colour of the devices. Moreover, because of the synthetic flexibility, the solubility and aggregation of these materials can be altered, which is helpful in the optimization of the fabrication of these devices, which is usually done via solution processing techniques.

As organic materials typically have high extinction coefficients, thin (~100 nm) layers can be used, which, when processed on flexible substrates, can allow for flexible and light-weight devices.[10] In this way a range of applications in portable or mobile products can be imagined. Furthermore, by using transparent contacts, semi-transparent solar cells can be made in a variety of colours, allowing building-integrated applications such as solar

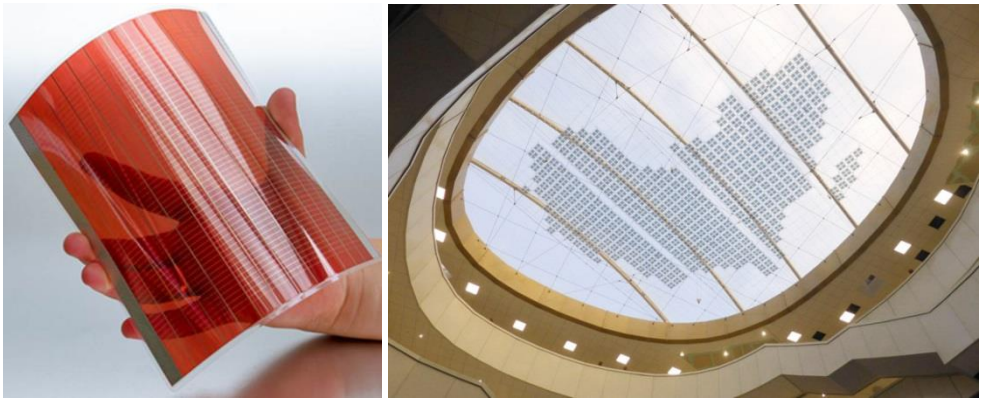

Fig. 1.1: Transparent organic solar cell demonstrator (left)[11] and transparent organic solar cells integrated in a roof (right).[12]

cell windows.[13] In this regard the aesthetic qualities of organic solar cells can be an important advantage over other types of photovoltaics.[14]

Another advantage of OPV is their rather low energy payback term (EPBT). The EPBT is the time it would take to generate the same amount of energy which was consumed during production of the solar cells. For organic solar cells this time has been calculated to be in the order of 6 months, with a rather low assumed PCE of 2%, and has even the potential to reach one day. In this regard OPV by far outperforms any other type of PV technology or sustainable energy production.[15-20] Also the levelized cost of energy for OPV has been shown to be no obstacle for adoption of the technology, as it is approaching the same levels as crystalline silicon.[21] This has opened up the possibility of commercialization of OPV over the last years, as has been shown by companies like infinityPV,[22] Heliatek[23] and OPVIUS.[24]

The photovoltaic effect was first observed in organic materials in 1959 when Pope and Kallmann observed a photocurrent upon illuminating anthracene single crystals.[25] The research in organic semiconductors was, however, only started in earnest in 1977 by the discovery of electrical conductivity in doped polyacetylene films by Heeger, MacDiarmid and Shirakawa.[26,27] Like in other semiconductors, light can be absorbed in organic molecules when the energy of the incident photons is higher or equal to the optical band gap of the material. Photons with energy above the optical band gap will be absorbed and then lose the excess energy via a thermalisation process, while photons with energies lower than the band gap will be transmitted. Due to the rather low relative dielectric constants typically found in organic materials ($\varepsilon_r \approx 3$), the excited state which is formed in this process will be tightly bound, preventing spontaneous separation of charges in the material.[28] This state is a quasiparticle called an exciton, and features a small change in the bond lengths of the molecule, providing a stabilization of the excited state. The binding energy of excitons is typically of the order of several tenths of an electron volt, which is far greater than in inorganic semiconductors. Therefore, a driving force must be introduced to separate the charges.

In 1986, Tang explored a two material system in which one material acted as an electron donor, and the other as an electron acceptor.[29] Thus, by providing an offset in the energy levels of the materials, a driving force for charge separation was provided and a PCE of 1% could be achieved. The working principle of organic solar cells is depicted in

Figure 1.2. In a two material organic solar cell, the light is absorbed by one of the materials and forms an exciton. This exciton has a limited lifetime and mobility, and will have an average diffusion length in the order of 10 – 15 nm.[30] If the exciton encounters a material interface before recombining, free charges can be produced. The driving force for charge separation is provided by the offsets between the lowest unoccupied molecular orbitals (LUMOs) and the highest occupied molecular orbitals (HOMOs). Because excitons must reach an interface before decaying to produce charges, the materials must be mixed intimately to reduce non-radiative recombination losses. For this reason the bulk heterojunction (BHJ) configuration was developed, in which the two materials are intimately mixed and have a large interfacial area. By placing this BHJ between two electrodes with different work functions, an internal electric field is created, enabling the collection of the free charges. In this regard it is crucial that continuous pathways of pure donor or acceptor material to the electrodes exist to allow for the percolation of charges.[31]

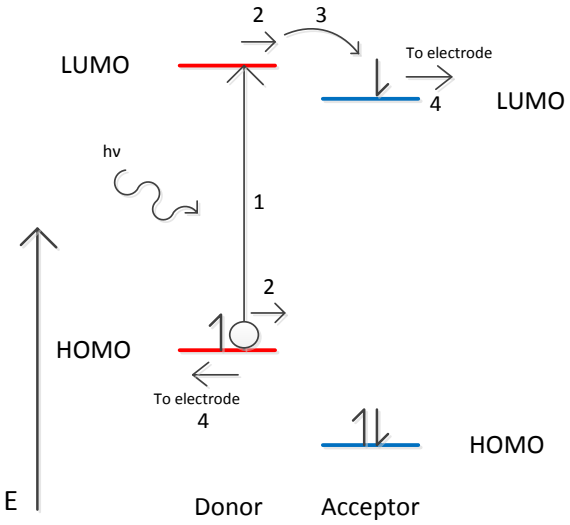

Fig 1.2: Schematic working of an organic solar cell. (1) Absorption of light resulting in an exciton, (2) migration of the exciton to an interface, (3) charge separation, and (4) migration of the separated charges to the electrodes.

1.3 Device architecture and characterization

To construct a single junction organic solar cell, multiple layers have to be stacked onto one another. These cells can be constructed with different polarities: in the "regular" structure the hole-collecting contact is on the bottom of the stack, while in the "inverted" structure the electron-collecting contact is on the bottom. The solar cells are constructed on a substrate, which can be glass but can also consist of flexible materials such as polyethylene terephthalate (PET), covered with a transparent conductive oxide (TCO), typically indium tin oxide (ITO), to ensure efficient transport of the charges out of the device. The top contact is usually an opaque metal, such as aluminium or silver, but can also be made (semi-)transparent to either make a semi-transparent device or to allow an opaque substrate.

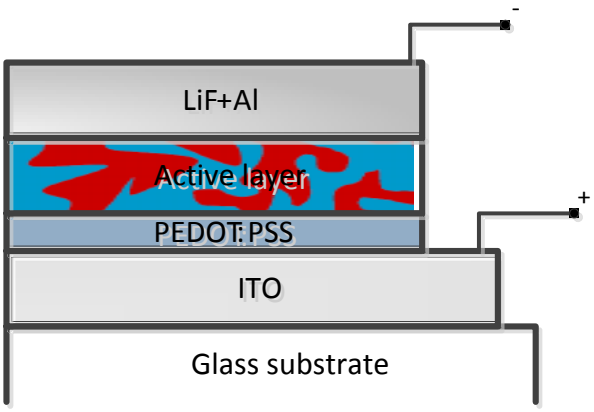

Fig 1.3: An example of a typical regular device structure used in this work.

To improve the performance of the cell, hole and electron transport layers are employed between the electrodes and the active layer, providing an ohmic contact to the active layer by aligning the work functions and enhancing the extraction of charges. These layers also offer charge selectivity, reducing interfacial recombination losses, and can in some cases also provide a smooth surface for the next layer. Typical hole transport layers include poly(3,4-ethylenedioxythiophene):polystyrene sulfonate (PEDOT:PSS), MoO_3, NiO and CuS. Among the electron transport layers LiF, ZnO, poly[(9,9-bis(3'-(*N*,*N*-dimethylamino)propyl)-2,7-fluorene)-*alt*-(9,9-dioctylfluorene)] (PFN) and ethoxylated polyethylenimine (PEIE) are popular. The deposition of these materials can be done by

thermal evaporation in some cases, or via solution processing techniques like spin coating, doctor blading, slot-die coating or inkjet printing. In the case of solution processing it is important that the solvents which are used are "orthogonal", i.e. that they do not dissolve any previously deposited layers.[32]

To characterize the solar cell, both electrodes are connected to an external circuit, which enables a voltage sweep while recording the current density resulting in a current density – voltage (*J*-*V*) curve. In the dark, the solar cell exhibits diode behaviour, with typically only a small leakage current being present at reverse bias, and a large current density in forward bias. Under illumination a photocurrent is created and power is produced, as can be seen in the fourth quadrant of the *J*-*V* curve (Figure 1.4a). The curve can be characterized by certain key parameters. The short-circuit current density (J_{sc}) is the current density recorded when no voltage is applied (short circuit conditions) and can be seen in the point where the *J*-*V* curve intersects the current density axis. The open circuit voltage (V_{oc}) is the voltage when the current density is zero (open circuit conditions), and can be seen in the point where the *J*-*V* curve intersects the voltage axis. The product of the current density and voltage provides the power output of the device and reaches a maximum (P_{MPP}) in the maximum power point.

$$P_{\mathrm{MPP}} = V_{\mathrm{MPP}} \cdot J_{\mathrm{MPP}}$$

From this point the fill factor (FF) of the cell can be determined as it is the ratio between the P_{MPP} and the product of the V_{oc} and J_{sc}.

$$\mathrm{FF} = \frac{P_{\mathrm{MPP}}}{V_{\mathrm{oc}} \cdot J_{\mathrm{sc}}} = \frac{V_{\mathrm{MPP}} \cdot J_{\mathrm{MPP}}}{V_{\mathrm{oc}} \cdot J_{\mathrm{sc}}}$$

This allows the maximum extractable power to be re-written as:

$$P_{\mathrm{MPP}} = J_{\mathrm{sc}} \cdot V_{\mathrm{oc}} \cdot \mathrm{FF}$$

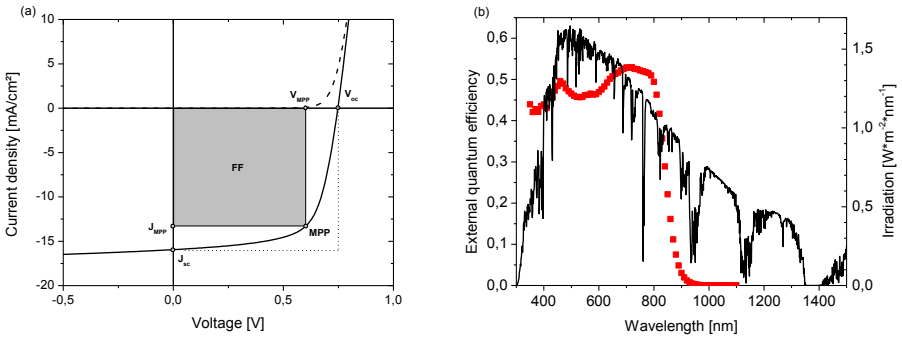

Fig. 1.4: *J-V* curve with the important points indicated. The fill factor is the ratio between the small and the large rectangle (a). An EQE spectrum (red) and the AM1.5G spectrum (black) (b).

The performance of solar cells is measured under AM 1.5G (air mass 1.5 global) illumination at 1000 W/m² (Figure 1.4b).[33] AM 1.5G is the spectral distribution of sunlight after passing through 1.5 times the thickness of the Earth atmosphere, which corresponds to the illumination on Earth on a clear day with the sun at 48.2° relative to the zenith. In the lab, this is simulated by illumination with a lamp and appropriate filters. This means that the *J-V* measurement occurs under simulated solar light, which provides a good estimation of the V_{oc} and fill factor, but can induce an error in the J_{sc} because of spectral mismatch.[34] To measure the J_{sc} more accurately, the wavelength (λ) dependent spectral responsivity of the device ($S(\lambda)$) is measured. $S(\lambda)$ is related to the external quantum efficiency (EQE), which is defined as the ratio of collected charges to the number of incident photons on the device per wavelength:

$$S(\lambda) = \mathrm{EQE}(\lambda)\frac{e\lambda}{hc}$$

with e the elemental charge, h Planck's constant and c the speed of light. Integrating the product of the spectral response and the AM 1.5G reference spectrum over all wavelengths then yields a better estimation of the J_{sc}.

$$J_{sc} = \int S(\lambda) \cdot E_{\mathrm{AM1.5G}}(\lambda)\mathrm{d}\lambda$$

A power conversion efficiency can then be calculated by dividing the (corrected) maximum power point by the power of the incident light (P_{in}).

$$\mathrm{PCE} = \frac{P_{\mathrm{MPP}}}{P_{\mathrm{in}}} = \frac{J_{\mathrm{sc}} \cdot V_{\mathrm{oc}} \cdot \mathrm{FF}}{P_{\mathrm{in}}}$$

When measuring the EQE, commonly a low intensity light source is used as the probe light, which means the cell is operating at light intensities well under AM 1.5G conditions. As a consequence, less charge carriers will be generated and be present in the device during this measurement, causing less charge recombination than in a cell operating under AM 1.5G. As this can lead to an overestimation of the EQE, the cell is illuminated with a bias light approximating the conditions under 1 sun illumination.[35]

1.4 Energy levels

As mentioned above, the active layer of organic solar cells generally consists of a mixture of two materials, with one acting as an electron donor and the other as an electron acceptor. Optimization of the energy levels in these materials is important as they determine in large part the photovoltaic properties of the cell.[36] First, the optical band gaps of the materials are important, as they determine how much of the solar spectrum can be absorbed, in this way influencing the maximum photocurrent that can be reached. Second, the offset between the HOMOs and LUMOs of the materials must be large enough to ensure charge separation. Any light that is absorbed by the donor will create an exciton on the donor material. The offset between the LUMOs and the HOMOs of the donor and acceptor provide the driving force to transform this exciton into free charges by allowing the electron and hole to migrate to the acceptor and donor, respectively. If the HOMO-HOMO and LUMO-LUMO offsets are not large enough, no charges will be generated by light absorbed by the acceptor or donor, respectively. In such case, energy transfer may occur in which the excitation energy is transferred from the materials with higher optical band gap to the one with the lower optical band gap. Third, the V_{oc} is influenced by the difference in energy between the HOMO of the donor and the LUMO of the acceptor. This is because this energy difference directly influences the energy of the charge transfer state,

which has been shown to be related to the V_{oc}.[37,38] In practice an empirical relation between the V_{oc} and the energy levels has been established: $eV_{oc} = E_{HOMO,D} - E_{LUMO,A} - 0.4$ eV.[39]

These relations have to be kept in mind when designing new materials for solar cells. For example, decreasing the band gap of a donor material will result in a red-shifted absorption profile and thus a higher J_{sc}, but also in a reduction of the V_{oc} by raising the HOMO level. Therefore, this will not necessarily lead to an improved PCE. If on the other hand the optical band gap of the donor is reduced by lowering the LUMO level, the V_{oc} will not be affected, but when the LUMO becomes too low compared to the LUMO of the acceptor, no charge transfer will take place anymore. When designing new materials, the impact of chemical changes on the energy levels therefore has to be carefully considered.[38]

Since both the optical band gap and V_{oc} can easily be measured, the minimum photon energy loss (E_{loss}) is a useful parameter when describing materials.

$$E_{loss} = E_{g,eff} - eV_{oc}$$

E_{loss} is a combination of the energy loss incurred by the LUMO-LUMO or HOMO-HOMO offsets required to split the exciton, the Coulomb energy gained by spatially separating the electron and hole, and the subsequent voltage loss due to non-radiative recombination of electrons and holes. At room temperature and AM1.5G illumination, the minimum photon energy loss required to ensure a working device has been found to be around 0.6 eV in the case of fullerene-based cells,[39] although isolated examples of working devices with $E_{loss} \approx 0.5$ eV have been found.[40] When E_{loss} is below this threshold, the quantum efficiency for charge generation drops steeply and becomes negligible.[40] It is important to keep this E_{loss} as low as possible to ensure the maximum V_{oc} possible. This intrinsic energy loss reduces the maximal theoretical limit for the PCE from 33.7%[41] (the Shockley-Queisser limit for single junction solar cells) to ~23%.[42]

1.5 Design and synthesis of materials

Donor materials for OPV have been extensively researched in the past, and many examples of both small molecules and polymers exist. These materials are composed of a conjugated core to which solubilizing (usually aliphatic) side chains are attached. The first

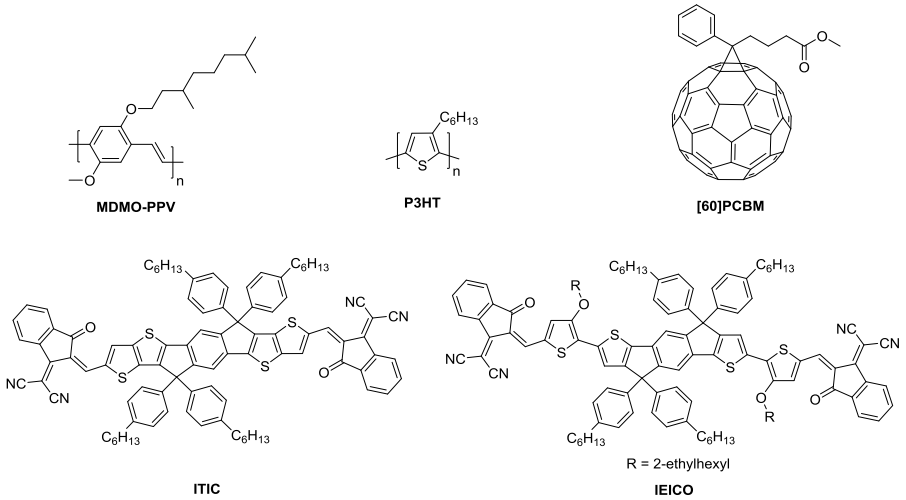

Scheme 1.1: Selection of historically important molecules and polymers.

polymer to rise to prominence was poly[2-methoxy-5-(3′,7′-dimethyloctyloxy)-1,4-phenylenevinylene] (MDMO-PPV),[43] followed by poly(3-hexylthiophene) P3HT (Scheme 1.1).[44] Both materials have relatively high optical band gaps, restricting the maximal J_{sc} that could be obtained. Hence, low band gap polymers were developed.

To reduce the band gap of a conjugated polymer, two design strategies have emerged: the stabilized quinoid form approach and the donor-acceptor or push-pull design. The quinoid approach is based on reducing the bond length alternation between single and double bonds when the polymer is excited (Peierls distortion). This is achieved by stabilizing the structure of the excited state or quinoid form of the polymer. An example of this is polyisothianaphthene (PITN), where the benzene ring gains aromaticity when the polymer is in the quinoid form, thus reducing the band gap from ~2 eV for polythiophene to ~1 eV for PITN (Scheme 1.2).[45]

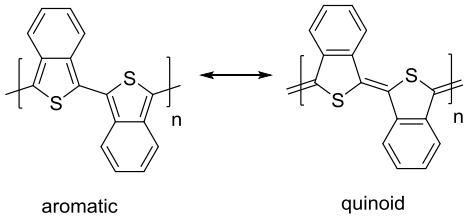

Scheme 1.2: PITN in the aromatic and quinoid form.

The donor-acceptor design (not to be confused with donor and acceptor materials, and therefore also called the push-pull mechanism) works by stabilizing the excited state via charge stabilization. In this architecture, electron-rich moieties (donors) are combined with electron-poor moieties (acceptors) in an alternating copolymer structure.[46,47] As can be seen in the energy diagram in Figure 1.5, the HOMO energy level is mostly determined by the donor, while the LUMO energy level is mostly determined by the acceptor. In this way, the energy levels can be controlled by changing donor or acceptor moieties or by making small adjustments to the chemical structure of the donor or acceptor. Also the solubility and tendency of aggregation can be controlled by tuning the solubilizing side chains. A recent development is the use of two donor or acceptor moieties in the same polymer backbone, thus creating a terpolymer architecture.[48]

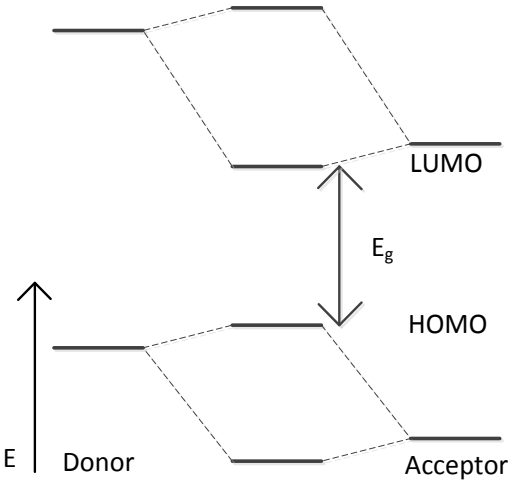

Fig. 1.5: Qualitative molecular orbital theory (QMOT) picture of the orbital mixing of an electron-deficient (Acceptor) and an electron-rich (Donor) moiety.

As these polymers are built up out of two distinct alternating groups, palladium-catalysed polycondensation reactions are mostly used to produce these polymers. In particular the Suzuki-Miyaura[49] and the Stille[50] reactions, in which one monomer is functionalized with a bromide and the other with an organometallic group (a boronic ester or trialkylstannyl, respectively), are used extensively throughout literature. Also the direct heteroarylation is gaining in popularity as a polymerization method.[51] In these reactions, it is important for the monomers to be pure and in stoichiometric balance with each other to

ensure high degrees of polymerization.[52] In the past we have found in our group that reactions under unoptimized conditions can lead to defects wherein two monomers functionalized with bromide can be coupled with one another, leading to lowered photovoltaic performance, stressing the importance of the optimization of the polymerization reaction.[53]

As acceptor materials, fullerene derivatives were introduced by Sariciftci et al.[54] and subsequently adopted as the standard acceptor material for many years. The most commonly used materials are [6,6]-phenyl-C_{61}-butyric acid methyl ester ([60]PCBM) (Scheme 1.1) and its C_{71} analogue ([70]PCBM). The latter absorbs light more strongly and therefore contributes more to current generation.[55] Good solubility, a high electron mobility[56] and affinity,[54] and their spatial symmetry all contributed to the success of these materials.[57] Recently, new acceptor materials have emerged as promising materials for the further development of organic photovoltaics such as ITIC and IEICO (Scheme 1.1).[58]

In blends with fullerene acceptors, PffBT4T (Scheme 1.3) is a class of highly efficient polymers. Developed in the group of He Yan, the solubilizing alkyl chains on these polymers can be finely tuned to achieve the optimal morphology of the blend in the active layers, illustrating the notion that the photovoltaic performance can be carefully optimized via structural modifications in the polymer. A record-high efficiency of 11.7% was thus reached with PffBT4T-C_9C_{11} (Scheme 1.3) in combination with [70]PCBM.[59] An example of structural modification used to tune the energy levels of non-fullerene acceptors was recently provided by Chen et al. By using a halogenation strategy on the acceptor FDICTF (Scheme 1.3), they were able to reach a PCE over 12% in combination with PBDB-T (Scheme 1.3).[60] Structural optimization of the polymer to reach the desired morphologies with non-fullerene acceptors remains important as well, as demonstrated in the case of PBT1 (Scheme 1.3). By careful optimization of the side chains, a PCE of 10% with [70]PCBM, and 12.7% with ITCPTC (Scheme 1.3) could be reached.[61] At the time of writing, the world record single junction solar cell consists of PM6 and Y6 as active layer materials (Scheme 1.3) and has a PCE of 15.7%.[62] The efficiency world record for organic tandem solar cells has now reached 17.3%, with a stack using PBDB-T and F-M as the front cell materials, and a ternary blend containing PTB7-Th, [70]PCBM and O6T-4F as the back cell (Scheme 1.3).[63]

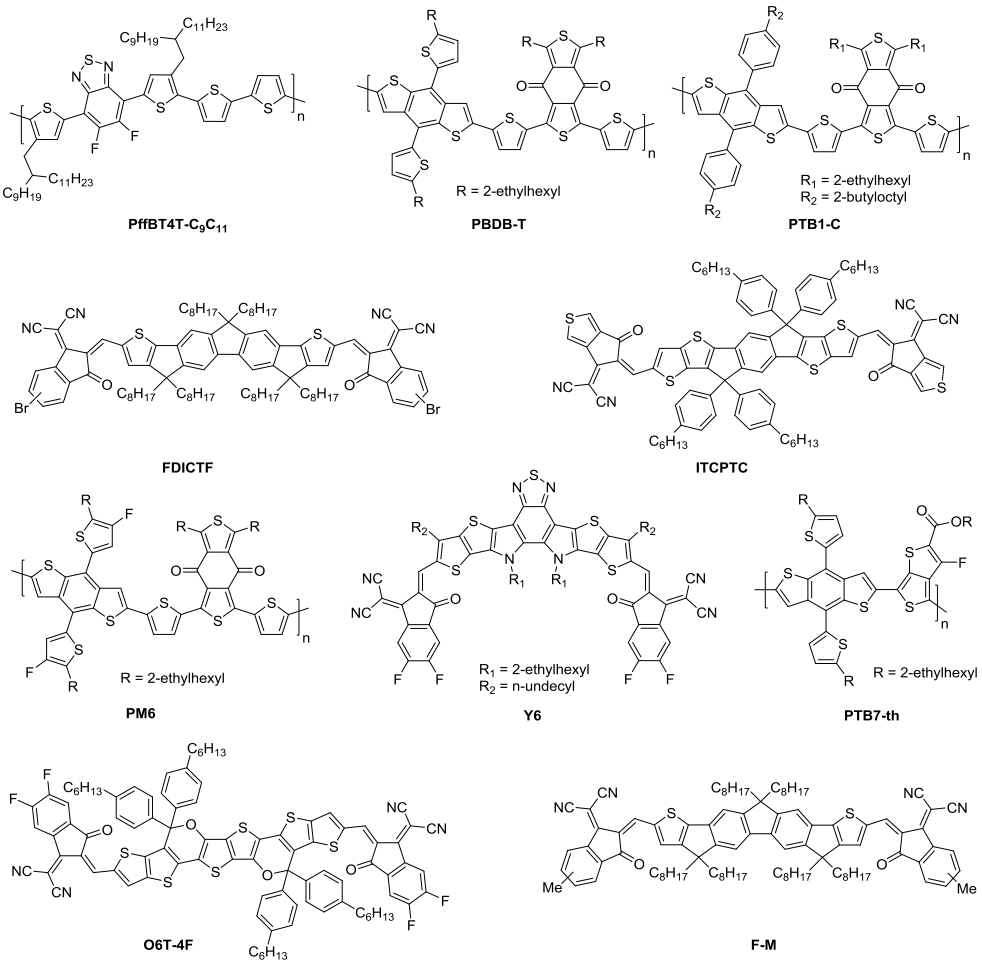

Scheme 1.3: Selection of highly efficient polymers and molecules used in OPV.

A class of polymers which has been extensively investigated in the past in our group is based on diketopyrrolopyrrole (DPP).[64] Having first been synthesized by Farnum in 1974 as phenyl flanked DPP,[65] its high absorption coefficient and good stability made it a good candidate as a base for photovoltaic materials. By using thiophene flanked DPP, first synthesized by Turbiez,[66] planarity was achieved which drastically improved the photovoltaic performance of these materials.[67] Other heteroaryl groups such as furan,[68] selenophene[69] and pyridine[70] have been used over the years to tune the properties of the

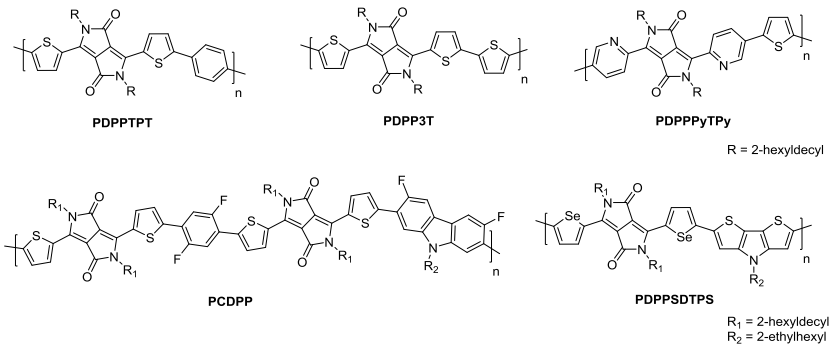

Scheme 1.4: Selection of DPP-based polymers.

materials. One interesting property is the strong π-π interaction between the DPP cores, causing a strong tendency of aggregation.[71] This is visible even in solution and can lead to semi-crystalline domains in the solid state. A higher degree of crystallinity can lead to both higher charge carrier mobilities, as well as a better morphology formation in combination with PCBM.[72] This has led to efficient DPP-based materials breaking the barrier of 9% PCE in combination with [70]PCBM.[73,74]

1.6 Morphology

As alluded to previously, the performance of organic solar cells is strongly dependent on the morphology of the active layer. To ensure that all excitons can reach an interface during their limited lifetime, an intimate mixture of the donor and acceptor is preferred. On the other hand, as soon the charges are separated, continuous pathways of donor and acceptor to the electrodes must be present to ensure efficient charge percolation. Thus, in case of a mixture which is too fine, charge generation will be efficient, but not all charges will be able to reach the electrodes, leading to greater non-geminate recombination and resulting in low fill factors and a reduced J_{sc}. In case of too coarse mixing, the reduction in charge generation efficiency will lead to a low J_{sc}. To maximize the J_{sc} and fill factor, the morphology must therefore be tuned between these two extremes.[75] In this regard not only the size but also the purity of the domains is important.[76] Since the morphology is defined during the deposition of the layer, the processing conditions, besides the physical properties of the materials, must be optimized to ensure the best morphology. Concentration, solvent, co-solvent, temperature, donor-acceptor ratio and post treatment

steps such as thermal or solvent annealing all have been found to influence the morphology in some way.[75]

Bulk heterojunctions of DPP-based polymers and methanofullerenes have been shown to produce fibre-like morphologies in the case of highly efficient cells processed from solvent mixtures containing chloroform and a co-solvent such as *ortho*-dichlorobenzene (*o*-DCB), 1,8-diiodooctane (DIO) or diphenyl ether (DPE) (Figure 1.6). The width of these fibres has been linked directly to the EQE and J_{sc} of the cells, with smaller widths producing higher J_{sc}s.[77,78] In cells processed from pure chloroform it was, however, found that large domains of PCBM are formed with polymer phase in between, which was attributed to liquid-liquid phase separation during the final stages of drying of the layer.[79] This large scale phase separation can be repressed by the addition of co-solvents. In this case, the polymers aggregate before liquid-liquid phase separation occurs, forming a fibrous network which traps the PCBM in between. Previous research in our group showed that the solubility of the polymer in the final solvent mixture just before drying directly influences the size and width of the fibres, which can be rationalized using a nucleation-and-growth model.[80,81] Reducing the solubility by reducing the length of the side chains was thus found to positively influence the morphology. Likewise, polymers with higher molecular weights were shown to produce better morphologies, which was attributed to the lower solubility associated with this higher molecular weight.

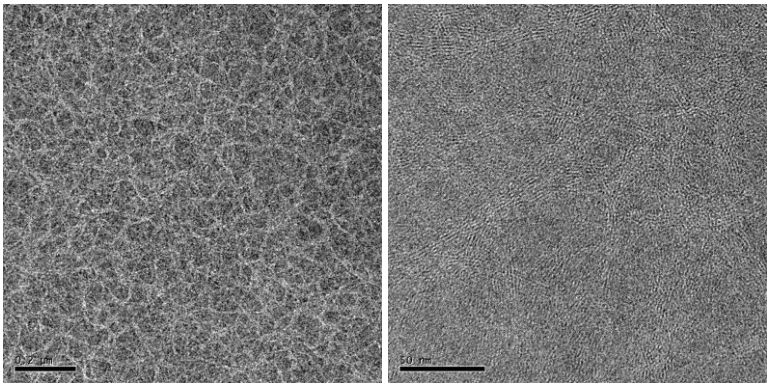

Fig. 1.6: Example of a TEM image of a blend between a DPP-based polymer and [70]PCBM. The polymer domains are visible as bright fibres against the darker [70]PCBM regions. In the right image crystalline fringes can be seen in the polymer domains.

1.7 Aim

The work described in this thesis aims to further the understanding of DPP polymer-fullerene solar cells, with an emphasis on active layer morphology formation, using structural modification of the polymers. An unanswered question in organic solar cell literature is the extent of the influence of defects in the polymer chain. Especially in the case of homocoupling of stannyl monomers it remains unclear what is the occurrence and influence on the photovoltaic properties. Another question that remains to be explained relates to the exact factors that influence morphology formation. As mentioned above, one theory is based on the solubility of the polymers, but more competing theories exist. The influence of structural elements in the polymer remains therefore hard to predict, and new insights into this are required to deepen our understanding. Finally the terpolymer design motif has been developed over the past years, but the use of this structural motif as a design tool can benefit from a better understanding and theory with predictive powers as to what the optoelectronic properties of the new polymers are going to be.

In chapter 2 the influence of homocoupling of trialkylstannyl monomers is investigated. In two DPP polymers (PDPP3T and PDPP4T) these defects are deliberately introduced to test their influence on the optoelectronic and photovoltaic properties of the materials. It is found that this type of homocoupling, unlike the homocoupling of bromide monomers, does not have a large influence in these materials. The occurrence of this type of defects is also found to be low in a representative test reaction, although the presence of air is found to play a role.

Chapter 3 describes the synthesis of a branched DPP polymer in order to influence the morphology of the active layer. By mixing a trifunctional monomer in the polymerization mixture, branched polymers are easily obtained. It is found that the solubility of the branched polymers is significantly lower than that of the corresponding linear polymer, resulting in an improved morphology formation. A strong increase in J_{sc} from 8.6 to 12.5 mA/cm² and PCE from 4.4% to 6.3% can in this way be achieved.

In chapter 4 DPP polymers with linear alkyl chains on the DPP core and branched alkyl chains on the adjacent thiophenes are presented. Through this alkyl chain substitution pattern a strong temperature dependency of the aggregation of the polymers in solution can be engineered. Unlike some reports in literature, processing these materials from hot solutions provides no enhancement in the morphology and efficiency compared to

processing from cold solutions. This temperature effect on the morphology formation can be understood in the framework of the nucleation-and-growth model, wherein the increased solubility of the polymer in hot solutions is not beneficial for the morphology. This result provides further insights in the role of temperature dependent solubility on the morphology formation.

Chapter 5 describes the synthesis and properties of DPP polymers substituted with siloxane containing side chains. By varying the amount of siloxane and alkyl chains, a series of polymers is obtained wherein the solubility reduces with the amount of siloxanes incorporated. This decrease in solubility coincides with a decrease in molecular weight, in this way providing low solubility materials with a low molecular weight, and highly soluble materials with high molecular weight. It is found that the materials with the lowest solubility show slightly larger fibre widths than materials with higher solubility, suggesting that the influence of molecular weight on the morphology formation is more complex than previously assumed. A decrease in J_{sc} and PCE with higher siloxane concentrations is observed, which can be attributed both to the aforementioned unfavourable influence on the morphology, as well as a decrease in the efficiency of charge generation. The hole mobility is, however, positively influenced by the presence of siloxane chains in any concentration.

A rule to predict the optoelectronic properties of regioregular terpolymers is established in chapter 6 by comparing seven terpolymers synthesized in our group to their related copolymers. It is found that the band gaps of the terpolymers are the arithmetic averages of the band gaps of the related copolymers. Likewise, the HOMO and LUMO energy levels of the terpolymers are the averages of the related copolymers. Solar cell devices made with these materials reveal that also the V_{oc} and energy loss are similarly related. Other examples of regular terpolymers in literature are found to follow the same behaviour, thus providing a rule to predict the optoelectronic properties of new terpolymers.

1.8 References

1 U.S. Energy Information Administration, International Energy Outlook 2013, DOE/EIQ-0484(2013).

2 J. Goldemberg World Energy Assessment; United Nations Development Programme: New York, NY, 2000.

3 N. S. Lewis, *Science*, 2007, **315**, 798-801.

4 A. E. Becquerel, *Comptes Rendus*, 1839, **9**, 561-567.

5 D. M. Chapin, C. S. Fuller, G. L. Pearson, *J. Appl. Phys.*, 1954, **25**, 676-677.

6 M. A. Green, Y. Hishikawa, E. D. Dunlop, D. H. Levi, J. Hohl-Ebinger, M. Yoshita, A. W. Y. Ho-Baillie, *Prog. Photovolt:.Res. Appl*., 2019, **27**, 3-12.

7 R. Fu, D. Feldman, R. Margolis, *U.S. Solar Photovoltaic System Cost Benchmark: Q1 2018*.

8 A. Honrubia-Escribano, F. J. Ramirez, E. Gómez-Lázaro, P. M. Garcia-Villaverde, M. J. Ruiz-Ortega, G. Parra-Requena, *Renew. Sust. Energy Rev*., 2018, **82**, 488-501.

9 https://www.nrel.gov/pv/assets/pdfs/best-research-cell-efficiencies-190416.pdf, consulted 15/05/2019.

10 Y. Li, G. Xu, C. Cui, Y. Li, *Adv. Energy Mater.*, 2018, **8**, 1701791.

11 Photo courtesy of Solliance/TNO.

12 http://www.opvius.com/energy-generating-shade-sail-in-shape-of-african-continent.html, consulted 16/05/2019.

13 D. Chemisana, A. Moreno, M. Polo, C. Aranda, A. Riverola, E. Ortega, Chr. Lamnatou, A. Domenech, G. Blanco, A. Cot, *Renew. Energy*, 2019, **137**, 177-188.

14 C. L. Chochos, M. Spanos, A. Katsouras, E. Tatsi, S. Drakopoulou, G. G. Fregoriou, A. Avgeropoulos, *Prog. Polym. Sci.*, 2019, **91**, 51-79.

15 S. Lizin, S. Van Passel, E. De Schepper, W. Maes, L. Lutsen, J. Manca, D. Vanderzande, *Energy Environ. Sci.*, 2013, **6**, 3136-3149.

16 M. P. Tsang, G. W. Sonnemann, D. M. Bassani, *Prog. Photovolt:.Res. Appl.*, 2016, **24**, 645-655.

17 M. P. Tsang, G. W. Sonnemann, D. M. Bassani, *Sol. Energy Mater. Sol. Cells*, 2016, **156**, 37-48.

18 N. Espinosa, M. Hösel, D. Angmo, F. C. Krebs, *Energy Environ. Sci.*, 2012, **5**, 5117-5132.

19 Z. Zhou, M. Carbajales-Dale, *Energy Environ. Sci.*, 2018, **11**, 603-608.

20 N. A. Ludin, N. I. Mustafa, M. M. Hanafiah, M. A. Ibrahim, M. A. M. Teridi, A. Zaharim, K. Sopian, *Renew. Sustain. Energy Rev.*, 2018, **96**, 11-28.

21 J. Guo, J. Min, *Adv. Energy Mater.*, 2019, **9**, 1802521.

22 https://infinitypv.com

23 https://www.heliatek.com

24 http://www.opvius.com

25 H. Kallmann, M. Pope, *J. Chem. Phys.*, 1959, **30**, 585-586.

26 C. K. Chiang, C. R. Fincher, Y. W. Park, A. J. Heeger, H. Shirakawa, E. J. Louis, S. C. Gau, A. G. MacDiarmid, *Phys. Rev. Lett.*, 1977, **39**, 1098-1101.

27 H. Shirakawa, E. J. Louis, A. G. MacDiarmid, C. K. Chiang, A. J. Heeger, *J. Chem Soc., Chem. Commun.*, 1977, **16**, 578-580.

28 B. A. Gregg, *J. Phys. Chem. B*, 2003, **107**, 4688-4698.

29 C. W. Tang, *Appl. Phys. Lett.*, 1986, **48**, 183-185.

30 J. D. A. Lin, O. V. Mikhnenko, J. Chen, Z. Masri, A. Ruseckas, A. Mikhailocsky, R. P. Raab, J. Liu, P. W. M. Blom, M. A. Loi, C. J. Garcia-Cervera, I. D. W. Samuel, T-Q. Nguyen, *Mater. Horiz.*, 2014, **1**, 280-285.

31 B. C. Thompson, J. M. J. Fréchet, *Angew. Chem. Int. Ed.*, 2007, **47**, 58-77.

32 Z. Yin, J. Wei, Q. Zheng, *Adv. Sci.*, 2016, **3**, 1500362.

33 American Society for Testing and Materials (ASTM) Standard G173-03, available at: http://rredc.nrel.gov/solar/spectra/am1.5.

34 E. Zimmermann, P. Ehrenreich, T. Pfadler, J. A. Dorman, J. Weickert, L. Schmidt-Mende, *Nat. Photon.*, 2014, **8**, 669-672.

35 D. J. Wehenkel, K. H. Hendriks, M. M. Wienk, R. A. J. Janssen, *Org. Electron.*, 2012, **13**, 3284-3290.

36 P. W. M. Blom, V. D. Michailetchi, L. J. A. Koster, D. E. Markov, *Adv. Mater.*, 2007, **19**, 1551-1566.

37 K. Vandewal, K. Tvingstedt, A. Gadisa, O. Inganäs, J. V. Manca, *Nat. Mater.*, 2009, **8**, 904-909.

38 M. C. Scharber, D. Mülhbacher, M. Koppe, P. Denk, C. Waldauf, A. J. Heeger, C. J. Brabec, *Adv. Mater.*, 2006, **18**, 789-794.

39 D. Veldman, S. C. J. Meskers, R. A. J. Janssen, *Adv. Func. Mater.*, 2009, **19**, 1939-1948.

40 W. Li, K. H. Hendriks, A. Furlan, M. M. Wienk, R. A. J. Janssen, *J. Am. Chem. Soc.*, 2015, **137**, 2231-2234.

41 W. Shockley, H. J. Queisser, *J. Appl. Phys.*, 1961, **32**, 510-519.

42 T. Kirchartz, K. Taretto, U. Rau, *J. Phys. Chem. C*, 2009, **113**, 17958-17966.

43 S. E. Shaheen, C. J. Brabec, N. S. Sariciftci, F. Padinger, T. Fromherz, J. C. Hummelen, *Appl. Phys. Lett.*, 2001, **78**, 841-843.

44 P. Schilinsky, C. Waldauf, C. J. Brabec, *Appl. Phys. Lett.*, 2002, **81**, 3885-3887.

45 F. Wudl, M. Kobayashi, A. J. Heeger, *J. Org. Chem.*, 1984, **49**, 3382-3384.

46 C. Duan, F. Huang, Y. Cao, *J. Mater. Chem.*, 2012, **22**, 10416-10434.

47 S. Holliday, Y. Li, C. K. Luscombe, *Prog. Polym. Sci.*, 2017, **70**, 34-51.

48 H. Luo, Z. Liu, *Polym. J.*, 2018, **50**, 21-31.

49 A. Suzuki, *Angew. Chem. Int. Ed.*, 2011, **50**, 6722-6737.

50 B. Carsten, F. He, H. J. Son, T. Xu, L. Yu, *Chem. Rev.*, 2011, **111**, 1493-1528.

51 L. G. Mercier, M. Leclerc, *Acc. Chem. Res.*, 2013, **46**, 1597-1605.

52 W. H. Carothers, *Trans. Faraday Soc.*, 1936, **32**, 39-49.

53 K. H. Hendriks, W. Li, G. H. L. Heintges, G. W. P. van Pruissen, M. M. Wienk, R. A. J. Janssen, *J. Am. Chem. Soc.*, 2014, **136**, 11128-11133.

54 N. S. Sariciftci, L. Smilowitz, A. J. Heeger, F. Wudl, *Synt. Met.*, 1993, **59**, 333-352.

55 M. M. Wienk, J. M. Kroon, W. J. H. Verhees, J. Knol, J. C. Hummelen, P. A. van Hal, R. A. J. Janssen, *Angew. Chem. Int. Ed.*, 2003, **115**, 3493-3375.

56 P. H. Wobkenberg, D. D. C. Bradley, D. Kronholm, J. C. Hummelen, D. M. de Leeuw, M. Colle, T. D. Anthopoulos, *Synt. Met.*, 2008, **158**, 468-472.

57 R. Ganesamoorthy, G. Sathiyan, P. Sakthivel, *Sol. Energy Mater. Sol. Cells*, 2017, **161**, 102-148.

58 J. Hou, O. Inganäs, R. H. Friend, F. Gao, *Nat. Mater.*, 2018, **17**, 119-128.

59 H. Hu, P .C. Y. Chow, G. Zhang, T. Ma, J. Liu, G. Yang, H. Yan, *Acc. Chem. Res.*, 2017, **50**, 2519-2528.

60 Y. Wang, Y. Zhang, N. Qiu, H. Feng, H. Gao, B. Kan, Y. Ma, C. Li, X. Wan, Y. Chen, *Adv. Energy Mater.*, 2018, **8**, 1702870.

61 T. Liu, L. Huo, S. Chandrabose, K. Chen, G. Han, F. Qi, X. Meng, D. Xie, W. Ma, Y. Yi, J. M. Hodgkiss, F. Liu, J. Wang, C. Yang, Y. Sun, *Adv. Mater.*, 2018, **30**, 1707353.

62 J. Yuan, Y. Zhang, L. Zhou, G. Zhang, H-L. Yip, T-K. Lau, X. Lu, C. Xhu, H. Peng, P. A. Johnson, M. Leclerc, Y. Cao, J. Ulanski, Y. Li, Y. Zou, *Joule*, 2019, **3**, 1140-1151.

63 L. Meng, Y. Zhang, X. Wan, C. Li, X. Zhang, Y. Wang, X. Ke, Z. Xiao, L. Ding, R. Xia, H-L. Yip, Y. Cao, Y. Chen, *Science*, 2018, **361**, 1094-1098.

64 W. Li, K. H. Hendriks, M. M. Wienk, R. A. J. Janssen, *Acc. Chem. Res.*, 2016, **49**, 78-85.

65 D. G. Farnum G., Mehta, G. G. I. Moor, F. P. Diegal, *Tetr. Lett.*, 1974, **29**, 2549-2552.

66 L. Bürgi, M. Turbiez, R. Pfeiffer, F. Bienewald, H-J. Kirner, C. Winnewisser, *Adv. Mater.*, 2008, **20**, 2217-2224.

67 M. M. Wienk, M. Turbiez, J. Gilot, R. A. J. Janssen, *Adv. Mater.*, 2008, **20**, 2556-2560.

68 G. Oklem, X. Song, L. Toppare, D. Baran, G. Gunbas, *J. Mater. Chem. C*, 2018, **6**, 2957-2961.

69 K. H. Hendriks, W. Li, M. M. Wienk, R. A. J. Janssen, *J. Am. Chem. Soc.*, 2014, **136**, 12130-12136.

70 J. W. Jung, F. Liu, T. P. Russell, W. H. Jo, *Chem. Commun.*, 2013, **49**, 8495-8497.

71 J. H. Kim, D. H. Lee, D. S. Yang, D. U. Heo, K. H. Kim, J. Shin, H-J. Kim, K-Y. Baek, K. Lee, H. Baik, M. J. Cho, D. H. Choi, *Adv. Mater.*, 2013, **25**, 4102-4106.

72 I. Meager, R. S. Ashraf, S. Mollinger, B. C. Schroeder, H. Bronstein, D. Beatrup, M. S. Vezie, T. Kirchartz, A. Salleo, J. Nelson, I. McCulloch, *J. Am. Chem. Soc.*, 2013, **135**, 11537-11540.

73 Y. Liu, G. Li, Z. Zhang, L. Wu, J. Chen, X. Xu, X. Chen, W. Ma, Z. Bo, *J. Mater. Chem. A*, 2016, **4**, 13265-13270.

74 M. Li, J. Li, D. Di Carlo Rasi, F. J. M. Colberts, J. Wang, G. H. L. Heintges, B. Lin, W. Li, W. Ma, M. M. Wienk, Janssen R. A. J., *Adv. Energy Mater.*, 2018, **8**, 1800550.

75 H. Lee, C. Park, D. H. Sin, J. H. Park, K. Cho, *Adv. Mater.*, 2018, **30**, 1800453.

76 T. Ferron, M. Waldrip, M. Pope, B. A. Collins, *J. Mater. Chem. A*, 2019, **7**, 4536-4548.

77 W. Li, K. H. Hendriks, A. Furlan, W. S. C. Roelofs, S. C. J. Meskers, M. M. Wienk, R. A. J. Janssen, *Adv. Mater.*, 2014, **26**, 1565-1570.

78 W. Li, K. H. Hendriks, A. Furlan, W. S. C. Roelofs, M. M. Wienk, R. A. J. Janssen, *J. Am. Chem. Soc.*, 2013, **135**, 18942-18948.

79 S. Kouijzer, J. J. Michels, M. van den Berg, V. S. Gevaerts, M. Turbiez, M. M. Wienk, R. A. J. Janssen, *J. Am. Chem. Soc.*, 2013, **135**, 12057-12067.

80 J. J. van Franeker, G. H. L. Heintges, C. Schaefer, G. Portale, W. Li, M. M. Wienk, P. van der Schoot, R. A. J. Janssen, *J. Am. Chem. Soc*¸ 2015, **137**, 11783-11794.

81 J. J. van Franeker, M. Turbiez, W. Li, M. M. Wienk, R. A. J. Janssen, *Nat. Commun.*, 2015, **6**, 6229.

Chapter 2

On the homocoupling of trialkylstannyl monomers in the synthesis of diketopyrrolopyrrole polymers and its effect on performance of polymer-fullerene photovoltaic cells

Abstract

Homocoupling of monomers in a palladium-catalysed copolymerization towards donor-acceptor polymers affects the perfect alternating structure and may deteriorate the performance of such materials in solar cells. Here we investigate the effect of homocoupling bis(trialkylstannyl)-thiophene and -bithiophene monomers in two low band gap poly(diketopyrrolopyrrole-alt-oligothiophene) polymers by deliberately introducing extended oligothiophene defects in a controlled fashion. We find that extension of the oligothiophene by one or two thiophenes and creating defects up to at least 10% does not significantly affect the opto-electronic properties of the polymers or their photovoltaic performance as electron donor in solar cells in combination with [6,6]-phenyl-C_{71}-butyric acid methyl ester as acceptor. By using model reactions, we further demonstrate that for the optimized synthetic protocol and palladium-catalyst system the naturally occurring defect concentration in the polymers is expected to be less than 0.5%.

This work has been published: G. H. L. Heintges, R. A. J. Janssen, *RSC Adv.*, 2019, **9**, 15703-15714.

2.1 Introduction

The performance of conjugated polymers in organic solar cells is primarily determined by the chemical structure of the backbone and side chains that provide the material with its semiconducting and structural properties. However, also other factors such as the molecular weight distribution,[1-3] the presence of end groups,[4,5] possible branching of the main chain,[6] and impurities in the polymer can affect the functional properties.[7-9] In addition, structural defects in the polymer main chain have been found to be important. For asymmetric monomers, head-to-head or tail-to-tail couplings may occur, next to the preferred head-to-tail linkages.[10,11] Alternatively, in the case of cross-coupling polymerizations where two complementary comonomers are used, a coupling reaction between two identical monomers introduces a defect in the perfect alternating structure. This last phenomenon is referred to as homocoupling. Homocoupling reactions are known to occur in the Suzuki,[12] Stille,[13] and direct arylation[14] cross-coupling polycondenstation reactions that are commonly used to synthesize donor-acceptor small molecules and polymers that find widespread use organic solar cells. The topic of structural defects is finding increasing awareness and was recently reviewed by Maes *et al.*[15]

The homocoupling of two bromoaryl monomers in the Suzuki and Stille polymerization reaction towards low band gap diketopyrrolopyrrole (DPP) polymers has previously been investigated in our group in some detail.[16] The defect is caused by homocoupling of two brominated dithienyl-diketopyrrolopyrrole (T-DPP-T) units, creating T-DPP-2T-DPP-T defects in the polymer main chain. These defects generate a low-energy feature in the absorption spectrum. As a result, the 2T defect can act as a trap for excitons and charges, and thereby explains the significant decrease in photovoltaic performance of solar cells when polymers with increasing 2T defect concentration were blended with [6,6]-phenyl-C_{71}-butyric acid methyl ester ([70]PCBM).[16] An extensive overview of the literature showed that the same homocoupling defect is present in many DPP polymers that were reported up to 2014.[16] We found it to occur when a too low ligand-to-palladium ratio is used in the reaction and that it can largely be avoided by modifying the catalyst system. The results also clearly demonstrated that this type of defect should be avoided because it is detrimental to the photovoltaic performance of these materials.

In a subsequent study Li *et al.* confirmed the formation of T-DPP-2T-DPP-T low-energy defects occurring in the Stille polymerization of poly(diketopyrrolopyrrole-*alt*-

quaterthiophene) (PDPP4T).[17] Li *et al.* also suggested that homocoupling of the trialkylstannyl monomers would occur to a significant extent.[17] They were unable to obtain direct structural or spectroscopic evidence, but argued that because of the almost quantitative reaction yield of the polymerization, the two different homocoupling reactions should occur to a similar extent. In a recent study, Costantini *et al.* used scanning tunnelling microscopy to investigate structural defects in poly(diketopyrrolopyrrole-*alt*-terfurane) (PDPP3F) deposited on a Au(111) surface. They found a significant amount (ca. 12%) of defects in which an extra furan ring is present as a result of the homocoupling reaction between two 2,5-bis(trimethylstannyl)furan monomers.[18] Coupling of the trialkylstannyl monomers in a Stille cross-coupling polymerization reaction can occur whenever palladium is existent in an oxidized form.[19-22] This oxidized palladium can be present in the reaction mixture due to the ageing or improper storage of the catalyst, insufficient degassing of the reaction mixture, or because the catalyst system is designed as such, as is in the case of bis(triphenylphosphine)palladium(II) dichloride. In these cases a double transmetallation step occurs, followed by a reductive elimination transforming the Pd(II) into a Pd(0) species, which can then proceed to catalyse the reaction as usual, and results in a coupling between two organometallic partners.

Recently, Sommer *et al.* investigated this type of homocoupling in poly(*N*-9′-heptadecanyl-2,7-carbazole-*alt*-5,5-(4′,7′-di-2-thienyl-2′,1′,3′-benzothiadiazole)) (PCDTBT) polymers synthesized via a Suzuki reaction and found that the homocoupling of the boronic ester substituted carbazole monomers resulted in a remarkably lower performance in organic solar cells from defect concentrations as low as 2.4% onwards.[23] Whether this decrease was due to electronic or morphological effects was, however, not very clear.

In DPP polymers, the effect of extended donor segment defects has not yet been systematically investigated, even though its occurrence, for the reasons mentioned above, can be expected. Usually, DPP donor-acceptor polymers are synthesized using Stille coupling reactions employing a dibromide monomer containing the electron-deficient DPP unit and a bis(trialkylstannyl) monomer comprising the electron-rich moiety. The reason for this choice is that oxidative addition is facilitated by electron withdrawing groups and transmetallation is facilitated by electron rich organotin compounds. Hence, homocoupling of the organotin compounds typically results in extended electron-rich segments in the

polymer.[24] These can have two distinct effects. First, the energy levels of the polymer might be affected, because the extended donor defect can have energy levels that deviate from those of the polymer and cause a shift of the oxidation potential. Depending on the direction of this shift of the energy levels, the defects can act as traps and contribute to an increased non-radiative recombination which lowers the open-circuit voltage (V_{oc}) of the cells. Because DPP polymers usually display a wider optical band gap when the donor block is extended, it is not expected that these defects will form energetic traps, although optical effects could still be visible. Second, the homocoupling defect effectively reduces the number of DPP units in the chain that generally carry the solubilizing side chains, such that the solubility could be affected. This could have an influence on the morphology of the active layers, resulting in differences in short-circuit current (J_{sc}) or fill factor (FF).[3]

Here we investigate the effect and extent of the homocoupling reaction of the trialkylstannyl monomers in two archetype DPP polymers by deliberate introduction of defected conjugated segments and by performing model reactions on monomer analogues. As it is a frequently used monomer, thiophene and its defect, bithiophene, are chosen initially. In a second example, the structural difference between the parent polymer and its homocoupling defect is enhanced by using bithiophene and its defect, quaterthiophene, as monomer. We demonstrate that for these polymers, this type of homocoupling does not occur to a significant extent and that if it would occur, the effects on the opto-electronic properties and photovoltaic performance are small or even absent.

2.2 Results and discussion

2.2.1 Poly(diketopyrrolopyrrole-*alt*-terthiophene) with quaterthiophene defects

Poly{2,2′-[(2,5-bis(2-hexyldecyl)-3,6-dioxo-2,3,5,6-tetrahydropyrrolo[3,4-*c*]pyrrole-1,4-diyl)dithiophene]-5,5′-diyl-*alt*-thiophen-2,5-diyl}) (PDPP3T) is a well-known small band gap DPP polymer used for high-performing organic field-effect transistors and solar cells and a good model system to investigate the effect of homocoupling. To simulate the homocoupling of two trialkylstannyl monomers, a random terpolymer approach was used in which 3,6-bis(5-bromothiophen-2-yl)-2,5-bis(2-hexyldecyl)-2,5-dihydropyrrolo[3,4-*c*]pyrrole-1,4-dione (**1**) was co-polymerized with 2,5-

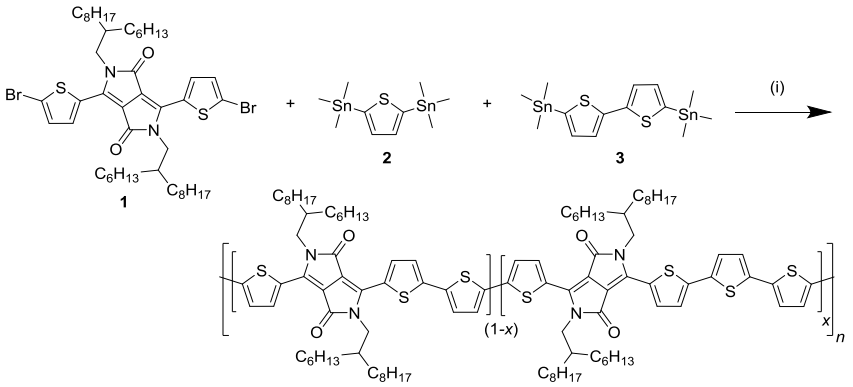

Scheme 2.1: Synthesis of the PDPP3T polymers with 4T defects. The stoichiometry of monomers **2** and **3** was altered to obtain x = 5, 10 and 20% of intentional defects. (i) $Pd_2(dba)_3/PPh_3$, toluene/DMF, 115 °C.

bis(trimethylstannyl)thiophene (**2**) and 5,5'-bis(trimethylstannyl)-2,2'-bithiophene (**3**) in varying ratios (Scheme 2.1). This resulted in PDPP3T polymers with 5, 10 and 20% of 4T defects added in the chain.

Gel permeation chromatography (GPC) in *ortho*-dichlorobenzene (*o*-DCB) at 140 °C revealed a decreasing trend in the number average molecular weight (M_n) from 148 to 88 kDa when increasing the amounts of 4T defects from 5% to 20% (Table 2.1). Several reasons can explain a reduced M_n. We tentatively ascribe this trend to a decrease in solubility with increasing defect content. As mentioned above, the 4T segments effectively dilute the side chain-bearing DPP units in the main chain. This lowers the solubility and may cause the polymers above a certain length to precipitate out of solution during the polymerization. To fairly compare the defect containing polymers with defect-free PDPP3T, two batches of differing molecular weight were chosen corresponding roughly to the molecular weights obtained in defect containing polymers.

The UV-vis-NIR absorption spectra of the PDPP3T polymers measured in solution and thin films (Figure 2.1) show no differences in shape of the absorption or optical band gap as function of the number of defects. When compared to an essentially defect-free PDPP3T, a difference in absorption maximum is visible in the solution spectra. This could be due to a different tendency towards aggregation in solution, and would suggest that the defect-free PDPP3T aggregates more than the defect-containing polymers. The shift in absorption maximum is, however, unlikely to be linked to the electronic nature of the defects as between varying levels of 4T defects no difference can be seen. We note that the

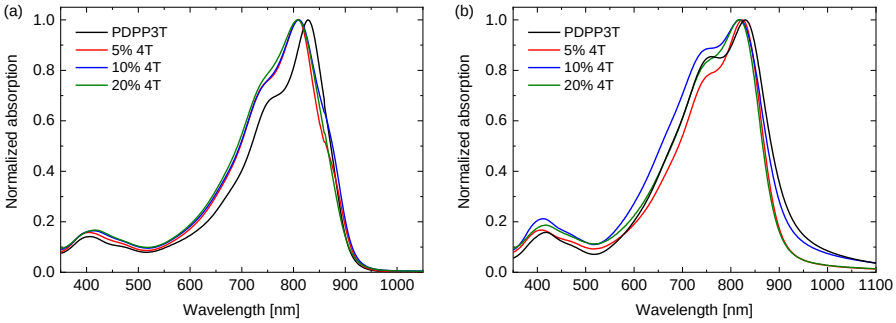

Fig. 2.1: UV-vis-NIR spectra of PDPP3T polymers with 4T defects. (a) Dissolved in chloroform. (b) In thin films.

Table 2.1: Physical properties of the PDPP3T polymers with different defect ratios.

Polymer	M_n [kDa]	M_w [kDa]	$Đ$	$E_{g,\,opt}$[a] [eV]	HOMO[b] [eV]	LUMO[b] [eV]
PDPP3T	147	400	2.7	1.33	−5.14	−3.34
	68	255	3.7			
5% 4T	148	399	2.7	1.35	−5.13	−3.35
10% 4T	123	330	2.7	1.36	−5.03	−3.35
20% 4T	88	215	2.4	1.36	−5.10	−3.34

[a] Determined from the absorption onset in thin films.

[b] Determined with square wave voltammetry vs. Fc/Fc^+, which was set at −4.8 eV vs. vacuum.

signal at ~400 nm, which is assigned to a transition to a higher-energy state, shows a gradual shift from 3.06 eV for PDPP3T, via 3.07 (5% 4T) and 3.01 (10% 4T), to 2.98 eV (20% 4T) when the defect level is increased. Such small shift with extending the donor segment is also seen in the corresponding small molecule compounds T-DPP-3T-DDP-T and T-DPP-4T-DDP-T where the corresponding peaks are found at 3.16 eV for the 3T derivative and at 3.10 eV for the 4T derivative. In thin films the differences are also small. Because the optical band gap of PDPP4T (the defect segments) is at 1.46 eV (vide infra) and larger than the band gap of PDPP3T at 1.33 eV, the presence of 4T segments will unlikely result in a clear change of the absorption spectrum and 4T defects are not expected to influence the optical band gap.

Square wave voltammetry was used to determine the energy levels of the polymers. Table 2.1 reveals there are no significant differences in energy levels between the polymers. Again, 4T defects are also not expected to exert a strong effect because the HOMO and LUMO energy levels of PDPP4T (HOMO: −5.13 eV, LUMO: −3.26 eV) are not too dissimilar from those of PDPP3T (HOMO: −5.14 eV, LUMO: −3.34 eV).

Solar cells with an ITO/PEDOT:PSS/active layer/LiF/Al device configuration were produced by spin coating mixed solutions of the PDPP3T polymers and [70]PCBM (1:2 w/w) in chloroform containing 7.5 vol% of *o*-DCB. As can be seen in Table 2.2 and Figure 2.2 there are no clear trends in the power conversion efficiencies (PCEs) of the defect-containing polymers. They all perform slightly worse than PDPP3T for a similar M_n. The V_{oc} of the defect-containing polymers lies between 0.65 V and 0.67 V, which coincides with the range generally observed for defect-free PDPP3T. This indicates, in accordance with the results from the square wave voltammetry, that this type of defect has little to no influence on the energy levels of the polymer and therefore does not affect the V_{oc}. The fill factors lie between 0.64 and 0.68, and are also comparable with the FF of defect-free PDPP3T cells. This indicates that the 4T segments do not strongly increase the recombination of free charges, which is concurrent with the notion that these defects do not act as energetic traps.

The main difference between the cells listed in Table 2.2 occurs in the J_{sc}. When comparing the 20% defect polymer with the low M_n defect-free PDPP3T batch, a slightly lower J_{sc} is found, even though the molecular weights are comparable. The same is the case in the comparison between the 5% defect polymer and the high M_n defect-free PDPP3T batch. Taken separately, these observations could suggest that the homocoupling defects negatively influence the J_{sc} of the solar cells. However, this conclusion is weakened when considering the lack of a trend in J_{sc} with increasing amounts of defects. If defects negatively influence J_{sc}, the 10% defect polymer would be expected to have a lower J_{sc} than the 5% defect polymer, both on account of the higher amount of 4T segments and the lower M_n. This is, however, not the case and leads to the conclusion that these differences in J_{sc} are most likely caused by other factors such as molecular weight and nanomorphology and that the possible influence of the 4T defects, even in quite large concentrations (10% and 20%), is small enough to be eclipsed by other effects.

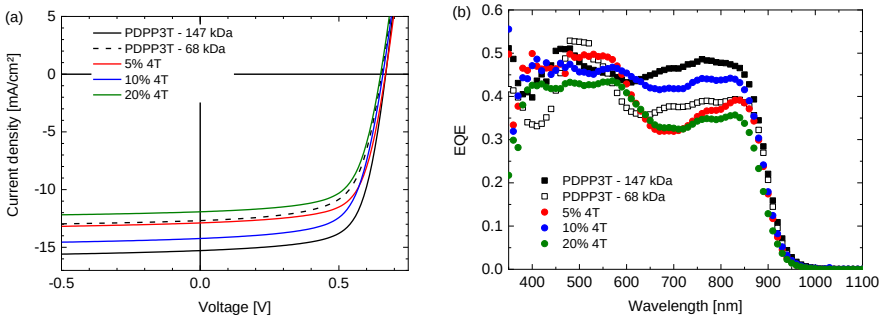

Fig. 2.2: (a) *J*–*V*-characteristics of PDPP3T:[70]PCBM (1:2 w/w) polymer solar cells in which the PDPP3T polymers contain 4T defects (see legends). (b) Corresponding EQE spectra.

Table 2.2: Photovoltaic performance of the PDPP3T polymers with 4T defects.[a]

Polymer	M_n [kDa]	J_{sc} [mA/cm²]	V_{oc} [V]	FF	PCE [%]
PDPP3T	147	15.4 (15.3)	0.67 (0.66)	0.69 (0.68)	7.1 (6.9)
PDPP3T	68	13.6 (13.5)	0.65 (0.65)	0.66 (0.66)	5.9 (5.8)
5% 4T	148	13.4 (14.1)	0.67 (0.66)	0.68 (0.64)	6.1 (6.0)
10% 4T	123	14.6 (14.6)	0.66 (0.65)	0.66 (0.65)	6.4 (6.2)
20% 4T	88	12.4 (12.5)	0.65 (0.65)	0.67 (0.66)	5.4 (5.3)

[a] Best cells are shown, numbers between parentheses refer to the average over 4 cells.

2.2.2 Poly(diketopyrrolopyrrole-*alt*-quaterthiophene) with sexithiophene defects

To introduce a larger defect, PDPP4T was chosen as the next target for modification. PDPP4T can be synthesized by polymerization of a dibrominated DPP monomer such as **1** and 5,5'-bis(trimethylstannyl)-2,2'-bithiophene (**3**). The associated homocoupling defect would them be a 6T segment. Introducing 6T segments in PDPP4T in a fashion analogous to Scheme 2.1 proved to be a synthetic challenge, owing to the difficulty of obtaining a bis(trialkylstannyl) derivative of the unsubstituted quaterthiophene. It was therefore decided to asymmetrically extend a DPP monomer. By reacting 3-(5-bromothiophen-2-yl)-2,5-bis(2-decyltetradecyl)-6-(thiophen-2-yl)-2,5-dihydropyrrolo[3,4-*c*]pyrrole-1,4-dione (**4**) with 2-([2,2'-bithiophen]-5-yl)-4,4,5,5-tetramethyl-1,3,2-dioxaborolane (**5**) it was possible to obtain **6**, which was converted by bromination with *N*-bromosuccinimide into **7** as shown in Scheme 2.2. We used long 2-decyltetradecyl side

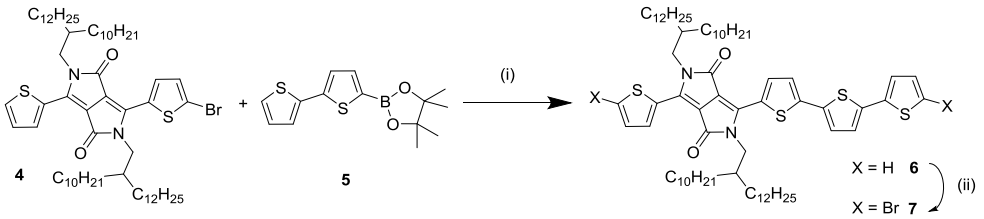

Scheme 2.2: Synthesis of the asymmetrically extended monomer **7** to introduce 6T defects in a PDPP4T polymer. (i)) $Pd_2(dba)_3/PPh_3$, toluene, $K_3PO_{4\ (aq)}$, 115 °C; (ii) *N*-bromosuccinimide, $CHCl_3$, RT.

chains on the DPP unit in **4** to ensure sufficient solubility of the extended monomer **7** and of the resulting PDPP4T polymers.

This asymmetrically extended DPP monomer **7** introduces the possibility of creating 8T segments, even in the absence of homocoupling reactions. To keep this possibility small and to keep the defect concentration within levels which are expected to occur during a normal polymerization reaction, polymers with 2% and 5% of defects were synthesized, together with defect-free PDPP4T as a reference, as shown in Scheme 2.3.

GPC analysis in *o*-DCB at 140 °C revealed comparable molecular weights for the three PDPP4T polymers, which should allow for a more direct comparison of the materials and enable to observe the effects of the 6T segments more clearly.

The UV-vis-NIR absorption spectra showed no significant difference between the three polymers (Figure 2.3). In thin films the optical band gap is at 1.46 eV (Table 2.3). It is

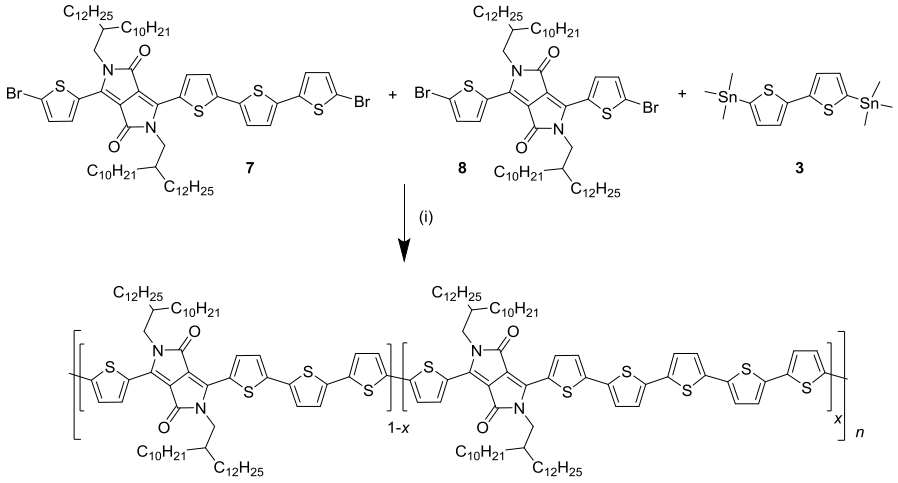

Scheme 2.3: Synthesis of the PDPP4T polymers with 6T defects. The stoichiometry of the monomers **7** and **8** was altered to obtain x = 0, 2 and 5% of intentional defects. (i) $Pd_2(dba)_3/PPh_3$, toluene/DMF, 115 °C.

not expected that 6T segments would have a lower optical band gap than the 4T segments, because the optical band gap of a PDPP6T polymer of 1.48 eV[25] is close to that of PDPP4T (1.46 eV). Analysis of the HOMO and LUMO energy levels with square wave voltammetry also revealed no significant differences (Table 2.3). As in the case of PDPP3T, the defects seem to have no important influence on the electronic structure of the materials.

Solar cells were made from a chloroform solution containing 10 vol% *o*-DCB, using the PDPP4T polymers and [70]PCBM (1:2 w/w) as active layer, employing the ITO/PEDOT:PSS/active layer/LiF/Al cell configuration. As can be seen in Figure 2.4 and Table 2.4, the solar cells all show very similar performance. The V_{oc} remains exactly the same, in concurrence with the results obtained from square wave voltammetry. The FF and J_{sc} show some variation, but differences are within the margin of error as can be seen in the averages over multiple cells. This indicates very clearly that the 6T segments, despite having a particularly low solubility, do not change the morphology of the layer

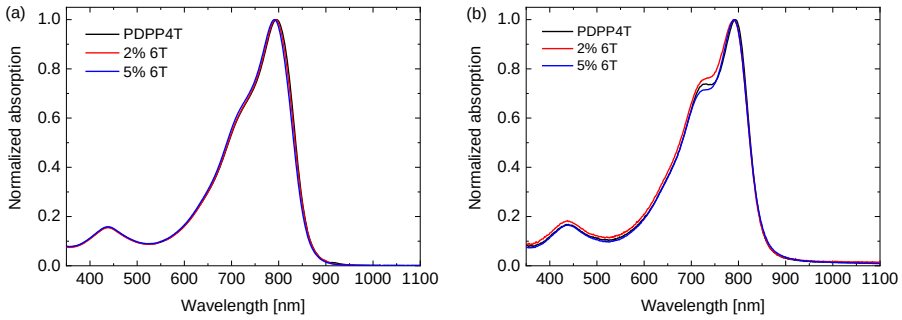

Fig. 2.3: UV-vis-NIR spectra of the PDPP4T polymers with 6T defects. (a) Dissolved in chloroform. (b) In thin films.

Table 2.3: Physical properties of the PDPP3T polymers with 6T defects.

Polymer	M_n [kDa]	M_w [kDa]	$Đ$	$E_{g,\,opt}$ [eV]	HOMO[a] [eV]	LUMO[a] [eV]
PDPP4T	83	150	1.8	1.46	−5.13	−3.26
2% 6T	79	150	1.9	1.47	−5.13	−3.26
5% 6T	79	144	1.8	1.46	−5.13	−3.25

[a] Determined with square wave voltammetry vs. Fc/Fc^+, which was set at −4.8 eV vs. vacuum.

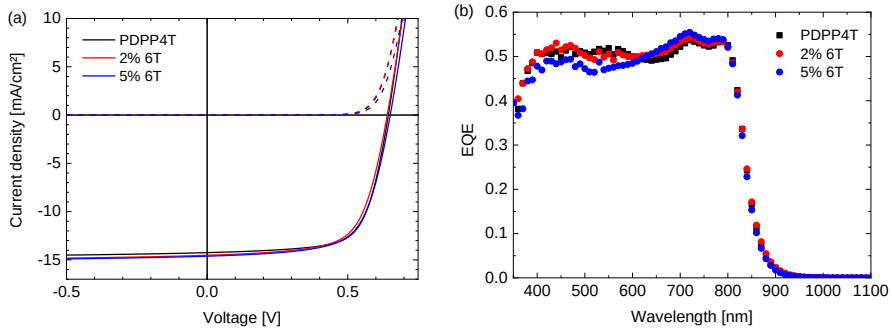

Fig. 2.4: (a) *J*–*V*-characteristics of PDPP4T:[70]PCBM (1:2 w/w) polymer solar cells in which the PDPP4T polymers contain 6T defects (see legends). (b) Corresponding EQE spectra.

Table 2.4: Photovoltaic performance of the PDPP4T polymers.[a]

Polymer	M_n [kDa]	J_{sc} [mA/cm²]	V_{oc} [V]	FF	PCE [%]
PDPP4T	83	15.3 (15.2)	0.64 (0.64)	0.69 (0.66)	6.8 (6.4)
2% 6T	79	15.4 (15.0)	0.64 (0.64)	0.66 (0.66)	6.5 (6.3)
5% 6T	79	15.0 (14.8)	0.65 (0.64)	0.66 (0.66)	6.5 (6.3)

[a] Best cells are shown, numbers between parentheses refer to the average over 4 cells.

significantly. Therefore it has to be concluded that this 6T defect has no influence on the optoelectronic properties or solar cell performance in concentrations up to 5%.

2.2.3 Model homocoupling reactions

In the previous sections is was established that deliberately introducing homocoupling defects exerts no consistent effect on the optical and photovoltaic properties of the resulting PDPP3T and PDPP4T polymers in concentrations up to 5% or maybe even 20%. Hence, from these data it is not possible to estimate the amount of naturally occurring defect during the synthesis and the question arises how much homocoupling occurs in these Stille polymerizations. To address this question, the following experiment was conceived. A monobrominated DPP monomer, 3-(5-bromothiophen-2-yl)-2,5-bis(2-decyltetradecyl)-6-(thiophen-2-yl)-2,5-dihydropyrrolo[3,4-*c*]pyrrole-1,4-dione (**4**), was reacted with 5,5′-bis(trimethylstannyl)-2,2′-bithiophene (**3**) (Scheme 2.4). The mixture of reactants was prepared and dissolved before being separated in three flasks. One flask was treated in the

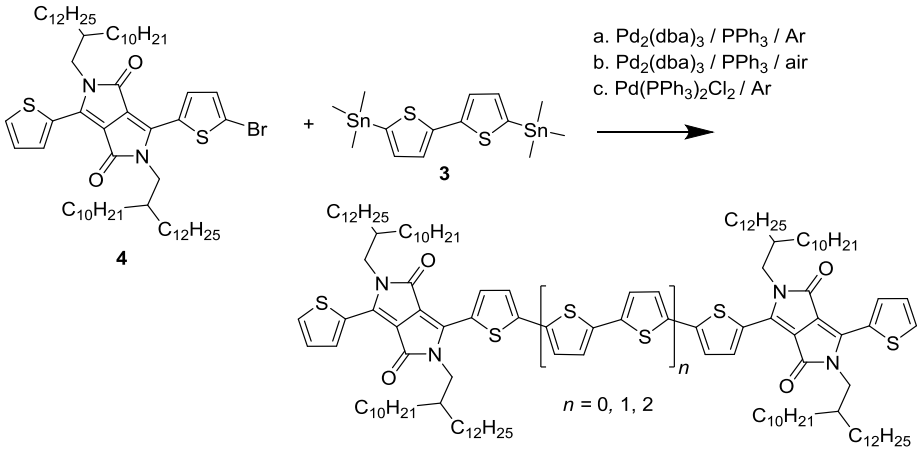

Scheme 2.4: Model homocoupling Stille reaction under three different catalytic conditions. The main product is *n* = 1. Homocoupling of **4** will result in the product with *n* = 0, while homocoupling of **3** and subsequent reactions with **4** will result in the product with *n* = 2.

same way as Stille polymerizations are usually conducted: 1.5% of tris(dibenzylideneacetone)dipalladium(0) ($Pd_2(dba)_3$) and 6% of triphenylphosphine (PPh_3) were added before being degassed with argon, sealed and heated. Another flask was subjected to the same treatment except that it was not degassed and ambient air was allowed to remain in the flask. This was considered as a simulation of an error or oversight during normal polymerization. To the last flask, 3% of bis(triphenylphosphine)palladium(II) dichloride ($Pd_2(PPh_3)_2Cl_2$) was added as a catalyst, before the mixture was degassed with argon, sealed and heated. This was used as a reference, as the presence of 3% of Pd(II) should cause around 3% of homocoupling defect if all Pd(II) is converted to Pd(0).

All reactions were left overnight and the crude products were isolated without any purification. MALDI-TOF-MS was then used to investigate the composition of the product mixtures. Figure 2.5c shows that in the case of the reaction with Pd(II) as catalyst, the main peak, belonging to the product with four thiophene rings between DPP cores (*n* = 1, *m*/*z* = 2107 amu), is flanked by peaks at 2271 and 1943 amu. These peaks correspond to the products with six (*n* = 2) and two (*n* = 0) thiophene rings in between the DPP moieties. Assuming that the ionization efficiency of these three species is the same, which is likely due to their similar chemical structures, the intensity of the peaks relative to the main peak can indicate the concentration of these species. The relative intensity of the 6T product is

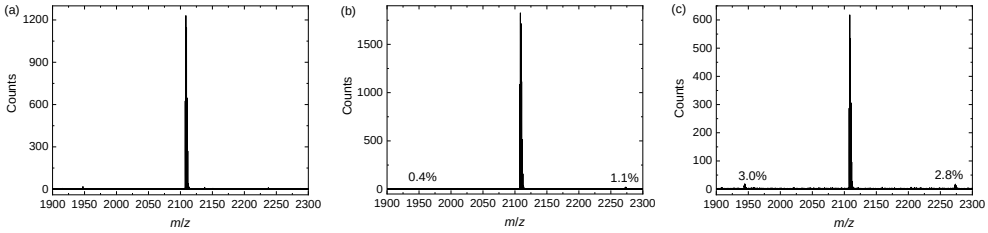

Fig. 2.5: MALDI-TOF-MS of the homocoupling model reaction mixtures (Scheme 2.4). (a) With standard conditions. (b) With air. (c) With Pd(II).

2.8% is due to homocoupling of **3** and in good agreement expected value of 3% when all Pd(II) catalyst is reduced to Pd(0). The 2T product, which is the result of homocoupling of (**4**), is present in 3.0% relative intensity. The presence of this product is slightly unexpected but possibly due to the age of the catalyst.

Repeating this analysis for the degassed sample and Pd(0) catalyst (Figure 2.5a), it is clear that no homocoupling of any kind can be detected above the noise level. This indicates that if any homocoupling is present in this sample, its relative concentration is under 0.5%. For the Pd(0) catalysed reaction exposed to ambient air (Figure 2.5b), both kinds of homocoupling can be detected: 1.1% of the trialkylstannyl-based homocoupling product (n = 2 in Scheme 2.4) is present, which suggests that oxidation of palladium can occur when the reaction mixture is exposed to air. Also, 0.4% of the bromide-based homocoupling (n = 0 in Scheme 2.4) can be observed, indicating that exposure to air can

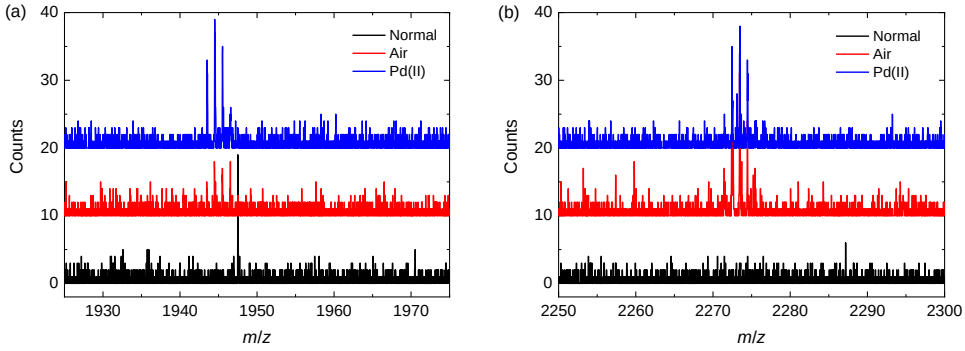

Fig. 2.6 Detail of the MALDI-TOF mass spectra of the three mixtures, showing the peaks corresponding to the product with two central thiophene rings (n = 0 in Scheme 2.4) (a) and the product with six central thiophene rings (n = 2 in Scheme 2.4) (b).

also influence this coupling mechanism. This is possibly due to oxidation of the triphenylphosphine ligand, leading to an imbalance in the ligand to palladium ratio, which was proven before to have an effect on this type of homocoupling.[16] Figure 2.6 shows details of the MALDI-TOF mass spectra in the region where homocoupling products $n = 0$ and $n = 2$ are expected.

2.3 Conclusion

By deliberately creating defects in the monomers of donor-acceptor DPP polymers, we investigated the effect of homocoupling reactions between two organometallic trialkylstannyl monomers in palladium-catalysed cross-coupling polymerization reactions. In the case of PDPP3T, the 4T defects that were introduced seemed to have little effect on the optoelectronic properties of the resulting materials. Also in solar cells no consistent effect of the homocoupling defects on the photovoltaic performance was observed, even though the defect-containing polymers generally gave a reduced performance as a result of a lower short-circuit current density than the defect-free polymers of comparable molecular weight. In all cases open-circuit voltage and fill factor were identical. The variation in short-circuit current density is not uncommon for different batches of the same polymer and can result from variations in molecular weight and polydispersity, which often affect the nanomorphology, or from other factors such as the presence of impurities. The results suggests that even for large concentrations (at least up to 10%), the effects of these defects are smaller than common batch-to-batch variations. In the case of PDPP4T, the 6T defects also did not have any measurable effect on the energy levels of the polymer. The solar cells all showed very similar performance, thus excluding that the 6T segments had any large effect on the morphology of the layer.

With a model reaction, the naturally occurring amount of homocoupling during a Stille reaction was investigated. It was found that under optimum reaction conditions no homocoupling of trialkylstannyl monomers could be detected and that the level of defects is therefore below 0.5%. This validates the experiments with the intentionally introduced defects, by confirming that the naturally occurring defect level is far below the amounts that were deliberately added to the polymers. It was also found that exposure to air could induce 1.1% of homocoupling defects, thus confirming that this side reaction could easily take place if mistakes or inaccuracies occur during the polymerization reaction. Interestingly,

also 0.4% homocoupling of the bromide monomer was detected, indicating that air exposure could also influence this side reaction.

In previous work we have shown that in the case of homocoupling of dibromide monomers (Br-T-DPP-T-Br) in the synthesis of DPP polymers, the resulting DPP-2T-DPP defects have a lower band gap and constitute traps for excitons and charges. In contrast, in organometallic-based homocoupling of bis(trialkylstannyl) monomers (Sn-*n*T-Sn), the DPP units in the resulting DPP-T-2*n*T-T-DPP chain defects will be further apart. Hence their interaction is weakened, such that these defects will not give rise to traps in the same way. This was confirmed by the defect-containing polymers because even with 20% of defects no change in the optoelectronic properties or the V_{oc} could be observed. As it is clear from the PDPP4T polymers that homocoupling defects, even 6T segments with significantly lower solubility, up to 5% are unlikely to have a significant impact on morphology, the conclusion must be that these homocoupling defects can be ignored when assessing the photovoltaic performance of these DPP polymers. We emphasize that this is not a general conclusion, but depends on the actual chemical structure of the polymer main chain and the precise nature of the defect. As an example, if the functional groups on the reaction components would be inverted, i.e. a DPP unit incorporated in the bis(trialkylstannyl) monomer in a polymerization reaction with dibromodithiophene, the defect resulting from organometallic-based homocoupling will have a large impact on the performance of the resulting PDPP4T. Also, Sommer *et al.* established a large impact of carbazole homocoupling on the photovoltaic performance in PCDTBT polymers with [70]PCBM.[23] Sommer *et al.* showed that mainly the J_{SC} and FF are affected, while the V_{OC} remained essentially unchanged. The exact reason could not be identified. In PCDTBT, the carbazole units bear 1-octylnonyl sidechains. Hence homocoupling of the carbazoles could increase the solubility of the polymers and give rise to an unfavourable more mixed morphology.[3]

Summarizing, defects that can be associated with homocoupled trialkylstannyl thiophene monomers do not give rise to significant changes of the opto-electronic properties of DPP based polymers PDPP3T and PDPP4T. Moreover, using the optimized synthesis protocol for DPP polymers, we find no evidence of significant homocoupling of any kind. We stress that this conclusion holds for the specific cases investigated and that for other donor-acceptor polymers the result could be different.

2.4 Experimental section

2.4.1 Materials and methods

Unless indicated otherwise, all synthetic procedures were performed under a protective argon atmosphere. Commercial (dry) solvents and reactants were used without further purification, unless stated otherwise. *N*-bromosuccinimide (NBS) was recrystallized from deionized water prior to use. 2,5-Bis(trimethylstannyl)thiophene (**2**), 5,5′-bis(trimethylstannyl)-2,2′-bithiophene (**3**) and triphenylphosphine (PPh_3) were recrystallized from methanol prior to polymerization. Tris(dibenzylideneacetone)dipalladium ($Pd_2(dba)_3$) and bis(triphenylphosphine)palladium(II) dichloride ($Pd(PPh_3)_2Cl_2$) were purchased from Strem Chemicals, Inc., [70]PCBM (purity 90-95%) was purchased from Solenne BV. All other chemicals and solvents were obtained from Sigma-Aldrich Co. 3,6-Bis(5-bromothiophen-2-yl)-2,5-bis(2-hexyldecyl)-2,5-pyrrolo[3,4-*c*]pyrrole-1,4-dione (**1**),[26] 3-(5-bromothiophen-2-yl)-2,5-bis(2-decyltetradecyl)-6-(thiophen-2-yl)-2,5-pyrrolo[3,4-*c*]pyrrole-1,4-dione (**4**),[27] and 3,6-bis(5-bromothiophen-2-yl)-2,5-bis(2-decyltetradecyl)-2,5-pyrrolo[3,4-*c*]pyrrole-1,4-dione (**8**)[28] were synthesized according to previously published procedures.

^{1}H-NMR (400 MHz) spectra were recorded on a Varian Mercury spectrometer. Chemical shifts are given in ppm with respect to tetramethylsilane as internal standard. Matrix assisted laser desorption ionization time of flight (MALDI-TOF) mass spectrometry was measured on a Bruker Autoflex Speed spectrometer. For the analysis of the model homocoupling reaction, *trans*-2-[3-(4-*tert*-butylphenyl)-2-methyl-2-propenylidene]malononitrile (DCTB) was used as matrix for all samples. Polymer molecular-weight distributions were estimated by GPC at 140 °C on a PL-GPC 120 system using a PL-GEL 10 mm MIXED-C column with *ortho*-dichlorobenzene (*o*-DCB) as the eluent and using polystyrene internal standards. Samples were dissolved at a concentration of 0.1 mg/mL in *o*-DCB at 140 °C for 1 h before being measured.

UV-vis-NIR absorption spectroscopy was conducted on a PerkinElmer Lambda 1050 spectrophotometer with a 3D WB PMT/InGaAs/PbS detector module. Solid films were obtained by spin coating (2000 rpm) solutions of the materials (4 mg/mL) in chloroform onto glass substrates which were pre-cleaned with acetone and isopropanol, before being treated with UV-ozone for 30 min. Square wave voltammetry was measured on the polymers in solid state which were deposited onto a platinum wire by dipping the wire in the hot solutions (chloroform). A silver rod was employed as counter electrode and a silver chloride coated silver rod (Ag/AgCl) was used as a quasi-reference electrode. 0.1 M tetrabutylammonium hexafluorophosphate in acetonitrile was used as electrolyte solution. The measurement was carried out under inert atmosphere with an AutoLab PGSTAT 12 at a scan speed of 0.125 V/s, a modulation amplitude of 20 mV and at a frequency of 25 Hz. Ferrocene/ferrocenium (Fc/Fc^+) was employed as a standard with $E = -4.8$ eV.

Photovoltaic devices with an active area of 0.09 and 0.16 cm² were fabricated in air on patterned indium tin oxide (ITO) glass substrates (Naranjo Substrates). The substrates were cleaned by sonication in acetone for 15 min., followed by scrubbing with a sodium dodecyl sulfate solution (99%, Acros), rinsing with deionized water and a final sonication step in 2-propanol. Before deposition of the device layers the substrates underwent a 30 min. UV-ozone treatment. Clevios PEDOT:PSS Al 4083 (Heraeus), was deposited by spin coating at 3000 rpm. The active layers were deposited from a solution of polymer (4 mg/mL) and [70]PCBM (8 mg/mL) in chloroform containing 7.5 vol% of *o*-DCB in the case of the PDPP3T polymers and 10 vol% of *o*-DCB in the case of the PDPP4T polymers. The solutions were heated to 90 °C for one hour to ensure that the polymers were completely dissolved, then kept at 60 °C and were finally cooled to room temperature under vigorous stirring during 2 min. before spin coating at 2000 or 3000 rpm. LiF (1 nm and Al (100 nm) were deposited by thermal evaporation under high vacuum (~3×10^{-7} mbar) as a back contact.

Current density – voltage ($J-V$) characteristics were measured with a Keithley 2400 source meter under ~100 mW/cm^2 white light illumination from a tungsten-halogen lamp filtered by a Schott GG385 UV filter and a Hoya LB120 daylight filter. The short-circuit current density (J_{sc}) was determined more accurately from external quantum efficiency (EQE) measurements by integration of the EQE with the AM1.5G solar spectrum. EQE measurements were carried out under 1 sun equivalent operating conditions in a setup consisting of a modulated monochromatic light, a preamplifier (Stanford Research Systems SR570) and a lock-in amplifier (Stanford Research Systems, SR830). The modulated monochromatic light was generated by using an optical chopper (Stanford Research Systems, SR540), a monochromator (Oriel Cornerstone 130) and a 50 W (Osram 64610) tungsten-halogen lamp. The 1 sun conditions were provided by the use of a 730 nm light-emitting diode (Thorlabs) at different intensities for appropriate bias illumination. The devices were kept in a nitrogen-filled box with a quartz window. A calibrated silicon cell was used as reference for $J-V$ and EQE measurements.

2.4.2 Synthesis

General polymerization procedure for the PDPP3T polymers

3,6-Bis(5-bromothiophen-2-yl)-2,5-bis(2-hexyldecyl)-2,5-pyrrolo[3,4-*c*]pyrrole-1,4-dione (**1**) (1 eq.) was loaded together with 2,5-bis(trimethylstannyl)thiophene (**2**) and 5,5′-bis(trimethylstannyl)-2,2′-bithiophene (**3**) (together 1 eq.) in a Schlenk tube containing tris(dibenzylideneacetone)dipalladium (1.5%) and triphenylphosphine (6%). The solids were placed under argon before being dissolved in a mixture of toluene and *N*,*N*-dimethylformamide (DMF) (9:1). The mixture was degassed with argon for 15 min. and then sealed in the tube for reaction at 115 °C overnight. 1,1,2,2-tetrachloroethane (TCE) was then added to dissolve and dilute the mixture before it

was precipitated in methanol. The solids were then filtered, dissolved in TCE at 110 °C and stirred with ethylenediaminetetraacetic acid (EDTA) for one hour after which water was added and the mixture was stirred for another hour. The organic layer was then separated, washed twice with water and partially reduced in volume under reduced pressure. The polymer was then precipitated in methanol and the solids were subjected to Soxhlet extraction with subsequently acetone, hexane and dichloromethane. The remaining solids were then dissolved in TCE, the solution was filtered and precipitated in acetone. The polymers were then filtered and dried at 40 °C in vacuum overnight.

PDPP3T (5% 4T)

The general procedure was followed with 3,6-bis(5-bromothiophen-2-yl)-2,5-bis(2-hexyldecyl)-2,5-pyrrolo[3,4-*c*]pyrrole-1,4-dione (**1**) (70 mg, 77.2 µmol, 1 eq.), 2,5-bis(trimethylstannyl)thiophene (**2**) (30 mg, 73.3 µmol, 0.95 eq.), 5,5′-bis(trimethylstannyl)-2,2′-bithiophene (**3**) (1.9 mg, 3.9 µmol, 0.05 eq.), tris(dibenzylideneacetone)dipalladium (1.066 mg, 1.16 µmol, 1.5%) and triphenylphosphine (1.215 mg, 4.63 µmol, 6%) in toluene/DMF (9:1) (1.5 mL). GPC (*o*-DCB, 140 °C): M_n = 148 kDa, M_w = 399 kDa, $Đ$ = 2.7.

PDPP3T (10% 4T)

The general procedure was followed with 3,6-bis(5-bromothiophen-2-yl)-2,5-bis(2-hexyldecyl)-2,5-pyrrolo[3,4-*c*]pyrrole-1,4-dione (**1**) (70 mg, 77.2 µmol, 1 eq.), 2,5-bis(trimethylstannyl)thiophene (**2**) (28.5 mg, 69.5 µmol, 0.90 eq.), 5,5′-bis(trimethylstannyl)-2,2′-bithiophene (**3**) (3.8 mg, 7.7 µmol, 0.10 eq.), tris(dibenzylideneacetone)dipalladium (1.066 mg, 1.16 µmol, 1.5%) and triphenylphosphine (1.215 mg, 4.63 µmol, 6%) in toluene/DMF (9:1) (1.5 mL). GPC (*o*-DCB, 140 °C): M_n = 123 kDa, M_w = 330 kDa, $Đ$ = 2.7.

PDPP3T (20% 4T)

The general procedure was followed with of 3,6-bis(5-bromothiophen-2-yl)-2,5-bis(2-hexyldecyl)-2,5-pyrrolo[3,4-*c*]pyrrole-1,4-dione (**1**) (70 mg, 77.2 µmol, 1 eq.), 2,5-bis(trimethylstannyl)thiophene (**2**) (25.3 mg, 61.7 µmol, 0.80 eq.), 5,5′-bis(trimethylstannyl)-2,2′-bithiophene (**3**) (7.6 mg, 15.4 µmol, 0.20 eq.), tris(dibenzylideneacetone)dipalladium (1.066 mg, 1.16 µmol, 1.5%) and triphenylphosphine (1.215 mg. 4.63 µmol. 6%) in toluene/DMF (9:1) (1.5 mL). GPC (*o*-DCB, 140 °C): M_n = 148 kDa, M_w = 399 kDa, $Đ$ = 2.7.

3-([2,2':5',2''-Terthiophen]-5-yl)-2,5-bis(2-decyltetradecyl)-6-(thiophen-2-yl)-2,5-pyrrolo[3,4-*c*]pyrrole-1,4-dione (6)

3-(5-Bromothiophen-2-yl)-2,5-bis(2-decyltetradecyl)-6-(thiophen-2-yl)-2,5-pyrrolo[3,4-*c*]pyrrole-1,4-dione (**4**) (150 mg, 143 µmol), 2-([2,2'-bithiophen]-5-yl)-4,4,5,5-tetramethyl-1,3,2-

dioxaborolane (**5**) (62.5 mg, 214 µmol), tris(dibenzylideneacetone)dipalladium (1.96 mg, 2.14 µmol) and triphenylphosphine (2.24 mg, 8.55 µmol) were placed in a Schlenk tube and put under argon. Then toluene (2 mL) was added and the mixture was degassed for 15 min. before a previously degassed 2M K_3PO_4 solution in water (0.36 mL) was added along with 1 drop of Aliquat 336. The tube was then sealed and heated to 115 °C and left to react overnight. The reaction mixture was then left to cool before being diluted with dichloromethane and washed with water. Column chromatography was then performed (7:3 heptane:dichloromethane, gradient to 5:5) and the obtained solid was recrystallized in methanol to yield the product as a blue solid (78 mg, yield 48%). ^{1}H NMR (400 MHz, $CDCl_3$) *δ:* 8.92 (d, *J* = 4.2 Hz, 1H), 8.87 (dd, *J* = 3.9, 1.2 Hz, 1H), 7.61 (dd, *J* = 5.0, 1.2 Hz, 1H), 7.30 (d, *J* = 4.2 Hz, 1H), 7.26 (m, 2H), 7.22 (m, 2H), 7.13 (d, *J* = 3.9 Hz, 1H), 7.05 (dd, *J* = 5.1, 3.6 Hz, 1H), 4.03 (d, *J* = 7.6 Hz, 4H), 1.94 (m, 2H), 1.40 – 1.11 (m, 80H), 0.87 (t, *J* = 6.3 Hz, 6H), 0.86 (t, *J* = 6.3 Hz, 6H).

3-(5''-Bromo-[2,2':5',2''-terthiophen]-5-yl)-6-(5-bromothiophen-2-yl)-2,5-bis(2-decyltetradecyl)-2,5-pyrrolo[3,4-*c*]pyrrole-1,4-dione (7)

3-([2,2':5',2"-Terthiophen]-5-yl)-2,5-bis(2-decyltetradecyl)-6-(thiophen-2-yl)-2,5-pyrrolo[3,4-*c*]pyrrole-1,4-dione (**6**) (65 mg, 58 µmol) was dissolved in chloroform (2 mL) and cooled to 0 °C. *N*-bromosuccinimide (14 mg, 119 µmol) was then added in 3 portions, before the mixture was allowed to warm up to room temperature and left to react overnight. To achieve full conversion, 1 mg of *N*-bromosuccinimide and later another 2 mg were added and allowed to react for 2 h. The mixture was then washed with water, dried over $MgSO_4$ and the solvents were evaporated under reduced pressure. The solids were purified via column chromatography (4:6 heptane:dichloromethane, gradient to 5:5) and recrystallized three times from methanol and once from acetone to achieve maximum purity. The product was isolated as a blue solid (30 mg, yield 40%). ^{1}H NMR (400 MHz, $CDCl_3$) *δ:* 8.92 (d, *J* = 4.2 Hz, 1H), 8.62 (d, *J* = 4.2 Hz, 1H), 7.30 (d, *J* = 4.1 Hz, 1H), 7.22 (d, *J* = 4.0 Hz, 2H), 7.06 (d, *J* = 3.8 Hz, 1H), 7.00 (d, *J* = 3.9 Hz, 1H), 6.96 (d, *J* = 3.8 Hz, 1H), 4.02 (d, *J* = 7.6 Hz, 2H), 3.95 (d, *J* = 7.7 Hz, 2H), 1.94 (m, 2H), 1.40 – 1.15 (m, 80H), 0.91 – 0.82 (m, 12H). MALDI-TOF-MS: predicted: 1292.55, found: 1292.58.

General polymerization procedure for the PDPP4T polymers

3,6-Bis(5-bromothiophen-2-yl)-2,5-bis(2-decyltetradecyl)-2,5-pyrrolo[3,4-*c*]pyrrole-1,4-dione (**8**) and 3-(5"-bromo-[2,2':5',2"-terthiophen]-5-yl)-6-(5-bromothiophen-2-yl)-2,5-bis(2-decyltetradecyl)-2,5-pyrrolo[3,4-*c*]pyrrole-1,4-dione (**7**) (together 1 eq.) were loaded with 5,5′-bis(trimethylstannyl)-2,2′-bithiophene (**3**) (1 eq.) in a Schlenk tube together with tris(dibenzylidene-acetone)dipalladium (1.5%) and triphenylphosphine (6%). The solids were placed under argon before

being dissolved in a mixture of toluene and DMF (9:1). The mixture was degassed with argon for 15 min. and then sealed in the tube for reaction at 115 °C overnight. TCE was then added to dissolve and dilute the mixture before being precipitated in methanol. The solids were then filtered, dissolved in TCE at 110 °C and stirred with EDTA for one hour after which water was added and the mixture was stirred for another hour. The organic layer was then separated, washed twice with water and partially reduced in volume under reduced pressure. The polymer was then precipitated in methanol and the solids were subjected to Soxhlet extraction with subsequently acetone, hexane and dichloromethane. The remaining solids were then dissolved in TCE, the solution was filtered and precipitated in acetone. The polymers were then filtered and dried at 40 °C in vacuum overnight.

PDPP4T (0% 6T)

The general procedure was followed with 3,6-bis(5-bromothiophen-2-yl)-2,5-bis(2-decyltetradecyl)-2,5-pyrrolo[3,4-*c*]pyrrole-1,4-dione (**8**) (70.2 mg, 62 μmol, 1 eq.), no 3-(5"-bromo-[2,2':5',2"-terthiophen]-5-yl)-6-(5-bromothiophen-2-yl)-2,5-bis(2-decyltetradecyl)-2,5-pyrrolo[3,4-*c*]pyrrole-1,4-dione (**7**) (0 eq.), 5,5′-bis(trimethylstannyl)-2,2′-bithiophene (**3**) (30.5 mg, 62 μmol, 1 eq.), tris(dibenzylideneacetone)dipalladium (0.85 mg, 9.3 μmol, 1.5%) and triphenylphosphine (0.98 mg, 3.7 μmol, 6%). GPC (*o*-DCB, 140 °C): M_n = 83 kDa, M_w = 150 kDa, $Đ$ = 1.8.

PDPP4T (2% 6T)

The general procedure was followed with 3,6-bis(5-bromothiophen-2-yl)-2,5-bis(2-decyltetradecyl)-2,5-pyrrolo[3,4-*c*]pyrrole-1,4-dione (**8**) (68.7 mg, 60.8 μmol, 0.98 eq.), 3-(5"-bromo-[2,2':5',2"-terthiophen]-5-yl)-6-(5-bromothiophen-2-yl)-2,5-bis(2-decyltetradecyl)-2,5-pyrrolo[3,4-*c*]pyrrole-1,4-dione (**7**) (1.61 mg, 1.2 μmol, 0.02 eq.), 5,5′-bis(trimethylstannyl)-2,2′-bithiophene (**3**) (30.5 mg, 62 μmol, 1 eq.), tris(dibenzylideneacetone)dipalladium (0.85 mg, 9.3 μmol, 1.5%) and triphenylphosphine (0.98 mg, 3.7 μmol, 6%). GPC (*o*-DCB, 140 °C): M_n = 79 kDa, M_w = 150 kDa, $Đ$ = 1.9.

PDPP4T (5% 6T)

The general procedure was followed with 3,6-bis(5-bromothiophen-2-yl)-2,5-bis(2-decyltetradecyl)-2,5-pyrrolo[3,4-*c*]pyrrole-1,4-dione (**8**) (66.6 mg, 58.9 μmol, 0.95 eq.), 3-(5"-bromo-[2,2':5',2"-terthiophen]-5-yl)-6-(5-bromothiophen-2-yl)-2,5-bis(2-decyltetradecyl)-2,5-pyrrolo[3,4-*c*]pyrrole-1,4-dione (**7**) (4.0 mg, 3.1 μmol, 0.05 eq.), 5,5′-bis(trimethylstannyl)-2,2′-bithiophene (**3**) (30.5 mg, 62 μmol, 1 eq.), of tris(dibenzylideneacetone)dipalladium (0.85 mg, 9.3 μmol, 1.5%) and triphenylphosphine (0.98 mg, 3.7 μmol, 6%). GPC (*o*-DCB, 140 °C): M_n = 79 kDa, M_w = 144 kDa, $Đ$ = 1.8.

Model homocoupling reaction

3-(5-Bromothiophen-2-yl)-2,5-bis(2-decyltetradecyl)-6-(thiophen-2-yl)-2,5-pyrrolo[3,4-*c*]pyrrole-1,4-dione (150 mg, 143 µmol) (**4**) and 5,5'-bis(trimethylstannyl)-2,2'-bithiophene (**3**) (35 mg, 71 µmol) were weighed and dissolved in a mixture of dry toluene (2.7 mL) and dry DMF (0.3 mL). The mixture was then separated in three equal parts (1 mL). To the first reaction mixture, tris(dibenzylideneacetone)dipalladium (0.33 mg, 3.56 µmol) and triphenylphosphine (0.37 mg, 14.3 µmol) were added. The mixture was then degassed with argon for 15 min., before being sealed and heated to 115 °C overnight. The solvents were then removed under reduced pressure and the solids were analysed without further purification. To the second reaction mixture, tris(dibenzylidene-acetone)dipalladium (0.33 mg, 3.56 µmol) and triphenylphosphine (0.37 mg, 14.3 µmol) were added. The mixture was left in air and sealed with air in the flask before being heated to 115 °C overnight. The solvents were then removed under reduced pressure and the solids were analysed without further purification. To the third reaction mixture, bis(triphenylphosphine)palladium(II) dichloride (0.50 mg, 7.13 µmol) was added. The mixture was then degassed with argon for 15 min., before being sealed and heated to 115° C overnight. The solvents were then removed under reduced pressure and the solids were analysed without further purification.

2.5 References

1 A. Katsouras, N. Gasparini, C. Koulogiannis, M. Spanos, T. Ameri, C. J. Brabec, C. L. Chochos, A. Avgeropoulos, *Macromol. Rapid Commun.*, 2015, **36**, 1778-1797.

2 K. H. Hendriks, G. H. L. Heintges, V. S. Gevaerts, M. M. Wienk, R. A. J. Janssen, *Angew. Chem. Int. Ed.*, 2013, **52**, 8341-8344.

3 J. J. van Franeker, G. H. L. Heintges, C. Schaefer, G. Portale, W. Li, M. M. Wienk, P. van der Schoot, R. A. J. Janssen, *J. Am. Chem. Soc.*, 2015, **137**, 11783-11794.

4 Z. B. Henson, K. Müllen, G. C. Bazan, *Nat. Chem.*, 2012, **4**, 699-704.

5 J. K. Park, J. Jo, J. H. Seo, J. S. Moon, Y. D. Park, K. Lee, A. J. Heeger, G. C. Bazan, *Adv. Mater.*, 2011, **23**, 2430-2435.

6 G. H. L. Heintges, J. J. van Franeker, M. M. Wienk, R. A. J. Janssen, *Chem. Commun.*, 2016, **52**, 92-95.

7 C. Bracher, H. Yi, N. W. Scarratt, R. Masters, A. J. Pearson, C. Rodenburg, A. Iraqi, D. G. Lidzey, *Org. Electron.*, 2015, **27**, 266-273.

8 M. P. Nikiforov, B. Lai, W. Chen, S. Chen, R. D. Schaller, J. Strzalka, J. Maser, S. B. Darling, *Energy Environ. Sci.*, 2013, **6**, 1513-1520.

9 W. R. Mateker, J. D. Douglas, C. Cabaneto, I. T. Sachs-Quintana, J. A. Bartelt, E. T. Hoke. A. El Labban, P. Beaujuge, J. M. J. Fréchet, M. D. McGehee, *Energy Environ. Sci.*, 2013, **6**, 2529-2537.

10 I. Osaka, R. D. McCullough *Acc. Chem. Res.* 2008, **41**, 1202–1214.

11 L. Ying, F. Huang, G. C. Bazan, *Nat. Commun.*, 2017, **8**, 14047.

12 F. Koch, W. Heitz, *Macromol. Chem. Phys.*, 1997, **198**, 1531-1544.

13 V. Farina, B. Krishnan, D. R. Marshall, G. P. Roth, *J. Org. Chem.*, 1993, **58**, 5434-5444.

14 F. Lombeck, H. Komber, S. I. Gorelsky, M. Sommer, *ACS Macro Lett.*, 2014, **3**, 819-823.

15 G. Pirotte, P. Verstappen, D. Vanderzande, W. Maes, *Adv. Electron. Mater.*, 2018, **4**, 1700481.

16 K. H. Hendriks, W. Li, G. H. L. Heintges, G. W. P. van Pruissen, M. M. Wienk, R. A. J. Janssen, *J. Am. Chem. Soc.*, 2014, **136**, 11128-11133.

17 W. Hong, S. Chen, B. Sun, M. A. Arnould, Y. Meng, Y. Li, *Chem. Sci.* 2015, **6**, 3225-3235.

18 D. A. Warr, L. M. A. Perdigão, H. Pinfold, J. Blohm, D. Stringer, A. Leventis, H. Bronstein, A. Troisi, G. Costantini, *Sci. Adv.* 2018, **4**, eaas9543.

19 S. Ostrowska. S. Rogalski, J. Lorkowski, J. Walkowiak, C. Pietraszuk, *Synlett*, 2018, **29**, 1735-1740.

20 C. A. Contreras-Celedón, J. A. Rincón-Medina, D. Mendoza-Rayo, L. Chacón-Garcia, *Appl. Organometal. Chem.*, 2015, **29**, 439-442.

21 H. Bohra, M. Wang, *J. Mater. Chem. A*, 2017, **5**, 11550-11571.

22 M. Moreno-Mañas, M. Perez, R. Pleixats, *J. Org. Chem.*, 1996, **61**, 2346-2351.

23 F. Lombeck, H. Komber, D. Fazzi, D. Nava, J. Kuhlmann, D. Stegerer, K. Strassel, J. Brandt, A. Diaz, Z. Mendaza, C. Müller, W. Thiel, M. Caironi, R. Friend, M. Sommer, *Adv. Energy Mater.*, 2016, **6**, 1601232.

24 B. Carsten, F. He, H. J. Son, T. Xu, L. Yu, *Chem. Rev*., 2011, **111**, 1493-1528.

25 W. Li, R. S. C. Roelofs, M. M. Wienk, R. A. J. Janssen, *J. Am. Chem. Soc.*, 2012, **134**, 13787-13795.

26 L. Bürgi, M. Turbiez, R. Pfeiffer, F. Bienewald, H. J. Kirner, C. Winnewisser, *Adv. Mater.* 2008, **20**, 2217-2224.

27 E. Y. Ko, G. E. Park, D. H. Lee, H. A. Um, J. Shin, M. J. Cho, D H. Choi, *ACS Appl. Mater. Interfaces*, 2015, **7**, 28303-28310.

28 S. Cho, J. Lee, M. H. Tong, J. H. Seo, C. Yang, *Adv. Funct. Mater.* 2011, **21**, 1910-1916.

Chapter 3

The effect of branching in a semiconducting polymer on the efficiency of organic photovoltaic cells

Abstract

The impact of branching in a diketopyrrolopyrrole polymer on the performance of polymer-fullerene photovoltaic cells is investigated. Compared to the linear polymer, the branched polymer affords a more finely dispersed fibrillar network in the photoactive layer and as a result a large enhancement of the photocurrent and power conversion efficiency.

This work has been published: G. H. L. Heintges, J. J. van Franeker, M. M. Wienk, R. A. J. Janssen, *Chem. Commun.*, 2016, **52**, 92-95.

3.1 Introduction

Polymer-fullerene photovoltaic cells have recently broken the barrier of 10% power conversion efficiency.[1-4] In these cells, the conjugated polymer is usually based on an alternating pattern of electron-rich and electron-poor moieties, offering control over the electronic and optical nature of the material. Among the more extensively investigated electron-poor moieties is diketopyrrolopyrrole (DPP), a unit known to provide access to small band gap polymers with high efficiencies[5-7] and good ambipolar charge transport.[8,9] Research efforts into these polymers have focused on the fine-tuning of the electronic and optical properties on the one hand,[10] and the fine-tuning of the polymer-fullerene blend morphology on the other. The latter is done mostly via the influence of the solubilizing side-chains,[11,12] or via the influence of the processing conditions.[13-15] Almost all polymers that have been used in photovoltaic cells have a linear architecture, leaving the topic of alternative architectures largely unexplored. These alternative architectures are, however, synthetically accessible via the polycondensation reactions that are usually employed for conjugated polymers. These include brush-type structures, containing conjugated segments of defined length attached to the main chain,[16,17] and defined or randomly branched structures.[18-21] No reports on the photovoltaic properties of truly randomly branched polymers are available in literature to date. A possible advantage of this random architecture is the higher molecular weight that could be attained by increasing the average functionality of the monomers, as the influence of molecular weight on the blend morphology and the efficiency of polymer solar cells is often significant.[6,15] Other effects potentially caused by the branching of stiff conjugated polymers remain unknown.

In this work, we present the effect of branching on DT-PDPPTPT, a polymer consisting of a DPP unit, substituted with relatively long 2-decyltetradecyl (DT) solubilizing side chains, alternating along the chain with a thiophene-phenylene-thiophene (TPT) conjugated segment (Scheme 3.1). DT-PDPPTPT was selected because of its good solubility and reasonable photovoltaic efficiency.[5] It was found that introducing branching severely decreased solubility, even in the case of 1% of branching unit. However, this proved to have a surprisingly large effect on the photovoltaic efficiency and morphology.

3.2 Results and discussion

DT-PDPPTPT was synthesized via the previously published procedure,[5] which was adapted by replacing a controlled amount of 1,4-bis(4,4,5,5-tetramethyl-1,3,2-dioxaborolan-2-yl)benzene by commercially available 1,3,5-tris(4,4,5,5-tetramethyl-1,3,2-dioxaborolan-2-yl)benzene to obtain the branched polymers. Two polymers were synthesized replacing 5% and 1% (5B-DT-PDPPTPT and 1B-DT-PDPPTPT respectively) of all bifunctional phenylene units by trifunctional units. The polymer containing 5% of branching proved to be insoluble and will be excluded in the further discussion.

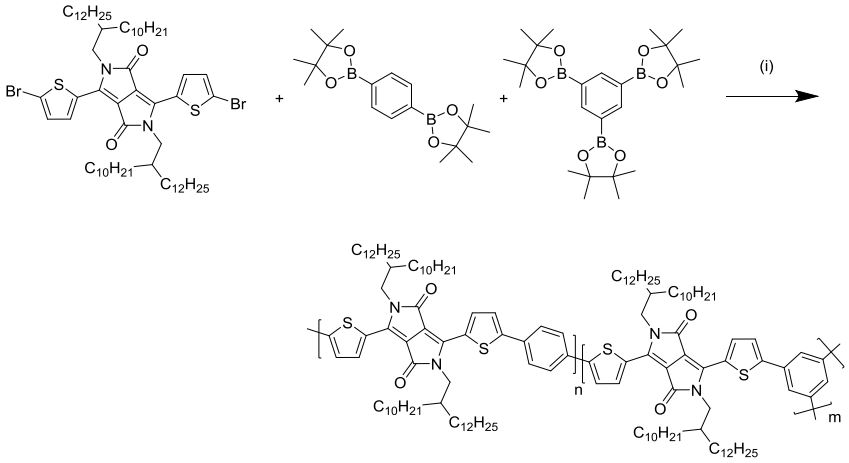

Scheme 3.1: Polymerization of branched DT-PDPPTPT, using a trifunctional phenylene core as branching unit. (i) $Pd_2(dba)_3/PPh_3$, $K_3PO_{4\,(aq)}$, toluene, 115 °C. $m/(m + n) = 0$, 0.01, or 0.05.

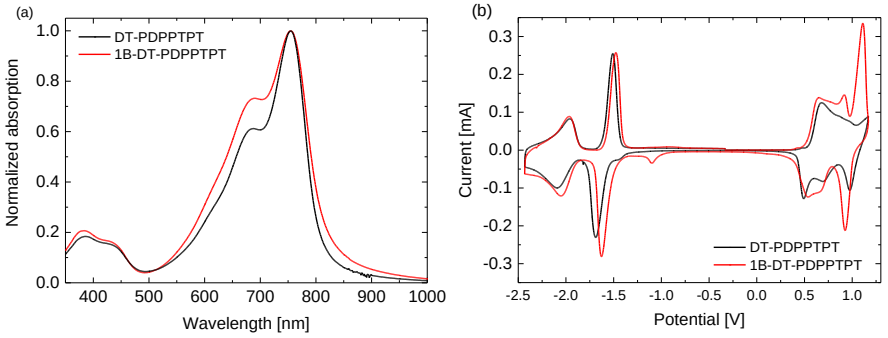

Fig. 3.1: (a) UV-vis-NIR absorption of both polymers in film. (b) Cyclic voltammetry of both polymer films recorded in acetonitrile, referenced versus Fc/Fc^+.

The electronic and optical properties of the linear and branched polymers were expected and found to be very similar owing to their identical conjugated backbone. In both cyclic voltammetry and UV-vis-NIR absorption spectroscopy (Figure 3.1) very similar properties were observed for both polymers. The molecular weight was estimated using gel permeation chromatography (GPC) analysis in hot *ortho*-dichlorobenzene (*o*-DCB) at 140 °C (Figure 3.2). A distinct shoulder was observed in the high molecular weight range for 1B-DT-PDPPTPT. This was attributed to aggregation as the UV-vis-NIR absorption profile of the material in this shoulder showed a red-shifted absorption profile. This indicates that 1B-DT-PDPPTPT has a strong tendency to aggregate compared to DT-PDPPTPT, where this shoulder and red-shift are absent in *o*-DCB at 140 °C. The values extracted from the GPC trace are therefore likely overestimated for 1B-DT-PDPPTPT. Nevertheless, the branched polymer showed both lower number average (M_n) and lower peak (M_p) molecular weights of 31.4 and 43.1 kDa respectively, compared to the linear polymer (45.4 and 85.0 kDa) (Table 3.1). A further problem with this analysis is that GPC estimates the molecular weight based on hydrodynamic volume, and the exact impact of branching in stiff polymers on this volume is not well known. As branching diminishes the hydrodynamic volume, the molecular weight of the branched polymer could be underestimated.

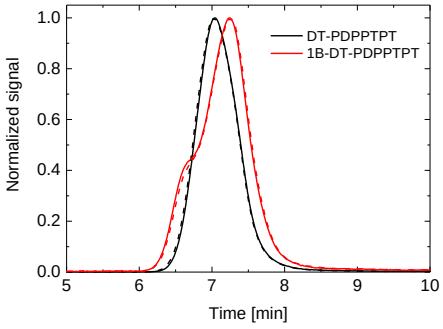

Fig. 3.2: GPC traces of DT-PDPPTPT and 1B-DT-PDPPTPT recorded in *o*-DCB at 140 °C. Two measurements are shown for each polymer, the second is indicated by the dotted line. The material corresponding to the shoulder around 6.3 min. for 1B-DT-PDPPTPT showed a red-shifted absorption, and was assigned to aggregated 1B-DT-PDPPTPT.

Table 3.1: GPC results of both polymers. Two measurements were performed on each polymer sample, to ensure that the result was reproducible. The values given in the main text are averages of the two measurements.

Polymer	M_n **[kDa]**[a]	M_w **[kDa]**[b]	$Đ$[c]	M_p **[kDa]**[d]
DT-PDPPTPT	44.2	97.7	2.21	82.8
DT-PDPPTPT	46.5	102	2.20	87.1
1B-DT-PDPPTPT	33.0	112	3.38	43.9
1B-DT-PDPPTPT	29.8	105	3.53	42.2

[a] Number average molecular weight, [b] Weight average molecular weight, [c] Polydispersity, [d] Peak molecular weight.

Photovoltaic cells of both polymers were made using [6,6]-phenyl-C_{71}-butyric acid methyl ester ([70]PCBM) as an acceptor, sandwiching the active layer between ITO/PEDOT:PSS and LiF/Al electrodes. The active layers were optimized in terms of thickness, polymer-fullerene ratio, and solvent composition of the casting solution. It was found that the optimal conditions for 1B-DT-PDPPTPT were similar to the previously[5] optimized conditions for DT-PDPPTPT, using a 1:2 polymer to [70]PCBM weight ratio dissolved in a mixture of chloroform with 3 vol% of 1,8-diiodooctane (DIO), while the best cell of DT-PDPPTPT in this study was made using 6 vol% of DIO. The photovoltaic performance is summarized in Table 3.2 and Figure 3.3. The open circuit voltage (V_{oc}) was found to be very similar for both materials, as was expected from the similar backbone. The fill factor (FF) does not show a big difference either, but an important difference was found in the short circuit current density (J_{sc}). A dramatic increase of from 8.7 to 12.5 mA/cm² resulted in an improved power conversion efficiency (PCE) of 6.3% for 1B-DT-PDPPTPT compared to 4.4% for DT-PDPPTPT for the best devices. As can be seen Figure 3.3b the branched polymer shows a higher response in the spectrally resolved external quantum efficiency (EQE) over the whole absorption range of the device. Although there is a small difference in absorption, most of this increase is caused by a change in internal quantum efficiency (IQE) (Figure 3.4).

To investigate the morphology, transmission electron microscopy (TEM) was performed on the active layers of the cells (Figure 3.5). Both blends show a fibre-like morphology, as was seen earlier for many DPP-containing blends.[5,6,15] The fringes observed in the TEM of these fibres at high magnification indicate that they consist of

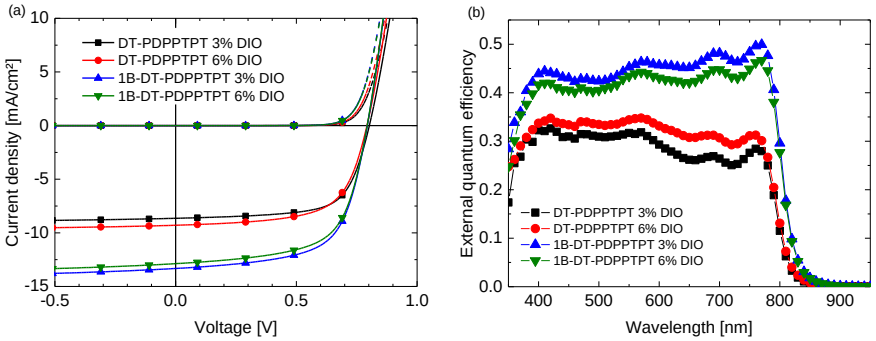

Fig. 3.3: (a) Current density – voltage (*J*–*V*) and (b) external quantum efficiency (EQE) of DT-PDPPTPT:[70]PCBM and 1B-DT-PDPPTPT:[70]PCBM solar cells processed from chloroform using 3 vol% and 6 vol% of DIO as co-solvent.

Table 3.2: Photovoltaic performance of DT-PDPPTPT:[70]PCBM and 1B-DT-PDPPTPT:[70]PCBM solar cells processed chloroform using DIO as co-solvent.

Polymer	**DIO (vol%)**	**J_{sc} [mA/cm²]**[a]	**V_{oc} [V]**	**FF**	**PCE [%]**[b]
DT-PDPPTPT	3	7.75 (7.43)	0.80 (0.80)	0.68 (0.67)	4.2 (4.0)
DT-PDPPTPT	6	8.65 (8.25)	0.79 (0.80)	0.64 (0.65)	4.4 (4.3)
1B-DT-PDPPTPT	3	12.5 (12.4)	0.79 (0.79)	0.64 (0.63)	6.3 (6.2)
1B-DT-PDPPTPT	6	11.7 (11.5)	0.79 (0.79)	0.63 (0.63)	5.9 (5.7)

[a] J_{sc} is obtained by integrating the EQE-measurement with the AM1.5G spectrum. [b] Values between brackets indicate the average over 5 devices.

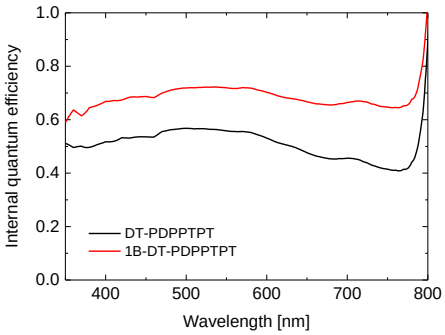

Fig. 3.4: Spectrally resolved internal quantum efficiency of the best devices made with DT-PDPPTPT and 1B-DT-PDPPTPT.

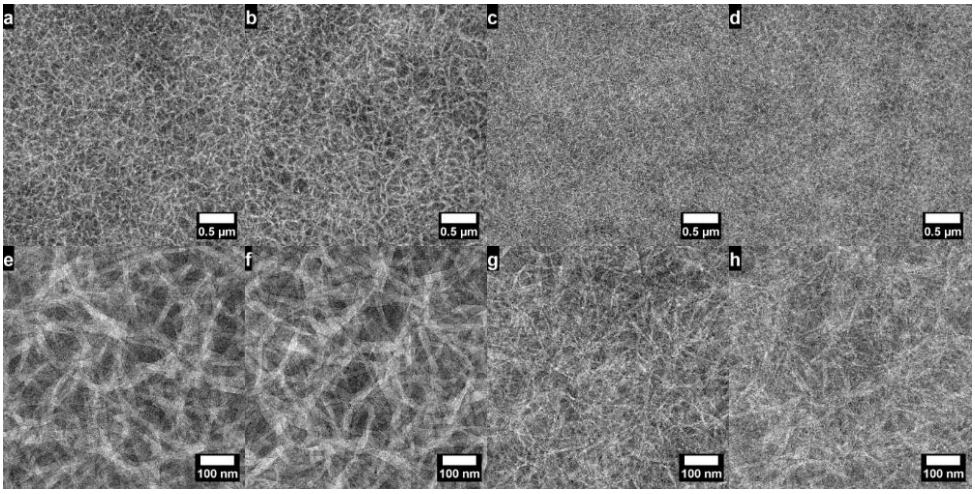

Fig 3.5: TEM images of the active layer blends of DT-PDPPTPT processed with 3 vol% DIO (a, e), DT-PDPPTPT with 6 vol% DIO (b, f), 1B-DT-PDPPTPT with 3 vol% DIO (c, g) and 1B-DT-PDPPTPT with 6 vol% DIO (d, h).

relatively pure semi-crystalline polymer. There is however a large difference between the fibre width in both blends. The branching units in 1B-DT-PDPPTPT significantly reduce the fibre width compared to DT-PDPPTPT, leading to a more intimately mixed morphology, explaining the increased EQE and gain in efficiency, as charge generation is more efficient. It has been shown that increasing the molecular weight in DPP-polymers leads to more finely dispersed fibre-morphologies.[15] However, in this case the GPC results indicate the opposite to be true. Even when taking into account errors in this measurement induced by the branched nature of the polymer, it is unlikely that the molecular weight of 1B-DT-PDPPTPT is dramatically higher than that of DT-PDPPTPT, and the difference in morphology in both blends is greater than any change we have seen in the past due to a small change in molecular weight. Therefore, we hypothesize that another effect, caused by the branching, is at play here.

To gain more insight in the morphology formation, in-situ light scattering experiments were performed during spin coating of the layer.[22] In this experiment, the polymer-fullerene solutions were spin coated onto a silicon wafer covered with PEDOT:PSS. The thickness of the liquid layer during spin coating was monitored by recording the interference of a specular reflected laser beam, while a photodetector placed to the side of this set-up recorded simultaneously the light scattered from the solution.

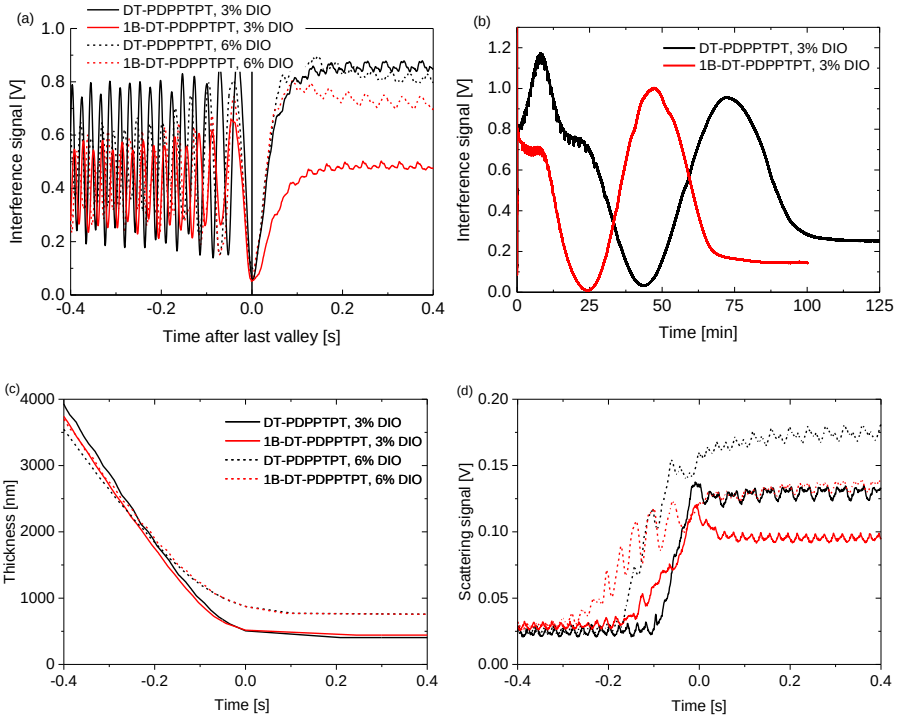

Fig. 3.6: (a) Interference signal of the laser light during spin coating of the mixture of polymer, fullerene, solvent and co-solvent versus time. The signals of different experiments are manually synchronized at the last valley of the interference signal. (b) The interference signal during the slow drying regime. (c) The drying curve extracted from the data above and the scattering signal (d) versus time.

Given the dimensions of the polymer fibres, we conjecture that an increase in scattering signal indicates fibre formation. This experiment was performed on active layer blends of both materials, using both 3 vol% and 6 vol% of DIO as co-solvent concentration. In all experiments, a fast (< 1 s) drying regime (Figure 3.6a and c) and a slow (>1 h) drying regime (Figure 3.6b) can be distinguished, which we attribute to the evaporation of chloroform in the first stage of drying, followed by a long drying period for DIO.[15] To be able to directly compare the experiments, the curves were synchronized to the point where all chloroform is evaporated (Figure 3.6a, for more details see the Experimental section). In Figure 3.6d, it can be seen that the branched polymer shows an onset of scattering before the linear polymer, meaning that fibre formation starts earlier, at lower concentration, when the same solvent mixture is used. Using the final thickness of the layers, the polymer

content by volume at the onset of scattering was calculated to be 9.3% and 7.7% for the linear and branched polymer respectively when 3 vol% DIO was used, and 6.2% and 4.0% for 6 vol% DIO. However, the polymer concentration at the onset of scattering does not seem to determine the fibre width, as can be seen when comparing the linear polymer spin coated from 6 vol% DIO in chloroform with the branched polymer from 3 vol% DIO in chloroform. In these cases, the linear polymer has an onset of scattering at a higher solvent content than the branched polymer, yet the former has a larger fibre width (Figure 3.5).

We have recently shown that the width of the semi-crystalline polymer fibres in bulk-heterojunction blends is not the result of a frozen dynamical state but determined by nucleation, which is governed by the solubility of the polymer and related to the side chains, the molecular weight and the nature of the solvent/co-solvent system.[15] Also the present results can be interpreted in the context of this nucleation-and-growth model.[15] Classic nucleation theory states that that a free-energy barrier must be overcome to form a nucleus of critical size, which can subsequently grow. The higher this barrier is, the lower the number of nuclei will be, and the bigger they will be. A large barrier for nucleation can therefore result in wide fibres either because a small number of nuclei grow into large aggregates (when there is a long growth period) or because the nuclei are large and the fibre size is determined by this (when there is a very limited growth time). For DT-PDPPTPT a large free-energy barrier can be expected as it has good solubility owing to the lengthy DT chain resulting in relatively wide fibres, which is consistent with our observations. According to this theory, the branched polymer must have a lower energy barrier as the fibres are found to be thinner. An increased tendency of aggregation is consistent with the observations made in the GPC analysis and the decreased solubility observed in the light scattering experiments, lending credence to this theory. The correlation between polymer solubility and fibre width has been pointed out before.[23,24] The origin of the lowered barrier for nucleation is not clear at this point, although one might speculate that the branching causes a decreased number of degrees of freedom of the polymer in solution, leading to a lower entropic penalty for nucleation.

3.3 Conclusion

In conclusion, introducing only 1% of branching in DT-PDPPTPT has a significant effect on the photovoltaic performance and results in a PCE of 6.3%, compared to 4.4% for the linear polymer due to an increase in photocurrent. This increase is explained by a reduction of the polymer fibre width in the active layer. In-situ scattering experiments revealed an onset of fibre formation during spin coating at lower concentration for the branched material, which was explained in terms of a lowered solubility. The increased tendency of aggregation is consistent with a lower barrier for nucleation, leading to thinner fibres through the theory of nucleation-and-growth. We propose that this decrease in the energetic barrier for nucleation finds its origin in entropic effects caused by the branched nature of the polymer. The results therefore demonstrate that introducing branching can be an effective tool to increase photovoltaic efficiency.

3.4 Experimental section

3.4.1 Materials and methods

Commercial solvents and reactants were used as received unless stated otherwise. [70]PCBM (purity 90-95%) was purchased from Solenne BV. 3,6-Bis(5-bromothiophen-2-yl)-2,5-bis(2-decyltetradecyl)-2,5-dihydropyrrolo[3,4-c]pyrrole-1,4-dione was synthesized according to literature procedure.[23] All other chemicals were purchased from Aldrich Chemical Co. 1,4-Bis(4,4,5,5-tetramethyl-1,3,2-dioxaborolan-2-yl)benzene and 1,3,5-tris(4,4,5,5-tetramethyl-1,3,2-dioxaborolan-2-yl)benzene were recrystallized from methanol prior to polymerization. DT-PDPPTPT was synthesized according to the previously published procedure.[23]

Photovoltaic devices with an active area of 0.09 and 0.16 cm² were fabricated on patterned indium tin oxide (ITO) glass substrates (Naranjo Substrates). Substrates were cleaned by sonication in acetone for 15 minutes, followed by scrubbing with a sodium dodecyl sulfate solution (99%, Acros), rinsing with deionized water and a final sonication step in 2-propanol. Finally, they underwent with UV-ozone treatment for 30 min. Poly(ethylenedioxythiophene):poly(styrenesulfonate) (PEDOT:PSS) (Clevios P, VP Al4083) was deposited via spin coating (3000 rpm, 40 nm), followed by the active layer. The polymers were dissolved at a concentration of 4 mg/mL together with [70]PCBM (8 mg/mL) in chloroform containing 3 vol% or 6 vol% of DIO by stirring one hour at 90 °C. The solutions were cooled to room temperature (stirring for 2 min.) prior to spin coating. The best devices were made using a spin coat rate of 1500 rpm, resulting in an active layer thickness of 104 nm in both

cases. The back electrode, consisting of LiF (1 nm) and Al (100 nm), was deposited by evaporation under high vacuum (~3×10^{-7} mbar).

Current density – voltage ($J-V$) characteristics were measured with a Keithley 2400 source meter under ca. 100 mW/cm^2 white-light illumination from a tungsten–halogen lamp filtered by a Schott GG385 UV filter and a Hoya LB120 daylight filter. Short-circuit currents under AM 1.5G conditions were estimated by convoluting the spectral response with the solar spectrum. Spectral response measurements were conducted under 1 sun operating conditions by using a 532 nm solid state laser (Edmund Optics) for bias illumination. The device was kept in a nitrogen filled box behind a quartz window and irradiated with modulated monochromatic light, from a 50 W tungsten-halogen lamp (Philips focusline) and monochromator (Oriel, Cornerstone 130) with the use of a mechanical chopper. The modulated photocurrent was amplified with a Stanford Research System Model SR570 current preamplifier and then measured using a lock-in amplifier (Stanford research Systems SR830). A calibrated silicon cell was used as reference. TEM was performed on a Tecnai G 2 Sphera TEM (FEI) operated at 200 kV. Layer thicknesses were measured with a Veeco Dektak 150 profilometer.

The wavelength dependent index of refraction (n) and extinction coefficient (k) were obtained from the reflection and transmission of blend films of the optimized active layers on quartz (3 thicknesses) that were measured using a calibrated integrating sphere. Light absorption in the device stack was then modelled using Setfos 3.2 (Fluxim AG) software using the optical constants (n, k) of all layers in the stack and the transfer matrix formalism. By dividing the EQE with the fraction of photons absorbed by the active layer the internal quantum efficiency (IQE) was obtained at each wavelength (Figure 3.4). The spectrally averaged IQE was found to be 51% in the case of DT-PDPPTPT and 71% in the case of 1B-DT-PDPPTPT. Hence, the increase in IQE represents 90% of the increase in spectrally averaged EQE, the other 10% being accounted for by the higher absorption of 1B-DT-PDPPTPT.

For the light scattering experiments, silicon substrates (Si-Mat, 525 μm thickness with 200 nm SiO_2 layer) were used, which were cleaned in the same way as the ITO substrates, but UV-ozone was replaced with an air plasma treatment (Diener Electronic Femto PCCE, 100% power, 10 minutes). A layer of poly(ethylenedioxythiophene):poly(styrene sulfonate) (PEDOT:PSS, Heraeus Clevios PVP Al 4083) was spin coated before the measurement, to ensure similar wetting properties as the ITO substrates. Simultaneously with the scattering experiments, solar cell devices were fabricated from the same solutions. All solar cells showed the same behaviour as before.

A Melles-Griot 5 mW HeNe laser (632.8 nm) was spread to a spot of ~3 mm radius using a biconvex lens. The specular reflection (which contains the interference signal) from the spinning silicon substrate (1500 rpm) was diffused using white paper and collected with a Thorlabs SM1PD1A photodiode. A second photodiode (Hamamatsu S2281) collected light scattered by inhomogeneities in

the spin-coating film. Both photodiodes were behind a Thorlabs FL632.8-3 laser line filter to remove unwanted environmental light from the signal. Two Stanford Research System Model SR570 current preamplifiers (high bandwidth mode, 10 nA/V) amplified the signals, which were then recorded simultaneously with a time resolution of ~1 ms by a Keithley 2636A sourcemeter.

The intensity of the specular reflected laser light is dependent on the interference of the light reflected from the top of the layer and the light reflected from the substrate. This intensity oscillates in time as the layer dries and the interference goes through maxima and minima as shown in Figure 3.4a. A script in Wolfram Mathematica 10.0 was used to select peaks and valleys in the interference signal, which were used to back-calculate the thickness evolution during solvent evaporation. Working backwards, each peak-valley adds a thickness of ~100 nm ($\lambda/(4n\cos\theta)$) to the layer thickness after chloroform evaporation, which is the final layer thickness and the remaining amount of DIO. The amount of DIO at that point is calculated using the volume ratio of DIO to solids in the initial spin coating solution. λ is the wavelength of the laser, θ the angle of incidence and the refractive index n was estimated using the approximate volume fractions of all components. Figure 3.6c shows the layer thickness vs. time for the short times (> 1 s).

Figure 3.6d shows the corresponding intensity of the scattered light that we attribute to the formation of fibres. To be able to directly compare the experiments, the curves were synchronized with respect to the last valley in the interference signal during the fast drying stage (Figure 3.6a). To demonstrate that drying of the layer continues after this fast drying stage, two long measurements were performed, which indicate that the layer only dries completely after 1 to 1.5 hours (Figure 3.6b). This long drying time is related to the slow evaporation of DIO, which has a high boiling point. This indicates that only a very small amount of DIO will evaporate during the first 2 s of spin coating, which justifies the assumption made above that at point t = 0 s the DIO content is the same as the initial DIO content.

Molecular-weight distributions of the polymers were estimated by GPC at 140 °C on a PL-GPC 120 system using a PL-GEL 10 mm MIXED-C column with *o*-DCB as the eluent and using polystyrene internal standards. Samples were dissolved in *o*-DCB at 140 °C for 2 hours and filtered hot through a heated 2 µm PTFE filter. UV-vis-NIR spectroscopy was conducted on a PerkinElmer Lambda 900 or PerkinElmer Lambda 1050 spectrophotometer. Cyclic voltammetry was performed under an inert atmosphere with a scan speed of 0.1 V/s on polymer films using a solution of 1 M tetrabutylammonium hexafluorophosphate in acetonitrile. A polymer-covered ITO substrate was used as the working electrode, a silver rod as counter electrode and a silver rod coated with silver chloride (Ag/AgCl) as quasi-reference electrode in combination with Fc/Fc^+ as an internal standard.

3.4.2 Synthesis of 1B-DT-PDPPTPT

3,6-Bis(5-bromothiophen-2-yl)-2,5-bis(2-decyltetradecyl)-2,5-dihydropyrrolo[3,4-*c*]pyrrole-1,4-dione (100 mg, 88.4 μmol), 1,4-bis(4,4,5,5-tetramethyl-1,3,2-dioxaborolan-2-yl)benzene (28.7 mg, 87.1 μmol), 1,3,5-tris(4,4,5,5-tetramethyl-1,3,2-dioxaborolan-2-yl)benzene (0.40 mg, 0.88 μmol), triphenylphosphine (1.39 mg, 5.30 μmol) and tris(dibenzylideneacetone)dipalladium (1.21 mg, 1.331 μmol) were placed in a Schlenk flask under argon. Dry toluene (2 mL) was added and the resulting solution was degassed with argon. A degassed aqueous 2M solution of tripotassium phosphate was subsequently added (0.22 mL) with a drop of Aliquat 336 and the mixture was heated to 115 °C. After reaction overnight, the crude product was dispersed in 1,1,2,2-tetrachloroethane (TCE) and subsequently poured into methanol. The filtered product was redissolved in TCE at 150 °C. Ethylenediaminetetraacetic acid (200 mg) was added to this hot solution and stirred during one hour. Water was added, and the mixture was stirred vigorously for another hour at 110 °C, after which the organic layer was separated, and washed with water. The polymer was then precipitated in methanol, and filtered in a Soxhlet thimble. Soxhlet extraction using acetone, hexane, and dichloromethane was performed, after which the residue in the thimble was dissolved in hot TCE. This solution was subsequently precipitated in methanol and filtered, giving 1B-DT-PDPPTPT as a dark green solid.

3.5 References

1 Z. He, B. Xiao, F. Liu, H. Wu, Y. Yang, S. Xiao, C. Wang, T. P. Russell, Y. Cao, *Nat. Photon.*, 2015, **9**, 174-179.

2 Y. Liu, J. Zhao, Z. Li, C. Mu , W. Ma, H. Hu, K. Jiang, H. Lin, H. Ade, H. Yan, *Nat. Commun.*, 2015, **5**, 5293.

3 S.-H. Lia, H.-J. Jhuo, P.-N. Yeh, Y.-S. Cheng, Y.-L. Li, Y.-H. Lee, S. Sharma, S.-A. Chen, *Sci. Rep.*, 2014, **4**, 6813.

4 J.-D. Chen, C. Cui, Y.-Q. Li, L. Zhou, Q.-D. Ou, C. Li, Y. Li, J.-X. Tang, *Adv. Mater.*, 2015, **27**, 1035-1041.

5 W. Li, K. H. Hendriks, A. Furlan, W. S. C. Roelofs, M. M. Wienk, R. A. J. Janssen, *J. Am. Chem. Soc.*, 2013, **135**, 18942-18948.

6 K. H. Hendriks, G. H. L. Heintges, V. S. Gevaerts, M. M. Wienk, R. A. J. Janssen, *Angew. Chem. Int. Ed.*, 2013, **52**, 8341-8344.

7 L. Dou, H.-H. Chang, J. Gao, C.-C. Chen, J. Jou, Y. Yang, *Adv. Mater.*, 2013, **25**, 825-831.

8 Y. Li, P. Sonar, L. Murphy, W. Hong, *Energy Environ. Sci.*, 2013, **6**, 1684-1710.

9 J.-R. Pouliot, B. Sun, M. Leduc, A. Najari, Y. Li, M. Leclerc, *Polym. Chem.*, 2015, **6**, 278-282.

10 C. Duan, F. Huang, Y. Cao, *J. Mater. Chem.*, 2012, **22**, 10416-10434.

11 C. Cabanetos, A. El Labban, J. A. Bartelt, J. D. Douglas, W. R. Mateker, J. M. J. Fréchet, M. D. McGehee, P. M. Beaujuge *J. Am. Chem. Soc.*, 2013, **135**, 4656-4659

12 W.-H. Chang, J. Gao, L. Dou, C.-C. Chen, Y. Liu, Y. Yang, *Adv. Energy Mater.*, 2014, **4**, 1300864.

13 J. K. Lee, W. L. Ma, C. J. Brabec, J. Yuen, J. S. Moon, J. Y. Kim, K. Lee, G. C. Bazan, A. J. Heeger, *J. Am. Chem. Soc.*, 2008, **130**, 3619-3623.

14 H.-C. Liao, C.-C. Ho, C.-Y. Chang, M.-H. Jao, S. B. Darling, W.-F. Su, *Mater. Today*, 2013, **16**, 326-336.

15 J. J. van Franeker G. H. L. Heintges, C. Schaefer, G. Portale, W. Li, M. M. Wienk, P. van der Schoot, R. A. J. Janssen, *J. Am. Chem. Soc.*, 2015, **137**, 11783-117945.

16 E. Zhou, J. Cong, K. Hashimoto, K. Tajima, *Energy Environ. Sci.*, 2012, **5**, 9756-9759.

17 Z. Gu, P. Tang, B. Zhao, H. Luo, X. Guo, H. Chen, G. Yu, X. Liu, P. Shen, S. Tan, *Macromolecules*, 2012, **45**, 2359-2366.

18 J. Qiao, C. Yang, Q. He, F. Bai, Y. Li, *J. Appl. Polym. Sci.*, 2004, **92**, 1459-1466.

19 C. Q. Ma, E. Mena-Osteritz, T. Debaerdemaeker, M. M. Wienk, R. A. J. Janssen, P. Bäuerle, *Angew. Chem. Int. Ed.*, 2007, **46**, 1679-1683.

20 C.-Q. Ma, M. Fonrodona, M. C. Schikora, M. M. Wienk, R. A. J. Janssen, P. Bäuerle, *Adv. Funct. Mater.*, 2008, **18**, 3323-3331

21 H. S. Mangold, T. V Richter, S. Link, U. Würfel, S. Ludwigs, *J. Phys. Chem. B*, 2012, **116**, 154-159.

22 J. J. van Franeker, M. Turbiez, W. Li, M. M. Wienk, R. A. J. Janssen, *Nat. Commun.*, 2015, **6**, 6229.

23 W. Li, K. H. Hendriks, A. Furlan, W. S. C. Roelofs, S. C. J. Meskers, M. M. Wienk, R. A. J. Janssen, *Adv. Mater.*, 2014, **26**, 1565-1570.

24 X. Cao, M. Li, J. Liu, H. Wang, K. Zhou, Y. Han, *Org. Electron.*, 2015, **24**, 280-287.

Chapter 4

The effect of side-chain substitution and hot processing on diketopyrrolopyrrole-based polymers for organic solar cells

Abstract

The effects of cold and hot processing on the performance of polymer-fullerene solar cells are investigated for diketopyrrolopyrrole (DPP) based polymers that were specifically designed and synthesized to exhibit a strong temperature-dependent aggregation in solution. The polymers, consisting of alternating DPP and oligothiophene units, are substituted with linear and second position branched alkyl side chains. For the polymer-fullerene blends that can be processed at room temperature, hot processing does not enhance the power conversion efficiencies compared to cold processing because the increased solubility at elevated temperatures results in the formation of wider polymer fibres that reduce charge generation. Instead, hot processing seems to be only advantageous when cold processing is not possible due to a limited solubility at room temperature. The resulting morphologies are consistent with a nucleation-growth mechanism for polymer fibres during drying of the films.

This work has been published: G. H. L. Heintges, P. J. Leenaers, R. A. J. Janssen, *J. Mater. Chem. A*, 2017, **5**, 13748-13756.

4.1 Introduction

Organic photovoltaic cells have been extensively investigated as an interesting alternative photovoltaic technology, displaying the potential for semi-flexible devices produced via roll-to-roll methods.[1-3] Typically, the active layer in these cells consists of light harvesting donor and acceptor materials of which the blend morphology strongly influences the efficiency of the cell. The mechanisms of morphology formation have been studied extensively in the past. In polymer-fullerene bulk heterojunctions multiple methods have been used to fine-tune the morphology such as changing processing conditions, increasing the molecular weight of the polymer and adjusting the solubility by changing the solubilizing side chains.[4]

Recently, Yan and co-workers have developed an interesting new class of semiconducting polymers that exhibit a strong temperature-dependent aggregation behaviour in solution, providing polymer-fullerene solar cells with a power conversion efficiency (PCE) of 10.8%.[5] The strong temperature-dependent aggregation was introduced via alkyl side chains on the polymer backbone that have a branching point on the second carbon atom from the main chain. When these 2-alkylalkyl substituents were introduced on an oligothiophene segment in the main chain, controlled aggregation and strong crystallization of the polymer during the film cooling and drying process was achieved, resulting in optimal bulk heterojunction morphologies and high PCEs under hot processing conditions.[5] This same principle has been applied by Yan et al. to wide band gap (1.90 eV),[6] medium band gap (1.65 eV),[5] and low band gap (1.43 eV)[7] polymer donors, all reaching excellent PCEs in solar cells with fullerene acceptors. In these examples it was essential to tune the aggregation behaviour of the polymer by balancing the tendency of the π-conjugated main chain units to aggregate with the solubilizing power of the 2-alkylalkyl substituents.

Such balance has also been found to be important for morphology formation in photoactive blends based on diketopyrrolopyrrole (DPP) based π-conjugated polymers and fullerenes.[8-14] In these DPP polymers, solubility in organic solvents is typically provided by solubilizing 2-alkylalkyl side chains on the nitrogen atoms of the electron deficient DPP core, in relevant cases further enhanced by side chains on the heteroaromatic electron-rich units of these push-pull low band gap materials. The final blend morphologies are determined by the chemical structure, the processing conditions and the molecular weight

of the polymer.[10,12] One result that emerges from this work is that reducing the solubility, either via the molecular structure, increasing the molecular weight, or a specific processing additive, leads to morphologies in which narrow crystalline DPP polymer fibres are present that provide high power conversion efficiencies.[9–14] Under conditions where the solubility of the polymer is too high, the fibre width in the photoactive layer increases, resulting in a loss in device performance because the width of the fibre exceeds the exciton diffusion length. The reasons for forming wider fibres with more soluble materials are not yet fully understood but can be rationalized with a nucleation-growth model to originate from either a minimum width of stable polymer fibres (fast-nucleation limit) or from the number of nuclei formed (fast-growth limit).[12] Fibre formation has also been observed for other polymer-fullerene systems.[15,16]

Here we investigate the effects of hot versus cold processing of polymer-fullerene based solar cells using newly synthesized DPP-based polymers with solubilizing 2-alkylalkyl substituents on the terthiophene and quaterthiophene units and linear or branched alkyl chains on the DPP unit. Changing from the common branched to a linear alkyl chain on the DPP units is expected to enhance aggregation and reduce solubility such that more narrow fibres are formed, while the branched alkyl side chains can endow the polymer with sufficient solubility at elevated temperatures.[7] Each of the new DPP polymers exhibits a temperature-dependent aggregation. We find that for the polymers that can be processed at room temperature, hot processing does not offer an advantage in terms of device performance, because the increased processing temperature enhances the solubility and results in wider fibres.

4.2 Results and discussion

The synthesis of the monomers is shown in Scheme 4.1. The 2-ethylhexyl or 2-hexyldecyl side chains were introduced on the thiophene rings via a Kumada reaction between 3-bromothiophene and the corresponding 2-alkylalkyl magnesium bromide. Formylation and subsequent reaction with hydroxylamine hydrochloride afforded the 4-(2-alkylalkyl)-2-cyanothiophenes which were used as the starting point for the DPP formation reaction. Modified literature procedures then afforded the DPP monomers (denoted as R_2-DPP-R_1),[7,17] which were brominated and used in a Stille polymerization reaction with either 2,5-bis(trimethylstannyl)thiophene or 5,5′-bis(trimethylstannyl)-2,2′-bithiophene under

optimized conditions[18] to afford the R_2-PDPP3T-R_1 and R_2-PDPP4T-R_1 polymers depicted in Scheme 4.2. The details of the synthetic procedures and characterization of the intermediates can be found in the Experimental section.

The D-DPP-EH monomer was polymerized in a Stille reaction with thiophene and the resulting polymer, D-DPP3T-EH (Scheme 4.2), showed high solubility despite a reasonably high number average molecular weight of M_n = 39 kDa (Table 4.1). We attribute the high solubility to the two branched side chains on the terthiophene moieties that separate the DPP units along the chain. As we know that a too high solubility at room temperature of these polymers causes a reduction of the solar cell performance by forming a too coarse phase separation,[9-12] we reduced the solubility by introducing an additional unsubstituted thiophene ring in the main chain via polymerization of D-DPP-EH and bithiophene. In the resulting D-PDPP4T-EH (Scheme 4.2) polymer, the alkyl substituents are more distant and point in opposite directions along the thiophene chain. The additional thiophene ring in the repeating unit had a dramatic effect and resulted in a significant decrease in solubility. The rather low M_n of 24.3 kDa of D-PDPP4T-EH can be explained by precipitation of the material during the reaction before polymerization was completed. To achieve a solubility in between that of D-PDPP3T-EH and D-PDPP4T-EH, two additional polymers were synthesized (Scheme 4.2). D-PDPP4T-HD features extended 2-hexyldecyl side chains on the thiophenes flanking the DPP unit, while in EH-PDPP4T-EH

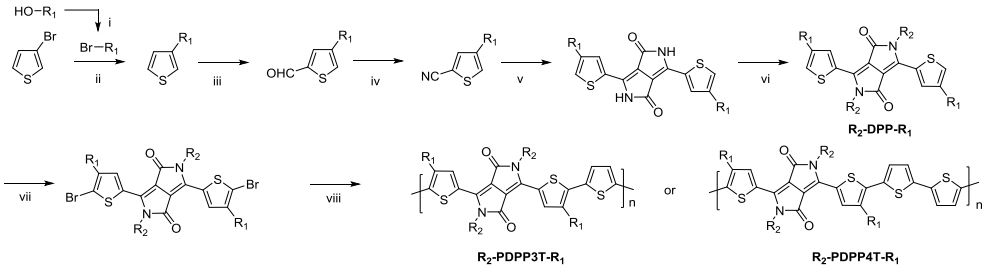

Scheme 4.1: R_1 = 2-ethylhexyl (EH) or 2-hexyldecyl (HD), R_2 = dodecyl (D) or 2-ethylhexyl, (i) PPh_3, *N*-bromosuccinimide (NBS), DCM, 0 °C; (ii) Mg, Ni(dppp)Cl_2, diethyl ether; (iii) (1) LDA, THF, −78 °C; (2) DMF, −78 °C; (iv) $NH_2OH.HCl$, DMF, 145 °C; (v) Na, diethyl succinate, *t*-amyl alcohol, 120 ºC; (vi) K_2CO_3, Br−R_2, DMF, 120 °C; (vii) NBS, $CHCl_3$, 0 °C; (viii) 2,5-bis(trimethylstannyl)thiophene or 5,5′-bis(trimethylstannyl)-2,2′-bithiophene, $Pd_2(dba)_3$/PPh_3, toluene/DMF, 115 °C.

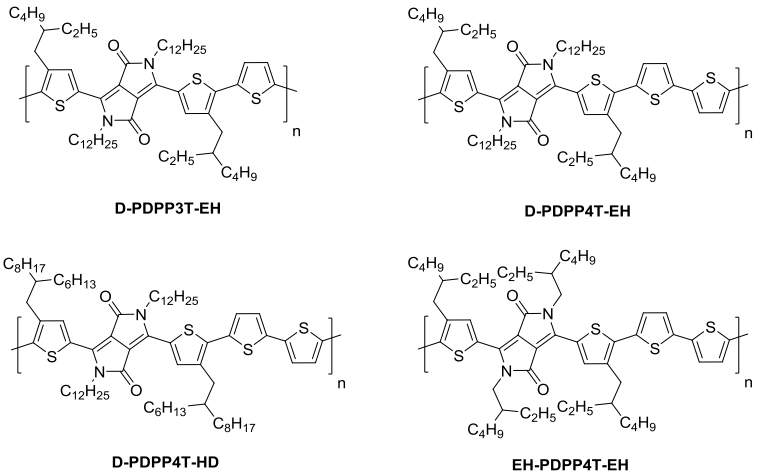

Scheme 4.2: Structures of DPP polymers with branched side chains on the thiophene substituents that flank the DPP unit.

the linear dodecyl chain on the DPP unit is replaced by a branched 2-ethylhexyl chain. A rather high M_n of 57.3 kDa was obtained for D-PDPP4T-HD, indicating that it has an improved solubility in the polymerization reaction yielding a higher molecular weight. The M_n of EH-PDPP4T-EH could, however, not be determined by GPC as it showed a remarkably low solubility in *o*-dichlorobenzene (*o*-DCB), even at 140 °C.

UV-vis-NIR absorption spectra of the materials measured in chloroform and thin films (Figure 4.1) reveal an interesting behaviour. For D-PDPP3T-EH there is a significant red shift in the optical band gap when going from solution to thin film. While it is common for many conjugated polymers to exhibit such shift, the effect is larger for D-PDPP3T-EH than for the previously studied polymers HD-PDPP3T[18] and HD-PDDP3T-Me[17] that have no or a small ($-CH_3$) substituent on the thiophene rings flanking the DPP unit. The shift of the onsets of absorption in solution and film, determined from the crossing point of the tangent in the inflection point in the spectrum at long wavelength with the horizontal axis, decreases from 58 nm for D-PDPP3T-EH, to 48 nm for DT-PDPP3T, 36 nm for HD-PDDP3T-Me and 12 nm for HD-PDPP3T (Figure 4.2). This supports the notion that in solution D-PDPP3T-EH is less aggregated due to the branched side chains on the thiophene rings. The higher solubility is associated with twisting of the polymer chain, which reduces the effective conjugation length. In the solid state, the optical band gap of all three PDPP3T

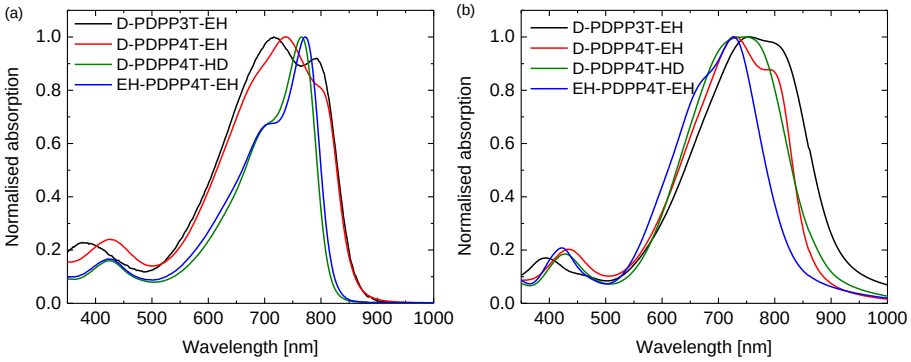

Fig. 4.1: Normalized UV-vis-NIR absorption spectra of the DPP polymers. (a) In chloroform solution. (b) As thin film on glass.

derivatives is very similar and amounts to E_g = 1.34 eV. As we will demonstrate in further detail below, the vibronic peaks in the spectrum of D-PDPP3T-EH are associated with its partial aggregation under these conditions.

The PDPP4T polymers behave quite differently. D-PDPP4T-EH shows a rather low band gap in solution and the absorption is not shifted in the solid state (Figure 4.1). This behaviour is similar to that of DT-PDPP4T (DT = 2-decyltetradecyl) which also did not show a shift in the onset of the absorption between solution and thin film spectra.[9] The two more soluble D-PDPP4T-HD and EH-PDPP4T-EH polymers do have significantly blue-shifted onsets of absorption in solution compared to D-DPP4T-EH (Figure 4.1). This suggests that they are less aggregated, but we note that they show a clear vibronic shoulder at higher energies that often appears when interchain interactions are also present. Of these two more soluble derivatives, D-PDPP4T-HD exhibits a pronounced red shift of its thin film absorption spectrum, to an onset that is similar to that of DT-PDPP4T and D-PDPP4T-EH (Figure 4.1, Table 4.1). Remarkably, for EH-PDPP4T-EH the absorption onset does not shift significantly between solution and solid state. This suggests that upon casting a film of EH-PDPP4T-EH the chains do not undergo more aggregation.

Cyclic voltammetry was performed on polymer films cast on indium tin oxide (ITO) glass substrates in acetonitrile containing tetrabutylammonium hexafluorophosphate as electrolyte (Table 4.1). The HOMO and LUMO levels determined from the onsets of the oxidation and reductions waves vary little, suggesting a small effect of the alkyl chain

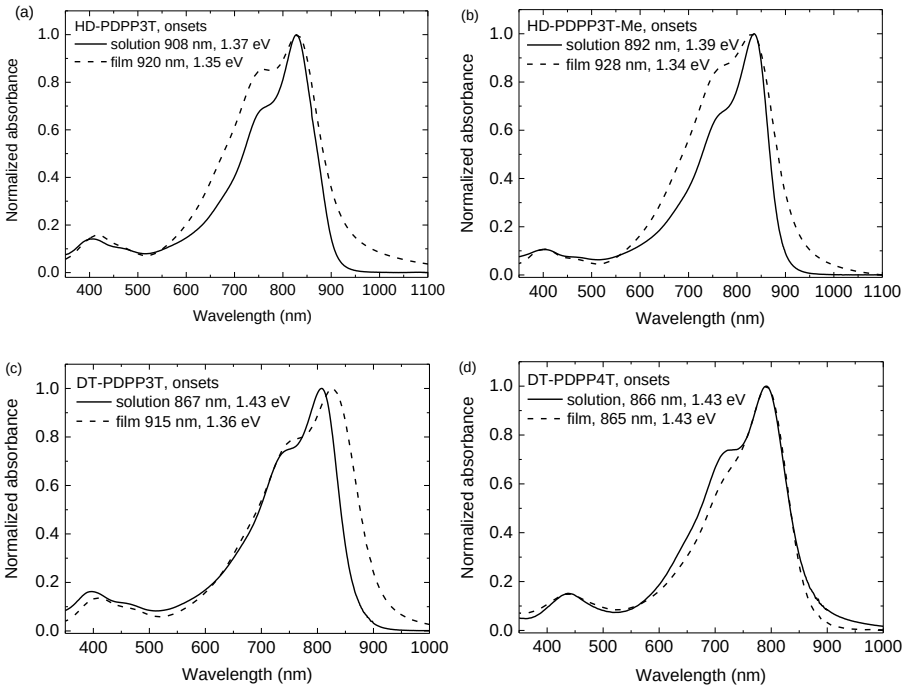

Fig. 4.2: UV-vis-NIR spectra of (a) HD-PDPP3T in solution and film,[18] the onset shifts 12 nm. (b) HD-PDPP3T-Me in solution and film,[17] the onset shifts 36 nm. (c) DT-PDPP3T in solution and film, the onset shifts 48 nm. (d) DT-PDPP4T in solution and film, the onset shifts -1 nm.[9]

Table 4.1: Physical properties of the polymers.

Polymer	M_n **[kDa]**	M_w **[kDa]**	**PDI**	E_g **[eV]**[a]	**HOMO [eV]**[b]	**LUMO [eV]**[b]	E_g, **[eV]**[c]	**Ref.**
HD-PDPP3T	147	400	2.72	1.35	−5.60	−3.76	1.84	18
DT-PDPP3T	137	458	3.34	1.36	-	-		9
HD-PDPP3T-Me	110	282	2.56	1.34	−5.61	−3.71	1.90	17
D-PDPP3T-EH	39.0	90.0	2.31	1.35	−5.60	−3.66	1.94	
DT-PDPP4T	219	641	2.93	1.43	−5.59	−3.65	1.94	9
EH-PDPP4T-HD	-	-	-	1.45	-	-		7
D-PDPP4T-EH	24.3	59.3	2.44	1.43	−5.54	−3.69	1.85	
D-PDPP4T-HD	57.3	173	3.02	1.41	−5.59	−3.58	2.01	
EH-PDPP4T-EH	-	-	-	1.48	−5.58	−3.65	1.93	

[a] From the absorption onset in thin films. [b] From the onsets of the redox waves and using −5.23 eV for the energy of ferrocene/ferrocenium. [c] Electrochemical band gap.

substitution pattern on the energy levels of the polymer. In each case, the electrochemical band gap is significantly larger than the optical band gap.

The aggregation behaviour of the polymers was further explored using temperature-dependent UV-vis-NIR measurements in 1,1,2,2-tetrachloroethane (TCE) (Figure 4.3). TCE is a slightly less good solvent for DPP polymers compared to chloroform, but its higher boiling point (147 °C vs. 61 °C) allows to study solutions over a much wider temperature range. At the highest temperature used (100 °C) each polymer is truly molecularly dissolved. At this stage the spectra show a single unresolved absorption band centred at ~650 nm (Figure 4.3). With decreasing temperature the UV-vis-NIR spectra of all four polymers in TCE show a transition from the molecular dissolved state to an aggregated state, which is evidenced from the appearance of a long wavelength peak and associated vibronic structure. This transition starts at ~60 °C for D-PDPP4T-EH, at ~50 °C for D-PDPP4T-HD and EH-PDPP4T-EH, while it only occurs at ~20 °C for D-PDPP3T-EH, which is the most soluble polymer of the four derivatives. For the three PDPP4T polymers further cooling below the onset of aggregation is accompanied by an isosbestic point in the spectra, which we interpret as the transition between an aggregated and a molecular dissolved state. Above the transition temperature, where no aggregates exist, there is no isosbestic point. In this regime the absorption maxima simply shift gradually to lower energy when reducing the temperature. This is attributed to a gradual decrease of the twisting of the polymer chains. This planarization increases the average effective conjugation length of chain segments and moves the absorption maximum to lower energies. The small increase in intensity at lower temperatures is, at least partly, due to thermal contraction of the solvent.

UV-vis-NIR spectra were also recorded for the four polymers in *o*-DCB at different temperatures (Figure 4.4). *o*-DCB is a less good solvent for these polymers than chloroform or TCE. With increasing temperature of *o*-DCB D-PDPP3T-EH, D-PDPP4T-EH and D-PDPP4T-HD show a more or less gradual loss of the long wavelength peak and its vibronic structure. At ~60 °C D-PDPP3T-EH and D-PDPP4T-HD reach a state in which the polymer chains are truly molecularly dissolved. For D-PDPP4T-EH a small shoulder around 800 nm remained until 100 °C, which agrees with the lower solubility of this material. For EH-PDPP4T-EH the results (Figure 4.4d) were different from the other three

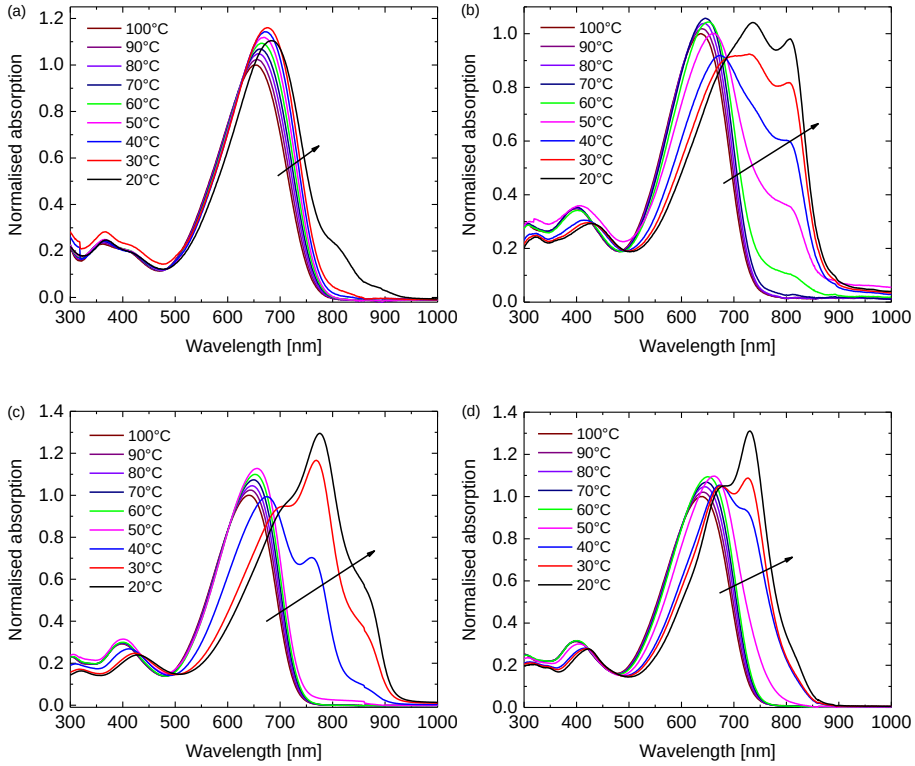

Fig. 4.3: Temperature-dependent UV-vis-NIR absorption of the polymers in TCE solution. (a) D-PDPP3T-EH. (b) D-PDPP4T-EH. (c) D-PDPP4T-HD. (d) EH-PDPP4T-EH.

polymers. At room temperature the material is sparsely soluble in *o*-DCB and when conducting the experiment from high to low temperature the polymer precipitated in its aggregated state in the cuvette, resulting in a loss of signal at lower temperatures.

Solar cell devices were made using the polymers as electron donor in combination with [6,6]-phenyl-C_{71}-butyric acid methyl ester ([70]PCBM) as electron acceptor on glass substrates patterned with ITO, covered with poly(3,4-ethylenedioxythiophene)-poly(styrenesulfonate) (PEDOT:PSS) as hole extracting contact and LiF/Al as electron extracting contact. The processing conditions for the active layers were carefully optimized for each individual polymer using *o*-DCB, diphenyl ether (DPE), or 1,8-diiodooctane (DIO) as co-solvent where appropriate. We evaluated both room temperature (20 °C from chloroform (CF)) and hot (100 to 140 °C from TCE) deposition conditions.

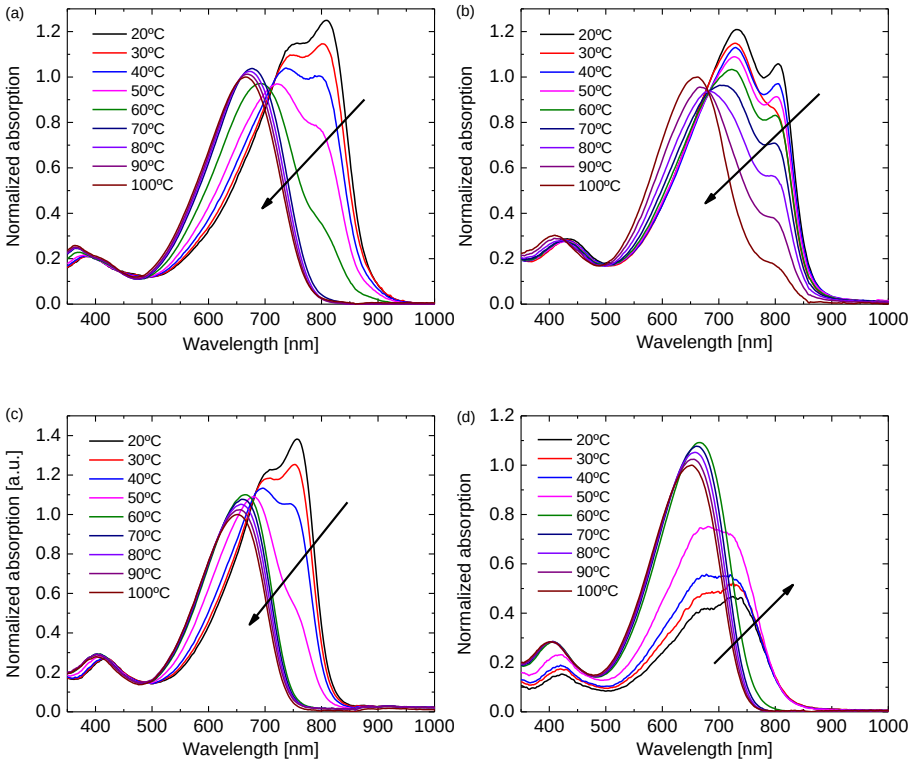

Fig. 4.4: The temperature dependent UV-vis-NIR absorption of the polymers in *o*-DCB solution. (a) D-PDPP3T-EH. (b) D-PDPP4T-EH. (c) D-PDPP4T-HD. (d) EH-PDPP4T-EH.

Room temperature processing was performed using chloroform as main solvent with *o*-DCB, DPE or DIO as co-solvent. Because D-PDPP3T-EH is not sufficiently soluble in chloroform at room temperature, the analysis was limited to the three more soluble polymers. It was found that using DPE as co-solvent affords higher PCEs than use of *o*-DCB or DIO (not shown here). The current density – voltage (*J*−*V*) characteristics and external quantum efficiency (EQE) of the optimized devices processed at room temperature from chloroform/DPE (98:2) are shown in Figure 4.5 and the relevant solar cell parameters are collected in Table 4.2.

The PCE of D-PDPP3T-EH:[70]PCBM cells reaches 5.4%. The open-circuit voltage (V_{oc}) of this cell (0.57 V) is lower than that of the related HD-PDPP3T:[70]PCBM (V_{oc} = 0.67 V) cell,[18] but almost identical to that of HD-PDPP3T-Me:[70]PCBM (V_{oc} = 0.59 V) cells.[17] This difference can be attributed to the inductive electron donating effect of the

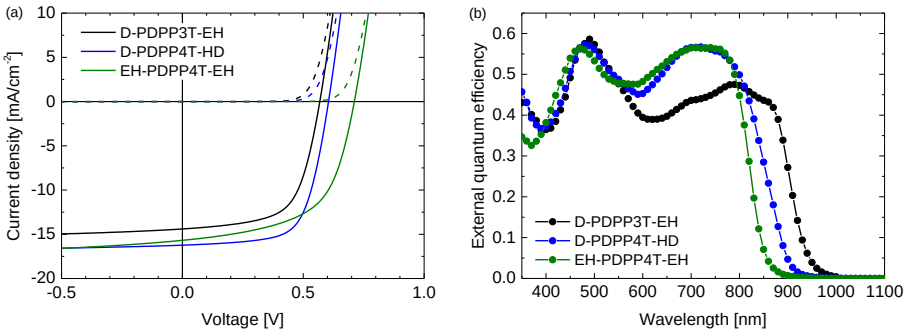

Fig. 4.5: Characteristics of optimized R2-PDPP-R1:[70]PCBM solar cells processed at room temperature from CF/DPE (98:2). (a) J−V characteristics under white light illumination. (b) EQE.

Table 4.2: Processing conditions and device characteristics for R_2-PDPP-R_1:[70]PCBM solar cells.

Polymer	Solution	T [°C]	μ_h [cm²/Vs]	d [nm]	J_{sc} [mA/cm²]	V_{oc} [V]	FF	PCE [%]
D-PDPP3T-EH	CF/DPE (98:2)	20	6.8×10^{-4}	154	15.2	0.57	0.63	5.4
	TCE	120	1.9×10^{-3}	140	11.3	0.70	0.55	4.4
	TCE/DPE (98:2)	120	5.9×10^{-4}	135	10.4	0.59	0.62	3.8
D-PDPP4T-EH	TCE/DPE (98:2)	120	6.5×10^{-4}	121	10.1	0.59	0.57	3.4
D-PDPP4T-HD	CF/DPE (98:2)	20	6.6×10^{-4}	101	15.8	0.60	0.67	6.3
	TCE/DIO (98:2)	100	1.0×10^{-3}	88	11.9	0.61	0.70	5.1
	TCE/DPE (98:2)	120	8.3×10^{-4}	147	12.1	0.63	0.60	4.5
EH-PDPP4T-EH	CF/DPE (98:2)	20	1.4×10^{-3}	106	14.9	0.71	0.58	6.1
	TCE/*o*-DCB (9:1)	140	1.2×10^{-3}	96	10.1	0.75	0.66	5.0
	TCE/DPE (98:2)	120	8.1×10^{-4}	92	11.4	0.74	0.59	4.9

alkyl substituents on the thiophene rings which raise the HOMO level and lower the V_{oc}. We note, however, that these rather subtle effects on the HOMO energy do not show up in the oxidation potentials determined by cyclic voltammetry. Compared to HD-PDPP3T and HD-PDPP3T-Me the EQE and, hence, the short-circuit current density (J_{sc}) of the cells based on D-PDPP3T-EH are lower, resulting in a lower overall PCE (5.4% vs. 7.1%[18] and 6.8%[17]). For all three PDPP3T polymers the onset of the EQE is found at about 950 nm.

D-PDPP4T-HD and EH-PDPP4T-EH reach comparable PCEs (6.3% and 6.1%) in solar cells when blended with [70]PCBM. These values are only slightly less than the PCE = 7.1% for DT-PDPP4T:[70]PCBM cells studied previously.[9] For the D-PDPP4T-HD cell the main difference is in the V_{oc} = 0.60 V, which shows the expected decrease compared to the V_{oc} = 0.64 V of DT-PDPP4T as a result of the electron donating alkyl substituents on the main chain. The onsets of the EQEs for D-PDPP4T-HD and DT-PDPP4T cells are both at about 900 nm. For EH-DPP4T-EH, on the other hand, the solar cell characteristics are quite different despite the similar polymer backbone. A significantly increased V_{oc} = 0.71 V is found for EH-PDPP4T-EH cells, which is in accordance with the higher optical band gap. The fill factor (FF) of the EH-PDPP4T-EH cell is lower as result of field-dependent charge extraction, which can be seen from the significant slope of the $J-V$ curve at short circuit. This slope is not present in the dark $J-V$ curve and hence not simply due to a low shunt (parallel) resistance.

The morphology of the three photoactive layers was investigated by transmission electron microscopy (TEM) (Figure 4.6). In each case a fibre-like morphology is observed. These fibres appear brighter and originate from semi-crystalline aggregates of the DPP polymers.[9–12]

A slightly coarser morphology, with wider fibres, is observed for the D-PDPP3T-EH:[70]PCBM film compared to the EH-PDPP4T-EH:[70]PCBM film (Figure 4.6, top row). The wider fibres are in accordance with the higher solubility of this polymer and rationalize the reduced EQE (45%) in the wavelength region above 700 nm were only the polymer absorbs light.[9-12] As expected, the higher EQE of the cells based on EH-PDPP4T-EH is associated with narrower fibres in TEM. However, the finer morphology of the EH-PDPP4T-EH-based layer compared to D-PDPP4T-HD is not clearly reflected in the EQE. Figure 4.5a shows that the photocurrent in the EH-PDPP4T-EH-based blend is strongly field dependent, while that of D-PDPP4T-HD saturates quicker below V_{oc}. This is consistent with the more intimate morphology of the EH-PDPP4T-EH:[70]PCBM blend which can hinder charge extraction due to longer or non-continuous pathways for charges, causing more non-geminate charge recombination, a bias voltage just below V_{oc} and a reduced fill factor. The difference in EQE for the D-PDPP3T-EH and D-PDPP4T-HD based cells cannot be readily explained by the fibre width, which is comparable and must hence be determined by other factors.

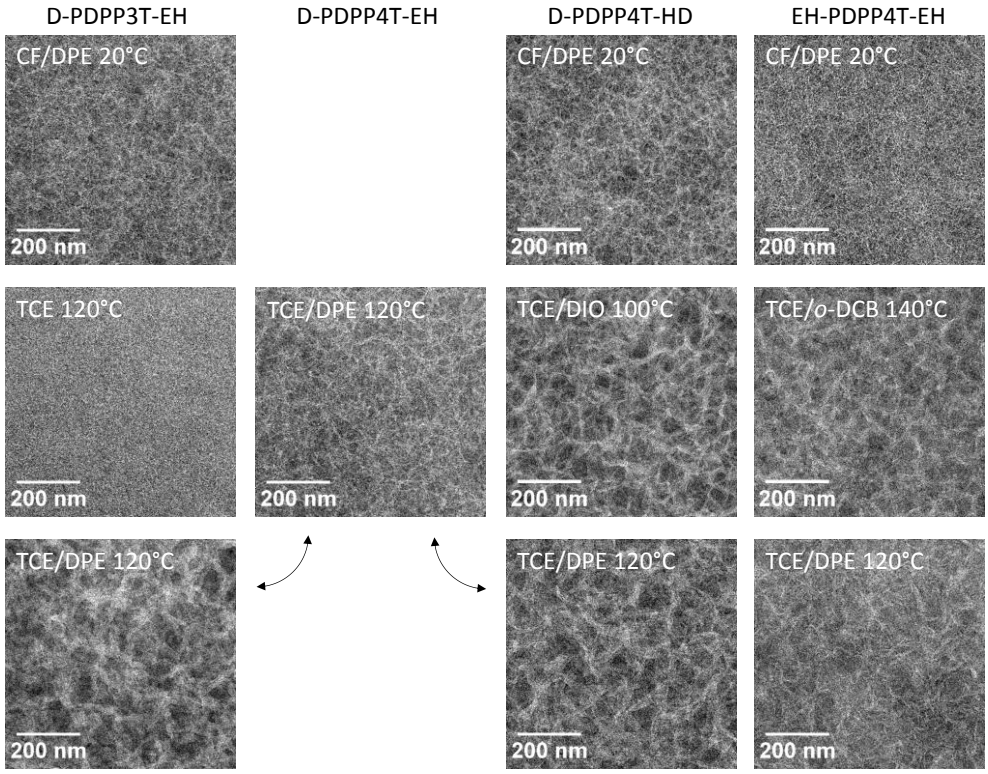

Fig. 4.6: TEM images of the photoactive layers. Left to right: blends of D-PDPP3T-EH, D-PDPP4T-EH, D-PDPP4T-HD and EH-PDPP4T-EH with [70]PCBM. Top row: room temperature processing from chloroform/DPE (98:2); middle row: optimized hot-processed devices from TCE/co-solvent; bottom row: hot-processed devices from TCE/DPE (98:2).

Hot processing of the active layers was performed to take advantage of the temperature-dependent aggregation behaviour of the polymers. We used TCE as the main solvent and solutions were heated to 100, 120, or 140 °C. Again we tested *o*-DCB, DPE and DIO as co-solvent, next to using pure TCE. For hot processing the co-solvent that affords the highest PCE varies among the different polymers, but in each case TCE/DPE (98:2) provides a PCE that is comparable to the best device. In Figure 4.7 and Table 4.2 we have included the best performing hot-processed solar cells, but also included the TCE/DPE-processed devices, such that a direct comparison under identical conditions can also be made.

The $J-V$ characteristics and EQE data shown in Figure 4.7 and Table 4.2 reveal that hot processing of these active layers from TCE/co-solvent does not improve the device

performance compared to the room temperature processing from chloroform/DPE. The EQE and concomitantly the J_{sc} of the hot processed cells is lower, while the V_{oc} remains the same or even slightly increases, except in the case of D-PDPP3T-EH.

The difference in V_{oc} in the case of D-PDPP3T-EH cells processed from pure TCE can be explained by a lack of aggregation, which is also evidenced by a shift of the band gap visible in the EQE of these cells, as well as TEM analysis. This indicates that the good solubility of D-PDPP3T-EH in TCE (Figure 4.3) prevents aggregation while spin coating, which is achieved when using a co-solvent.

Compared to room temperature processing, the FF of the optimised cells decreases in the case of D-PDPP3T-EH, but increases for D-PDPP4T-HD and EH-PDPP4T-EH. To investigate these differences in FF further, hole-only devices were fabricated using ITO/PEDOT:PSS and MoO_3/Ag electrodes with active layers processed under identical conditions to determine the hole mobility from the space charge limited current. The hole moblities varied in the range of 0.5 to 2.0×10^{-3} cm^2/Vs but there is consistent correlation between the hole mobility and fill factor (Table 4.2). Bartesaghi et al. demonstrated that the fill factor is not only dependent on the mobility of charges,[19] but also on the generation rate, thickness of the device and the Langevin prefactor. The latter corrects for the reduced recombination found in solar cells compared to Langevin theory. In this case, the generation rate and thicknesses of the devices are not sufficient to explain these differences in fill factor. The Langevin prefactor will decrease with a coarser phase separation, which will induce an increase in fill factor. In this way, we can correlate, at least in part, the changes of morphology (see TEM discussion below) with these changes in fill factor.

We note that the device performance of the D-PDPP4T-HD and EH-PDPP4T-EH hot-processed solar cells is better than that of a structurally closely related and more soluble HD-PDPP4T-HD polymer where J_{sc} = 9.65 mA/cm^2, V_{oc} = 0.70 V, FF = 0.46 and PCE = 3.1% has been found for hot-processed cells.[7]

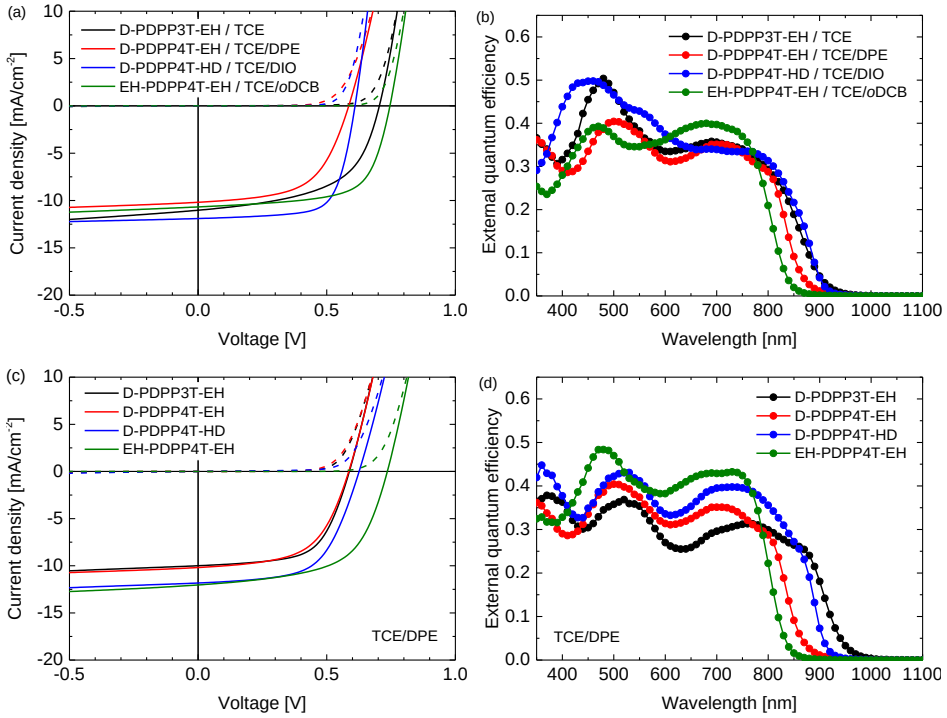

Fig. 4.7: Characteristics of optimized R_2-PDPP-R_1:[70]PCBM solar cells processed at 120 °C from TCE/co-solvent. (a, c) *J*–*V* characteristics under white light illumination. (b, d) EQE. (a, b) Best devices from solvent/co-solvent combination indicated in the legends. (c, d) Devices processed from TCE/DPE.

The TEM images of the photoactive layers (Figure 4.6) demonstrate that hot-processing generally results in wider fibres and a coarser phase separation except for D-PDPP3T-EH. In fact, the TEM data enable to rationalize the changes in *J*–*V* characteristics consistently. For D-PDPP3T-EH:[70]PCBM cells, hot processing from pure TCE results in a very homogeneous morphology without visible phase separation. For the blend processed from hot TCE the onset of the EQE (Figure 4.7b) is blue-shifted compared to that from chloroform/DPE (Figure 4.5b) and TCE/DPE (Figure 4.7d). The larger band gap, the reduced aggregation and the more intimately mixed morphology causes an increase in V_{oc} and a lower FF. When processed from TCE/DPE, the polymer does aggregate during spin coating, but forms clearly broader fibres than during room temperature processing from CF/DPE. The wider fibres reduce exciton dissociation and charge generation, explaining the loss in J_{sc}. Also for D-PDPP4T-HD:[70]PCBM and EH-PDPP4T-EH:[70]PCBM the

hot-processed layers show wider fibres than the room-temperature processed layers, irrespective of the co-solvent used (Figure 4.6). This explains the loss of photocurrent, as the width of the fibres becomes larger than the exciton diffusion length, such that not all photoexcitations result in charge formation. This behaviour is common to many DPP polymer-fullerene blends.[9-12] In these cases the cells are limited by charge generation. The wider fibres in the D-PDPP4T-HD:[70]PCBM and EH-PDPP4T-EH:[70]PCBM photoactive layers do, however, improve the charge collection, likely via a reduced bimolecular (Langevin) recombination because charges are confined to larger domains as evidenced by the increase of the fill factors.

To understand these results it is sufficient to realize that the most important effect of raising the temperature is the increase in solubility. In this case the width of the fibres is determined by the solubility, with wider fibres being formed when the solubility is higher.[9-12] This is clearly seen in the TEM analysis, as hot processing results in wider fibres than cold processing in all cases except for D-PDPP3T-EH cast from pure TCE, where polymer aggregation is completely supressed. The fibre width in these blends can be rationalized with a nucleation-growth model. In this model, high solubility results in wider fibres because either the critical nucleus size is larger for more soluble polymers, or the size is determined by fast growth of an initial amount of nuclei formed.[12]

It must be noted that the increased solubility and formation of larger fibres could also be caused by using TCE as a main solvent. To investigate this, attempts were made to produce devices from TCE solutions at room temperature. However, gelation of the solution prevented casting of a closed layer. Instead, chloroform-based solutions were heated to 40 °C and 60 °C and solar cell devices were made at these temperatures (Table 4.3). In all cases the J_{sc} and PCE of the devices remained similar when comparing devices fabricated at room temperature to devices made at 40 °C, but clearly decreased when going to 60 °C. This result demonstrates that hot processing in the case of these materials does not offer an advantage over cold processing.

In the discussion above we have related the fibre width and morphology to the solubility of the polymer in the solvent/co-solvent combination. In principle, the volatility of the solvents can also influence the width of the fibres and the film morphology. Chloroform is a low-boiling solvent, and when spin-cast, the active layer may dry more rapidly, inducing smaller fibres than when using (hot) TCE. Indeed, the volatility of the

Table 4.3: Device characteristics of the best devices for R_2-PDPP-R_1:[70]PCBM solar cells processed from chloroform/DPE (98:2) at different temperatures.

Polymer	***T*** **[°C]**	J_{sc} [a] **[mA/cm²]**	V_{oc} **[V]**	**FF**	**PCE** [b] **[%]**
D-PDPP3T-EH	20	15.3 (14.8)	0.56 (0.55)	0.51 (0.48)	4.4 (3.9)
	40	15.8 (15.6)	0.56 (0.56)	0.54 (0.52)	4.8 (4.6)
	60	13.9 (13.6)	0.56 (0.56)	0.50 (0.49)	3.9 (3.7)
D-PDPP4T-HD	20	13.3 (13.1)	0.60 (0.60)	0.55 (0.54)	4.4 (4.2)
	40	12.7 (12.3)	0.60 (0.60)	0.53 (0.51)	4.1 (3.8)
	60	9.0 (9.0)	0.60 (0.60)	0.60 (0.56)	3.2 (3.0)
EH-PDPP4T-EH	20	15.3 (15.1)	0.69 (0.69)	0.52 (0.51)	5.5 (5.3)
	40	15.2 (14.8)	0.70 (0.70)	0.52 (0.51)	5.6 (5.2)
	60	13.5 (13.2)	0.71 (0.70)	0.53 (0.52)	5.1 (4.8)

[a] Values between parentheses are the values for the average performance (based on 4 devices). The J_{sc} values were based on integration of the EQE (measured with 1 sun bias illumination) with the AM1.5G spectrum. [b] The PCE is determined from the EQE integrated J_{sc}. All devices were made on the same day from the same solutions.

solvent determines how fast the drying line in the ternary phase diagram of solvent, fullerene and polymer is traversed. Although this may have an effect on the fibre width, we demonstrated in a recent kinetic study on a related DPP-based polymer that the drying rate does not significantly affect the fibre width, in contrast to solubility.[12] Also in the examples presented in this work, the changing solubility provides a consistent explanation for the observations.

4.3 Conclusion

Four new semiconducting polymers were designed and synthesized to investigate the effects of cold and hot processing on the performance of polymer-fullerene solar cells. The polymers comprise electron-deficient DPP and electron-rich oligothiophenes that are substituted with linear and branched alkyl side chains to create a strong temperature-dependent solubility. All polymers show a strong temperature-dependent aggregation behaviour in solution as evidenced from temperature-dependent UV-vis-NIR absorption spectra. In thin solid films, the side chains induce significant differences in the packing and

interchain interactions, causing the optical absorption spectra to differ significantly even for polymers with the same conjugated backbone. Hot processing of these materials into polymer-fullerene bulk heterojunctions does not lead to an increased performance compared to cold processing. This is attributed to the enhanced solubility of the polymers at elevated temperature, which results in coarser morphologies with wider polymer fibres. This can be rationalized with a nucleation-growth mechanism that was recently prosposed.[12] Of the studied polymers, D-PDPP4T-HD provided the highest PCE of 6.3% in combination with [70]PCBM when cold-processed from chloroform with 2 vol% DPE as processing additive. Hot processing (100 °C) of the same blend from TCE with 2 vol% DIO gave a PCE of 5%. For these DPP polymers, hot processing seems to be advantageous only when cold processing is not possible due to a too limited solubility.

4.4 Experimental section

4.4.1 Materials and methods

All synthetic procedures were performed under an argon atmosphere. Commercial (dry) solvents and reactants were used without further purification, unless stated otherwise. Diethyl ether was dried over a column containing 4 Å molecular sieves. *N*-bromosuccinimide (NBS) was recrystallized from deionized water prior to use. 2,5-Bis(trimethylstannyl)thiophene (9), bis(trimethylstannyl)-2,2′-bithiophene (**10**) and triphenylphosphine (PPh_3) were recrystallized from methanol prior to polymerization. 2-Ethylhexylbromide (**2a**) was purchased from TCI Europe N.V. Dichloro(1,3-bis(diphenylphosphino)propane)nickel ($Ni(dppp)Cl_2$) and tris(dibenzylideneacetone)dipalladium ($Pd_2(dba)_3$) were purchased from Strem Chemicals Inc. [70]PCBM (purity 90-95%) was purchased from Solenne BV. All other chemicals and solvents were obtained from Sigma-Aldrich Co.

Fourier transform infrared spectroscopy (FTIR) was performed on a PerkinElmer Spectrum Two spectrometer in ATR mode. ^{1}H-NMR and ^{13}C-NMR spectra were recorded on a Varian Mercury (^{1}H 400 MHz or 200 MHz, ^{13}C 100 MHz) spectrometer. Chemical shifts are given in ppm with respect to tetramethylsilane as internal standard. The GC-MS system consisted of a Shimadzu (GC-2010) gas chromatograph and a Shimadzu (GCMS-QP2010plus) gas chromatograph mass spectrometer. The gas chromatograph contained a 30 meter Phenomenex Zebron ZB-5MS column with an internal diameter of 0.25 mm and a 0.25 μm stationary phase film thickness. Matrix assisted laser desorption ionization time of flight (MALDI-TOF) mass spectrometry was performed on a

Bruker Autoflex Speed spectrometer. Polymer molecular-weight distributions were estimated by GPC at 140 °C on a PL-GPC 120 system using a PL-GEL 10 mm MIXED-C column with *o*-DCB as the eluent and using polystyrene internal standards. Samples were first dissolved in *o*-DCB at 140 °C for 1 hour and filtered hot through a heated 2 μm PTFE filter.

UV-vis-NIR absorption spectroscopy was conducted on a PerkinElmer Lambda 1050 spectrophotometer at room temperature. Room temperature solution spectra were recorded in $CHCl_3$. Temperature-dependent spectra were recorded in *o*-DCB and TCE at temperatures between 20 °C and 100 °C using a PerkinElmer Peltier temperature controller. The polymer films were prepared by spin coating a polymer solution (6 mg/mL) in $CHCl_3$:*o*-DCB (9:1 v/v) (for D-PDPP3T-EH, D-PDPP4T-HD and EH-PDPP4T-EH) or pure 1,1,2,2-tetrachloroethane (TCE) (for D-PDDP4T-HD) on glass substrates at 1500 rpm. The glass substrates were cleaned with acetone and isopropanol and threated with UV-ozone for 30 min. prior to use.

Cyclic voltammetry was performed on polymer films under an inert atmosphere with a scan speed of 0.2 V/s using a solution of 1 M tetrabutylammonium hexafluorophosphate in acetonitrile. A polymer-covered ITO substrate was used as the working electrode, a silver rod as counter electrode and a silver rod coated with silver chloride (Ag/AgCl) as quasi-reference electrode in combination with Fc/Fc^+ as an internal standard.

Transmission electron microscopy (TEM) was performed on a Tecnai G2 Sphera transmission electron microscope (FEI) operating at 200 kV.

Photovoltaic devices with an active area of 0.09 and 0.16 cm² were fabricated in air on patterned indium tin oxide (ITO) glass substrates (Naranjo Substrates). The substrates were cleaned by sonication in acetone for 15 min., followed by scrubbing with a sodium dodecyl sulfate solution (99%, Acros), rinsing with deionized water, and a final sonication step in 2-propanol. Before deposition of the device layers the substrates underwent a 30 min. UV-ozone treatment. Poly(ethylenedioxythiophene):poly(styrenesulfonate) (PEDOT:PSS) (Clevios P, VP Al4083) was spin coated at 3000 rpm to form a 40 nm layer.

For the room-temperature (20 °C) processed devices, the polymers (D-PDPP3T-EH, D-PDPP4T-HD and EH-PDPP4T-EH) were mixed with [70]PCBM in a 1:2 weight ratio and dissolved in $CHCl_3$ (at concentrations of 6, 5 and 6 mg/mL, respectively). The solutions were heated to 90 °C for 1 h and cooled to room temperature prior to spin coating. The best photovoltaic devices for D-PDPP3T-EH were fabricated by spin coating using 10 vol% *o*-DCB as processing additive at 1500 rpm. The best photovoltaic devices for D-PDPP4T-HD and EH-PDPP4T-EH were fabricated by spin coating using 2 vol% diphenyl ether (DPE) as processing additive at 2000 and 3000 rpm, respectively.

For the hot processed devices the D-PDPP3T-EH, D-PDPP4T-EH, D-PDPP4T-HD and EH-PDPP4T-EH polymers were mixed with [70]PCBM in a 1:2 weight ratio and dissolved in TCE at a concentration of 10, 10, 6 and 6 mg/mL, respectively. Optimal processing temperatures varied between 100 and 140 °C (see Table 4.2). The solution, pipettes and substrates were heated to the required temperature between 100 and 140 °C for 1 h prior to spin coating. For D-PDPP3T-EH the best photovoltaic devices were fabricated by spin coating at 120 °C using 10 vol% *o*-DCB as processing additive at 3000 rpm. For D-PDPP4T-EH no processing additive was used, for D-PDPP4T-HD 2 vol% of DIO was optimal and for EH-PDPP4T-EH 10 vol% of *o*-DCB was used. Optimal active layer thicknesses were obtained by spin coating the polymer solutions at spin speeds between 1500 and 2500 rpm.

The 1 nm LiF and 100 nm Al back electrode layers were deposited by thermal evaporation under high vacuum (~3×10^{-7} mbar).

Current density – voltage ($J-V$) characteristics were measured with a Keithley 2400 source meter under ~100 mW/cm^2 white light illumination from a tungsten-halogen lamp filtered by a Schott GG385 UV filter and a Hoya LB120 daylight filter. The accurate short-circuit current density (J_{sc}) was determined from external quantum efficiency (EQE) measurements by integration of the EQE with the AM 1.5G solar spectrum. EQE measurements were conducted under 1 sun operating conditions in a homebuilt setup consisting of a modulated monochromatic light, a preamplifier (Stanford Research Systems SR570) and a lock-in amplifier (Stanford Research Systems SR830). The modulated monochromatic light was generated by using an optical chopper from Stanford Research Systems (SR540), an Oriel Cornerstone 130 monochromator and a 50 W (Osram 64610) tungsten-halogen lamp. The 1 sun conditions were provided by the use of a 730 nm LED (Thorlabs) at different intensities for appropriate bias illumination. A calibrated silicon cell was used as reference prior to the $J-V$ and EQE measurements. Thermal evaporation of the back electrode and $J-V$ measurements were both performed inside a nitrogen filled glove-box. For the EQE measurements, the photovoltaic devices were encapsulated in a nitrogen filled box with a quartz window. The active layer thickness was determined on a Veeco Dektak150 profilometer.

Hole-only devices with an active area of 0.09 and 0.16 cm² were fabricated in air on patterned indium tin oxide (ITO) glass substrates (Naranjo Substrates). The substrates were cleaned with the same procedure as mentioned before for the solar cell devices. Poly(ethylenedioxythiophene):poly(styrenesulfonate) (PEDOT:PSS) (Clevios P, VP Al4083) was then spin coated at 3000 rpm to form a 40 nm layer. The active layers were then cast under the same conditions as for the solar cell devices. By varying the spin speed, thicknesses from 120 to 250 nm were obtained. 10 nm of MoO_3 and 100 nm of Ag were then deposited by thermal evaporation under high vacuum (~3×10^{-7} mbar). Current density – voltage ($J-V$) characteristics were measured with a

Keithley 2400 source meter, after illumination of the cell with UV light to dope the MoO_3 for at least 10 minutes, sweeping from 0 to 6 V. For each type of active layer, three layers of different thicknesses were cast and measured. No thickness dependence of the mobility was observed. The mobility was determined by fitting the $J-V$ curves with the Mott-Gurney square law, using an empirical series resistance correction, which varied between 5 and 20 Ω. The published hole mobility is the average of 12 individual devices using three active layer thicknesses.

4.4.2. Synthesis

Scheme 4.3 shows the synthesis route to the four DPP polymers. In the subsequent sections the synthetic procedures and molecular characterization are provided.

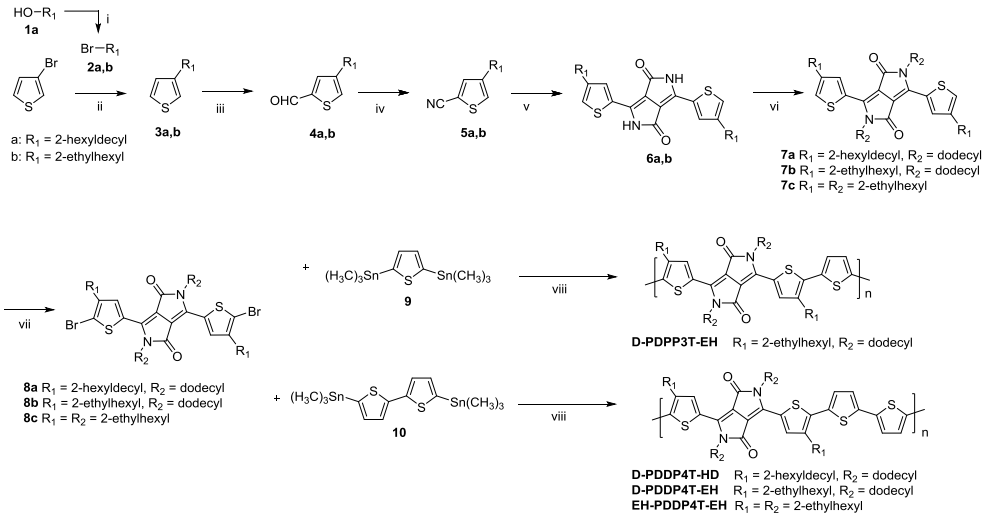

Scheme 4.3: (i) PPh_3, NBS, DCM, 0 °C; (ii) Mg, $Ni(dppp)Cl_2$, diethyl ether; (iii) (1) LDA, THF, −78 °C; (2) DMF, −78 °C; (iv) $NH_2OH.HCl$, DMF, 145 °C; (v) Na, diethyl succinate, *t*-amyl alcohol, 120 ºC; (vi) K_2CO_3, $Br-R_2$, DMF, 120 °C; (vii) NBS, $CHCl_3$, 0 °C; (viii) $Pd_2(dba)_3/PPh_3$, toluene/DMF, 115 °C.

1-Bromo-2-hexyldecane (2a)

2-Hexyldecan-1-ol (**1a**) (40.0 g, 165 mmol) was dissolved in dichloromethane (DCM) (200 mL) and cooled to 0 °C. Triphenylphosphine (47.6 g, 181 mmol) was added in several portions. Subsequently NBS (29.4 g, 165 mmol) was also added in portions at 0 °C. The reaction mixture was allowed to warm to room temperature and kept in the dark for 90 minutes. NBS (about 3 g) and PPh_3 (5 g) were added again until the reaction was found to be complete via ^{1}H-NMR. The mixture was then poured over a glass filter, washed with water and dried over magnesium sulfate. Triphenylphosphine oxide was removed by filtration after precipitation in heptane. The solvents were

removed under reduced pressure and the crude oil was purified further by column chromatography using heptane as eluent. The product was obtained as a colourless oil (34.9 g, yield: 70%). ^{1}H-NMR (400 MHz, $CDCl_3$, δ): 3.44 (d, J = 4.7 Hz, 2H); 1.64-1.54 (m, 1H); 1.43-1.19 (m, 24H); 0.88 (t, J = 5.8 Hz, 6H).

3-(2-Hexyldecyl)-thiophene (3a)

A dried 3-neck flask was filled with magnesium chips (3.46 g, 142 mmol) and dry diethyl ether (19 mL). Compound **2a** (21.7 g, 71.2 mmol), mixed with dry diethyl ether (77 mL), was added dropwise to this mixture and subsequently heated to reflux for 2 hours. The prepared Grignard reagent was carefully transferred to a dry addition funnel and added dropwise to a mixture of 3-bromothiophene (9.67 g, 59.3 mmol) and a Ni(dppp)Cl_2 catalyst (0.482 g, 8.90×10^{-4} mol) in dry diethyl ether (58 mL). The mixture was left overnight under reflux. The reaction mixture was then quenched with hydrochloric acid and extracted with diethyl ether. The combined organic layers were washed with water, dried over magnesium sulfate and concentrated *in vacuo*. The remaining 3-bromothiophene was removed under high vacuum (0.2 mbar) at 50 °C and the residue was purified by column chromatography using heptane as eluent. Compound **3a** was obtained as a colourless oil (4.28 g, yield: 23%). ^{1}H-NMR (200 MHz, $CDCl_3$, δ): 7.25-7.20 (dd, J = 4.9 Hz, 3.0 Hz, 1H); 6.93-6.87 (m, 2H); 2.57 (d, J = 6.7 Hz, 2H); 1.69-1.55 (m, 1H); 1.36-1.19 (m, 24H); 0.89 (t, J = 5.7 Hz, 6H). ^{13}C-NMR (100 MHz, $CDCl_3$, δ): 141.90; 128.79; 124.75; 120.61; 38.94; 34.70; 33.33; 31.91; 30.01; 29.69; 29.63; 29.34; 26.62; 26.59; 22.69; 14.13 (Note: some peaks in the ^{13}C-NMR spectrum overlap). GC-MS: 7.57 min., m/z = 307 (2, $M{-}1^+$), 223 (2, $C_{14}H_{23}S^+$), 98 (100, $C_5H_6S^+$), 97 (29, $C_5H_5S^+$), 71 (10, $C_5H_{11}^+$), 57 (19, $C_4H_9^+$), 43 (21, $C_3H_7^+$).

3-(2-Ethylhexyl)-thiophene (3b)

The same procedure as for compound **3a** was employed. 1-Bromo-2-ethylhexane (20.01 g, 103.6 mmol) in diethyl ether (110 mL) and magnesium chips (5.036 g, 207.2 mmol) in diethyl ether (30 mL) were used to prepared the Grignard reagent which was reacted with 3-bromothiophene (14.07 g, 86.33 mmol) using Ni(dppp)Cl_2 (0.702 g, 12.95×10^{-4} mol) as a catalyst in diethyl ether (30 mL). Compound **3b** was obtained as a colourless oil. (9.5 g, yield: 56%). ^{1}H-NMR (400 MHz, tetrachloroethane-d_2, δ): 7.21-7.18 (dd, J = 4.9 Hz, 3.0 Hz, 1H); 6.90-6.86 (m, 2H); 2.52 (d, J = 6.8 Hz, 2H); 1.55-1.45 (m, 1H); 1.29-1.15 (m, 8H); 0.87-0.80 (m, 6H). ^{13}C-NMR (100 MHz, $CDCl_3$, δ): 141.89; 128.78; 124.79; 120.64; 40.42; 34.30; 32.54; 28.93; 25.65; 23.07; 14.15; 10.86. GC-MS: 4.77 min., m/z = 196 (6, M^+), 98 (100, $C_5H_6S^+$), 97 (52, $C_5H_5S^+$), 57 (34, $C_4H_9^+$).

4-(2-Hexyldecyl)-2-thiophenecarbaldehyde (4a)

Compound **3a** (4.12 g, 13.4 mmol) was dissolved in dry tetrahydrofuran (THF) (20 mL). The solution was cooled to −78 °C and a lithium diisopropylamide (LDA) solution in THF (2 M, 7.4 mL 14.7 mmol) was added dropwise. The reaction mixture was warmed to room temperature after 30 minutes of stirring. After 4 hours, dry *N*,*N*-dimethylformamide (DMF) (2.0 mL, 26.72 mmol) was added dropwise at −78 °C. Subsequently, the mixture was allowed to warm to room temperature and stirred overnight. The reaction mixture was quenched with water and extracted with diethyl ether. The combined organic layers were washed with water, dried over magnesium sulfate and concentrated under reduced pressure. The residue was purified using column chromatography (silica gel, eluent gradient 60:40 > 50:50 heptane:DCM) to give an orange oil (3.40 g, yield: 53%). ^{1}H-NMR (200 MHz, $CDCl_3$, δ): 9.86 (d, J = 1.2 Hz, 1H); 7.55 (d, J = 1.5 Hz, 1H); 7.34-7.31 (m, 1H); 2.56 (d, J = 6.8 Hz, 2H); 1.68-1.48 (m, 1H); 1.36-1.15 (m, 24H); 0.86 (t, J = 6.4 Hz, 6H). ^{13}C-NMR (100 MHz, $CDCl_3$, δ): 182.94; 143.51; 143.44; 137.64; 131.19; 38.93; 34.58; 33.18; 33.17; 31.88; 31.84; 29.93; 29.60; 29.58; 29.30; 26.56; 26.54; 22.66; 22.64; 14.09; 14.08. FTIR: $\tilde{\nu}_{max}$ [cm^{-1}]: 3087 (CH aromatic); 2955, 1378 (s) (CH_3); 2923, 2853, 1457, 722 (CH_2); 1673 (CO); 1542 (CC aromatic). GC-MS: 8.55 min., m/z = 335 (3, $M-1^+$), 126 (100, $C_6H_6OS^+$), 125 (15, $C_6H_5OS^+$), 97 (16, $C_5H_5S^+$), 71 (14, $C_5H_{11}^+$), 57 (24, $C_4H_9^+$), 43 (24, $C_3H_7^+$).

4-(2-Ethylhexyl)-2-thiophenecarbaldehyde (4b)

The same procedure as for compound **4a** was used with compound **3b** (5.01 g, 25.5 mmol) in dry THF (39 mL), LDA solution in THF (2 M, 14.0 mL, 28 mmol) and dry DMF (4.0 mL, 51.1 mmol). A yellow oil (3.8 g, yield: 66%) was obtained after column chromatography. ^{1}H-NMR (200 MHz, $CDCl_3$, δ): 9.88 (d, J = 1.2 Hz, 1H); 7.58 (d, J = 1.5 Hz, 1H); 7.36-7.33 (m, 1H); 2.58 (d, J = 6.8 Hz, 2H); 1.65-1.45 (m, 1H); 1.34-1.14 (m, 8H); 0.88 (t, J = 7.3 Hz, 6H). ^{13}C-NMR (100 MHz, $CDCl_3$, δ): 182.94; 143.50; 143.44; 137.62; 131.18; 40.35; 34.12; 32.34; 28.82; 25.49; 22.95; 14.07; 10.78. FTIR: $\tilde{\nu}_{max}$ [cm^{-1}]: 3087 (CH aromatic); 2958, 1380 (s) (CH_3); 2927, 2859, 1459 (CH_2); 1669 (CO); 1542 (CC aromatic). GC-MS: 6.17 min., m/z = 224 (6, M^+), 126 (100, $C6H6OS^+$), 125 (22, $C6H5OS^+$), 97 (28, $C5H5S^+$), 57 (47, $C4H9^+$).

4-(2-Hexyldecyl)-2-thiophenecarbonitrile (5a)

Water-free $NH_2OH.HCl$ (0.766 g, 11.0 mmol) was added in portions to a solution of 4a (2.97 g, 8.82 mmol) in DMF (14 mL). Subsequently, the reaction mixture was heated to and kept for 3 hours at 145 °C. The resulting mixture was extracted with diethyl ether. The combined organic layers were washed with water, dried over magnesium sulfate and concentrated under reduced

pressure. The residue was purified using column chromatography (silica gel, eluent gradient 100:0 > 98:2 heptane:ethyl acetate) to give a dark orange oil (1.96 g, yield: 67%). ^{1}H-NMR (400 MHz, tetrachloroethane-d_2, δ): 7.39 (d, J = 1.4 Hz, 1H); 7.15 (d, J = 1.3 Hz, 1H); 2.50 (d, J = 6.8 Hz, 2H); 1.57-1.48 (m, 1H); 1.29-1.11 (m, 24H); 0.84 (t, J = 6.7 Hz, 6H). ^{13}C-NMR (100 MHz, $CDCl_3$, δ): 142.89; 138.74;128.18; 114.53; 109.24; 38.88; 34.40; 33.15; 33.13; 31.87; 31.82; 29.90; 29.57; 29.55; 29.28; 26.53; 26.51; 22.65; 22.63; 14.09; 14.07. FTIR: $\tilde{\nu}_{max}$ [cm^{-1}]: 3093 (CH aromatic); 2955, 1378 (s) (CH_3); 2923, 2854, 1465, 723 (CH_2); 2217 (CN); 1539 (CC aromatic). GC-MS: 8.49 min., m/z = 333 (4, M^+), 123 (100, $C_6H_5NS^+$), 85 (24, $C_6H_{13}^+$), 71 (34, $C_5H_{11}^+$), 57 (49, $C_4H_9^+$), 43 (44, $C_3H_7^+$).

4-(2-Ethylhexyl)-2-thiophenecarbonitrile (5b)

The same procedure as for compound **5a** was used with water-free $NH_2OH.HCl$ (1.39 g, 20.1 mmol) and 4b (3.60 g, 16.1 mmol) in dry DMF (25 mL). An orange oil (3.04 g, yield: 85%) was obtained after column chromatography. ^{1}H-NMR (400 MHz, tetrachloroethane-d_2, δ): 7.39 (d, J = 1.3 Hz, 1H); 7.17-7.14 (m, 1H); 2.50 (d, J = 6.9 Hz, 2H); 1.53-1.42 (m, 1H); 1.27-1.10 (m, 8H); 0.87-0.79 (m, 6H). ^{13}C-NMR (100 MHz, $CDCl_3$, δ): 142.87; 138.73; 128.22; 114.52; 109.23; 40.29; 33.93; 32.29; 28.78; 25.44; 22.93; 14.06; 10.74. FTIR: $\tilde{\nu}_{max}$ [cm^{-1}]: 3092 (CH aromatic); 2959, 1380 (s) (CH_3); 2927, 2859, 1460, 727 (CH_2); 2217 (CN); 1540 (CC aromatic). GC-MS: 6.11 min., m/z = 221 (5, M^+), 123 (100, $C_6H_5NS^+$), 57 (75, $C_4H_9^+$).

3,6-Bis(4-(2-hexyldecyl)thiophen-2-yl)-2,5-dihydropyrrolo[3,4-*c*]pyrrole-1,4-dione (6a)

A sodium 2-methyl-2-butoxide solution was prepared by heating elemental sodium (0.184 g, 8.01 mmol) and *tert*-amyl alcohol (10 mL) in a dried 2-neck flask to 120 °C. A catalytic amount of iron(III) chloride was added to the previous solution. A solution of diethyl succinate (0.465 g, 2.67 mmol) in *tert*-amyl alcohol (1.3 mL) was added dropwise to the alkaline solution and then **5a** (1.96 g, 5.88 mmol) was quickly added. The mixture was left reacting overnight until it was quenched with acetic acid (6 mL) and methanol (10 mL). The quenched mixture was refluxed at 85 °C for 30 min. After cooling a dark red precipitate (0.548 g) was filtered off, washed with water and methanol and dried overnight at 50 °C *in vacuo*. The compound was used in the next reaction without further purification. ^{1}H-NMR (400 MHz, $CDCl_3$, δ): 8.05 (s, 2H); 7.86 (s, 2H); 7.18 (s, 2H); 2.61 (d, J = 6.8 Hz, 4H); 1.72-1.62 (m, 2H); 1.30-1.20 (m, 48H); 0.90-0.83 (m, 12H). MALDI-TOF-MS: [M^+] calc: 748.50, found: 748.49.

3,6-Bis(4-(2-ethylhexyl)thiophen-2-yl)-2,5-dihydropyrrolo[3,4-*c*]pyrrole-1,4-dione (6b)

The same procedure as for compound **6a** was used. For this reaction a mixture of elemental sodium (0.409 g, 17.8 mmol) and *tert*-amyl alcohol (10 mL) was heated to 120 °C. A solution of diethyl succinate (1.03 g, 5.94 mmol) in *tert*-amyl alcohol (2.9 mL) was added dropwise to the alkaline solution and then **5b** (2.89 g, 13.1 mmol) was quickly added. After work-up, a black solid (1.04 g) was obtained. The compound was used in the next reaction without further purification. ^{1}H-NMR (400 MHz, 1:1 $CDCl_3$:DMSO-d_6, δ): 10.82 (s, 2H); 7.98 (s, 2H); 7.15 (s, 2H); 2.50 (m, 4H); 1.57-1.46 (m, 2H); 1.27-1.12 (m, 16H); 0.84-0.76 (m, 12H). MALDI-TOF-MS: [M+] calc: 524.25, found: 524.27.

2,5-Didodecyl-3,6-bis(4-(2-hexyldecyl)thiophen-2-yl)-2,5-dihydropyrrolo[3,4-*c*]pyrrole-1,4-dione (7a)

A flask was charged with **6a** (0.230 g, 3.07×10^{-4} mol), finely crushed potassium carbonate (K_2CO_3) powder (0.127 g, 9.21×10^{-4} mol) and DMF (3 mL). After heating the reaction mixture for 15 min. at 120 °C, 1-bromododecane (0.230 g, 9.21×10^{-4} mol) was added. The mixture was stirred overnight at 120 °C, subsequently quenched with water and extracted with DCM. The combined organic phase was washed with brine, dried over magnesium sulfate and concentrated under reduced pressure. The remaining purple solid was added to a mixture of 1,4-dioxane (120 mL), HCl (2 mL) and water (2 mL) and refluxed during 1 hour. After evaporation of the solvent the crude product was further purified by column chromatography (silica gel, eluent gradient 100:0 > 70:30 heptane:DCM). Finally the pure product (104 mg, yield: 31%) was obtained as purple flakes after recrystallization in ethanol. ^{1}H-NMR (200 MHz, $CDCl_3$, δ): 8.70 (d, J = 1.3 Hz, 2H); 7.20 (d, J = 1.2 Hz, 2H); 4.04 (m, 4H); 2.64 (d, J = 6.7 Hz, 4H); 1.82-1.64 (m, 6H); 1.46-1.10 (m, 88H); 0.87 (t, J = 6.2 Hz, 18H). ^{13}C-NMR (100 MHz, $CDCl_3$, δ): 161.31; 143.77; 139.83; 136.72; 129.28; 126.64; 107.40; 42.19; 38.79; 34.81; 33.23; 33.21; 31.93; 31.91; 31.89; 30.04; 29.96; 29.72; 29.64; 29.63; 29.58; 26.50; 26.48; 22.69; 14.12. (Note: several peaks in the ^{13}C-NMR spectrum overlap). MALDI-TOF-MS: [M^+] calc: 1084.88 found: 1084.90.

2,5-Didodecyl-3,6-bis(4-(2-ethylhexyl)thiophen-2-yl)-2,5-dihydropyrrolo[3,4-*c*]pyrrole-1,4-dione (7b)

The same procedure as for **7a** was followed, using **6b** (0.508 g, 9.68×10^{-4} mol), finely crushed potassium carbonate (K_2CO_3) powder (0.401 g, 2.90 mmol) and DMF (4 mL). After 15 min. at 120 °C, 1-bromododecane (0.724 g, 2.90 mmol) was added. The pure product (438 mg, yield: 53%) was obtained as purple flakes after recrystallization in ethanol. ^{1}H-NMR (400 MHz, $CDCl_3$, δ): 8.71 (s, 2H); 7.21 (s, 2H); 4.04 (m, 4H); 2.65 (d, J = 6.9 Hz, 4H); 1.80-1.62 (m, 6H); 1.46-1.20 (m, 56H);

0.97-0.82 (m, 18H). ^{13}C-NMR (100 MHz, $CDCl_3$, δ): 161.32; 143.74; 139.84; 136.70; 129.31; 126.63; 107.43; 40.12; 34.38; 32.37; 31.89; 29.94; 29.61; 29.55; 29.32; 29.26; 28.76; 26.86; 25.50; 23.06; 22.67; 14.10; 10.71. MALDI-TOF-MS: [M^+] calc: 860.63 found: 860.63.

2,5-Bis(2-ethylhexyl)-3,6-bis(4-(2-ethylhexyl)thiophen-2-yl)-2,5-dihydropyrrolo[3,4-*c*]pyrrole-1,4-dione (7c)

The same procedure as for **7a** was followed, using **6b** (0.508 g, 9.68×10^{-4} mol), finely crushed potassium carbonate (K_2CO_3) powder (0.401 g, 2.90 mmol) and DMF (4 mL). After 15 min. at 120 ºC, 0.561 g (2.90 mmol) of 2-ethylhexylbromide was added. The pure product (125 mg, yield: 18%) was obtained as a waxy red solid after recrystallization in ethanol. ^{1}H-NMR (400 MHz, $CDCl_3$, δ): 8.62 (d, J = 1.0 Hz, 2H); 7.19 (s, 2H); 4.04-3.97 (m, 4H); 2.64 (d, J = 7.0 Hz, 4H); 1.91-1.81 (m, 2H); 1.71-1.61 (m, 2H); 1.38-1.18 (m, 32H); 0.92-0.82 (m, 24H). ^{13}C-NMR (100 MHz, $CDCl_3$, δ): 161.73; 143.48; 140.19; 136.48; 129.40; 126.49; 107.72; 45.73; 40.14; 40.12; 38.97; 34.35; 32.37; 32.34; 30.15; 30.13; 28.79; 28.77; 28.31; 25.54; 25.52; 23.52; 23.06; 23.05; 14.13; 14.02; 10.75; 10.54. (Note: several peaks in the 13C-NMR spectrum overlap). MALDI-TOF-MS: [M^+] calc: 748.50 found: 748.51.

3,6-Bis(5-bromo-4-(2-hexyldecyl)thiophen-2-yl)-2,5-didodecyl-2,5-dihydropyrrolo[3,4-*c*]pyrrole-1,4-dione (8a)

Compound **7a** (94 mg, 8.66×10^{-5} mol) was dissolved in chloroform (2 mL) in a dried Schlenk tube. The solution was cooled to 0 °C in the dark under stirring. After addition of recrystallized NBS (32 mg, 1.82×10^{-4} mol) in few portions, the reaction mixture was allowed to warm to room temperature. The reaction was followed by TLC and quenched with water after one hour. The organic phase was washed with water and dried over magnesium sulfate. Subsequently the solvent was evaporated *in vacuo*. The crude solid was purified further by recrystallization in ethanol with a small amount of toluene and dried overnight inside the vacuum oven. Monomer **8a** was obtained as a purple powder (77 mg, yield: 72%). ^{1}H-NMR (200 MHz, $CDCl_3$, δ): 8.55 (s, 2H); 3.96 (m, 4H); 2.58 (d, J = 7.2 Hz, 4H); 1.83-1.63 (m, 6H); 1.44-1.12 (m, 88H); 0.93-0.80 (m, 18H). ^{13}C-NMR (100 MHz, $CDCl_3$, δ): 161.00; 143.32; 138.88; 136.03; 129.00; 116.83; 107.61; 38.37; 34.12; 33.31; 33.27; 31.93; 31.91; 31.88; 30.01; 29.98; 29.69; 29.65; 29.64; 29.61; 29.58; 29.54; 29.35; 29.25; 26.84; 26.44; 26.42; 22.69; 14.13. (Note: several peaks in the 13C-NMR spectrum overlap). MALDI-TOF-MS: [M^+] calc: 1240.70 found: 1240.71.

3,6-Bis(5-bromo-4-(2-ethylhexyl)thiophen-2-yl)- 2,5-didodecyl-2,5-dihydropyrrolo[3,4-*c*]pyrrole-1,4-dione (8b)

The same procedure as for compound **8a** was used. Now compound 7b (400 mg, 4.64×10^{-4} mol) was dissolved in chloroform (9 mL) and recrystallized NBS (174 mg, 9.75×10^{-4} mol) was added in few portions Monomer **8b** was obtained as a purple powder (422 mg, yield: 89%). ^{1}H-NMR (400 MHz, $CDCl_3$, δ): 8.56 (s, 2H); 3.97 (m, 4H); 2.59 (d, J = 7.2 Hz, 4H); 1.80-1.64 (m, 6H); 1.46-1.16 (m, 56H); 0.97-0.81 (m, 18H). ^{13}C-NMR (100 MHz, $CDCl_3$, δ): 161.02; 143.28; 138.90; 136.00; 129.02; 116.83; 107.63; 39.70; 33.71; 32.40; 31.89; 29.96; 29.62; 29.55; 29.33; 29.22; 28.66; 26.80; 25.60; 23.06; 22.67; 14.10; 10.72. MALDI-TOF-MS: [M^+] calc: 1016.45 found: 1016.44.

3,6-Bis(5-bromo-4-(2-ethylhexyl)thiophen-2-yl)-2,5-bis(2-ethylhexyl)-2,5-dihydropyrrolo[3,4-*c*]pyrrole-1,4-dione (8c)

The same procedure as for compound **8a** was used. Now compound 2b (125 mg, 1.67×10^{-4} mol) was dissolved in chloroform (4 mL) and recrystallized NBS (62 mg, 3.50×10^{-4} mol) was added in few portions. Monomer **8c** was obtained as a purple solid (113 mg, yield: 75%). ^{1}H-NMR (400 MHz, $CDCl_3$, δ): 8.47 (d, J = 1.5 Hz, 2H); 3.95-3.90 (m, 4H); 2.59 (d, J = 7.2 Hz, 4H); 1.89-1.78 (m, 2H); 1.77-1.67 (m, 2H); 1.40-1.19 (m, 32H); 0.94-0.83 (m, 24H). ^{13}C-NMR (100 MHz, $CDCl_3$, δ): 161.40; 143.04; 139.24; 135.83; 129.13; 116.71; 107.87; 45.85; 39.71; 39.69; 39.01; 33.68; 32.40; 32.39; 32.37; 32.36; 30.09; 30.07; 28.69; 28.66; 28.26; 28.23; 25.65; 25.64; 25.62; 25.61; 23.53; 23.04; 14.12; 14.02; 10.75; 10.74; 10.52; 10.49. (Note: several peaks in the ^{13}C-NMR spectrum overlap). MALDI-TOF-MS: [M^+] calc: 904.32 found: 904.32.

D-PDDP3T-EH

Freshly recrystallized **9** (43.0 mg, 105 µmol), monomer **8a** (107 mg, 105 µmol), recrystallized triphenylphosphine (1.65 mg, 6.30 µmol) and $Pd_2(dba)_3$ (1.44 mg, 1.57 µmol) were placed inside a dried Schlenk tube and placed under argon. Toluene (1.8 mL) and DMF (0.2 mL) were added and the mixture was degassed with argon at 40 °C. The mixture was then reacted at 115 °C overnight. The viscous polymer solution was dissolved in warm $CHCl_3$ and precipitated in methanol. The polymer was dissolved in chloroform with ethylenediaminetetraacetic acid (EDTA) and refluxed during one hour. Water was added, refluxed for one hour and subsequently the organic layer was washed with water. The organic layer was concentrated under reduced pressure and the polymer precipitated in methanol. The polymer was then subjected to Soxhlet extraction with acetone, hexane, dichloromethane and chloroform. Finally, the purified polymer was precipitated in methanol. $CHCl_3$ fraction: 98 mg, yield: 99%. GPC (*o*-DCB, 140 °C): M_n = 39.0 kDa, M_w = 90.0 kDa, PDI = 2.31.

D-PDDP4T-EH

Freshly recrystallized **10** (33.8 mg, 68.7 μmol), **8b** (70.0 mg, 68.7 μmol), recrystallized triphenylphosphine (1.08 mg, 4.12 μmol) and $Pd_2(dba)_3$ (0.943 mg, 1.03 μmol) were placed under Ar in a dried Schlenk tube. Toluene (1.8 mL) and DMF (0.2 mL) were added and the mixture was degassed with argon at 40 °C. The mixture was then reacted at 115 °C overnight. The viscous polymer solution was dissolved in warm 1,1,2,2-tetrachloroethane (TCE) and precipitated in methanol. The polymer was dissolved in chloroform with ethylenediaminetetraacetic acid (EDTA) and refluxed during one hour. Water was added, refluxed for one hour and subsequently the organic layer was washed with water. The organic layer was concentrated under reduced pressure and the polymer precipitated in methanol. The precipitated polymer was then subjected to Soxhlet extraction with acetone, hexane, dichloromethane and chloroform. Swollen polymer remaining inside the Soxhlet thimble was dissolved in hot TCE and the solution was filtrated over a heated cellulose filter. Finally, the TCE solution was concentrated *in vacuo* and the purified polymer was precipitated in acetone. TCE-fraction: 54 mg, yield: 77%. GPC (*o*-DCB, 140 °C): M_n= 24.3 kDa, M_w = 59.3 kDa, PDI = 2.44. (Note: the polymer was not completely dissolved upon filtration).

D-PDDP4T-HD

The same procedure as for the polymerization of D-PDDP4T-EH was used, with **10** (27.7 mg, 56.3 μmol), **8a** (70.0 mg, 56.3 μmol), recrystallized PPh_3 (0.886 mg, 3.38 μmol) and $Pd_2(dba)_3$ (0.773 mg, 0.844 μmol). TCE- fraction: 60 mg, yield: 85%. GPC (*o*-DCB, 140 °C): M_n = 57.3 kDa, M_w = 173 kDa, PDI = 3.02.

EH-PDDP4T-EH

The same procedure as for the polymerization of D-PDDP4T-EH was used, with **10** (38.0 mg, 77.2 μmol), **8c** (70.0 mg, 77.2 μmol), recrystallized PPh_3 (1.22 mg, 4.63 μmol) and $Pd_2(dba)_3$ (1.06 mg, 1.16 μmol). TCE-fraction: 57 mg, yield: 81%. The molecular weight distribution of EH-PDPP4T-EH could not be determined by GPC because it has a very low solubility in *o*-DCB, even at 140 °C.

4.5 References

1 A. Facchetti, *Chem. Mater.*, 2011, **23**, 733-758.

2 G. Li, R. Zhu, Y. Yang, *Nat. Photon.*, 2012, **6**, 153-161.

3 T. M. Clarke, J. R. Durrant, *Chem. Rev.*, 2010, **110**, 6736-6767.

4 F. Liu, Y. Gu, J. W. Jung, W. H. Jo, T. P. Russell, *J. Polym. Sci. B*, 2012, **50**, 1018-1044.

5 Y. Liu, J. Zhao, Z. Li, C. Mu, W. Ma, H. Hu, K. Jiang, H. Lin, H. Ade, H. Yan, *Nat. Commun.*, 2014, **5**, 5293.

6 Z. Li, H. Lin, K. Jiang, J. Carpenter, Y. Li, Y. Liu, H. Hu, J. Zhao, W. Ma, H. Ade, H. Yan, *Nano Energy*, 2015, **15**, 607-615.

7 T. Ma, K. Jiang, S. Chen, H. Hu, H. Lin, Z. Li, J. Zhao, Y. Liu, Y.-M. Chang, C.-C. Hsiao, H. Yan, *Adv. Energy Mater.*, 2015, **5**, 1501282.

8 J. W. Jung, F. Liu, T. P. Russell, W. H. Jo, *Energy Environ. Sci.*, 2012, **5**, 6857-6861.

9 W. Li, K. H. Hendriks, A. Furlan, W. S. C. Roelofs, M. M. Wienk, R. A. J. Janssen, *J. Am. Chem. Soc.*, 2013, **135**, 18942-18948.

10 W. Li, K. H. Hendriks, A. Furlan, W. S. C. Roelofs, M. M. Wienk, R. A. J. Janssen, *Adv. Mater.*, 2014, **26**, 1565-1570.

11 G. H. L. Heintges, J. J. van Franeker, M. M. Wienk, R. A. J. Janssen, *Chem. Commun.*, 2016, **52**, 92-95.

12 J. J. van Franeker, G. H. L. Heintges, C. Schaefer, G. Portale, W. Li, M. M. Wienk, P. van der Schoot, R. A. J. Janssen, *J. Am. Chem. Soc.*, 2015, **137**, 11783-117945.

13 W. Li, K. H. Hendriks, M. M. Wienk, R. A. J. Janssen, *Acc. Chem. Res.*, 2016, **49**, 78-85.

14 X. Cao, M. Li, J. Liu, H. Wang, K. Zhou, Y. C. Han, *Org. Electron.*, 2015, **24**, 280-287.

15 D. Wang, F. Liu, N. Yagihashi, M. Nakaya, S. Ferdous, X. Liang, A. Muramatsu, K. Nakajima, T. P. *Nano Lett.*, 2014, **14**, 5727-5732.

16 G. J. Hedley, A. J. Ward, A. Alekseev, C. T. Howells, E. R. Martins, L. A. Serrano, G. Cooke, A. Ruseckas, I. D. W. Samuel, *Nat. Commun.*, 2013, **4**, 2867.

17 W. Li, A. Furlan, K. H. Hendriks, M. M. Wienk, R. A. J. Janssen, *J. Am. Chem. Soc.*, 2013, **135**, 5529-5532.

18 K. H. Hendriks, G. H. L. Heintges, V. S. Gevaerts, M. M. Wienk, R. A. J. Janssen, *Angew. Chem. Int. Ed.*, 2013, **52**, 8341-8344.

19 D. Bartesaghi, I. del Carmen Pérez, J. Kniepert, S. Roland, M. Turbiez, D. Neher, L. J. A. Koster, *Nat. Commun.*, 2015, **6**, 7083.

Chapter 5

The influence of siloxane side chains on the photovoltaic performance of a conjugated polymer

Abstract

The effect of gradually replacing the branched alkyl side chains of a diketopyrrolopyrrole (DPP) conjugated polymer by linear side chains containing branched siloxane end groups on the photovoltaic performance of blends of these polymers with a common fullerene acceptor is investigated. With an increasing proportion of siloxane side chains, the molecular weight and solubility of the polymers decreases. While the siloxane containing polymers exhibit a higher hole mobility in field-effect transistors, their performance in solar cells is less than the polymer with only alkyl side chains. Using grazing-incidence wide-angle X-ray scattering, transmission electron microscopy and fluorescence spectroscopy we identify two main reasons for the reduced performance of siloxane containing polymers in solar cells. The first one is a somewhat coarser phase-separated morphology with slightly wider polymer fibres. This is unexpected as often the fibre width is inversely correlated with polymer solubility. The second one is stronger non-radiative decay of the pristine polymers containing siloxane side chains.

This work has been published: G. H. L. Heintges, K. H. Hendriks, F. J. M. Colberts, M. Li, J. Li, R. A. J. Janssen, *RSC Adv.*, 2019, **9**, 8740-8747.

5.1 Introduction

Organic bulk heterojunction (BHJ) solar cells have attracted attention over the past years as a novel, green energy technology.[1,2] An essential parameter influencing the performance of these solar cells is the morphology of the BHJ layer, which has been shown to be directly influenced by the solubility of the components in the processing solvents, the intrinsic properties of the two components and their mutual interactions.[3-6] In particular, it has been found that in blends consisting of a polymer donor and a fullerene acceptor, the polymer should self-organize to achieve a high power conversion efficiency (PCE). For diketopyrrolopyrrole (DPP) polymers the most optimal, finely dispersed morphology in combination with fullerenes has been achieved for polymers with shorter side chains and higher molecular weights.[3,7] This behaviour has been explained by a nucleation-and-growth model applied to fibrous networks.[3] By using co-solvents in which the DPP polymers are only sparsely soluble these insights resulted in record high PCEs.[8] Following these trends, high PCEs can be obtained by reducing the solubility, of course maintaining a high enough level to ensure processablity. In conjugated polymers, a straightforward way to influence the solubility and tendency to aggregate is to alter the solubilizing side chains, which strongly influence the solar cell performance.[6–13] By introducing other chemical functionalities opposed to the commonly used alkyl side chains in these polymers, a further fine-tuning of the aggregation behaviour can be achieved.[9,11,14–16] Additionally, by changing the side chains, also the miscibility of the donor and acceptor[17,18] and the packing of the polymer, which also influence the morphology of the layer and the performance of the solar cells, can be affected.

Siloxane-containing side chains have been investigated in conjugated polymers for organic field-effect transistor (OFET) applications[19-24] and have shown to increase the crystallinity and decrease solubility, therefore directly affecting the charge carrier mobility of these materials. Also in solar cells siloxane-containing polymers have been introduced to increase crystallinity of the electron donor, influencing the morphology of the blend layers.[25-28] This has led to highly performant solar cells, with a PCE of 11%, when siloxane side chains were combined with regular alkyl chains within the same polymer.[27] Interestingly, it was shown that the number average molecular weight (M_n) decreased with increasing siloxane content, as polymers with high siloxane content were less soluble and could not reach high M_ns before becoming insoluble.[27]

In this chapter, siloxane side chains are employed on diketopyrrolopyrrole (DPP) polymers, a class of conjugated polymers that has shown high promise in solar cell applications.[29] In particular, siloxane side chains were introduced in varying concentrations on poly[{2,5-bis(2-hexyldecyl)-2,3,5,6-tetrahydro-3,6-dioxopyrrolo[3,4-*c*]pyrrole-1,4-diyl}-*alt*-{[2,2′-(1,4-phenylene)bisthiophene]-5,5′-diyl}] (PDPPTPT),[30] in this way finely tuning the solubility. In previous studies and theories on the morphology formation in active layers, the effect of solubility has always been observed and applied holistically. Looking in detail at the factors determining solubility and aggregation behaviour, two important properties can easily be identified: the solubility of the monomers or repeat units, from here on called the 'intrinsic solubility' and the average molecular weight of the polymers. Whereas the influence of molecular weight has separately been investigated in the past,[3,31-37] separating the influence of the intrinsic solubility from the influence of the molecular weight has proven difficult. By mixing siloxane and alkyl side chains, however, a series of polymers has been obtained with varying intrinsic solubility not positively correlated to the molecular weight, hereby providing further insight in the factors that govern morphology formation and solar cell performance.

5.2 Results and discussion

A series of DPP polymers was designed in which the 2-hexyldecyl side chains of PDPPTPT are gradually replaced by 6-(1,5-di-*tert*-butyl-1,1,3,5,5-pentamethyltrisiloxan-3-yl)hexyl side chains. This siloxane side chain with *tert*-butyl substituents was chosen to provide enough solubility while moving the branching point on the side chain far away from the DPP core to encourage π-π stacking. The siloxane was synthesized and then attached via a hydrosilylation reaction to a hexane-substituted DPP, as shown in Scheme 5.1, essentially following a procedure previously reported.[20,22] The monomer was then brominated in preparation for the Suzuki polymerization with 1,4-benzenediboronic acid bis(pinacol) ester (Scheme 5.2).

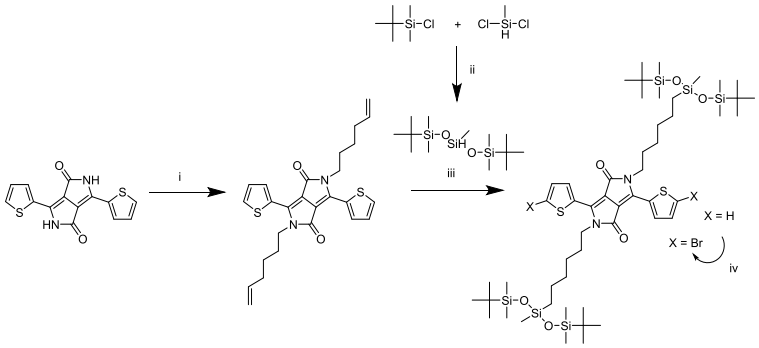

Scheme 5.1: Synthesis of the monomer adapted from a previously reported route.[20,22] (i) K_2CO_3, 6-bromohexene, *N*,*N*-dimethylformamide , 120 °C, (ii) isopropyl ether, 70 °C, (iii) Karstedt's catalyst, toluene, 80 °C, (iv) *N*-bromosuccinimide, chloroform, room temperature.

By combining different ratios of alkyl and siloxane-substituted DPP monomers with phenylene, a series of copolymers was obtained with similar electronic properties but different intrinsic solubilities. After the synthesis, differences in physical properties could be immediately observed, with the polymers having a high siloxane content being slightly more difficult to dissolve and being more brittle in the solid state.

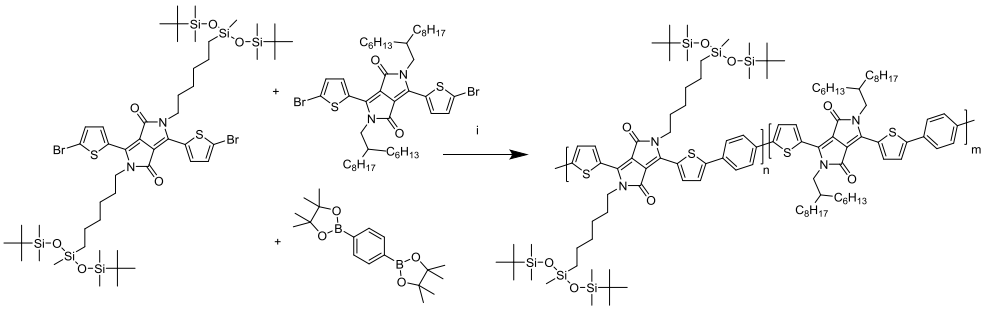

Scheme 5.2: Synthesis of the polymers. (i) $Pd_2(dba)_3/PPh_3$, $K_3PO_{4\ (aq)}$, toluene, 115 °C (monomer ratios are adjusted to obtain the different polymers).

Gel permeation chromatography (GPC) in *ortho*-dichlorobenzene (*o*-DCB) was performed at 140 °C to determine the molecular weights (Figure. 5.1). As is seen in Figure. 5.1, the polymers with high siloxane content showed two distinct peaks in the gel permeation chromatogram, with the peak at shorter retention times decreasing in intensity with diminishing siloxane content. The UV-vis-NIR absorption spectrum of the short

retention time peak (not shown) displayed a distinct red-shifted shoulder, which is commonly associated with aggregation of DPP polymers. This coincides with the solubility of the polymers decreasing with increased siloxane content. The peak at longer retention times revealed a more blue-shifted UV-vis-NIR spectrum (not shown) associated with molecularly dissolved polymers and is therefore most likely a better estimate of the true molecular weight. When considering the peak molecular weight (M_p) of the main peak (Table 5.1), a clear trend can be seen of decreasing M_p with increasing siloxane content, except for the 100% siloxane polymer, where aggregation seems to prevail. This trend indicates that a lower degree of polymerization was achieved for polymers with higher siloxane content. Despite their lower molecular weight with increasing siloxane content, the polymers show a higher tendency for aggregation in *o*-DCB at elevated temperature. The difference in degree of polymerization could therefore be related to premature aggregation in the polymerization mixture, thereby inhibiting the reaction, an effect previously observed by Liu et al.,[27] indicating that polymer solubility during polymerization can have an effect on the molecular weight obtained. This implies that polymers with a high siloxane content have a low intrinsic and overall solubility coupled with a low M_p, whereas polymers with a low siloxane content have higher intrinsic and overall solubility coupled with a high M_p. In this way this set of polymers provides a case where solubility is not positively correlated

Table 5.1: Physical properties of the PDPPTPT polymers with different fractions of siloxane side chains.

Siloxane fraction	M_p [kDa]	HOMO [b] [eV]	LUMO [b] [eV]	$E_{g,,SW}$ [c] [eV]	$E_{g,,opt}$ [c] [eV]	*d*-spacing (TEM) [Å]	*d*-spacing (GIWAXS) [Å]	Mobility [cm^2/Vs]
100%	15.1[a]	−5.20	−3.31	1.89	1.54	26.2	25.1	8.2×10^{-3}
50%	15.9	−5.22	−3.29	1.93	1.53	24.7	24.2	3.1×10^{-2}
20%	21.4	−5.26	−3.30	1.96	1.53	21.5	21.9	2.4×10^{-2}
10%	24.4	−5.29	−3.29	1.99	1.52	20.6	20.3	1.5×10^{-2}
5%	28.7	−5.27	−3.30	1.96	1.52	19.8	19.6	1.3×10^{-2}
0%	38.5	−5.27	−3.29	1.98	1.51	18.5	19.2	4.5×10^{-4}

[a] Estimate based on a Gaussian fit to the low-M_p shoulder of un-aggregated polymer chains in the GPC. [b] Determined with square wave voltammetry vs. Fc/Fc^+, which was set at −4.8 eV vs. vacuum. [c] $E_{g,\,SW}$ is the difference between HOMO and LUMO energies. $E_{g,\,opt}$ is the optical band gap.

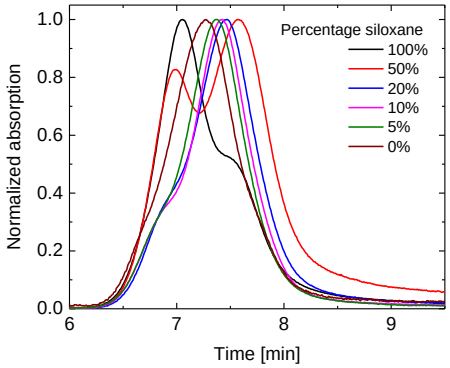

Fig. 5.1: Gel permeation chromatograms of the synthesized siloxane-containing PDPPTPT polymers.

with M_p, providing a platform to further investigate the effects of M_p and intrinsic solubility separately.

As can be seen in Figure. 5.2 the UV-vis-NIR absorption spectra of all polymers are virtually identical in the solid state. While the peak position shows no clear trend, the onset of absorption at long wavelengths shows a small blue shift with increasing siloxane content, indicating a small increase in optical band gap ($E_{g,\ opt}$) (Table 5.1). This is most likely due to differences in aggregation and packing caused by the more bulky siloxane groups.

To gain further insight in the aggregation behaviour of these polymers their temperature dependent UV-vis-NIR spectra were recorded in 1,1,2,2-tetrachloroethane (TCE) (Figure. 5.3). For the polymers with a higher siloxane content the peak at 760 nm, associated with aggregates, decreased less than for the polymers with low siloxane content

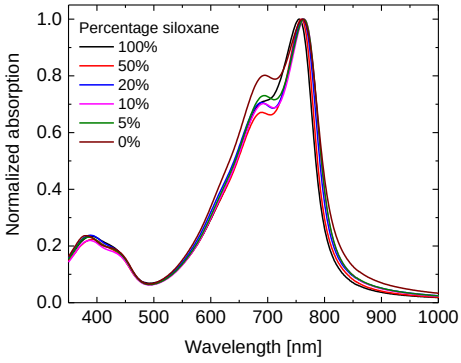

Fig. 5.2: Solid state UV-vis-NIR spectra of the PDPPTPT polymers.

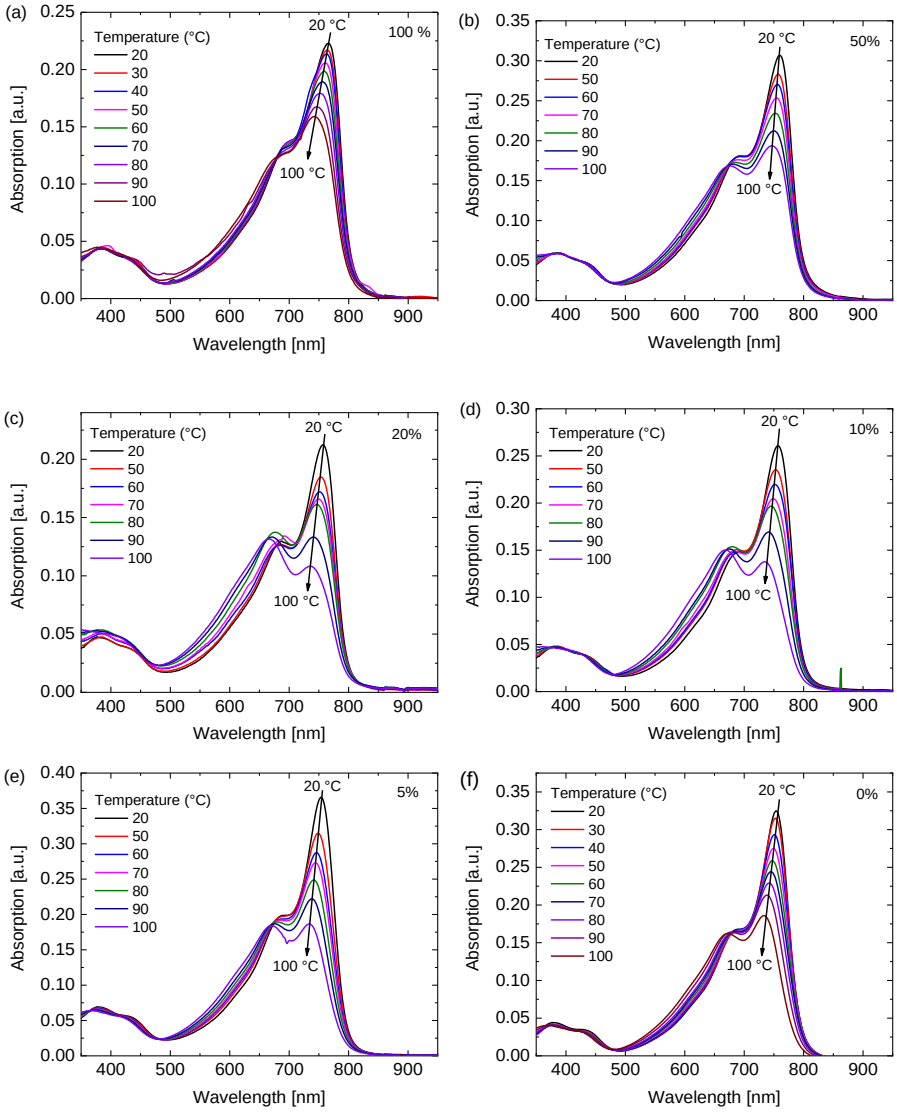

Fig. 5.3: Temperature dependent UV-vis-NIR absorption spectra in TCE of the polymers. Percentage siloxane (a) 100%. (b) 50%. (c) 20%. (d) 10%. (e) 5%. (f) 0%.

with increasing temperature, indicating once again that the polymers with high siloxane content have a stronger tendency for aggregation.

Square wave voltammetry was performed on the polymers to determine the

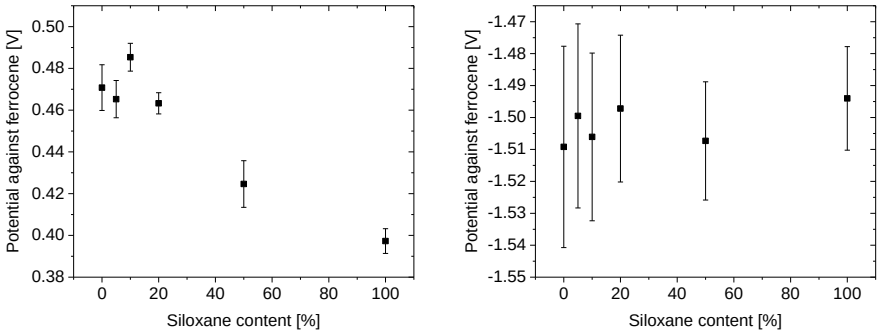

Fig. 5.4: Summary of the HOMO and LUMO energy levels measured by square wave voltammetry.

oxidation and reduction potentials (Figure. 5.4). The polymers were studied as thin films on a Pt wire and measured in acetonitrile containing 0.1 M tetrabutylammonium hexafluorophosphate as electrolyte. Ferrocene/ferrocenium (Fc/Fc^{+}) was used as an internal standard. The reduction waves of the six polymers are virtually identical, but the oxidation potentials slowly decrease with increasing siloxane content. The resulting HOMO and LUMO levels are summarized in Table 5.1.

To evaluate the effects of the side chains on the hole mobility, field-effect transistors were fabricated in a bottom-gate, bottom-contact architecture. The results are collected in Table 5.1. As can be seen in Figure. 5.5, the hole mobility increases by an order of magnitude upon the introduction of siloxanes and is comparable for all polymers containing siloxane side chains. The higher hole mobility of PDPPTPT with siloxane-terminated solubilizing groups is consistent with previous observations.[19,20]

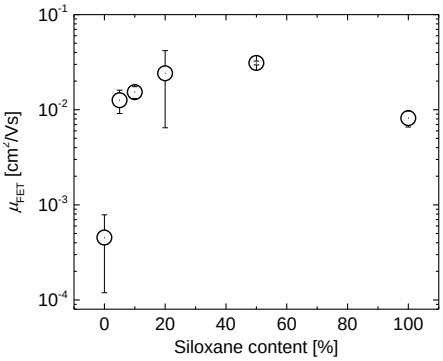

Fig. 5.5: Hole mobilities for the DPPTPT polymers.

The photovoltaic performance of the materials was evaluated by producing solar cells with an ITO/ZnO/active layer/MoO_3/Ag configuration. For the active layer, the polymers were combined with [6,6]-phenyl-C_{71}-butyric acid methyl ester ([70]PCBM) as an acceptor in a 1:2 weight ratio and spin coated from solutions in chloroform containing 2% diphenyl ether (DPE). These conditions were found to be optimal in terms of power conversion efficiency (PCE) for both the 100% siloxane as well as the 0% siloxane polymer after an optimization of the solvent and co-solvent ratio. Figure. 5.6 shows the current-density – voltage (*J-V*) characteristics in dark and under simulated AM1.5G (100 mW/cm^2) illumination and external quantum efficiencies (EQE) of the optimized devices. The photovoltaic parameters are summarized in Table 5.2. The short-circuit current density (J_{sc}) reduces for polymers with increased siloxane content. Analysis of the corresponding EQE spectra reveals that the decrease in current generation is proportional over all wavelengths.

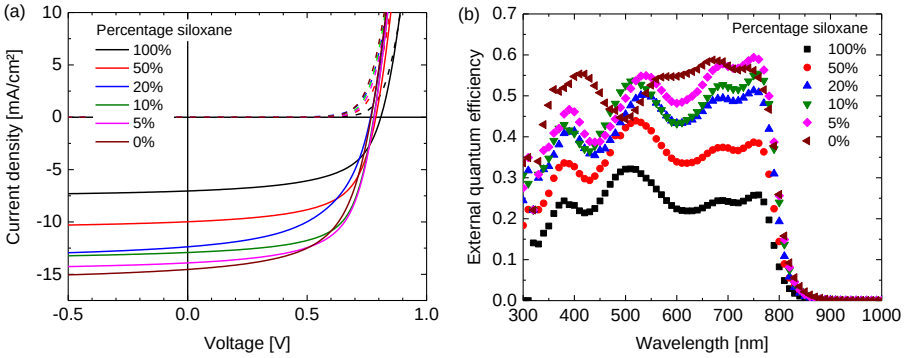

Fig. 5.6: (a) *J-V* characteristics of the PDPPTPT:[70]PCBM 1:2 (w/w) solar cells. (b) EQE spectra.

Table 5.2: Photovoltaic performance of the PDPPTPT:[70]PCBM 1:2 (w/w) blends.[a]

Siloxane fraction	*d* [nm]	J_{sc} [mA/cm²]	V_{oc} [V]	FF	PCE [%]
100%	125	6.8 (6.7)	0.81 (0.81)	0.58 (0.57)	3.2 (3.1)
50%	98	9.7 (9.6)	0.79 (0.79)	0.62 (0.62)	4.7 (4.7)
20%	123	12.4 (12.1)	0.77 (0.77)	0.54 (0.52)	5.1 (4.9)
10%	99	13.2 (13.4)	0.78 (0.77)	0.65 (0.63)	6.7 (6.6)
5%	100	14.0 (13.9)	0.78 (0.78)	0.63 (0.62)	6.9 (6.7)
0%	143	14.6 (14.6)	0.77 (0.77)	0.59 (0.59)	6.6 (6.6)

[a] Best cells are shown, numbers between parentheses refer to the average over 4 cells

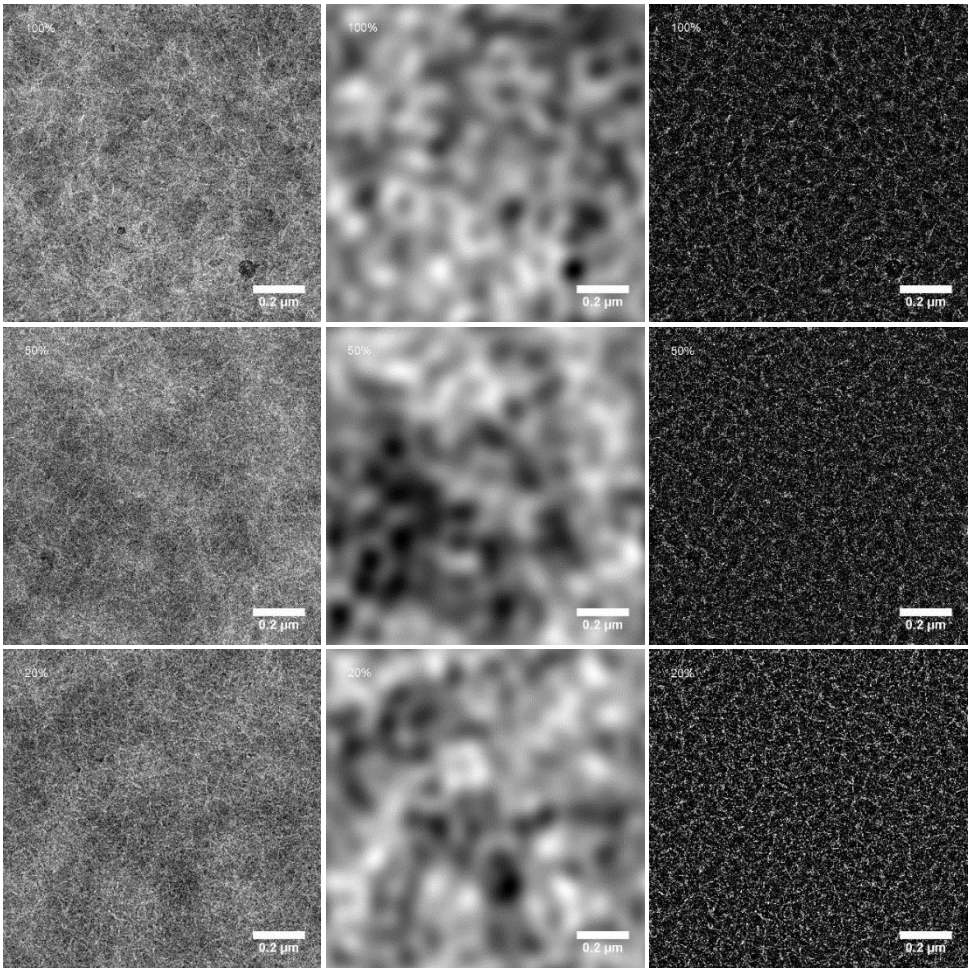

Fig. 5.7: Unfiltered (left), Fourier-filtered (> 100 nm, middle) and Fourier-filtered (< 100 nm, right) TEM images of the PDDPPTPT:[70]PCBM polymer blends with 100% siloxane side chains (top), 50% siloxane side chains (middle) and 20% siloxane side chains (bottom).

As the electronic and optical properties of all polymers are very similar, the most likely cause therefore is differences in the morphology of the blend layers. As can be seen in Table 5.2, there is no clear trend in the fill factor (FF). Since the fill factor relates to the competition between extraction and recombination of free charges,[38] the balance between these two processes appears similar in all layers. A weak trend between the siloxane content and the open-circuit voltage (V_{oc}) is observed, with a ~40 mV increase in V_{oc} with 100% siloxane content. Although differences are small, we note that this trend is opposite to the

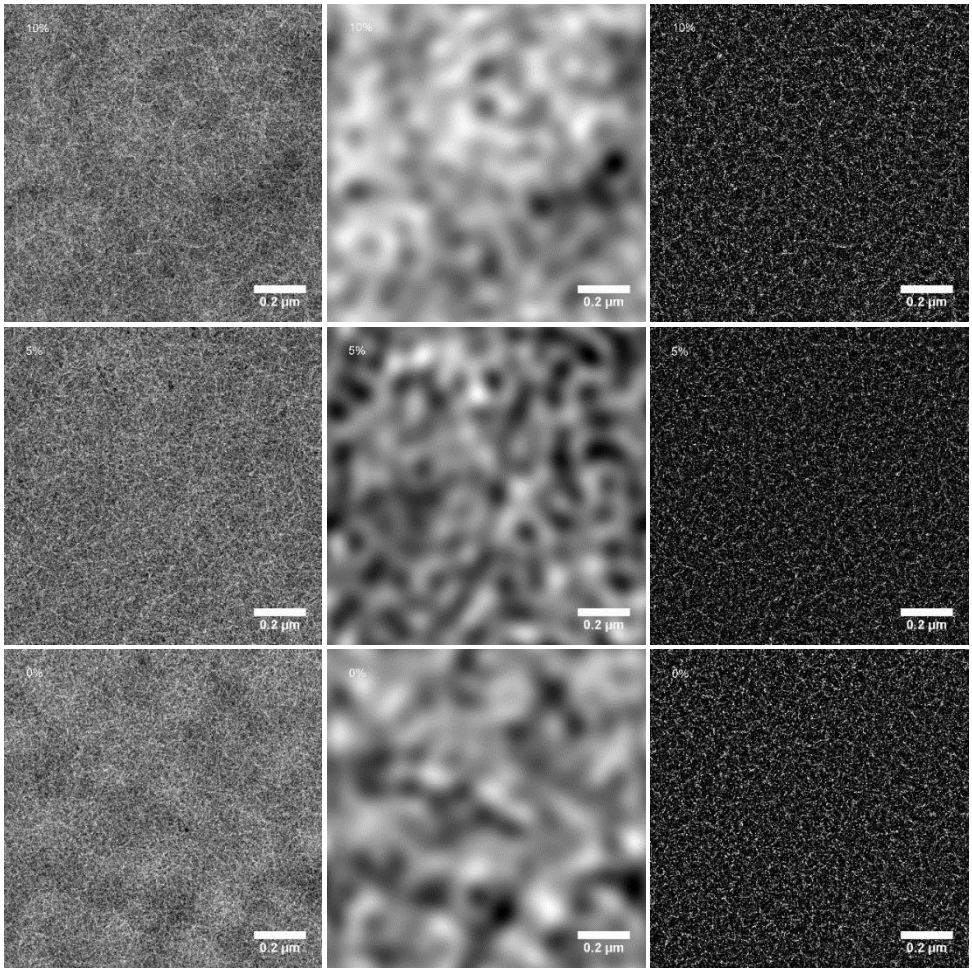

Fig. 5.8: Unfiltered (left), Fourier-filtered (> 100 nm, middle) and Fourier-filtered (< 100 nm, right) TEM images of the PDDPPTPT:[70]PCBM polymer blends with 10% siloxane side chains (top), 5% siloxane side chains (middle) and 0% siloxane side chains (bottom).

change in HOMO levels, where the 100% siloxane polymer has a ~70 meV shallower HOMO level (Table 5.1), which generally would provide a higher V_{oc}. Overall the PCE of the PDPPTPT:[70]PCBM blends drops by a factor of over 2 going from 0% to 100% siloxane side chains. A preliminary study on the stability revealed that the polymers can be safely stored under ambient conditions in the dark for >1 year, and that the photovoltaic devices do not degrade when stored under protective dry N_2 atmosphere for 6 months.

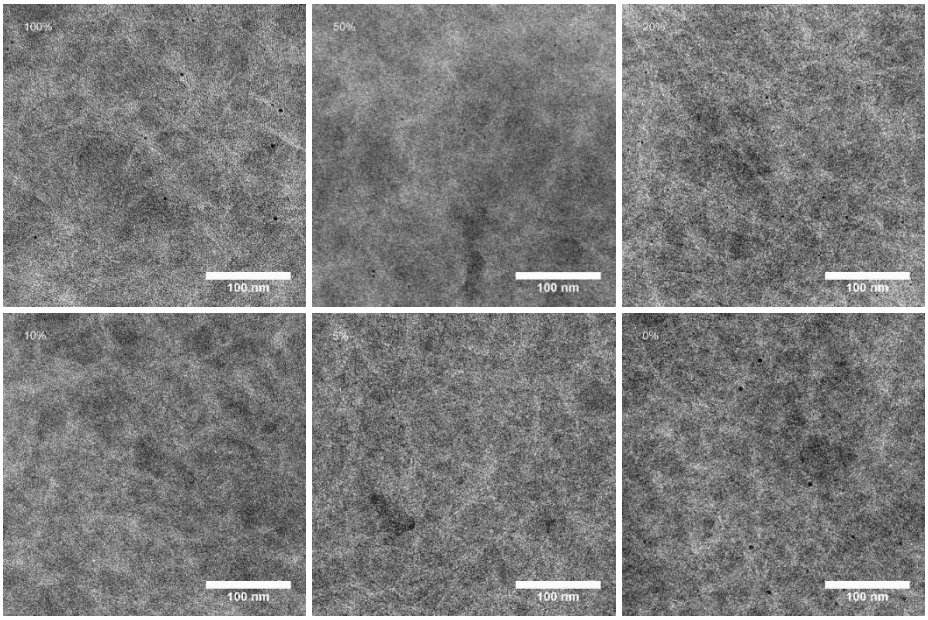

Fig. 5.9: TEM images of smaller scales of the polymer blends. First row: 100%, 50% and 20% siloxane polymers, second row 10%, 5% and 0% siloxane polymers.

To understand the change in performance with increasing percentage of siloxane side chains, transmission electron microscopy (TEM) was performed to analyse the morphology of the active layers. These are shown in Figure. 5.7 and Figure. 5.8 (left panels). All mixtures show a fine fibre-like morphology typical for blends of DPP-based polymers with [70]PCBM.[7,39] In all cases, the fibre width is small, making a detailed analysis difficult, but for the 100% siloxane the fibres appear wider than for the 0% polymer. At high magnification the TEM images (Figure. 5.9) show lattice fringes that can be associated with the lamellar packing distance (*d*-spacing) of the polymers chains. By performing a Fourier transform of the images in Figure. 5.9, an estimate of the *d*-spacing of the crystalline domains in the blend could be obtained. A significant increase in the d-spacing from 18.5 Å to 26.2 Å was found with increasing siloxane content (Table 5.1). This is assigned to the bulky nature of the siloxane side chains groups that hinder closer lamellar packing.

Further analysis of the blend morphology was done using two-dimensional grazing incidence wide angle X-ray scattering (2D GIWAXS) (Figure. 5.10). The 2D GIWAXS shows diffuse halos at $q \approx 0.7$ Å^{-1} and $q \approx 1.4$ Å^{-1} that can be attributed to [70]PCBM

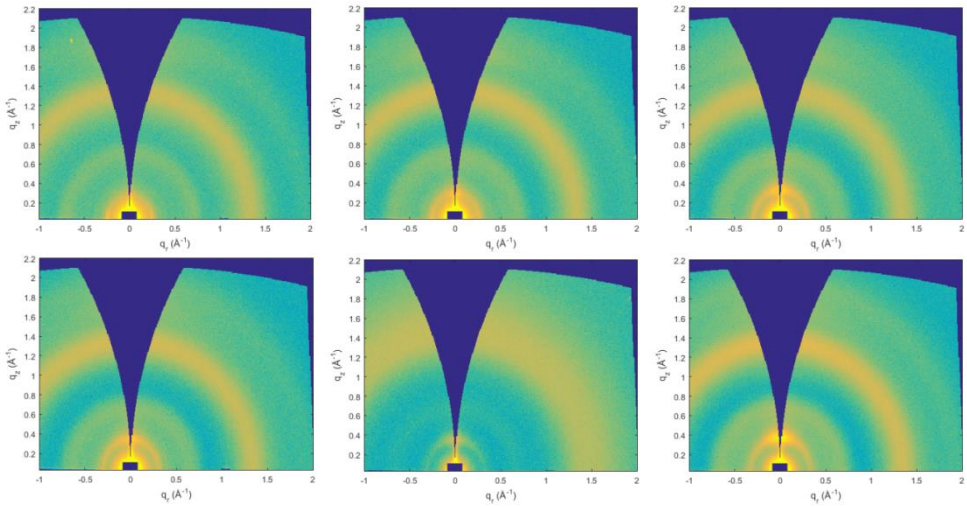

Fig. 5.10: Grazing incidence wide angle X-ray scattering of the polymer blends. First row: 100%, 50% and 20% siloxane polymers, second row 10%, 5% and 0% siloxane polymers.

clusters.[40,41] The diffraction around q = 0.25 Å^{-1} is associated with the lamellar d-spacing of the polymer and values for the different polymers are in accordance with the data obtained from the TEM (Table 5.1). The 2D GIWAXS and the corresponding in-plane and out-of-plane line cuts (Figure. 5.11) indicate a change in orientation of the polymer chains on the surface with increasing siloxane content. Here small angle approximation is valid and during the line cut analysis no further Fraser correction is made. If fibre symmetry with respect to the normal of the film plane is assumed, then we have complete information with respect to the orientation of 100 planes. From this plot a general decreasing trend of the

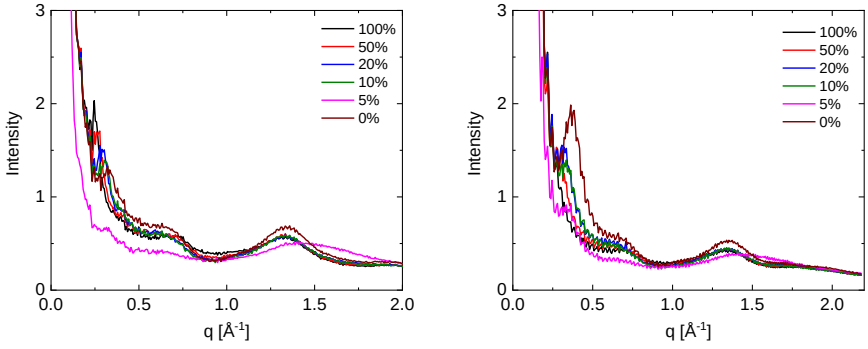

Fig. 5.11: In-plane and out-of-plane line cuts extracted from the GIWAXS analysis.

intensity at 90° and 270° (in plane direction) with decreasing siloxane content is visible. Thus, the orientation changes from relatively mostly edge-on for the polymers with low percentages of siloxane, via a mixed edge-on/face-on orientation for the 50% siloxane polymer, to relatively most face-on for the 100% siloxane polymer.

To roughly quantify this change, a pole figure analysis was carried out.[42] The intensity between 90°−135° and 225°−270° (A_{xy}) was integrated and compared to the integrated intensity between 145°−215° (A_z), ranges which correspond to the face-on and edge-on crystallites, respectively. By taking the ratio A_{xy}/A_z, a relative ratio between the face-on and edge-on orientation could be calculated. As can be seen in Figure. 5.11b, this ratio increases with increasing siloxane content, indicating a change in orientation from mostly edge-on (0% siloxane), through mixed orientation (50% siloxane), to mostly face-on (100% siloxane). Generally, a face-on orientation, in which the π-face lies in the plane of the substrate, is beneficial for solar cell performance as it favours vertical inter-chain charge transport and may even inhibit charge recombination.[43] For the siloxane containing polymers, however, we see an opposite trend in the solar cell performance and, hence, the difference in polymer orientation does not explain the differences in photovoltaic performance.

To gain further insight in the morphology a filtering was performed on the TEM images: in the Fourier transform image all information pertaining to features larger than 100 nm was cut out and stored separately. Next, the two images were inverse Fourier transformed resulting in two filtered images, one containing only features larger than 100

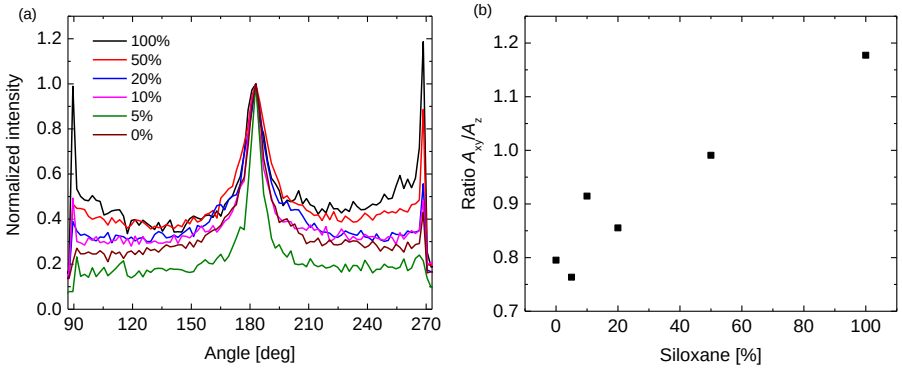

Fig. 5.11: (a) The (100) peak over all angles, (b) the ratio A_{xy}/A_z in function of the siloxane content, with A_{xy}/A_z the ratio of face-on to edge-on orientation.

nm and one with only smaller features (Figure. 5.7 and 5.8, middle and right panels). In the large-feature images a blurred pattern of dark and light domains can be seen with a distance of 300 to 400 nm, most likely associated with coarse phase separation over these larger length scales. All blends show a very similar distribution of these light and dark regions. In the small-feature images the fibrous structure of the polymers is now more clearly visible. The small size of the fibres still prohibits further formal characterization of the domain sizes. However, a clearer difference between the blends can now be seen. This difference lies mainly in the distances between fibres or fibre-clusters, with the blend of the 100% siloxane polymer showing the roughest structure and the fibres becoming gradually more finely dispersed with decreasing siloxane content. This difference is most clear when comparing the 100%, 50% and 0% siloxane polymer blends. Among the 0%, 5%, 10% and 20% polymer blends the differences are only very subtle. A finer fibrous morphology is known to provide higher quantum efficiencies for charge generation. For thicker fibres, typical exciton diffusion lengths are smaller than the fibre width, causing excitons to decay before charges can be generated at the interface with [70]PCBM.[3,7,8,39] Whereas this is a clear trend in the morphology of these layers, the differences remain subtle, and might not fully explain the trend seen in the EQE spectra.

To further investigate the diminishing J_{sc} with higher siloxane content, fluorescence spectra of pristine polymer layers and their blends with [70]PCBM were measured. The fluorescence intensity was corrected for the absorption intensity of the layers at 750 nm, which was the wavelength used for excitation. As can be seen in Figure.

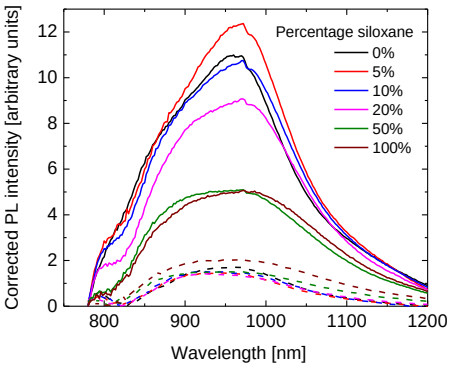

Fig. 5.12: Fluorescence spectra of the pristine polymers (solid lines) and their blends with [70]PCBM (dashed lines), corrected for the absorption at 750 nm.

5.12, a similar, broad, fluorescence spectrum was measured for all polymers. The fluorescence intensity of the pristine layers is comparable for the 0%, 5% and 10% polymers, and shows a downward trend with increasing siloxane content. The lower fluorescence intensity for the polymers with a high percentage of siloxane side chains indicates a lower fluorescence quantum yield. As the radiative lifetime is not expected to change with the change in side chains, the most likely cause is an increased non-radiative decay. The underlying cause for this trend is not fully understood at present, but could be related to the packing of the polymer chains influencing the amount of non-radiative decay. The fluorescence intensity of the blend layers with [70]PCBM is much lower and comparable for all polymers, except for the 100% polymer which shows a higher intensity. The fluorescence quenching is caused by photoinduced electron transfer between the PDPPTT polymers and [70]PCBM. The fluorescence quenching is significantly lower for the 50% and 100% polymers compared to the other PDPPTPT polymers. This indicates a lower tendency of charge generation, which is in line with the lower J_{sc} obtained from these polymers.

In summary, we have identified several effects that explain the lower J_{sc} of solar cells fabricated from polymers with high siloxane content. The (Fourier-filtered) TEM results point to the differences in fibre morphology, where a larger spatial distribution of wider fibres inhibits efficient charge separation. Moreover, the siloxane side chains give rise to a low fluorescence intensity, which is attributed to more efficient non-radiative exciton decay, causing a reduced excited-state lifetime and hence an intrinsic lower chance to generate charges from the corresponding polymers. While we have presented some evidence for the above two mechanisms, other factors may also contribute to the lower J_{sc}. Exciton mobility, e.g., could be affected by the increased *d*-spacing of the siloxane containing polymers, further hindering exciton dissociation at the donor-acceptor interface.

5.3 Conclusion

A varying ratio of siloxane and alkyl side chains was introduced on PDPPTPT to tune the molecular weight and solubility and investigate the effect of these two parameters on the performance of bulk heterojunction solar cells with a common fullerene acceptor. Increasing the siloxane to alkyl side chain ratio resulted in a reduced peak molecular weight and a reduced solubility. The short-circuit current density and power conversion efficiency

of the solar cells were lower with increasing percentage of siloxane. Fourier-filtered transmission electron microscopy and two-dimensional grazing-incidence wide-angle X-ray scattering revealed a fibrous morphology in which the fibres become wider and the chains are more face-oriented for higher siloxane content. Fluorescence spectroscopy indicated less fluorescence quenching with more siloxane side chains. The conclusion that emerges is that the siloxane side chains give rise to less charge generation due to a coarser morphology with slightly wider polymer fibres and increased non-radiative decay of the pristine polymers.

It has repeatedly been demonstrated that enhancing the tendency to aggregate of DPP polymers by reducing the solubility, leads to a better morphology with narrow fibres and higher PCEs.[3,7,39,44] Because an increase of the molecular weight of a polymer generally reduces its solubility, high molecular weight can be important for obtaining high PCEs. In the present example of PDPPTPT polymers, partly substituted with siloxane side chains, we have managed to decouple the solubility of the polymer from the molecular weight by using monomers with an intrinsic lower solubility and have made a series of polymers where the trend in solubility is opposite of the trend in molecular weight (M_p). The remarkable result is that in this case the lower solubility does not result in a finer fibre morphology of the bulk heterojunction blend, but rather in one that is similar or even slightly coarser. The fact that the PCE now decreases with decreasing solubility is related to two reasons. The first one is the slight increase in fibre width and coarser morphology; the second one is the intrinsically lower fluorescence of the siloxane containing polymers, which results in a less effective charge generation. It remains an interesting question why the fibre width of the siloxane containing PDPPTPT polymers is not reversely correlated with the solubility.

5.4 Experimental section

5.4.1 Materials and methods

All synthetic procedures were performed under a protective argon atmosphere. Commercial (dry) solvents and reactants were used without further purification, unless stated otherwise. *N*-bromosuccinimide (NBS) was recrystallized from deionized water prior to use. 1,4-Benzenediboronic acid bis(pinacol) ester and triphenylphosphine (PPh_3) were recrystallized from methanol prior to polymerization. Tris(dibenzylideneacetone)dipalladium ($Pd_2(dba)_3$) was purchased from Strem

Chemicals Inc, [70]PCBM (purity 90-95%) was purchased from Solenne BV. All other chemicals and solvents were obtained from Sigma-Aldrich Co. 3,6-Di(thiophen-2-yl)pyrrolo[3,4-*c*]pyrrole-1,4(2*H*,5*H*)-dione and 3,6-bis(5-bromothiophen-2-yl)-2,5-bis(2-hexyldecyl)-2,5-dihydropyrrolo[3,4-*c*]pyrrole-1,4-dione were synthesized according to previously published procedures.[45] 1,5-Di-*tert*-butyl-1,1,3,5,5-pentamethyltrisiloxane was synthesized using a modified published procedure.[46]

^{1}H-NMR and ^{13}C-NMR spectra were recorded on a Varian Mercury (^{1}H 400 MHz, ^{13}C 100 MHz) spectrometer. Chemical shifts are given in ppm with respect to tetramethylsilane as internal standard. Matrix assisted laser desorption ionization time of flight (MALDI-TOF) mass spectrometry was performed on a Bruker Autoflex Speed spectrometer. GC-MS was measured on a system consisting of a Shimadzu (GC-2010) gas chromatograph and a Shimadzu (GCMS-QP2010plus) mass spectrometer. The gas chromatograph contained a 30 meter Phenomenex Zebron ZB-5MS column with an internal diameter of 0.25 mm and 0.25 μm stationary phase film thickness. The temperature programme consisted of a steady ramp from 80 °C to 300 °C over 8 minutes. Polymer molecular-weight distributions were estimated by GPC at 140 °C on a PL-GPC 120 system using a PL-GEL 10 mm MIXED-C column with *o*-DCB as the eluent and using polystyrene internal standards. Samples were dissolved at a concentration of 0.1 mg/mL in *o*-DCB at 140 °C for 1 h before being measured.

UV-vis-NIR absorption spectroscopy was conducted on a PerkinElmer Lambda 1050 spectrophotometer with a 3D WB PMT/InGaAs/PbS detector module. Solid films were obtained by spin coating (2000 rpm) solutions of the materials (6 mg/mL) in chloroform onto glass substrates which were pre-cleaned with acetone and isopropanol, before being treated with UV-ozone for 30 minutes. Temperature-dependent spectra were recorded in TCE at temperatures between 20 °C and 100 °C using a PerkinElmer PTP1 Peltier temperature controller. Photoluminescence spectra were recorded with an Edinburgh Instruments FLSP920 double-monochromator luminescence spectrometer equipped with a nitrogen-cooled near-IR sensitive photomultiplier (Hamamatsu) using an excitation wavelength of 750 nm. Spectra were recorded of films processed onto glass substrates in a similar way to the samples used for the UV-vis-NIR spectroscopy measurements.

Square wave voltammetry was measured on the polymers in solid state which were deposited onto platinum wire by dipping the wire in the hot solutions (chloroform). A silver rod was employed as counter electrode and a silver chloride coated silver rod (Ag/AgCl) was used as a quasi-reference electrode. 0.1 M tetrabutylammonium hexafluorophosphate in acetonitrile was used as electrolyte solution. The measurement was carried out under inert atmosphere with an AutoLab PGSTAT 12 at a scan speed of 0.125 V/s, a modulation amplitude of 20 mV and at a frequency of 25 Hz. Fc/Fc^{+} was employed as a standard with $E = -4.8$ eV.

The grazing incidence wide angle x-ray scattering (GIWAXS) experiments were carried out on a GANESHA 300 XL+ system from JJ X-ray equipped with a Pilatus 300K detector (pixel size

172 µm × 172 µm). The X-ray source was a Genix 3D Microfocus sealed tube X-ray Cu-source with integrated monochromator and the wavelength used was λ = 1.5408 Å. Transmission electron microscopy (TEM) was performed on a Tecnai G2 Sphera transmission electron microscope (FEI) operating at 200 kV.

Bottom-gate top-contact transistors were fabricated to investigate charge carrier transport for all polymers. The 300 nm thick SiO_2 dielectric was functionalized with octyltrichlorosilane (OTS) to minimize interfacial trapping sites. The polymer films were prepared by drop casting from 1 mg/mL chloroform solution in ambient atmosphere, following by annealing at 100 °C for 30 min in nitrogen atmosphere.

Photovoltaic devices with an active area of 0.09 and 0.16 cm² were fabricated in air on patterned indium tin oxide (ITO) glass substrates (Naranjo Substrates). The substrates were cleaned by sonication in acetone for 15 min., followed by scrubbing with a sodium dodecyl sulfate solution (99%, Acros), rinsing with deionized water and a final sonication step in 2-propanol. Before deposition of the device layers the substrates underwent a 30 min. UV-ozone treatment. To obtain a ZnO layer, 0.5 M zinc acetate and 0.5 M ethanolamine were dissolved in 2-methoxyethanol by stirring overnight. The solution was then deposited onto the substrates by spin coating at 4000 rpm and annealing at 150 °C for 5 minutes. The substrates were then transferred to a nitrogen-filled glovebox to deposit the active layers. The active layers were deposited from a solution of polymer (5 mg/mL) and [70]PCBM (10 mg/mL) in chloroform containing 2 vol% of diphenyl ether. The solutions were heated to 90 °C for one hour to ensure that the polymers were completely dissolved, then kept at 60 °C and were finally cooled to room temperature under vigorous stirring during 2 minutes before spin coating at 2000 rpm. 10 nm of MoO_3 and 100 nm of Ag were deposited by thermal evaporation under high vacuum (~3×10^{-7} mbar) as a back contact.

Current density – voltage (J–V) characteristics were measured with a Keithley 2400 source meter under ~100 mW/cm^2 white light illumination from a tungsten-halogen lamp filtered by a Schott GG385 UV filter and a Hoya LB120 daylight filter. The short-circuit current density (J_{sc}) was more correctly determined from external quantum efficiency (EQE) measurements by integration of the EQE with the AM 1.5G solar spectrum. EQE measurements were carried out under 1 sun operating conditions in a setup consisting of a modulated monochromatic light, a preamplifier (Stanford Research Systems SR570) and a lock-in amplifier (Stanford Research Systems SR830). The modulated monochromatic light was generated by using an optical chopper from Stanford Research Systems (SR540), an Oriel Cornerstone 130 monochromator and a 50 W (Osram 64610) tungsten-halogen lamp. The 1 sun conditions were provided by the use of a 730 nm LED (Thorlabs) at different intensities for appropriate bias illumination. The device was kept in a nitrogen-filled box

with a quartz window. A calibrated silicon cell was used as reference prior to the *J*−*V* and EQE measurements.

Active layer thicknesses were determined with a Veeco Dektak150 profilometer.

5.4.2 Synthesis

2,5-Di(hex-5-ene)-3,6-di(thiophen-2-yl)-2,5-dihydropyrrolo[3,4-*c*]pyrrole-1,4-dione (1)[47,48]

3,6-Di(thiophen-2-yl)pyrrolo[3,4-*c*]pyrrole-1,4(2*H*,5*H*)-dione[45] (2.0 g, 6.66 mmol) and potassium carbonate (2.76 g, 19.98 mmol) were dissolved in *N*,*N*-dimethylformamide (30 mL) and heated to 120 °C. Then 6-bromohexene (2.715 g, 16.65 mmol) was added and the mixture was kept at 120 °C for 3 h. The mixture was then allowed to cool down and kept refrigerated overnight to allow the product to crystallize. The solids were then filtered and washed multiple times with water and subsequently methanol. Compound **1** was obtained as dark purple solid with a yield of 2.0 g (65%) and used without further purification. ^{1}H NMR (400 MHz, $CDCl_3$) δ 8.92 (dd, J = 3.8, 0.7 Hz, 2H), 7.64 (dd, J = 4.9, 0.7 Hz, 2H), 7.29 (dd J = 4.7, 4.2 Hz, 2H), 5.79 (m, 2H), 5.03 – 4.93 (m, 4H), 4.09 (t, J = 7.8 Hz, 4H), 2.11 (td, J = 7.4, 7.1 Hz, 4H), 1.77 (m, 4H), 1.52 (m, 4H). ^{13}C NMR (100 MHz, $CDCl_3$) δ 161.36, 139.99, 138.29, 135.28, 130.70, 129.72, 128.64, 114.90, 107.70, 42.04, 33.35, 29.48, 26.15. MALDI-TOF-MS: [M^+] calc: 464.16, found: 464.18.

1,5-Di-*tert*-butyl-1,1,3,5,5-pentamethyltrisiloxane (2)[46]

Tert-butyldimethylsilyl chloride (10 g, 66.35 mmol) and dichloromethylsilane (4.6 g, 40 mmol) were dissolved in isopropyl ether (15 mL) and added dropwise to a mixture of water (15 mL) and isopropyl ether (25 mL). After the dropwise addition, the whole mixture was heated to 70 °C for 24 h. The reaction mixture was then washed twice with water, once with saturated sodium bicarbonate and once with brine, before it was dried over $MgSO_4$ and the solvents were evaporated under reduced pressure. Three vacuum distillations (heating to 135 °C at 35 mbar) were then used to separate and purify the products, resulting the isolation of **2** in a purity of 96% and yield of 1.15 g (9%). ^{1}H NMR (400 MHz, $CDCl_3$) δ 4.67 (q, J = 1.6 Hz, 1H), 0.88 (s, 18H), 0.11 (d, J = 1.6 Hz, 3H), 0.05 (s, 12H). ^{13}C NMR (100 MHz, $CDCl_3$) δ 25.62, 18.07, 1.61, -3.12. GC-MS: 4.00 min., *m*/*z*: 254, 211 and 135.

2,5-Bis(6-(1,5-di-*tert*-butyl-1,1,3,5,5-pentamethyltrisiloxan-3-yl)hexyl)-3,6-di(thiophen-2-yl)-2,5-dihydropyrrolo[3,4-*c*]pyrrole-1,4-dione (3)

2,5-Bis(hex-5-ene)-3,6-di(thiophen-2-yl)pyrrolo[3,4-*c*]pyrrole-1,4(2*H*,5*H*)-dione (**1**) (500 mg, 1.076 mmol) was dissolved in dry toluene (10 mL), degassed and kept under argon. 1,5-Di-*tert*-butyl-1,1,3,5,5-pentamethyltrisiloxane (**2**) (825 mg, 2.69 mmol) was then added and degassed, before 1 drop of Karstedt's catalyst was added. The mixture was kept under argon and heated to 80 °C overnight. The solvent was subsequently evaporated under reduced pressure and the solids were purified using column chromatography (2:8 dichloromethane:heptane, gradient to 4:6). Compound **3** was obtained in a yield of 60%. ^{1}H NMR (400 MHz, $CDCl_3$) δ 8.93 (dd, J = 3.9, 1.1 Hz, 2H), 7.63 (dd, J = 5.0, 1.1 Hz, 2H), 7.29 (dd, J = 5.0, 3.9 Hz, 2H), 4.07 (t, J = 7.9 Hz, 4H), 1.74 (m, 4H), 1.41 – 1.26 (m, 12H), 0.86 (s, 36H), 0.46 (t, J = 7.8 Hz, 4H), -0.02 (s, 24H), -0.00 (s, 6H). ^{13}C NMR (100 MHz, $CDCl_3$) δ 161.55, 140.19, 135.44, 130.81, 129.97, 128.78, 107.88, 42.42, 33.14, 30.17, 26.84, 25.88, 23.32, 18.25, 17.86, 0.18, -2.74. MALDI-TOF-MS: [M^+] calc: 1076.53, found: 1076.55.

3,6-Bis(5-bromothiophen-2-yl)-2,5-bis(6-(1,5-di-*tert*-butyl-1,1,3,5,5-pentamethyltrisiloxan-3-yl)hexyl)-2,5-dihydropyrrolo[3,4-*c*]pyrrole-1,4-dione (4)

2,5-Bis(6-(1,5-di-*tert*-butyl-1,1,3,5,5-pentamethyltrisiloxan-3-yl)hexyl)-3,6-di(thiophen-2-yl)-2,5-dihydropyrrolo[3,4-*c*]pyrrole-1,4-dione (**3**) (394 mg, 0.365 mmol) was dissolved in chloroform (6 mL), degassed with argon and cooled to 0 °C. *N*-bromosuccinimide (135 mg, 0.768 mmol, 2.1 eq) was added and the mixture was kept at 0 °C for 10 minutes before allowing to heat to room temperature. After 5.5 h the reaction mixture was washed three times with water, dried over $MgSO_4$, and the solvent was evaporated under reduced pressure. The solids were then subjected to column chromatography (6:4 heptane:chloroform). The purified product was dissolved in dichloromethane and precipitated in methanol before being dried. Compound **4** was obtained as a dark purple solid in a yield of 334 mg (74%). ^{1}H NMR (400 MHz, $CDCl_3$) δ 8.68 (d, J = 4.2 Hz, 2H), 7.23 (d, J = 4.2 Hz, 2H), 3.98 (t, J = 7.9 Hz, 4H), 1.69 (m, 4H), 1.44 – 1.28 (m, 12H), 0.85 (s, 36H), 0.46 (t, J = 7.7 Hz, 4H), 0.02 (s, 24H), 0.00 (s, 6H). ^{13}C NMR (100 MHz, $CDCl_3$) δ 161.00, 138.95, 135.31, 131.61, 131.09, 119.10, 107.79, 42.27, 32.89, 30.01, 26.60, 25.67, 23.08, 18.04, 17.64, -0.19, -2.94. MALDI-TOF-MS: [M^+] calc: 1232.35, found: 1232.38.

General polymerization procedure

3,6-Bis(5-bromothiophen-2-yl)-2,5-bis(6-(1,5-di-*tert*-butyl-1,1,3,5,5-pentamethyltrisiloxan-3-yl)hexyl)-2,5-dihydropyrrolo[3,4-*c*]pyrrole-1,4-dione (**4**), 3,6-bis(5-bromothiophen-2-yl)-2,5-bis(2-hexyldecyl)-2,5-dihydropyrrolo[3,4-*c*]pyrrole-1,4-dione (**5**) (together 1 eq), freshly recrystallized 1,4-bis(4,4,5,5-tetramethyl-1,3,2-dioxaborolan-2-yl)benzene (**6**) (1 eq), recrystallized triphenylphosphine (1.5%) and $Pd_2(dba)_3$ (6%) were loaded in a Schlenk tube and placed under argon. Toluene (2 mL) was added before degassing the solution with argon for 10 minutes. A 2 M solution of K_3PO_4 in water (5 eq) was then added together with one drop of Aliquat 336. The tube was subsequently sealed and heated to 115 °C and the mixture was left to react overnight. 1,1,2,2-Tetrachloroethane (TCE) (5 mL) was then added to dissolve the gel-like substance and this solution was precipitated in methanol. The solids were filtered, dissolved in TCE at 120 °C and stirred with ethylenediaminetetraacetic acid (200 mg) for 1 h before water was added and stirred for a further 1 h. The mixture was then cooled and extracted three times with water. The organic phase was reduced in volume under lowered pressure and then precipitated in methanol. Soxhlet extraction was then carried out on the solids with acetone, hexane, dichloromethane and chloroform. The solids left in the thimble were then dissolved in TCE at high temperature, after which the solvent was partially evaporated under reduced pressure and the polymer was precipitated in acetone. The solids were then filtered and dried.

100-PDPPTPT

4 (70 mg (56.7 µmol), **6** (18.9 mg, 56.7 µmol), $Pd_2(dba)_3$ (1.56 mg, 1.7 µmol), triphenylphosphine (1.78 mg (6.8 µmol) and K_3PO_4 solution (0.14 mL) were used. GPC (*o*-DCB, 140 °C): M_n = 10.9 kDa, M_w = 73.7 kDa, $Đ$ = 6.7. Note: due to aggregation and tailing these numbers are approximate.

50-PDPPTPT

4 (54.5 mg, 44.1 µmol), **5** (40 mg, 44.1 µmol), **6** (29.1 mg, 88.2 µmol), $Pd_2(dba)_3$ (1.21 mg, 1.32 µmol), triphenylphosphine (1.39 mg, 5.3 µmol) and of K_3PO_4 solution (0.22 mL) were used. GPC (*o*-DCB, 140 °C): M_n = 2.7 kDa, M_w = 49.8 kDa, $Đ$ = 18.4 Note: due to aggregation and tailing these numbers are approximate.

20-PDPPTPT

4 (21.0 mg, 17.0 µmol), **5** (61.6 mg, 67.9 µmol), **6** (28.0 mg, 84.8 µmol), $Pd_2(dba)_3$ (1.16 mg, 1.27 µmol), triphenylphosphine (1.34 mg, 5.09 µmol) and K_3PO_4 solution (0.22 mL) were used. GPC (*o*-DCB, 140 °C): M_n = 4.5 kDa, Mw = 45.5 kDa, $Đ$ = 10.0. Note: due to aggregation and tailing these numbers are approximate.

10-PDPPTPT

4 (10.5 mg, 8.5 µmol), **5** (69.3 mg, 76.4 µmol), **6** (28.0 mg, 84.8 µmol), $Pd_2(dba)_3$ (1.16 mg, 1.27 µmol), triphenylphosphine (1.34 mg, 5.09 µmol) and K_3PO_4 solution (0.22 mL) were used. GPC (*o*-DCB, 140 °C): M_n = 15.6 kDa, M = 52.9 kDa, $Đ$ = 3.4. Note: due to aggregation and tailing these numbers are approximate.

5-PDPPTPT

4 (4.24 mg, 5.24 µmol), **5** (73.1 mg, 80.6 µmol), **6** (28.0 mg, 84.8 µmol), $Pd_2(dba)_3$ (1.16 mg, 1.27 µmol), triphenylphosphine (1.34 mg, 5.09 µmol) and K_3PO_4 solution (0.22 mL) were used. GPC (*o*-DCB, 140 °C): M_n = 11.5 kDa, M_w = 56.0 kDa, $Đ$ = 4.9. Note: due to aggregation and tailing these numbers are approximate.

0-PDPPTPT

5 (76.9 mg, 84.8 µmol), **6** (28.0 mg, 84.8 µmol), $Pd_2(dba)_3$ (1.16 mg, 1.27 µmol), triphenylphosphine (1.34 mg, 5.09 µmol) and K_3PO_4 solution (0.22 mL) were used. GPC (*o*-DCB, 140 °C): M_n = 21.2 kDa, M_w = 68.9 kDa, $Đ$ = 3.3.

5.5 References

1 S. Zhang, Y. Qin, J. Zhu, J. Hou, *Adv. Mater.*, 2018, **30**, 1800868.

2 S. Holliday, Y. Li, C. K. Luscombe, *Prog. Polym. Sci.*, 2017, **70**, 34-51.

3 J. J. van Franeker, G. H. L. Heintges, C. Schaefer, G. Portale, W. Li, M. M. Wienk, P. van der Schoot, R. A. J. Janssen, *J. Am. Chem. Soc.*, 2015, **137**, 11783-11794.

4 L. Ye, X. Jiao, W. Zhao, S. Zhang, H. Yao, S. Li, H. Ade, J. Hou, *Chem. Mater.*, 2016, **28**, 6178-6185.

5 J. Zhao, S. Zhao, Z. Xu, B. Qiao, D. Huang. L. Zhao, Y. Li, Y. Zhu, P. Wang, *ACS Appl. Mater. Interfaces*, 2016, **8**, 18231-18237.

6 G. H. L. Heintges, P. J. Leenaers, R. A. J. Janssen, *J. Mater. Chem. A*, 2017, **5**, 13748-13756.

7 W. Li, K. H. Hendriks, A. Furlan, W. S. C. Roelofs, M. M. Wienk, R. A. J. Janssen, *Adv. Mater.*, 2014, **26**, 1565-1570.

8 M. Li, D. Di Carlo Rasi, F. J. M. Colberts, J. Wang, G. H. L. Heintges, B. Lin, W. Li, W. Ma, M. M. Wienk, R. A. J. Janssen, *Adv. Energy Mater.*, 2018, **8**, 1800550.

9 W.-S. Chang, J. Gao, L. Dou, C.-C. Chen, Y, Liu, Y. Yang, *Adv. Energy Mater.*, 2014, **4**, 1300864.

10 C. Cabanetos, A. El Labban, J. A. Bartelt, J. D. Douglas, W. R. Mateker, J. M. J. Fréchet, M. D. McGehee, P. M. Beaujuge, *J. Am. Chem. Soc.*, 2013, **135**, 4656-4659.

11 X. Chen, Z. Zhang, J. Liu, L. Wang, *Polym. Chem.*, 2017, **8**, 5496-5503.

12 C. Duan, R. E. M. Willems, J. J. van Franeker, M. M. Wienk, R. A. J. Janssen, *J. Mater. Chem. A*, 2016, **4**, 1855-1866.

13 L Ye., X. Jiao, S. Zhang, H. Yao, Y. Qin, H. Ade, J. Hou, *Adv. Energy Mater.*, 2017, **7**, 1601138.

14 M. Zhang, X. Guo, W. Ma, H. Ade, J. Hou, *Adv. Mater.*, 2014, **26**, 5880-5885.

15 R. Heuvel, F. J. M. Colberts, M. M. Wienk, R. A. J. Janssen, *J. Mater. Chem. C.*, 2018, **6**, 3731-3742.

16 K. H. Hendriks, W. Li, M. M. Wienk, R. A.J. Janssen, *Adv. Energy Mater.*, 2013, **3**, 674-679.

17 N. D. Treat, A Varotto, C. J. Tackacs, N. Batara, M. Al-Hashimi, M. J. Heeney, A. J. Heeger, F. Wudl, C. Hawker, M. L. Chabinyc, *J. Am. Chem. Soc.*, 2012, **134**, 15869-15879.

18 L. Ye, H. Hu, M. Ghasemi, T. Wang, B. A. Colins, J-H. Kim, K. Jiang, J. H. Carpenter, H. Li, Z. Li, T. McAfee, J. Zhao, X. Chen, J. Lin Yuk Lai, T. Ma, J-L Brédas, H. Yan, H. Ade, *Nat. Mater.*, 2018, **17**, 253-260.

19 J. Mei, D. H. Kim, A. L. Ayzner, M. F. Toney, Z. Bao, *J. Am. Chem. Soc.*, 2011, **133**, 20130-20133.

20 H. Li, J. Mei, A. L. Ayzner, M. F. Toney, J. B.-H. Tok, Z. Bao, *Org. Electron.*, 2012, **13**, 2450-2460.

21 J. Lee, A-R. Han, J. Kim, Y. Kim, J. H. Oh, C. Yang, *J. Am. Chem. Soc.*, 2012, **134**, 20713-20721.

22 J. Lee, A.-R. Han, H. Yu, T. J. Shin, C. Yang, J. H. Oh, *J. Am. Chem. Soc.*, 2013, **135**, 9540-9547.

23 J. Mei, H.-C. Wu, Y. Diao, A. Appleton, H. Wang, Y. Zhou, W.-Y. Lee, T. Kurosawa, W.-C. Chen, Z. Bao, *Adv. Funct. Mater.*, 2015, **25**, 3455-3462.

24 A-R. Han, J. Lee, H. R. Lee, J. Lee, S-H. Kang, H. Ahn, T.J. Shin, J.H. Oh, C. Yang, *Macromolecules*, 2016, **49**, 3739-3748.

25 B. Fan, L. Ying, P. Zhu, F. Pan, F. Liu, J. Chen, F. Huang, Y. Cao, *Adv. Mater.*, 2017, **29**, 1703906.

26 D. H. Kim, A. L. Ayzner, A. L. Appleton, K. Schmidt, J. Mei, M. F. Toney, Z. Bao, *Chem. Mater.*, 2013, **25**, 431-440.

27 X. Liu, L. Nian, K. Gao, L. Zhang, L. Qing, Z. Wang, L. Ying, Z. Xie, Y. Ma, Y. Cao, F. Liu, J. J. Chen, *J. Mater. Chem. A*, 2017, **5**, 17619-17631.

28 S. Feng, C. Liu, X. Xu, X. Liu, L. Zhang, Y. Nian, Y. Cao, J. Chen, *ACS Macro Lett.*, 2017, **6**, 1310-1314.

29 W. Li, K. H. Hendriks, M. M. Wienk, R. A. J. Janssen, *Acc. Chem. Res.*, 2016, **49**, 78-85.

30 K. H. Hendriks, G. H. L. Heintges, V. S. Gevaerts, M. M. Wienk, R. A. J. Janssen, *Angew. Chem. Int. Ed.*, 2013, **52**, 8341-8344.

31 J. J. Intemann, K. Yao, H.-L. Yip, Y.-X. Xu, Y.-X. Li, P.-W. Liang, F.-Z. Ding, X. Li, A. K.-Y. Jen, *Chem. Mater.*, 2013, **25**, 3188-3195.

32 J. A. Bartelt, J. D. Douglas, W. R. Mateker, A. El Labban, C. J. Tassone, M. F. Toney, J. M. J. Fréchet, P. M. Beaujuge, M. D. McGehee, *Adv. Energy Mater.*, 2014, **4**, 1301733.

33 H. K. H. Lee, Z. Li, I. Constantinou, F. So, S. W. Tsang, S. K. So, *Adv. Energy Mater.*, 2014, **4**, 1400768.

34 H. Kang, M. A. Udding, C. Lee, K,-H. Kim, T.-L. Nguyen, W. Lee, Y. Li, C. Wang, H. Y. Woo and B. J. Kim, J. Am. Chem. Soc., 2015, 137, 2359-2365.

35 J. Subbiah, B. Purushothaman, M. Chen, T. Qin, M. Gao, D. Vak, F. H. Scholes, X. Chen, S. E. Watkins, G. J. Wilson, A. B. Holmes, W. W. H. Wong, D. J. Jones, *Adv. Mater.*, 2015, **27**, 702-705.

36 C. Liu, K. Wang, X. Hu, Y. Yang, C.-H. Hsu, W. Zhang, S. Xiao, X. Gong, Y. Cao, *ACS Appl. Mater. Interfaces*, 2013, **5**, 12163-12167.

37 Z. Xiao, K. Sun, J. Subbiah, T. Qin, S. Lu, B. Purushothaman, D. J. Jones, A. B. Holmes, W. W. H. Wong, *Polym. Chem.*, 2015, **6**, 2312-2318.

38 D. Bartesaghi, I. del Carmen Pérez, J. Kniepert, S. Roland, M. Turbiez, D. Neher, L. J. A. Koster, *Nat. Commun.*, 2015, **6**, 7083.

39 W. Li, K. H. Hendriks, A. Furlan, W. S. C. Roelofs, M. M. Wienk, R. A. J. Janssen, *J. Am. Chem. Soc.*, 2013, **135**, 18942-18948.

40 E. Verploegen, R. Mondal, C. J. Bettinger, S. Sok, M. F. Toney, Z. Bao , *Adv. Funct. Mater.*, 2010, **20**, 3519-3529.

41 J. A. Bartelt, Z. M. Beiley, E. T. Hoke, W. R. Mateker, J. D. Douglas, B. A. Collins, J. R. Tumbleston, K. R. Graham, A. Amassian, H. Ade, J. M. J. Fréchet, M. F. Toney, M. D. McGehee, *Adv. Energy Mater.*, 2013, **3**, 364-374.

42 V. Vohra, K Kawashima, T. Kakara, T. Koganezawa, I. Osaka, K. Takimiya, H. Murata, *Nat. Photon.*, 2015, **9**, 403-408.

43 J. R. Tumbleston, B. A. Collins, L. Yang, A. C. Stuart, E. Gann, W. Ma, W. You, H. Ade, *Nat. Photon.*, 2014, **8**, 385-391.

44 G . H. L. Heintges, J. J. van Franeker, M. M. Wienk, R. A. J. Janssen, *Chem. Commun.*, 2016, **52**, 92-95.

45 L. Bürgi, M. Turbiez, R. Pfeiffer, F. Bienewald. J.-J. Kirner, C. Winnewisser, *Adv. Mater.*, 2008, **20**, 2217-2224.

46 G. A. Policello, M. D. Leatherman, P. Wenqing, S. K. Rajaraman, Z. Xia, US Pat. 005 754, 2007.

47 H. Li, J. Mei, A. L. Ayzner, M. F. Toney, J. B.-H. Tok, Z. Bao, *Org. Electron.*, 2012, **13**, 2450-2460

48 J. Lee, A.-R. Han, J. Kim, Y. Kim, J. H. Oh, C. Yang, *J. Am. Chem. Soc.*, 2012, **134**, 20713-20721.

Chapter 6

Relation between the electronic properties of regioregular donor-acceptor terpolymers and their copolymers

Abstract

By analysing the optical band gap and energy levels of seven different regioregular terpolymers in which two different electron-rich donor moieties are alternating with a common electron-deficient acceptor unit along the backbone, we establish a direct correlation with the properties of the corresponding binary copolymers in which one donor and one acceptor are combined. For this study we use diketopyrrolopyrrole as the common acceptor and different π-conjugated aromatic oligomers as donors. We find that, with remarkable accuracy, the optical band gap and frontier orbital energies of the terpolymers are the arithmetic average of those of the parent copolymers. The same relationship is also found for the open-circuit voltage of the bulk heterojunction solar cells made with the ter- and copolymers in combination with [6,6]-phenyl-C_{71}-butyric acid methyl ester. Comparison of these findings with data in literature suggests that this is a universal rule that can be used as a tool when designing new π-conjugated polymers.

A manuscript on this work is being prepared for publication.

6.1 Introduction

Control over the optical band gap (E_g) by adjusting the chemical structure is one of the critical virtues of π-conjugated polymers and is often employed to create novel materials with tailored properties to enhance charge transport, light emission, or photovoltaic energy conversion. Optical band gap control can be achieved by enlarging fused-ring systems and controlling the conjugation length via planarization of conjugated segments to enhance delocalization of electrons.[1-4] A second important tool for optical band gap control is adjusting the balance between contributions of aromatic and quinoid resonance structures of fused π-conjugated rings in the main chain.[5] The classical example of this approach is poly(isothionaphthene), first prepared by Wudl et al.[6] In poly(isothionaphthene) a favourable quinoid structure reduces the bond length alternation and lowers the optical band gap to about 1 eV. Havinga[7] and Tanaka[8] advanced the donor-acceptor or "push-pull" concept, which became very popular for controlling the optical band gap and frontier energy levels of π-conjugated polymers. In this approach two conjugated units, one with electron-rich (donor) and one with electron-deficient (acceptor) properties, are combined in an alternating copolymer. By varying the strength of the donating and accepting properties, control over the optical band gap and energy levels of the highest occupied molecular orbital (HOMO) and lowest unoccupied molecular orbital (LUMO) can be achieved. This gives almost unlimited access to a range of materials with different electronic characteristics. More recently, π-extended quinoids with strong electron-withdrawing groups that include aromatic substructures in the resonance form have been used to create very small band gap polymers.[9] Donor-acceptor polymers have been particularly useful for polymer solar cells.[10-14] Structural variations that allow to control the optical band gap can maximize the open-circuit voltage (V_{oc}) and increase short-circuit current (J_{sc}). Recently, polymers with an extended π-system perpendicular to the backbone have been successfully introduced.[15-18] These combined efforts have resulted in a surge of the power conversion efficiency (PCE) of polymer solar cells and enhanced the likelihood they will be employed as a lightweight, form-free, or flexible power source.[19,20] Colour control is especially important for building-integrated photovoltaic applications[21,22] and essential to multi-junction solar cells.[23,24]

Lately, the terpolymer design motif has been established as a further tool to tune the HOMO and LUMO energy levels.[25] This class of materials is an evolution of the donor-

acceptor design motif, but in terpolymers three distinct π-conjugated units are used, allowing fine control of the electronic characteristics. Terpolymers can be obtained by incorporating two electron-rich and one electron-poor unit, or two electron-poor and one electron-rich unit in the polymer backbone in a random or in a regular sequence.[26-33] Materials with PCEs in organic solar cells above 9% have thus been achieved,[30-32] and in some cases this design can be more efficient than making ternary blends out of the respective copolymers.[33]

Despite the increased synthetic effort required, regioregular terpolymers might offer more control over the electronic parameters of the material than regiorandom terpolymers. Intuitively, it can be expected that the electronic parameters of these materials occupy a middle ground between the two "parent" copolymers. However, a systematic design rule to predict these properties has not yet been firmly established. It is not only important to be able to predict the band gap, but also to establish if the optical absorption broadens, shifts, or a combination of both. Herein we systematically investigate the optical band gap and redox potentials of regioregular $(-D1-A-D2-A-)_n$ terpolymers and compare

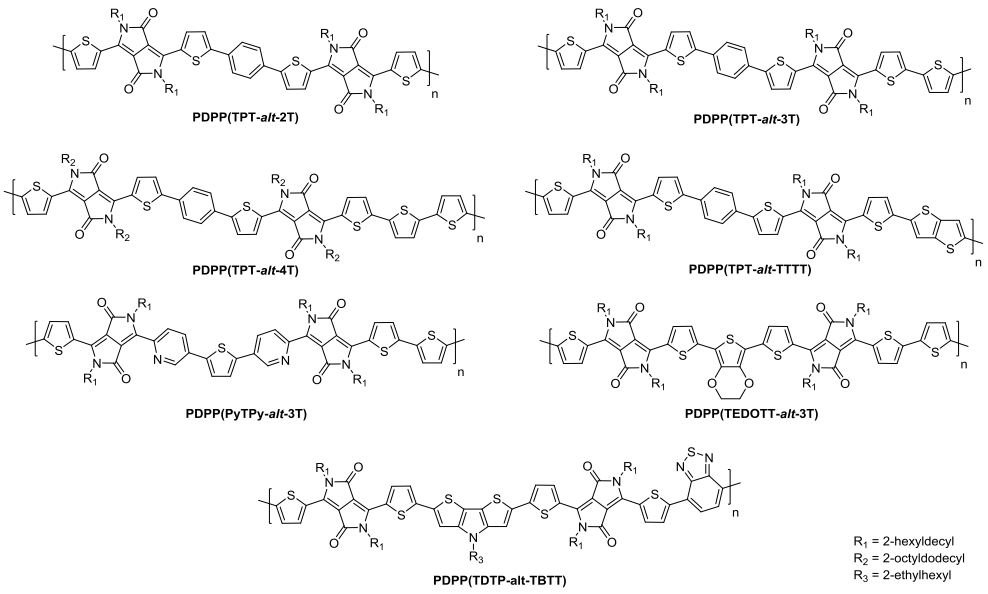

Scheme 6.1: Structures of the regioregular $(-D1-A-D2-A-)_n$ DDP-based terpolymers analysed in this work.

these to the corresponding parent $(-D1-A-)_n$ and $(-D2-A-)_n$ copolymers. For our study we use diketopyrrolopyrrole (DPP) as the common acceptor unit and vary the two donor

moieties. DPP based polymers have been extensively investigated in the past and show good performance in field-effect transistors and in single-junction and multi-junction polymer solar cells.[34,35] A wide range of optical band gaps has been achieved by combining DPP with different electron donating moieties. Here, seven regioregular DPP based terpolymers (Scheme 6.1) and their corresponding copolymers are synthesized and analysed. In this way we are able to provide predictive rules for the electronic properties of regioregular terpolymers, thus establishing the regioregular terpolymer design motif as a reliable tool for the design of conjugated polymers.

6.2 Results and discussion

To investigate the electronic properties, a variety of DPP-based terpolymers and their copolymers were selected. PDPP(TPT-*alt*-2T),[36] PDPP(TPT-*alt*-3T),[37] PDPP(PyTPy-*alt*-2T)[38] and PDPP(TDTPT-*alt*-TBTT)[39] (Scheme 6.1) were published before. To this dataset three new terpolymers were added: PDPP(TPT-*alt*-4T), PDPP(TPT-*alt*-TTTT) and PDPP(TEDOTT-*alt*-3T) (Scheme 6.1). These polymers were all synthesized using an extended monomer (A−D1−A) strategy wherein a central electron-rich (D1) unit is flanked by two electron deficient (A = DPP) units and reacted in a Stille or Suzuki condensation polymerization with the corresponding bisstannylated or bisboronic ester of the second donor moiety (D2) (Scheme 6.2). The details of the synthesis of the new polymers can be found in the Experimental section. For preparing PDPP(TPT-*alt*-4T) and PDPP(TPT-*alt*-TTTT), a T-DPP-T unit was first monobrominated before being coupled to a phenyl core to provide the extended precursor monomer (Scheme 6.3, Experimental section). This precursor monomer could then be brominated in preparation for a Stille polymerization reaction with either 5,5'-bis(trimethylstannyl)-2,2'-bithiophene or bis(trimethylstannyl)thieno[3,2-*b*]thiophene (Scheme 6.2). PDPP(TPT-*alt*-4T) carries 2-octyldodecyl side chains on the DPP units in contrast to the other polymers that carry 2-hexyldecyl side chains. This longer side chain was chosen because the electron-rich quaterthiophene (4T) unit in PDPP(TPT-*alt*-4T) reduces the solubility compared to the other derivatives. This is also reflected in the corresponding copolymer, PDPP4T, where a

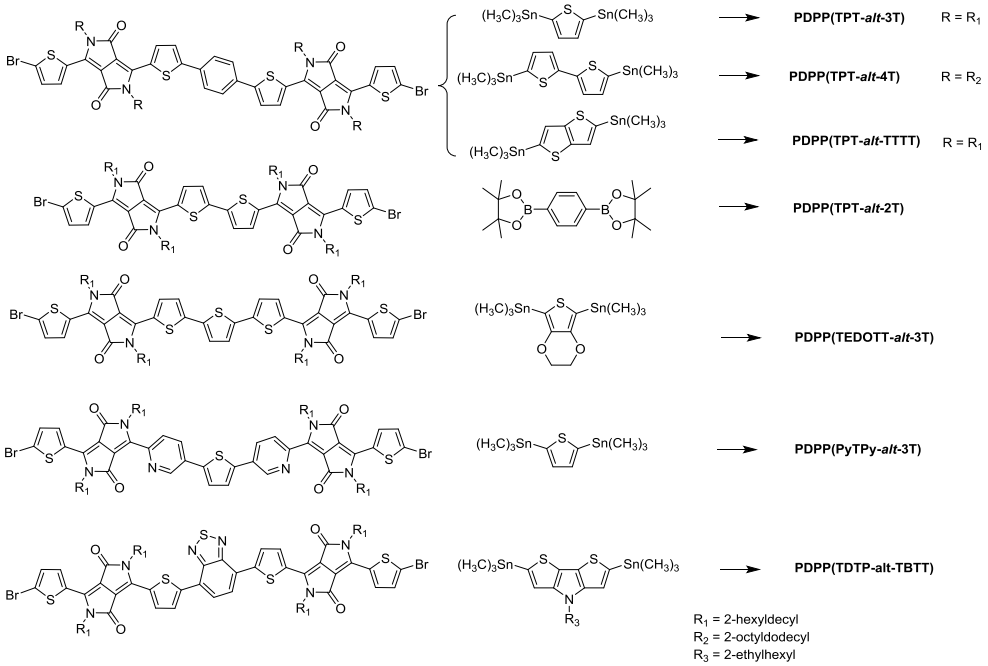

Scheme 6.2: Cross-coupling polymerization reactions towards the $(-D1-A-D2-A-)_n$ DDP-based terpolymers.

2-decyltetradecyl chain has been employed to achieve sufficient solubility. For PDPP(TEDOTT-*alt*-3T), a monoiodination reaction was carried out to offer the required asymmetry and allow coupling to a thiophene core (Scheme 6.4, Experimental section), after which the polymerization reaction could be carried out using 2,5-bis(trimethylstannyl)-3,4-ethylenedioxythiophene (Scheme 6.2). Except for PDPPTEDOTT,[40] all $(-D-A-)_n$ copolymers were synthesized before in our group.[37,39-44] PDPPTEDOTT was synthesized using a dibrominated thiophene-flanked DPP unit and 2,5-bis(trimethylstannyl)-3,4-ethylenedioxythiophene (Scheme 6.5, Experimental section). All co- and terpolymers showed high number average (M_n) and weight average (M_w) molecular weights when analysed with gel permeation chromatography in *ortho*-dichlorobenzene (*o*-DCB) at 140 °C (Table 6.1). A high M_n is important for achieving a high efficiency when these polymers are used in bulk heterojunction solar cells.[45,46]

Table 6.1: Molecular weight data for the copolymers and terpolymers.

Polymer	M_n [kDa]	M_w [kDa]	$Đ$
PDPPTPT	72	143	1.98
PDPP(TPT-*alt*-2T)	135	540	3.99
PDPP2T	85.0	322	3.80
PDPP(TPT-*alt*-3T)	42	154	3.68
PDPP3T	147	400	2.72
PDPP(TPT-*alt*-4T)	138	254	1.84
PDPP4T	83	150	1.80
PDPP(TPT-*alt*-TTTT)	94.1	273	2.90
PDPPTTTT	Above exclusion limit		
PDPP(PyTPy-*alt*-3T)	80.8	192	2.37
PDPPPyTPy	67.4	175.6	2.60
PDPP(TEDOTT-*alt*-3T)	Decomposes on column		
PDPPTEDOTT	Decomposes on column		
PDPPTDTPT	Interacts with column		
PDPP(TDTPT-*alt*-TBTT)	Interacts with column		
PDPPTBTT	72.5	177	2.44

UV-vis-NIR absorption spectra of thin, spin-coated films of the polymers were measured to establish the optical band gaps (Figure 6.1, Table 6.2). Figure 6.1 clearly shows that the optical absorption bands of the terpolymers are positioned in between those of the corresponding copolymers. The only real exception to this is in the case of PDPP(2TDTP-*alt*-2TBT) (Figure 6.1g), but in this case the absorption spectra of the copolymers are very close to one another and the deviation from the average is not large. The optical band gap, determined from the onset of the absorption is almost always exactly the average of the band gaps of its corresponding copolymers (Figure 6.1h, Table 6.2). Only small deviations (Δ_g) from the average are present, with a standard deviation of σ = 17 meV.

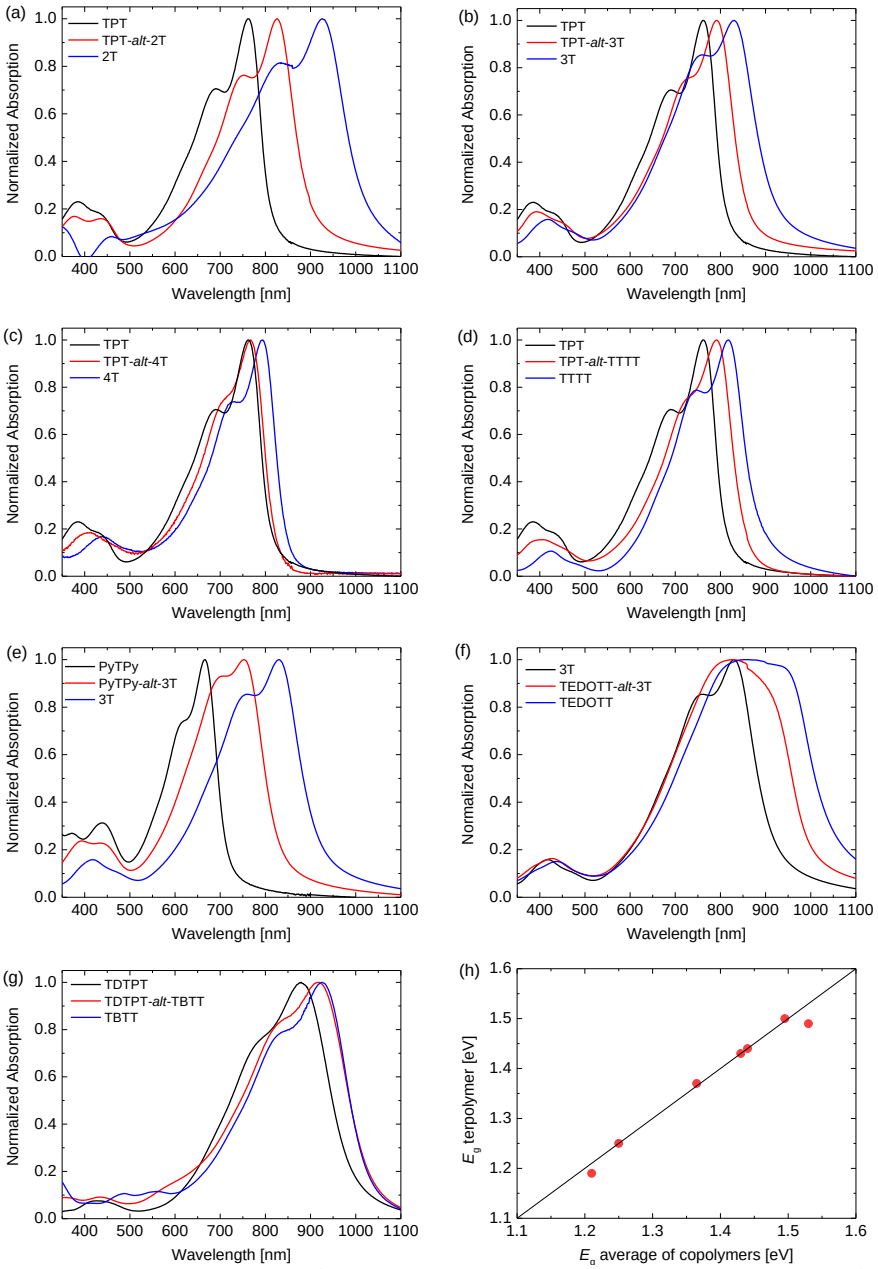

Fig. 6.1: UV-vis-NIR absorption spectra of terpolymers and the corresponding parent copolymers in thin films. (a) PDPP(TPT-*alt*-2T). (b) PDPP(TPT-*alt*-3T). (c) PDPP(TPT-*alt*-4T). (d) PDPP(TPT-*alt*-TTTT). (e) PDPP(PyTPy-*alt*-3T). (f) PDPP(TEDOTT-*alt*-3T). (g) PDPP(TDTPT-*alt*-TBTT). (h) E_g of the terpolymers vs. the average of the E_gs of the corresponding copolymers. The solid line represents slope = 1.

Table 6.2: The optical band gaps of the terpolymers and their respective copolymers.

D1	D2	E_g (D1−A) [eV]	E_g (D2−A) [eV]	E_g (D1−A−D2−A) [eV]	Δ_g [eV][a]
TPT	2T	1.53	1.20	1.37	−0.005
TPT	3T	1.53	1.33	1.43	0.000
TPT	4T	1.53	1.46	1.50	−0.005
TPT	TTTT	1.53	1.35	1.44	0.000
PyTPy	3T	1.73	1.33	1.49	0.040
TEDOTT	3T	1.17	1.33	1.25	0.000
TDTPT	TBTT	1.23	1.19	1.19	0.020

[a] $\Delta_g = [E_g(\text{D1−A}) + E_g(\text{D2−A})]/2 - E_g(\text{D1−A−D2−A})$.

Square wave voltammetry was used to estimate the energy levels of the HOMO (E_H) and LUMO (E_L) the polymers (Figure 6.2, Table 6.3 and 6.4). Similar to the optical band gap, the HOMO and LUMO energies of the terpolymers are very close to the average of the parent copolymers, with standard deviations of σ = 39 meV for E_H and σ = 38 meV for E_L. These results indicate that the electronic energy levels of the terpolymers can be quite accurately predicted, simply by taking the average of the related copolymers.

Having established that for the regioregular $(\text{D1−A−D2−A})_n$ terpolymers E_g, E_H, and E_L are close to the averages of the corresponding energies of the (D1−A) and (D2-A) copolymers, it is also of interest to assess their performance in solar cells to understand the relation between the optical band gap, open-circuit voltage, and minimal photon energy loss, defined as $E_{loss} = E_g - qV_{oc}$. Bulk heterojunction solar cells were fabricated, combining

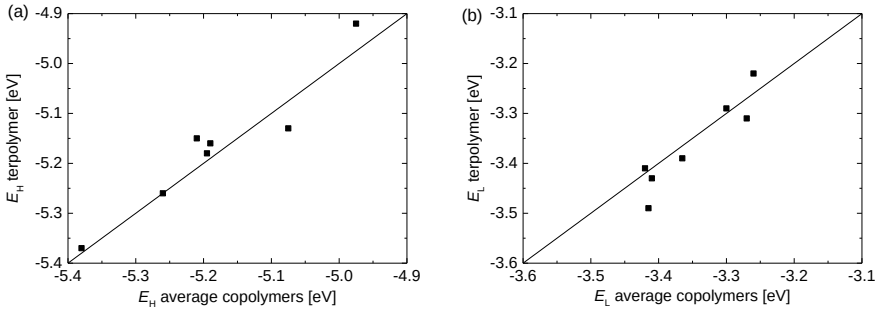

Fig. 6.2: The HOMO (a) and LUMO (b) energies of the terpolymers vs. the average of the HOMO and LUMO energies of the corresponding copolymers. The solid lines represent slope = 1.

Table 6.3: The energy of the HOMO levels of the terpolymers and their respective copolymers. [a]

D1	D2	E_H (D1−A) [eV]	E_H (D2−A) [eV]	E_H (D1−A−D2−A) [eV]	Δ_H [eV][a]
TPT	2T	−5.25	−5.27	−5.26	0.000
TPT	3T	−5.25	−5.14	−5.18	−0.015
TPT	4T	−5.25	−5.13	−5.16	−0.030
TPT	TTTT	−5.25	−5.17	−5.15	−0.060
PyTPy	3T	−5.62	−5.14	−5.37	−0.010
TEDOTT	3T	−5.01	−5.14	−5.13	0.055
TDTPT	TBTT	−4.83	−5.12	−4.92	−0.055

[a] Determined with square wave voltammetry vs. Fc/Fc^+, which was set at −4.8 eV vs. vacuum. [b] $\Delta_H = [E_H(D1-A) + E_H(D2-A)]/2 - E_H(D1-A-D2-A)$.

Table 6.4: The energy of the LUMO levels of the terpolymers and their respective copolymers.

D1	D2	E_L (D1−A) [eV]	E_L (D2−A) [eV]	E_L (D1−A−D2−A) [eV]	Δ_L [eV][a]
TPT	2T	−3.26	−3.56	−3.43	0.020
TPT	3T	−3.26	−3.34	−3.29	−0.010
TPT	4T	−3.26	−3.26	−3.22	−0.040
TPT	TTTT	−3.26	−3.28	−3.31	0.040
PyTPy	3T	−3.42	−3.42	−3.41	−0.010
TEDOTT	3T	−3.39	−3.34	−3.39	0.025
TDTPT	TBTT	−3.25	−3.58	−3.49	0.075

[a] Determined with square wave voltammetry vs. Fc/Fc^+, which was set at −4.8 eV vs. vacuum. [b] $\Delta_L = [E_L(D1-A) + E_L(D2-A)]/2 - E_L(D1-A-D2-A)$.

the co- and terpolymers as electron donor and [6,6]-phenyl-C_{71}-butyric acid methyl ester ([70]PCBM) as electron acceptor. The device configuration was ITO/PEDOT:PSS/polymer:[70]PCBM/LiF/Al for all cells, except for the polymers containing pyridine (PDPPPyTPy and PDPP(PyTPy-*alt*-3T)), in which PEDOT:PSS was replaced by molybdenum oxide. For depositing the layers, spin coating from chloroform with *o*-DCB as co-solvent was used. For each active layer, the amount of *o*-DCB was

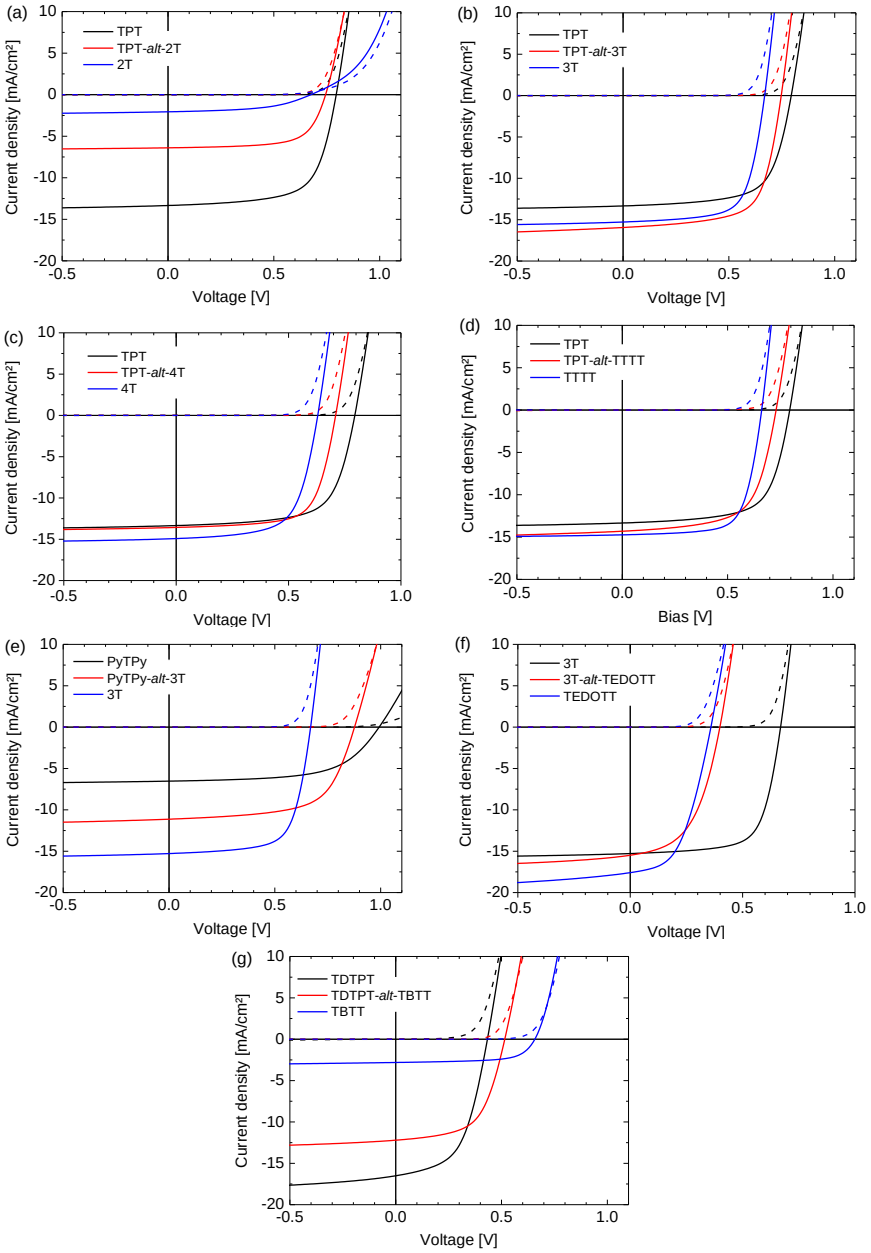

Fig. 6.3: The current density – voltage (*JV*) characteristics of solar cell devices made with the terpolymers and the corresponding parent copolymers in combination with [70]PCBM. (a) PDPP(TPT-*alt*-2T). (b) PDPP(TPT-*alt*-3T). (c) PDPP(TPT-*alt*-4T). (d) PDPP(TPT-*alt*-TTTT). (e) PDPP(PyTPy-*alt*-3T). (f) PDPP(TEDOTT-*alt*-3T). (g) PDPP(TDTPT-*alt*-TBTT).

Table 6.5: Photovoltaic characteristics of the optimized solar cells.

Polymer	J_{sc} [mA/cm²] [a]	V_{oc} [V]	FF	PCE [%]	E_{loss} [eV]
PDPPTPT	14.0	0.80	0.67	7.4	0.73
PDPP(TPT-*alt*-2T)	6.44	0.74	0.67	3.2	0.63
PDPP2T	2.03	0.68	0.50	0.7	0.52
PDPP(TPT-*alt*-3T)	15.9	0.75	0.67	8.0	0.68
PDPP3T	15.4	0.67	0.69	7.1	0.66
PDPP(TPT-*alt*-4T)	14.4	0.71	0.69	7.0	0.80
PDPP4T	15.3	0.64	0.69	6.8	0.82
PDPP(TPT-*alt*-TTTT)	14.2	0.74	0.66	6.9	0.70
PDPPTTTT	14.8	0.66	0.70	6.9	0.69
PDPP(PyTPy-*alt*-3T) [b]	11.9	0.88	0.63	6.6	0.61
PDPPPyTPy [b]	7.00	0.99	0.60	4.1	0.73
PDPP(TEDOTT-*alt*-3T)	14.1	0.47	0.53	3.5	0.78
PDPPTEDOTT	16.1	0.36	0.49	2.8	0.81
PDPPTDTPT	16.6	0.43	0.54	3.9	0.80
PDPP(TDTP-*alt*-TBTT)	12.2	0.52	0.58	3.7	0.67
PDPPTBTT	2.8	0.66	0.66	1.2	0.53

[a] J_{sc} was calculated by integrating the EQE spectrum with the AM1.5G spectrum. [b] MoO_3 was used as hole transport layer instead of PEDOT:PSS.

optimized. Figure 6.3 shows the current density – voltage characteristics of the optimized solar cells in the dark and under simulated AM1.5G (100 mW/cm^2) illumination. The short-circuit current density (J_{sc}), V_{oc}, fill factor (FF), PCE, and E_{loss} of all cells are listed in Table 6.5. In combination with [70]PCBM the terpolymers exhibit PCEs up to 8%, comparable to and sometimes surpassing those of the respective copolymers.

Transmission electron microscopy was used to check that for the newly synthesized materials the bulk heterojunction morphology of the blend with [70]PCBM corresponds to the finely dispersed fibrillary morphology that is characteristic for high-performing solar cells based on DPP polymers (Figure 6.4).[34,46] The external quantum efficiencies (EQEs) of the photovoltaic devices based on the terpolymers and their parent copolymers (Figure 6.5) give further insight into the charge generation. As expected, the

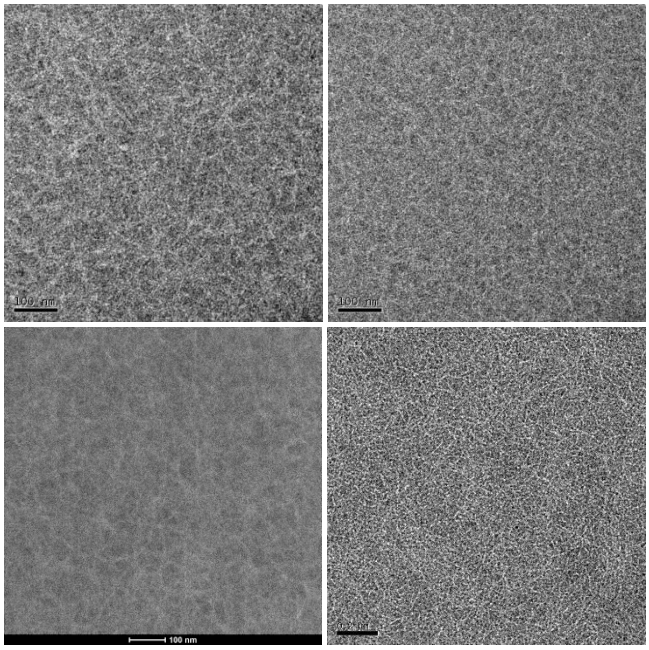

Fig 6.4: Transition electron microscopy of the PDPPTEDOTT:[70]PCBM (top left), PDPP(TEDOTT-*alt*-3T):[70]PCBM (top right), PDPP(TPT-*alt*-4T):[70]PCBM (bottom left) and PDPP(TPT-*alt*-TTTT):[70]PCBM blends (bottom right).

EQEs generally follow the thin-film absorption spectra and at the wavelength of maximum EQE, the magnitude is comparable for the terpolymers and corresponding copolymers. A noticeable deviation, however, is seen for PDPP(TPT-*alt*-2T), which has an EQE that is significantly lower than that of PDPPTPT, but higher than that of PDPP2T, which is virtually 0% in the region of where the polymer absorbs light. The deviation is due to the fact that, in case of PDPP2T, the energy of the interfacial PDPP2T^{+}/PCBM^{-} charge transfer state (E_{CT}) is comparable or even higher than the optical band gap of PDPP2T, E_g, such that photoinduced charge generation is slow or even inhibited.[47] In practice, electron transfer is slowed down when the minimal photon energy loss E_{loss} becomes less than 0.6 eV.[48] For PDPP2T, E_{loss} is only 0.52 eV and below this empirical threshold. For solar cells based on PDPP(TPT-*alt*-2T) and PDPPTPT, E_{loss} increases to 0.63 and 0.73 eV, respectively. For PDPP(TPT-*alt*-2T) E_{loss} is very close to the 0.60 eV threshold and it is therefore likely that this is the cause for the moderate EQE of the solar cells with PDPP(TPT-*alt*-2T). The same effect can be seen for PDPPTBTT:[70]PCBM solar cells, where the minimal photon energy

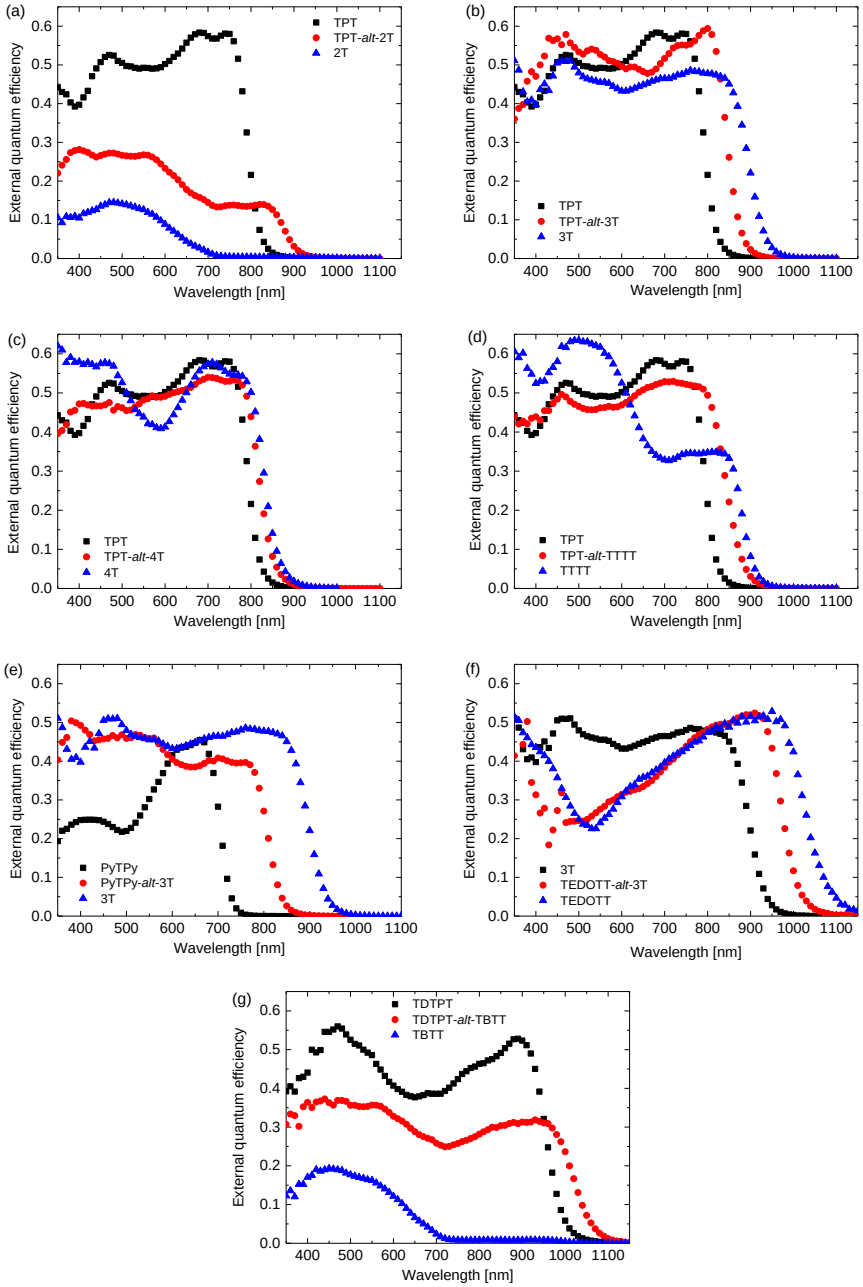

Fig. 6.5: External quantum efficiencies of bulk-heterojunction solar cells of the terpolymers and their related copolymers as donor with [70]PCBM as acceptor. (a) PDPP(TPT-*alt*-2T). (b) PDPP(TPT-*alt*-3T). (c) PDPP(TPT-*alt*-4T). (d) PDPP(TPT-*alt*-TTTT). (e) PDPP(PyTPy-*alt*-3T). (f) PDPP(TEDOTT-*alt*-3T). (g) PDPP(TDTPT-*alt*-TBTT).

loss is insufficient (0.53 eV), causing the very low EQE, whereas the cell based on PDPP(TDTPT-*alt*-TBTT) with E_{loss} = 0.67 eV shows a good EQE.

The V_{oc} of organic solar cells is related to the energy difference between the HOMO of the donor and LUMO of the acceptor. As the HOMO energies of the terpolymers are the average of those of the respective copolymers, the same can be expected for the V_{oc}. Figure 5a confirms this is indeed the case, with a standard deviation of σ = 30 mV of the V_{oc} of the terpolymer from the average V_{oc} of the copolymers. With 30 mV, the standard deviation in V_{oc} is on the same order of magnitude as the standard deviation for E_H. This correspondence is noteworthy because, unlike the optical band gap or the redox potentials, the V_{oc} is influenced by other factors than the HOMO energy of the polymer alone.[49] With clear correlations for E_g and V_{oc}, it is expected that also E_{loss} is correlated. As can be seen in Figure 6.6b and Table 6.5, most polymers are in good agreement with this expectation, with the notable exception of PDPP(PyTPy-*alt*-3T) which shows a E_{loss} of 0.61 eV, lower than that of either of the parent copolymers (0.66 and 0.73 eV). The standard deviation for E_{loss} is 41 meV.

These results clearly indicate that that the electronic characteristics of the terpolymers and their solar cells with [70]PCBM coincide with the average of the characteristics their respective copolymers. The standard deviation from the expected values of the V_{oc} and E_{loss} over all seven terpolymers is small. Even for J_{sc} Figure 6.3 shows that the photocurrent of the terpolymer solar cells is often close to the average of the two copolymer solar cells.

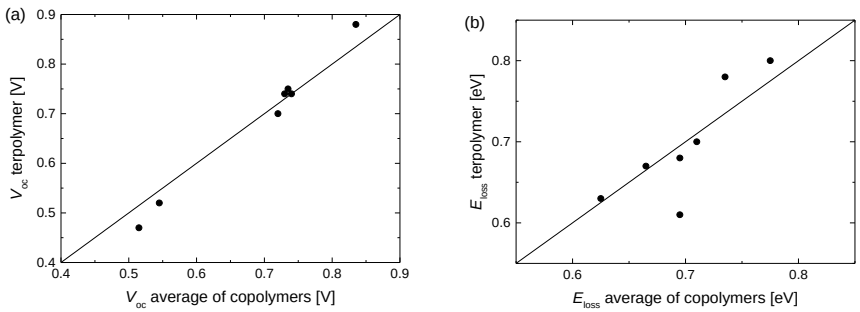

Fig. 6.6: The V_{oc} (a) and E_{loss} (b) the terpolymer vs. the average of the V_{oc} and E_{loss} energies of corresponding copolymers. The solid lines represent slope = 1.

To further substantiate the claim that the electronic characteristics of the terpolymers lie exactly in between those of the respective copolymers, a literature survey was carried out.[50-78] The band gaps of several terpolymers and their associated copolymers are summarized in Table 6.6. In some cases, the terpolymers were published without direct comparison to their copolymers, necessitating the use of other publications to extract the required data. Another issue was the presence of low-energy shoulders in the UV-vis-NIR spectra of some materials. In particular for diketopyrrolopyrrole polymers, these are known to be associated with homocoupling defects, which obscures the optical band gap of the perfectly alternating coplymer.[36] In the cases where other reports on the same copolymer were available, the highest reported optical band gap, which belongs to the material most likely to be free of defects, is included in the table. In cases where this data is not available, the material is marked as having a shoulder in the UV-vis-NIR absorption spectrum.

As can be seen, most terpolymers have a band gap in between those of the copolymers, and whenever this is not the case this can be attributed to homocoupling. The correlation of the expected with the effective band gap of the terpolymers is plotted in Figure 6.7a. Together with the seven terpolymers investigated in this work, the standard deviation is 34 meV for 28 terpolymers.

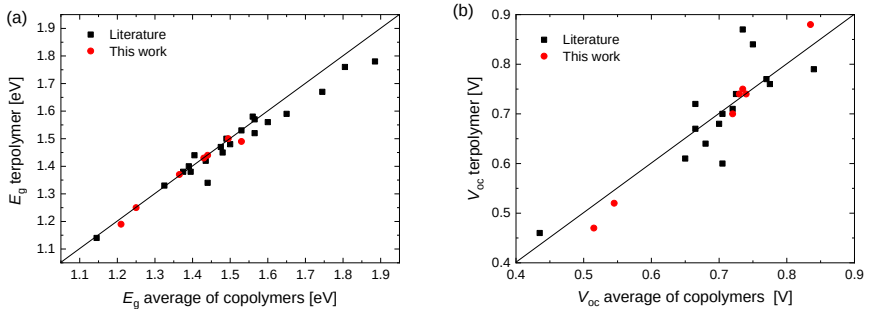

Fig. 6.7: (a) E_g of the terpolymers vs. the average of the E_gs of the corresponding copolymers. (b) The V_{oc} of the terpolymers vs. the average of the V_{oc}s of corresponding copolymers. The literature data are collected from References 50-78 and details can be found in Table 6.6 and 6.7. The solid lines represent slope = 1.

Table 6.6: Optical band gaps of terpolymers (E_g) and the parent copolymers (E_g1 and E_g2).

Unit 1[c]	Unit 2[c]	E_g1 [eV]	E_g2 [eV]	E_g [eV]	Reference
Diketopyrrolopyrrole (common acceptor)					
4T	2T-Biselenophene	1.46[a]	1.32[a]	1.40	50, 44, 51
4T	2T-Selenophene	1.46[a]	1.29	1.38	50, 44, 52
3T	2T-Biselenophene	1.33[a]	1.32[a]	1.33	50, 51, 37
2T-Benzodithiophene	4T	1.49	1.46[a]	1.47	44, 53
2T-Pyrene	2T-Benzodithiophene	1.65[a]	1.51[a]	1.58[b]	53, 56
2T-Biphenyl	4T	1.67[a]	1.46[a]	1.52[b]	44, 54, 55
2T-Pyrene	3T	1.65	1.33[a]	1.50	37, 56
4T	2f4T	1.46[a]	1.41[b]	1.42	44, 57
2T-Naphthalene	2f4T	1.59[b]	1.41[b]	1.48	57
2T-Alkoxybenzodithiophene	2T-Dithienopyrrole	1.56[a]	1.23[a]	1.38	58, 61, 39
2T-Fluorene	2T-Alkoxybenzodithiophene	1.74[a]	1.56[a]	1.59[b]	58, 61, 59
2T-Carbazole	2T-Alkoxybenzodithiophene	1.57[a]	1.56[a]	1.57[b]	58, 61, 60
Cyclopentadithiophene (common donor)					
2f-Benzothiadiazole	2T-Diketopyrrolopyrrole	1.59[a]	1.29[a]	1.34[b]	62, 65, 63
Thienopyrrolodione	2f-Benzothiadiazole	1.61[a]	1.59[a]	1.56	62, 65, 64
Thienopyrrolodione	Benzothiadiazole	1.61[a]	1.45	1.53	64, 66, 67
2T (common donor)					
Isoindigo	Diketopyrrolopyrrole	1.61[a]	1.20[a]	1.44	68, 69, 41
Diketopyrrolopyrrole	Thienoisoindigo	1.20[a]	1.09[a]	1.14	68, 41, 70
Alkoxybenzothiadiazole (common acceptor)					
Thienothiophene	3T	1.75[a]	1.74[a]	1.67[b]	71, 72, 73
2T-2f-Benzothiadiazole (common acceptor)					
Fluorene	Benzodithiophene	2.06	1.71	1.78	74
Thienothiophene (common donor)					
Benzodithiophene	Dithienosilole	1.55	1.41	1.45	75, 76, 77
Benzodithiophene (common donor)					
2T-Benzotriazole	2T-Alkylbenzothiadiazole	1.96	1.65	1.76	78

[a] Data pertaining to the copolymer is from a different paper than the terpolymer.

[b] Evidence of homocoupling.

[c] Systematic names for some units: benzo[1,2-*b*:4,5-*b'*]dithiophene, dithieno[3,2-*b*:2',3'-*d*]pyrrole, dithieno[3,2-*b*:2',3'-*d*]pyrrole, cyclopenta[2,1-*b*:3,4-*b'*]dithiophene, benzo[*c*][1,2,5]thiadiazole, thieno[3,4-*c*]pyrrole-4,6-dione, thieno[3,2-*b*]thiophene, silolo[3,2-*b*:4,5-*b'*]dithiophene, benzo[*d*][1,2,3]triazole. T = thiophene substituted, f = fluor substituted.

Table 6.7: Open circuit voltages of the terpolymers (V_{oc}) and the parent copolymers ($V_{oc}1$ and $V_{oc}2$).[a]

Unit 1	Unit 2	$V_{oc}1$ [V]	$V_{oc}2$ [V]	V_{oc} [V]	Reference
Diketopyrrolopyrrole (common acceptor)					
4T	2T-Biselenophene	0.64 [b]	0.66 [b]	0.61	50, 44, 51
3T	2T-Biselenophene	0.67 [b]	0.66	0.67	50, 51, 37
2T-Benzodithiophene	4T	0.77 [b]	0.64 [b]	0.60	44, 53
2T-Pyrene	2T-Benzodithiophene	0.78 [b]	0.77 [b]	0.76 [c]	53, 56
2T-Biphenyl	4T	0.75 [b]	0,64 [b]	0.71 [c]	44, 54, 55
2T-Pyrene	3T	0.78	0.67 [b]	0.74	37, 56
4T	2f4T	0.64 [b]	0.77 [c]	0.70	37, 56
2T-Naphthalene	2f4T	0.77	0.77 [c]	0.77	57
Cyclopentadithiophene (common donor)					
Thienopyrrolodione	2f-Benzothiadiazole	0.84 [b]	0.84 [b]	0.79	62, 65, 64
Thienopyrrolodione	Benzothiadiazole	0.79 [b]	0.61	0.68	64, 66, 67
2T (common donor)					
Isoindigo	Diketopyrrolopyrrole	0.65 [b]	0.68 [b]	0.72	68, 69, 41
Diketopyrrolopyrrole	Thienoisoindigo	0.68 [b]	0.19 [b]	0.46	68, 41, 70
2T-2f-Benzothiadiazole (common acceptor)					
Fluorene	Benzodithiophene	0.73 [d]	0.74	0.87	74
Thieno[3,4-b]thiophene (common donor)					
Benzodithiophene	Dithienosilole	0.76	0.60 [d]	0.64	75, 76, 77
Benzodithiophene (common donor)					
2T-Benzotriazole	2T-Benzothiadiazole	0.69	0.81	0.84	78

[a] Not all materials of Table 6.6 are present as not all solar cell data was available.

[b] Data pertaining to the copolymer is from a different paper than the terpolymer.

[c] Evidence of homocoupling.

[d] Leakage in the solar cells.

The solar cell characteristics of the terpolymers were further investigated and summarized in Table 6.7. Solar cells have not been reported for every material of interest. In some cases, a clear Ohmic current contribution could be seen in the current-voltage characteristics, thus potentially influencing the V_{oc}. Nevertheless, as can be seen in Figure 6.7b, the deviation from the expected value of the V_{oc} remains in most cases under 100 mV, with a standard deviation of 50 mV for 22 terpolymers.

These results confirm that in first approximation the electronic characteristics of the terpolymers are the arithmetic average of the corresponding values of the respective

copolymers. Especially in the case of the optical band gap this is very clear: 12 out of the 21 materials reported in literature have an optical band gap that is close to exactly the average of that of the copolymers with a deviation of less than 0.02 eV and only 4 materials have a deviation larger than 0.05 eV. Interestingly, the polymers with the largest deviations from the average all have a lower band gap than expected, which could be consistent with homocoupling defects. In the case of the solar cell characteristics, which are as indicated above subject to many other parameters, the spread in the data is larger, making the conclusion less clear. The deviations from the expected values remain, however, within 100 mV.

6.3 Conclusion

The electronic structure of seven regioregular $(-D1-A-D2-A-)_n$ terpolymers in which the common acceptor unit is a DPP moiety, of which three not previously published, have been studied and compared to their parent $(-D1-A-)_n$ and $(-D2-A-)_n$ copolymers. It was found that the optical band gap of the terpolymers is close to the average of the optical band gaps of their copolymers, with only minor deviations. This is a useful design rule and allows to precisely control the optical band gap of new conjugated polymers. Likewise, the HOMO and LUMO energies of the terpolymers are the average of their related copolymers, indicating that the electronic properties of terpolymers could be predicted on the basis of their related copolymers. In bulk heterojunction solar cells made of these terpolymers as donor with [70]PCBM as acceptor, the V_{oc} and E_{loss} were also found to be the average of the V_{oc} and E_{loss} of cells made with the corresponding copolymers. This is not unexpected as these parameters are closely related to the HOMO energy and optical band gap of the materials.

Comparison of these findings with data in literature confirmed the notion that the optical band gap is almost always the average of the band gaps of the copolymers, with only three polymers showing a substantial deviation from this rule. On average, this was also the case in terms of the V_{oc}, although the deviation from the expected value was larger for more materials. This could be due to the fact that V_{oc} is not exclusively influenced by the HOMO of the polymer but by many other factors. In conclusion, this study gives a predictive rule for the band gap and V_{oc} of regioregular terpolymers, namely that these

characteristics will be the average of those of their related copolymers. This could be a useful synthetic tool in the design of new conjugated polymers.

6.4 Experimental section

6.4.1 Materials and methods

All synthetic procedures were performed under a protective argon atmosphere. Commercial (dry) solvents and reactants were used without further purification, unless stated otherwise. *N*-bromosuccinimide (NBS) was recrystallized from deionized water prior to use. All monomers were recrystallized from methanol prior to polymerization. Tris(dibenzylideneacetone)dipalladium ($Pd_2(dba)_3$) was purchased from Strem Chemicals Inc, [70]PCBM (purity 90-95%) was purchased from Solenne BV. All other chemicals and solvents were obtained from Sigma-Aldrich Co. 3,6-Bis(5-bromothiophen-2-yl)-2,5-bis(2-hexyldecyl)-2,5-pyrrolo[3,4-*c*]pyrrole-1,4-dione,[79] 6,6'-(1,4-phenylenebis(thiophene-5,2-diyl))bis(3-(5-bromothiophen-2-yl)-2,5-bis(2-hexyldecyl)-pyrrolo[3,4-*c*]pyrrole-1,4-dione),[37] and 2,5-bis(2-octyldodecyl)-3,6-di(thiophen-2-yl)-2,5-pyrrolo[3,4-*c*]pyrrole-1,4-dione[79] were synthesized according to a previously published procedure.

^{1}H-NMR and ^{13}C-NMR spectra were recorded on a Varian Mercury (^{1}H 400 MHz or 200 MHz, ^{13}C 100 MHz) spectrometer. Chemical shifts are given in ppm with respect to tetramethylsilane as internal standard. Matrix assisted laser desorption ionization time of flight (MALDI-TOF) mass spectrometry was performed on a Bruker Autoflex Speed spectrometer. Molecular weight distributions were estimated by GPC at 140 °C on a PL-GPC 120 system using a PL-GEL 10 mm MIXED-C column with *o*-DCB as the eluent and using polystyrene internal standards. Samples were dissolved at a concentration of 0.1 mg/mL in *o*-DCB at 140 °C for 1 h before being measured.

UV-vis-NIR absorption spectroscopy was performed with a PerkinElmer Lambda 1050 spectrophotometer with a 3D WB PMT/InGaAs/PbS detector module. Solid films were obtained by spin coating (2000 rpm) solutions of the materials (≈4 mg/mL) in chloroform onto glass substrates which were pre-cleaned with acetone and isopropanol, before being treated with UV-ozone for 30 minutes. Square wave voltammetry was measured on the polymers in the solid state which were deposited onto a platinum wire by dipping the wire in hot chloroform solutions of the polymers. A silver rod was employed as counter electrode and a silver chloride coated silver rod (Ag/AgCl) was used as a quasi-reference electrode. 0.1 M Tetrabutylammonium hexafluorophosphate in acetonitrile was used as electrolyte. The measurements were carried out under inert atmosphere with an AutoLab PGSTAT 12 potentiostat at a scan speed of 0.125 V/s, a modulation amplitude of 20 mV, and at a frequency of 25 Hz. Fc/Fc+ was employed as a standard with $E = -4.8$ eV.

Photovoltaic devices with an active area of 0.09 and 0.16 cm² were fabricated in air on patterned indium tin oxide (ITO) glass substrates (Naranjo Substrates). The substrates were cleaned by sonication in acetone for 15 min., followed by scrubbing with a sodium dodecyl sulfate solution (99%, Acros), rinsing with deionized water, and a final sonication step in 2-propanol. Before deposition of the device layers the substrates underwent a 30 min. UV-ozone treatment. Clevios PEDOT:PSS Al 4083, purchased from Heraeus, was deposited by spin coating at 3000 rpm. In the case of PDPPPyTPy and PDPP(PyTPy-*alt*-3T) the PEDOT:PSS layer was substituted by a 10 nm layer of MoO_3, deposited via thermal evaporation. The active layers were deposited from solutions in chloroform with *o*-DCB as a co-solvent, using the polymer and [70]PCBM in a 1:2 weight ratio, except in the case of PDPPTTTT where a 1:3 weight ratio was used. In the case of PDPPTEDOTT, 4 mg/mL polymer in a 10 vol% *o*-DCB in chloroform solution was used. In the case of PDPP(TEDOTT-*alt*-3T), 3 mg/mL polymer in 5 vol% of *o*-DCB in chloroform was used. For PDPP(TPT-*alt*-TTTT) 5 mg/mL in 10 vol% *o*-DCB was used, and for PDPP(TPT-*alt*-4T) 4 mg/mL in 15 vol% of *o*-DCB in chloroform was employed. The solutions were heated to 90 °C for 1 h to ensure that the polymers were completely dissolved, then kept at 60 °C and were finally cooled to room temperature under vigorous stirring during 2 minutes before spin coating. LiF (1 nm) and Al (100 nm) were deposited by thermal evaporation under high vacuum (~3×10^{-7} mbar) as a back contact.

Current density – voltage ($J-V$) characteristics were measured with a Keithley 2400 source meter under ~100 mW/cm^2 white light illumination from a tungsten-halogen lamp filtered by a Schott GG385 UV filter and a Hoya LB120 daylight filter. The short-circuit current density (J_{sc}) was separately and more accurately determined from external quantum efficiency (EQE) measurements by integration of the EQE with the AM 1.5G solar spectrum. EQE measurements were carried out under 1 sun operating conditions in a setup consisting of a modulated monochromatic light, a preamplifier (Stanford Research Systems SR570) and a lock-in amplifier (Stanford Research Systems SR830). The modulated monochromatic light was generated by using an optical chopper from Stanford Research Systems (SR540), an Oriel Cornerstone 130 monochromator and a 50 W (Osram 64610) tungsten-halogen lamp. The 1 sun conditions were provided by the use of a 730 nm LED (Thorlabs) at different intensities for appropriate bias illumination. The device was kept in a nitrogen-filled box with a quartz window. A calibrated silicon cell was used as reference prior to the $J-V$ and EQE measurements.

6.4.2 Synthesis

The synthetic route to the extended monomer (**4**) is shown in Scheme 6.3.

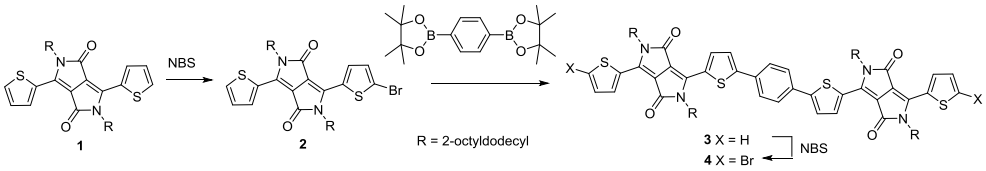

Scheme 6.3: Synthesis of 6,6'-(1,4-phenylenebis(thiophene-5,2-diyl))bis(3-(5-bromothiophen-2-yl)-2,5-bis(2-octyldodecyl)-pyrrolo[3,4-*c*]pyrrole-1,4-dione) (**4**)

3-(5-Bromothiophen-2-yl)-2,5-bis(2-octyldodecyl)-6-(thiophen-2-yl)-pyrrolo[3,4-*c*]pyrrole-1,4-dione (2)

2,5-Bis(2-octyldodecyl)-3,6-di(thiophen-2-yl)-2,5-pyrrolo[3,4-*c*]pyrrole-1,4-dione[79] (**1**) (2.5 g, 2.90 mmol) was dissolved in chloroform (60 mL), cooled to −20 °C and kept in the dark. *N*-bromosuccinimide (358 mg, 2.03 mmol, 0.7 eq.) was then added in portions over the course of 10 min. The mixture was allowed to warm to room temperature and left to react overnight. The mixture was washed twice with water and once with brine, the organic layer was dried over $MgSO_4$ and the solvent was removed under reduced pressure. The residue was purified using column chromatography (8:2 heptanes:dichloromethane, 0.1 vol% ethanol), followed by a final precipitation step from toluene in methanol to obtain **2** (1.28 g, 1.36 mmol, 47%). ^{1}H NMR (200 MHz, Chloroform-d) δ = 8.89 (dd, *J* = 3.9, 1.2 Hz, 1H), 8.61 (d, *J* = 4.2 Hz, 1H), 7.64 (dd, *J* = 5.1, 1.2 Hz, 1H), 7.27 (dd, *J* = 5.2, 3.8 Hz, 1H), 7.22 (d, *J* = 4.2 Hz, 1H), 4.01 (d, *J* = 7.7 Hz, 2H), 3.93 (d, *J* = 7.7 Hz, 2H), 1.89 (m, 4H), 1.40-1.10 (br, 64H), 0.94-0.80 (br, 12H). MS MALDI-TOF, *m*/*z*: [M^+] calc: 938.54, found: 938.54.

6,6'-(1,4-Phenylenebis(thiophene-5,2-diyl))bis(2,5-bis(2-octyldodecyl)-3-(thiophen-2-yl)-pyrrolo[3,4-*c*]pyrrole-1,4-dione) (3)

3-(5-Bromothiophen-2-yl)-2,5-bis(2-octyldodecyl)-6-(thiophen-2-yl)-pyrrolo[3,4-*c*]pyrrole-1,4-dione (**2**) (700 mg, 0.74 mmol, 2.05 eq), 1,4-bis(4,4,5,5-tetramethyl-1,3,2-dioxaborolan-2-yl)benzene (120 mg, 0.36 mmol, 1 eq), tris(dibenzylideneacetone)dipalladium(0) (4.99 mg, 5.45 µmol, 1.5%) and triphenylphosphine (5.72 mg, 21.8 µmol, 6%) were loaded into a Schlenk flask and put under argon. Toluene (25 mL) was added and the mixture was degassed with argon for 10 min., before a degassed 2 M solution of K_3PO_4 in water (0.91 mL, 5 eq) was added together with one drop of Aliquat 336. The mixture was sealed and heated to 115 °C for 6 h. After cooling, the mixture was

first partially reduced in volume and then precipitated in methanol. The filtrate was washed with water (3×) and methanol (3×) before being re-dissolved in dichloromethane, filtered and reduced in volume. The residue was recrystallized twice from acetone containing 2 vol% toluene, filtered over a silica plug with dichloromethane and finally precipitated in methanol. Compound **3** was obtained as a blue solid (603 mg, 92%). ^{1}H NMR (400 MHz, Chloroform-d) δ = 8.95 (d, J = 4.1 Hz, 2H), 8.89 (dd, J = 3.7, 1.0 Hz, 2H), 7.72 (s, 4H), 7.63 (dd, J = 4.9, 1.0 Hz, 2H), 7.52 (d, J = 4.2 Hz, 2H), 7.27 (dd, J = 4.9, 4.0 Hz, 2H), 4.07 (d, J = 7.7 Hz, 4H), 4.04 (d, J = 7.8 Hz, 4H) 1.99 (m, 2H), 1.92 (m, 2H), 1.40-1.15 (br, 128H), 0.89-0.82 (br, 24H). ^{13}C NMR (100 MHz, Chloroform-d) δ = 161.77, 161.68, 148.48, 140.25, 139.95, 136.78, 135.26, 133.41, 130.51, 129.88, 129.26, 128.42, 126.62, 124.78, 108.34, 108.15, 46.30, 37.92, 37.76, 31.93, 31.90, 31.32, 31.21, 30.07, 30.03, 29.67, 29.58, 29.51, 29.37, 29.31, 26.36, 26.23, 22.70, 22.68, 14.13. (Note: some peaks in the ^{13}C NMR spectrum overlap). MS (MALDI-TOF, m/z): [M^{+}] calc: 1795.27, found: 1795.27.

6,6'-(1,4-Phenylenebis(thiophene-5,2-diyl))bis(3-(5-bromothiophen-2-yl)-2,5-bis(2-octyldodecyl)-pyrrolo[3,4-*c*]pyrrole-1,4-dione) (4)

6,6'-(1,4-Phenylenebis(thiophene-5,2-diyl))bis(2,5-bis(2-octyldodecyl)-3-(thiophen-2-yl)-pyrrolo[3,4-*c*]pyrrole-1,4-dione) (**3**) (300 mg, 0.17 mmol, 1 eq) was dissolved in chloroform (7 mL), degassed with argon for 10 min., cooled to 0 °C and kept in the dark. *N*-bromosuccinimide (61.7 mg, 0.35 mmol, 2.1 eq) was added in portions over 10 min., after which the mixture was allowed to warm to room temperature. After 4 h this mixture was precipitated in methanol. The residue was then purified by column chromatography (5:5 heptanes:dichloromethane), followed by three recrystallizations from acetone containing 2 vol% of toluene. Compound **4** was obtained as blue product (233 mg, 71%). ^{1}H NMR (400 MHz, Chloroform-d) δ 8.93 (d, J = 4.0 Hz, 2H), 8.62 (d, J = 4.1 Hz, 2H), 7.69 (s, 4H), 7.49 (d, J = 4.2 Hz, 2H), 7.20 (d, J = 4.4 Hz, 2H), 4.05 (d, J = 7.7 Hz, 4H), 3.95 (d, J = 7.7 Hz, 4H), 1.96 (m, 2H), 1.89 (m, 2H), 1.38-1.16 (br, 128H), 0.89-0.81 (br, 24H). ^{13}C NMR (100 MHz, Chloroform-d) δ 161.58, 161.34, 148.72, 140.25, 138.69, 137.85, 135.09, 133.33, 131.28, 129.17, 126.54, 124.77, 118.63, 108.29, 108.13, 46.29, 37.87, 37.76, 31.91, 31.19, 30.04, 29.65, 29.56, 29.36, 29.29, 26.33, 26.20, 22.68, 14.11. (Note: some peaks in the ^{13}C NMR spectrum overlap). MS (MALDI-TOF, m/z): [M^{+}] calc: 1951.09, found: 1951.12.

PDPP(TPT-*alt*-4T)

6,6'-(1,4-Phenylenebis(thiophene-5,2-diyl))bis(3-(5-bromothiophen-2-yl)-2,5-bis(2-octyldodecyl)-pyrrolo[3,4-*c*]pyrrole-1,4-dione) (70 mg, 35.8 µmol), 5,5'-bis(trimethylstannyl)-2,2'-bithiophene (17.6 mg, 35.8 µmol), tris(dibenzylideneacetone)dipalladium(0) (0.49 mg, 0.54 µmol), and triphenylphosphine (0.56 mg, 2.1 µmol) were placed in a dry Schlenk flask and put under argon. Dry toluene (1.35 mL) and dry *N*,*N*-dimethylformamide (0.15 mL) were added and the mixture was degassed with argon before the mixture was sealed and heated to 115 °C. After leaving the mixture to react overnight, the products were dissolved in 1,1,2,2-tetrachloroethane (TCE) and precipitated in methanol. The solids were then dissolved in TCE (70 mL) and heated to 110 °C for 1 h together with ethylenediaminetetraacetic acid (200 mg), after which water (100 mL) was added and the mixture was vigorously stirred and heated for another hour. The organic layer was then separated and washed with water before being partially reduced in volume and precipitated in methanol. The solids were then subjected to Soxhlet extraction with acetone (2-3 h), hexanes (overnight), dichloromethane (2-3 h) and chloroform (1 h). The contents of the Soxhlet thimble were then dissolved in TCE at 110 °C, filtered and precipitated in acetone to yield PDPP(TPT-*alt*-4T) (53.6 mg, 76%).

PDPP(TPT-*alt*-TTTT)

6,6'-(1,4-phenylenebis(thiophene-5,2-diyl))bis(3-(5-bromothiophen-2-yl)-2,5-bis(2-hexyldecyl)-pyrrolo[3,4-*c*]pyrrole-1,4-dione) (70 mg, 40.5 µmol), freshly recrystallized 2,5-bis(trimethylstannyl)thieno[3,2-*b*]thiophene (16.6 mg, 40.5 µmol) and triphenylphosphine (0.74 mg, 0.81 µmol) were placed in a dry Schlenk flask under argon. A mixture of dry toluene and dry DMF (5:1, 8 mL) was added and the resulting solution was degassed with argon. Tris(dibenzylideneacetone)dipalladium (0.86 mg, 3.2 µmol) was subsequently added and the mixture was heated to 115 °C. After reaction overnight, the crude product was dissolved in hot chloroform (50 mL) and precipitated in methanol. The residue was again dissolved in hot chloroform and ethylenediaminetetraacetic acid (300 mg) was added to this solution and heated to 80 °C during 1 h. Water was added, and the mixture was stirred another hour at 80 °C, after which the organic layer was separated, and washed with water. The polymer was then precipitated in methanol, and filtered in a Soxhlet thimble. Soxhlet extraction using acetone, hexane, dichloromethane and chloroform was performed. PDPP(TPT-*alt*-TTTT) was recovered as a blue solid after precipitation of the chloroform fraction in methanol (57 mg, 85%).

The synthetic route to the extended monomer **7** is shown in Scheme 6.4.

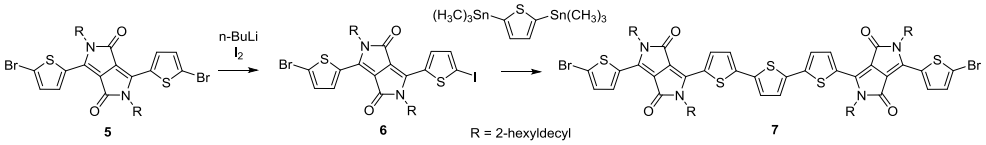

Scheme 6.4: Synthesis of 6,6'-([2,2':5',2"-terthiophene]-5,5'-diyl)bis(3-(5-bromothiophen-2-yl)-2,5-bis(2-hexyldecyl)-pyrrolo[3,4-*c*]pyrrole-1,4-dione) (**7**)

3-(5-Bromothiophen-2-yl)-2,5-bis(2-hexyldecyl)-6-(5-iodothiophen-2-yl)-pyrrolo[3,4-*c*]pyrrole-1,4-dione (6)

In a dry Schlenk flask, 3,6-bis(5-bromothiophen-2-yl)-2,5-bis(2-hexyldecyl)-pyrrolo[3,4-*c*]pyrrole-1,4-dione (**5**)[79] (0.6 g, 0.66 mmol) was dissolved in anhydrous THF (10 mL). The reaction was put at −78 °C and 2.5 M *n*-butyllithium (0.276 mL, 0.69 mmol) was added dropwise. The reaction was left to react at −78 °C for an hour before the addition of a solution of iodine (0.335 mg, 1.32 mmol) in THF. The reaction was put at room temperature and left to react overnight, before the mixture was extracted with chloroform / 1M potassium carbonate in water, followed by washing three times with water. The organic phases were then dried with $MgSO_4$, reconcentrated and purified by silica gel column chromatography with 80/20 heptane/dichloromethane to get a red powder (357 mg, 57%). ^{1}H NMR (400 MHz, $CDCl_3$) δ 8.62 (d, J = 4.0 Hz, 1H), 8.51 (d, J = 4.0 Hz, 1 H), 7.40 (d, J = 4.0 Hz, 1H), 7.22 (d, J = 4.0 Hz, 1H), 3.93 (d, J = 4.0 Hz, 2H), 3.91 (d, J = 4.0 Hz, 2H), 1.87 (br, 2H), 1.27 (br, 48H), 0.86 (br, Hz, 12H). ^{13}C NMR (100 MHz, $CDCl_3$) δ 161.38, 161.36, 139.49, 139.01, 138.30, 136.12, 135.67, 135.29, 131.39, 131.15, 118.92, 107.99, 107.84, 81.14, 46.32, 37.74, 29.96, 29.63, 29.28, 29.27, 22.61, 14.11, 14.08, 14.07. MALDI-TOF, *m*/*z*: [M^+] calc: 954.01, found: 954.33.

6,6'-([2,2':5',2"-Terthiophene]-5,5'-diyl)bis(3-(5-bromothiophen-2-yl)-2,5-bis(2-hexyldecyl)-pyrrolo[3,4-*c*]pyrrole-1,4-dione) (7)

Recrystallized 3-(5-bromothiophen-2-yl)-2,5-bis(2-hexyldecyl)-6-(5-iodothiophen-2-yl)-pyrrolo[3,4-*c*]pyrrole-1,4-dione (**6**) (200 mg, 0.200 mmol), 2,5-bis(trimethylstannyl)thiophene (42.2 mg, 0.103 mmol), tris(dibenzylideneacetone)dipalladium(0) (5.49 mg, 0.006 mmol), and triphenylphosphine (16.7 mg, 0.0251 mmol) were charged in a dry Schlenk flask and put under argon atmosphere. Anhydrous toluene (5 mL) and anhydrous *N*,*N*-dimethylformamide (0.5 mL) was then added and the solution was degassed with argon for 15 min. The reaction mixture was then slowly heated to 100 °C and left to react overnight. The mixture was then precipitated in methanol and filtered. The solids were purified by silica gel column chromatography using heptane and chloroform (50/50) as an eluent, followed by recrystallization from acetone to yield blue crystals (105 mg, 57%).

^{1}H NMR (500 MHz, 1,1,2,2-tetrachloroethane-d_2) δ 8.89 (d, J = 2.9 Hz, 2H), 8.56 (d, J = 3.4 Hz, 2H), 7.35 (d, J = 2.9 Hz, 2H), 7.31 (s, 2H), 7.24 (d, J = 3.4 Hz, 2H), 3.97 (m, 8H), 1.93 (br, s, 4H), 1.62 (s, 12 H), 1.23 (br, s, 106 H), 0.86 (br, s, 24H). ^{13}C NMR (125 MHz, 1,1,2,2-tetrachloroethane-d_2) δ 161.36, 161.12, 141.81, 139.75, 138.43, 136.71, 136.50, 134.77, 131.31, 131.10, 128.40, 126.25, 125.10, 123.40, 118.72, 108.20, 46.09, 37.71, 31.77, 31.66, 29.86, 29.57, 29.52, 29.39, 29.22, 22.60, 14.11. MALDI-TOF, m/z: [M^+] calc: 1734.80, found: 1734.81.

2,5-Bis(trimethylstannyl)-3,4-ethylenedioxythiophene (8)

In a dry Schlenk flask, 3,4-ethylenedioxythiophene (1.0 g, 7.03 mmol) was dissolved in dry THF (5 mL). The solution was put at −78 °C and 2.5 M *n*-butyllithium (7 mL, 17.58 mmol) was added dropwise. The solution was left to react for 1 h at room temperature to get a white liquid. Then, it was put back at −78 °C and a solution of trimethyltin chloride (3.5 g, 17.58 mmol) in dry THF (4.5 mL) was added dropwise. The reaction was then left overnight at room temperature under a blanket of argon. An extraction with water/chloroform (3×) was performed after the solvents were removed under reduced pressure. The solution was dried with $MgSO_4$ and chloroform was evaporated. The final product was obtained as white crystals upon recrystallization from acetonitrile (672 mg, 20%). ^{1}H NMR (400 MHz, $CDCl_3$) δ 4.16 (s, 4H), 0.35 (s, 18H). ^{13}C NMR (100 MHz, $CDCl_3$) δ 148.53, 115.87, 64.71, −8.64. MALDI-TOF, m/z: [M-CH_3^+] calc: 454.92, found: 454.95.

PDPP(TEDOTT-*alt*-3T)

In a dry Schlenk flask were placed recrystallized 6,6'-([2,2':5',2"-terthiophene]-5,5'-diyl)bis(3-(5-bromothiophen-2-yl)-2,5-bis(2-hexyldecyl)-pyrrolo[3,4-*c*]pyrrole-1,4-dione) (**7**) (40 mg, 0.023 mmol), 2,5-bis(trimethylstannyl)-3,4-ethylenedioxythiophene (**8**) (10.75 mg, 0.023 mmol), tris(dibenzylideneacetone)dipalladium(0) (1.26 mg, 0.0014 mmol), and triphenylphosphine (1.447 mg, 0.0055 mmol). The solids were put under argon before anhydrous toluene (1 mL) and *N*,*N*-dimethylformamide (0.1 mL) were added. The solution was degassed with argon for 15 min. before being heated at 115 °C overnight. The resulting green gel was dissolved in 1,1,2,2-tetrachloroethane (TCE) at 140 °C, precipitated into methanol and filtered. The powder was furthermore dissolved in TCE at 150 °C for 2 h. After 1 h, ethylenediaminetetraacetic acid (100 mg) was added into the solution. After cooling to 115 °C, water was added and the mixture was stirred for 30 min. The organic phase was then washed three times with water, reconcentrated, precipitated into methanol and filtered into a Soxhlet thimble. The polymer was purified by consecutive Soxhlet extractions in acetone (3 hours), hexanes (16 hours) and dichloromethane (3 hours). The resulting polymer was dissolved in TCE at 140 °C, precipitated in acetone and filtered to give a green film (30 mg, 76 %).

The synthetic route to **PDPPTEDOTT** is shown in Scheme 6.5.

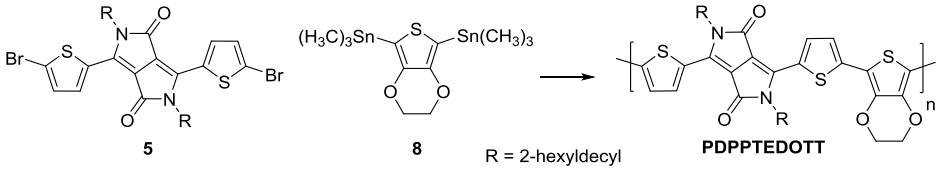

Scheme 6.5: Synthesis of PDPPTEDOTT.

PDPPTEDOTT

In a dry Schlenk flask, freshly recrystallized 3,6-bis(5-bromothiophen-2-yl)-2,5-bis(2-hexyldecyl)-pyrrolo[3,4-*c*]pyrrole-1,4-dione[79] (70 mg, 0.077 mmol), 2,5-bis(trimethylstannyl)-3,4-ethylenedioxythiophene (**8**) (35.9 mg, 0.077 mmol), tris(dibenzylideneacetone)dipalladium(0) (2.11 mg, 0.00231 mmol,) and triphenylphosphine (2.42 mg, 0.00924 mmol) were charged. The solids were put under argon before dry toluene (2 mL) and dry *N*,*N*-dimethylformamide (0.2 mL) were added in the flask. The solution was then degassed with argon for 15 min. before being heated at 115 °C overnight. The obtained green gel was dissolved in a minimal amount of 1,1,2,2-tetrachloroethane (TCE) at 140 °C before being precipitated in methanol and filtered. The resulting powder was then redissolved in TCE and heated at 160 °C for 2 h. After 1 h, ethylenediaminetetraacetic acid (200 mg) was added to remove the palladium residue. The solution was then cooled down at 115 °C and water was added and stirred for 30 min. The solution was cooled down and washed three times with water before the volume was reduced and precipitated in methanol and filtered into a Soxhlet thimble. The obtained polymer was purified by Soxhlet extraction with first acetone for 3 hours, hexanes overnight and dichloromethane for 3 hours. The undissolved residue was then solubilized in TCE at 140 °C, filtered and precipitated in acetone to obtain a green film (53 mg, 77%).

6.5 References

1 J. Roncali, *Chem. Rev.*, 1997, **97**, 1173-1206

2 W. Zhang, J. Smith., S. E. Watkins, R. Gysel, M. McGehee, A. Salleo, J. Kirkpatrick, S. Ashraf, T. Anthopoulos, M. Heeney, I. McCulloch, *J. Am. Chem. Soc.*, 2010, **132**, 11437.

3 F. He, W. Wang, W. Chen, T. Xu, S. B. Darling, J. Strzalka, Y. Liu, Yu L., *J. Am. Chem. Soc.*, 2011, **133**, 3284.

4 R. Mondal, H. A. Becerril, E. Verploegen, D. Kim, J. E. Norton, S. Ko, N. Miyaki, S. Lee, M. F. Toney, J.-L. Brédas, M. D. McGehee, Z. Bao, , *J. Mater. Chem.*, 2010, **20**, 5823.

5 J.-L. Brédas, *J. Chem. Phys.* 1985, **82**, 3808.

6 F. Wudl, M. K. Kobayashi, A. J. Heeger, *J. Org. Chem.*, 1984, **49**, 3382

7 E. E. Havinga, W. ten Hoeve, H. Wynberg, *Polym. Bull.*, 1992, **29**, 119.

8 C. Kitamura, S. Tanaka, Y. Yamashita, *Chem. Mater.*, 1996, **8**, 570.

9 K. Kawabata, M. Saito, I. Osaka, K. Takimiya, *J. Am. Chem. Soc.* 2016, **138**, 7725-7732

10 Y.-J. Cheng, S.-H. Yang, C.-S. Hsu, *Chem. Rev.*, 2009, **109**, 5868-5923

11 H. Zhou, L. Yang, W. You, , *Macromolecules*, 2012, **45**, 607-632.

12 L. Dou, Y. Liu, Z. Hong, G. Li, Y. Yang, *Chem. Rev.*, 2015, **115**, 12633-12665

13 J. W. Jung, J. W. Jo, E. H. Jung, W. H. Jo, *Org. Electron.*, 2016, **31**, 149-170.

14 G. Li, W.-H. Chang, Y. Yang, *Nat. Rev, Mater.*, 2017, **2**, 17043.

15 C. Cui, W.-Y. Wong, Y. Li, *Energy Environ. Sci.*, 2014, **7**, 2276.

16 J. Hou, Z. Tan, Y. Yan, Y. He, C. Yang, Y. Li, *J. Am. Chem. Soc.*, 2006, **128**, 4911.

17 L. Huo, S. Zhang, X. Guo, F. Xu, Y. Li, J. Hou, *Angew. Chem. Int. Ed.*, 2011, **50**, 9697.

18 M. Bolognesi, D. Gedefaw, D. Dang, P. Henriksson, W. Zhuang, M. Tessarolo, E. Wang, M. Muccini, M. Seri, M. R. Andersson, *RSC Adv.*, 2013, **3**, 24543.

19 M. Kaltenbrunner, M. S. White, E. D. Glowacki, T. Sekitani, T. Someya, N. S. Sariciftci, S. Bauer, *Nat. Commun.*, 2012, **3**, 1772-1779.

20 R. Ma, J. Feng, D. Yin, H-B. Sun, *Org. Electron.*, 2017, **43**, 77-81.

21 D. Chemisana, A. Moreno, M. Polo, C. Aranda, A. Riverola, E. Ortega, C. Lamnatou, A. Domenech, G. Blanco, A. Cot, *Renewable Energy*, 2019, **137**, 177-188.

22 K-S. Chen, J-F. Salinas, H-L. Yip, L. Huo, J. Hou, A. K-Y. Jen, *Energy Environ. Sci.*, 2012, **5**, 9551-9557.

23 D. Di Carlo Rasi, K. H. Hendriks, M. M. Wienk, R. A. J. Janssen, *Adv. Energy Mater.*, 2017, **7**, 1701664.

24 G. Li, W-H. Chang, Y. Yang, *Nat. Rev. Mater.*, 2017, **2**, 17043.

25 D. Dang, D.Yu, E. Wang, *Adv. Mater.* 2019, **31**, 1807019.

26 M. H. Hoang, G. E. Park, D. L. Phan, T. T. Ngo, T. V. Nguyen, S. H. Park, M. J. Cho, D. H. Choi, *J. Polym. Sci. Part A Polym. Chem.*, 2018, **56**, 1528-1535.

27 F. Tang, K. Wu, K. Duan, Y. Deng, B. Zhao, S. Tan, *Dyes Pigm.*, 2019, **160**, 79-85.

28 J. Ren, Z. Li, Z. Zhang, X. Wang, X. Zeng, Q. Sun, Y. Cui, H. Wang, Y. Hao, *Org. Electron.*, 2018, **62**, 56-64.

29 T. E. Kang, K-H. Kim, B. J. Kim, *J. Mater. Chem. A*, 2014, **2**, 15252-15267.

30 B. Xu, I. Pelse, S. Agarkar, S. Ito, J. Zhang, X. Yi, Y. Chujo, S. Marder, F. So, J. R. Reynolds, *ACS Appl. Mater. Interfaces*, 2018, **10**, 44583-44588.

31 H. J. Cho, Y. J. Kim, S. Chen, J. Lee, T. J. Shin, C. E. Park, C. Yang, *Nano Energy*, 2017, **39**, 229-237.

32 M. H. Hoang, G. E. Park, S. Choi, C. G. Park, S. H. Park, T. V. Nguyen, S. Kim, K. Kwak, M. J. Cho, D. H. Choi, *J. Mater. Chem. C*, 2019, **7**, 111-118.

33 Z. Genene, J. Wang, X. Xu, R. Yang, W. Mammo, Wang E., *RSC Adv.*, 2017, **7**, 17959-17967.

34 W. Li, K. H. Hendriks, M. M. Wienk, R. A. J. Janssen, *Acc. Chem. Res.*, 2016, **49**, 78-85.

35 R. E. M. Willems, C. H. L. Weijtens, X. de Vries, R. Coehoorn, R. A. J. Janssen, *Adv. Energy Mater*. 2019, **9**, 1803677.

36 K. H. Hendriks, W. Li, G. H. L. Heintges, G. W. P. van Pruissen, M. M. Wienk, R. A. J. Janssen, *J. Am. Chem. Soc.*, 2014, **136**, 11128-11133.

37 K. H. Hendriks, G. H. L. Heintges, V. S. Gevaerts, M. M. Wienk, R. A. J. Janssen, *Angew. Chem. Int. Ed.*, 2013, **52**, 8341-8344.

38 P. Leenaers, H. van Eersel, M. M. Wienk, R. A. J. Janssen, in preparation.

39 W. Li, K. H. Hendriks, A. Furlan, A. Zhang, M. M. Wienk, R. A. J. Janssen, *Chem. Commun.*, 2015, **51**, 4290-4293.

40 C. Wang, C. J. Mueller, E. Gann, A. C. Y. Liu, M. Thelakkat, C. R. McNeill, *J. Mater. Chem. A*, 2016, **4**, 3477-3486.

41 A. P. Zoombelt, S. G. J. Mathijssen, M. G. R. Turbiez, M. M. Wienk, R. A. J. Janssen, *J. Mater. Chem.*, 2010, **20**, 2240-2246.

42 W. Li, K. H. Hendriks, W. S. C. Roelofs, Y. Kim, M. M. Wienk, R. A. J. Janssen, *Adv. Mater.*, 2013, **25**, 3182-3186.

43 K. H. Hendriks, A. S. G. Wijpkema, J. J. van Franeker, M. M. Wienk, R. A. J. Janssen, *J. Am. Chem. Soc.*, 2016, **138**, 10026-10031.

44 W. Li, K. H. Hendriks, A. Furlan, W. S. C. Roelofs, M. M. Wienk, R. A. J. Janssen, *J. Am. Chem. Soc.*, 2013, **138**, 18942-18948.

45 J. J. van Franeker, G. H. L. Heintges, C. Schaefer, G. Portale, W. Li, M. M. Wienk, P. van der Schoot, R. A. J. Janssen, *J. Am. Chem. Soc.*, 2015, **137**, 11783−11794

46 M. Li, D. Di Carlo Rasi, F. J. M. Colberts, J. Wang, G. H. L. Heintges, B. Lin, W. Li, W. Ma, M. M. Wienk, R. A. J. Janssen, *Adv. Energy Mater.*, 2018, **8**, 1800550.

47 D. Veldman, S. C. J. Meskers, R. A. J. Janssen, *Adv. Funct. Mater.*, 2009, **19**, 1939-1948.

48 W. Li, K. H. Hendriks, A. Furlan, M. M. Wienk, R. A. J. Janssen, *J. Am. Chem. Soc.* 2015, **137**, 2231−2234.

49 K. Vandewal, K. Tvingstedt, A. Gadisa, O. Inganäs, J. V. Manca, *Nat. Mater.*, 2009, **8**, 904-909.

50 J. H. Lee, G. E. Park, S. Choi, D. H. Lee, H. A. Um, J. Shin, M. J. Cho, D. H. Choi, *Polymer*, 2016, **94**, 43-52.

51 S. J. Ha, K. H. Kim, D. H. Choi, *J. Am. Chem. Soc.*, 2011, **133**, 10364-10367.

52 H-W. Lin, W-Y. Lee, W-C. Chen, *J. Mater. Chem.*, 2012, **22**, 2120-2128.

53 A. Kim, J. H. Lee, H. J. Kim, S. Choi, Y. U. Kim, C. G. Park, C. H. Jeong, M. J. Cho, D. H. Choi, *Synth. Metals*, 2018, **236**, 36-43.

54 S. B. Kim, H. A. Um, H. J. Kim, M. J. Cho, D. H. Choi, *Org. Electron.*, 2016, **31**, 198-206.

55 W. Li, A. Furlan, W. S. C. Roelofs, K. H. Hendriks, G. W. P. van Pruissen, M. M. Wienk, R. A. J. Janssen, *Chem. Commun.*, 2014, **50**, 679-681.

56 A. K. Kim, D. H. Lee, H. A. Um, J. Shin, M. J. Cho, D. H. Choi, *Polym. Chem.*, 2015, **6**, 5478-5486.

57 G. E. Park, H. J. Kim, D. H. Lee, M. J. Cho, D. H. Choi, *Polym. Chem.*, 2016, **7**, 5069-5078.

58 Z. Chen, J. Yang, F. Wu, L. Chen, C. Yiwang, *Chem. Res. Chin. Univ.*, 2017, **33**, 305-311.

59 W. Li, T. Michinobu, *J. Photopolym. Sci. Tech.*, 2017, **30**, 495-499.

60 Y. Zou, D. Gendron, R. Badrou-Aïch, A. Najari, Y. Tao, M. Leclerc, *Macromolecules*, 2009, **42**, 2891-2894.

61 Y. Wang, F. Yang, Y. Liu, R. Peng, S. Chen, Z. Ge, *Macromolecules*, 2013, **46**, 1368-1375.

62 C. Li, Y. Li, X. Wang, B. Zhang, Y. Chen, *J. Polym. Res.*, 2015, **22**, 96-103.

63 C-T. Gu, Y-W. Zhu, Y-W. Miao, M. Qiu, H-L. Cong, B. Yu, *Ferroelectrics*, 2018, **530**, 112-115.

64 Z. Li, S-W. Tsang, X. Du, L. Scoles, G. Robertson, Y. Zhang, F. Toll, Y. Toa, J. Lu, J. Ding, *Adv. Funct. Mater.*, 2011, **21**, 3331-3336.

65 Y. Li, J. Zou, H-L. Yip, C-Z. Li, Y. Zhang, C-C. Chueh, J. Intemann, Y. Xu, P-W. Liang, Y. Chen, A. K-Y. Jen, *Macromolecules*, 2013, **46**, 5497-5503.

66 S-W. Chang, T. Muto, T. Kondo, M-J. Kiao, M. Horie, *Polym. J.*, 2017, **49**, 113-122.

67 S. Albrecht, S. Janietz, W. Schindler, J. Frisch, J. Kurpiers, J. Kniepert, S. Inal, P. Pingel, K. Fortiropoulos, N. Koch, D. Neher, *J. Am. Chem. Soc.*, 2012, **134**, 14932-14944.

68 H. J. Kim, G. E. Park, D. H. Lee, M. J. Cho, D. H. Choi, *Org. Electron.*, 2016, **38**, 256-263.

69 R. Stalder, J. Mei, K. R. Graham, L. A. Estrada, J. R. Reynolds, *Chem. Mater.*, 2014, **26**, 664-678.

70 M. S. Chen, J. R. Niskala, D. A. Unruh, C. K. Chu, O. P. Lee, J. M. J. Fréchet, *Chem. Mater.*, 2013, **25**, 4088-4096.

71 Z. Li, G. Gan, C. Liu, J. Ren, H. Wang, Y. Hao, J. Yu, *Synth. Metals*, 2019, **247**, 46-52.

72 G. P. Kini, S. Oh, Z. Abbas, S. Rasool, M. Jahandar, C. E. Song, S. K. Lee, W. S. Shin, W-W. So, J-C. Lee, *ACS Appl. Mater. Interfaces*, 2017, **9**, 12617-12628.

73 Z. B. Lim, B. Xue, S. Bomma, H. Li, S. Sun, Y. M. Lam, W. J. Belcher, P. C. Dastoor, A. C. Grimsdale, *J. Polym. Sci. Part A Polym. Chem.*, 2011, **49**, 4387-4397.

74 Z. Deng, F. Wu, L. Chen, Y. Chen, *RSC Adv.*, 2015, **5**, 12087-12093.

75 H. Heo, H. Kim, D. Lee, S. Jang, L. Ban, B. Lim, J. Lee, Y. Lee, *Macromolecules*, 2016, **49**, 3328-3335.

76 L. Chen, S. Cai, X. Wang, Y. Chen, *Chin. J. Chem.*, 2013, **31**, 1455-1462.

77 H. Kim, H. Lee, D. Seo, Y. Jeong, K. Cho, J. Lee, Y. Lee, *Chem. Mater.*, 2015, **27**, 3102-3107.

78 Q. Zhang, M. A. Kelly, A. Hunt, H. Ade, W. You, *Macromolecules*, 2016, **49**, 2533-2540.

79 L. Bürgi, M. Turbiez, R. Pfeiffer, F. Bienewald, H. J. Kirner, C. Winnewisser, *Adv. Mater.*, 2008, **20**, 2217-2224.

Outlook

The research presented in this thesis has focussed on the influence of structural defects in DPP polymers, the factors that influence the morphology of blends of these materials and the terpolymer design motif.

In the second chapter the presence and influence of structural defects in DPP polymers was investigated. It was found that the trialkylstannyl-based homocoupling does not frequently occur and that it has a negligible impact on the photovoltaic properties of the polymer. The finding that this homocoupling is influenced by the presence of air can be of importance for other researchers who aim to avoid these defects and for production of such polymers on a larger scale. The conclusion that trialkylstannyl-based homocoupling does not influence the photovoltaic properties is, however, intrinsically linked to the polymer structure that was investigated. As indicated in the chapter, this type of defect can have an influence for other structures. It is therefore important to consider the possible defects for each polymerisation reaction and how much of an influence such defects are expected to have.

In the third, fourth and fifth chapter the morphology of the active layer was influenced via structural modification of the polymer. Through this work we have gained a further understanding of the factors that influence morphology. In chapter 3, it was shown that branching can dramatically lower the solubility of the polymer. A better morphology could be achieved with a polymer with both lower molecular weight and lower solubility, indicating that solubility is an important parameter that governs the morphology formation. In chapter 4, the molecular weight difference between the polymers was larger, and polymers with an intrinsic lower solubility showed lower molecular weights. This led to less dramatic differences in J_{sc} and morphology between the polymers. In chapter 5, a series of polymers was synthesized wherein the materials with the lowest intrinsic solubility had the lowest molecular weight, and showed the worst morphology. This points to the notion that the molecular weight of the polymers can have a larger influence on the morphology formation than the intrinsic solubility. These insights can be valuable for researchers developing materials in the future.

While all solar cells in this thesis were made with fullerene acceptors, recent breakthroughs in non-fullerene acceptors have pushed efficiencies higher than before, and efficiencies of 20% seem to be in reach within the next years. This is partially due to the lower offsets between energy levels that are necessary for charge transfer in these material blends, allowing for higher V_{oc}s, and partially due to the high J_{sc}s achieved in these systems. In this regard, combining DPP polymers with non-fullerene acceptors can form an interesting line of research. Morphology formation in non-fullerene cells remains just as crucial as in fullerene-based cells, and it is likely that the mechanisms behind the morphology formation are similar to an extent in both types of cells. The work presented in this thesis can therefore inform further research into the morphology of non-fullerene cells combined with DPP polymers. Initial studies have shown that efficiencies above 9% are possible in these systems, but that many material combinations fall short of this benchmark. It is not fully understood why this is. Research into the causes is hampered by the difficulty of easy morphology characterisation, such as TEM analysis, because of the lack of contrast between conjugated polymers and most non-fullerene acceptors. A balance between the solubility of the DPP polymer and non-fullerene acceptor seems to be the crucial point to obtain a good morphology. If such a balance can be found, it can be expected that DPP polymers will continue to play a role in the development of the field, as a fine control over the energy levels can already be achieved.

In chapter 6, the terpolymer design motif was explored as a way to the control energy levels of the materials. It was found that the optoelectronic properties of the terpolymers could be predicted based on those of the related copolymers, thus enabling the synthesis of materials with specific properties on demand. No negative effects like the formation of trap states were found, making this a promising design tool. As the requirement for precisely engineered materials with specific optical and electronic properties remains present, both in the field of organic photovoltaics as in the larger field of organic electronics, the work done on the terpolymer design motif can help to design new materials for a variety of applications. More data on the optoelectronic properties of terpolymers can furthermore test the hypothesis that these properties can be predicted based on the properties of the copolymers.

Now that organic photovoltaics are approaching of a PCE of 20%, commercialisation of the technology becomes more and more attractive. The best possible

avenue toward real-world applications seems to be in building integration and semi-transparent cells, as no other current technology can be implemented with the same ease and aesthetics as OPV. For large scale energy production in solar parks, crystalline silicon seems to remain the best option for the foreseeable future, while for other niche applications where lightweight cells are necessary, perovskites form an attractive option. To achieve a larger dissemination of OPV technology in the solar market, large scale production and stability of solar cell modules should be developed further, and large scale printing of modules should become reliable and easy. Although relatively low amounts of active layer materials are used and availability of these materials is not a fundamental problem, the present high costs of the state of the art materials (> € 1000 g^{-1}) form an obstacle in developing a large-area technology. Batch-to-batch variations in polymers can also be an issue when producing these materials on a large scale, and further research into how these variations can be reduced is therefore needed. In this regard, flow chemistry can be a possible avenue to further explore.

As the implementation of green energy continues and sustainability becomes ever more important in the public consciousness, it is likely that there will be more opportunities towards commercialisation of OPV technology and that OPV will be contributing to energy production.

References

X. Song, N. Gasparini, M. M. Nahid, S. H. K. Paleti, C. Li, W. Li, H. Ade, D. Baran, *Adv. Funct. Mater.*, 2019, **29**, 1902441.

X. Jiang, Y. Xu, X. Wang, Y. Wu, G. Feng, C. Li, W. Ma, W. Li, *Phys. Chem. Chem. Phys.*, 2017, **19**, 8069-8075.

Summary

Influencing the photovoltaic properties and aggregation of diketopyrrolopyrrole based polymers via structural modification

Organic photovoltaics provide a promising addition to green energy technologies and have therefore been extensively investigated over the last years. These solar cells can be fabricated from a multitude of organic molecules and polymers, thus providing control over the colour and aesthetics on the one hand, and the photovoltaic properties on the other. The active layer of the cells generally consists of an electron donating and an electron accepting molecule or polymer. As the offset in the energy levels between these two materials provides the driving force for charge separation, careful tuning of these energy levels can directly impact the photovoltaic characteristics of the cell. Also the degree of mixing of these materials (the morphology of the active layer) can severely impact the efficiency of the cells. Control over the morphology via structural modification of the molecules and via the processing of these materials is therefore important.

Diketopyrrolopyrrole (DPP) is a widely used building block for electron donating polymers and small molecules, usually used in combination with [60]PCBM or [70]PCBM as an acceptor. Its high absorption coefficient and good stability make it a good candidate for new materials, while its strong aggregation properties usually lead to favourable morphologies. By using structural modification of DPP-based polymers, we aim to further the understanding of both energy level and morphology control in these materials.

One problem that has been identified in DPP polymers in the past is the presence of homocoupling defects due to undesirable couplings between bromide substituted monomers during the polymerisation reaction. This type of homocoupling leads in the case of DPP materials to a decreased bandgap, a decreased open circuit voltage (V_{oc}), and in some cases to a loss of short circuit current (J_{sc}). The influence of the homocoupling between trialkylstannyl monomers in these materials is, however, less well known. In order to investigate the influence of this defect, two DPP polymers (PDPP3T and PDPP4T) were modified with deliberately introduced homocoupling defects. In both cases it was found

that the optoelectronic properties are not significantly influenced by this type of homocoupling and no effect on the active layer morphology was observed. To test the occurrence of this type of defect during a typical polymerisation reaction, representative test reactions on small molecules were conducted. It was found that under typical polymerisation conditions this defect does not occur, but that the presence of air can lead to homocoupling. These results indicate that, in the case of DPP polymers, this defect can be ignored when assessing the photovoltaic performance of these materials and that it does not occur under normal polymerisation conditions.

Factors that influence the morphology of the active layer in DPP based solar cells have been found in the past to include the tendency of aggregation of the polymer. In order to influence this aggregation behaviour and therefore the morphology, a branched DPP polymer was synthesized, which was easily achieved by mixing a trifunctional monomer in the polymerisation mixture. The presence of even 1% of branching led to a dramatically reduced solubility compared to the linear polymer. This reduced solubility resulted in a more finely dispersed fibrillary network in the active layer, and thus in a large increase of the J_{sc} and efficiency of the cell. To gain more insight in the formation of this morphology, in-situ light scattering experiments were carried out. These experiments indicated a faster nucleation and formation of aggregates in the case of the branched polymer.

Another way to influence the aggregation of DPP polymers is via modification of the solubilising alkyl chains. By placing a linear chain on the DPP core itself and branched chains on the adjacent thiophenes, a strong temperature dependence of the aggregation of the polymers in solution could be obtained. Three polymers with four thiophenes (PDPP4T) between the DPP units, all with different alkyl chains, as well as one polymer with three thiophenes (PDPP3T) were synthesised. While all polymers showed this temperature dependant aggregation behaviour, and this has led for other polymers to increased photovoltaic efficiencies when they were processed from hot solutions, this was not the case for our materials. Processing from hot solutions led to the formation of wider polymer fibres, reducing charge generation. This result is consistent with a nucleation-growth mechanism for polymer fibres, which has been observed for other DPP polymers in the past. The only polymer for which hot processing was advantageous is the case where cold processing is impossible due to a limited solubility at room temperature.

The solubilising side chains can also be modified by introducing other functionalities, such as siloxanes. By varying the amount of siloxane chains and alkyl chains incorporated in the polymer, a series of polymers was obtained. Polymers with increased proportions of siloxane chains showed reduced solubility and a decreased molecular weight. While the hole mobilities in field effect transistors increased with higher siloxane concentrations, the performance in solar cells was greatly reduced. The morphology was investigated by grazing incidence wide angle X-ray scattering (GIWAXS) and by careful analysis of the transition electron microscopy images. An increasing polymer fibre width was found with higher siloxane concentrations, which is consistent with the decrease in J_{sc} observed. This result is unexpected based on the solubility of these polymers, as in the past reduced solubility has been shown to result in smaller fibres. Therefore, this suggests that the influence of molecular weight on the morphology formation is more complex than previously assumed, and can be more important than the overall solubility of the polymer. Another reason for the reduced performance of polymers with high siloxane concentrations is a stronger non-radiative decay of the pristine polymers.

The terpolymer design strategy has been used in the past as a way to control the energy levels and photovoltaic properties of polymers. By analysing the optoelectronic properties of seven regioregular terpolymers synthesised in our group, we established a rule to predict these properties. A direct correlation between the properties of the terpolymers and those of their corresponding copolymers could be found. With good accuracy, the optical band gap as well as the frontier molecular orbital energies of the terpolymers could be predicted by taking the arithmetic average of those of the related copolymers. Also the V_{oc} of solar cells made with these materials was found to follow the same rule. This was further confirmed by analysing 21 previously published terpolymers and their copolymers.

In conclusion, the work described in this thesis has led to a deeper understanding of the factors that influence morphology formation in DPP polymers, such as branching or new side chains. Also further insight in the relation of solubility, aggregation and molecular weight to the morphology has been obtained. Furthermore, understanding of the factors that influence the energy levels, like homocoupling and the terpolymer design strategy, has been refined, resulting in a universal rule to predict the optoelectronic properties of terpolymers.

Samenvatting

Het beïnvloeden van de fotovoltaïsche eigenschappen en aggregatie van diketopyrrolopyrrool gebaseerde polymeren via structurele modificatie

Organische zonnecellen zijn een veelbelovende toevoeging aan de groene energietechnologie en zijn daarom uitgebreid bestudeerd gedurende de voorbije jaren. Deze zonnecellen kunnen gemaakt worden met een grote verscheidenheid aan organische moleculen en polymeren waardoor er controle over de kleur en esthetiek enerzijds, en de fotovoltaïsche eigenschappen anderzijds, mogelijk is. De actieve lagen van de cellen bestaan over het algemeen uit elektron-rijke of donerende en elektron-arme of accepterende moleculen of polymeren. Aangezien het verschil van de energieniveaus tussen de elektron-donerende en -accepterende materialen de drijvende kracht vormt voor ladingsscheiding kan het aanpassen van deze energieniveaus een rechtstreekse invloed hebben op de fotovoltaïsche eigenschappen van de cel. Ook de mate waarin deze materialen gemengd zijn (de morfologie van actieve laag) kan een grote invloed hebben op de efficiëntie van de cel. Controle over de morfologie via modificatie van de chemische structuur van de moleculen en via de modificatie van de depositiecondities van de materialen in de actieve laag is daarom belangrijk.

Diketopyrrolopyrrool (DPP) is een veelgebruikte moleculaire bouwsteen voor elektron-donerende polymeren en kleine moleculen en wordt meestal gebruikt in combinatie met de fullereenderivaten [60]PCBM of [70]PCBM als elektron-acceptor. De hoge absorptiecoëfficiënt en goede stabiliteit van DPP maakt het een goede kandidaat voor nieuwe materialen en zijn sterke aggregatie leidt meestal tot een goede morfologie. Door de structuren van DPP gebaseerde polymeren aan te passen hopen we tot een beter begrip te komen over de factoren die de energieniveaus en morfologie van deze materialen beïnvloeden.

Een probleem dat reeds in het verleden is vastgesteld in DPP polymeren is de aanwezigheid van homokoppelingsdefecten door ongewilde koppelingen tussen broom gesubstitueerde monomeren tijdens de polymerisatiereactie. Dit type van homokoppeling

leidt in het geval van DPP materialen tot een verminderde bandkloof, een verminderde openklemspanning (V_{oc}), en in sommige gevallen tot een verlies van kortsluitstroom (J_{sc}). De invloed van de homokoppeling tussen trialkylstannylmonomeren in deze materialen is echter minder bekend. Om dit defect te onderzoeken hebben we de structuur van twee DPP polymeren (PDPP3T en PDPP4T) aangepast door met opzet deze homokoppelingsdefecten te introduceren. In beide gevallen werd vastgesteld dat de opto-elektronische eigenschappen van de materialen niet significant wordt beïnvloed door dit type homokoppeling en ook werd geen verandering in de morfologie van de actieve laag waargenomen. Om te testen of dit type defect tijdens een typische polymerisatiereactie ontstaat werden representatieve testreacties op kleine moleculen uitgevoerd. We vonden dat onder typische reactiecondities dit defect niet voorkomt, maar dat de aanwezigheid van lucht wel kan leiden tot homokoppeling. De resultaten tonen aan dat in het geval van DPP polymeren deze defecten de fotovoltaïsche eigenschappen van de materialen niet beïnvloeden en dat deze defecten onder normale reactiecondities ook niet of nauwelijks ontstaan.

In het verleden is vastgesteld dat de morfologie van de actieve laag in DPP gebaseerde zonnecellen mede bepaald wordt door de neiging van het polymeer om te aggregeren. Om dit aggregatiegedrag en daarmee de morfologie te beïnvloeden werd een vertakt DPP polymeer gesynthetiseerd. Dit werd eenvoudigweg bereikt door een drievoudig gefunctionaliseerd monomeer toe te voegen aan de polymerisatiereactie. De aanwezigheid van slechts 1% aan vertakkingen was voldoende om de oplosbaarheid van het polymeer ernstig te verminderen. Deze verlaagde oplosbaarheid leidde tot een fijnere vezelachtige morfologie, en hiermee tot een verhoging van de J_{sc} en de efficiëntie van de cel. Om een beter inzicht te krijgen in de vorming van de morfologie werden in-situ lichtverstrooiingsexperimenten uitgevoerd. Deze experimenten suggereerden een snellere nucleatie en vorming van aggregaten voor het vertakte polymeer.

Een andere manier om de aggregatie van DPP polymeren te beïnvloeden is via modificatie van de alkylzijketens die zorgen voor oplosbaarheid. Door een lineaire keten op de DPP bouwsteen zelf, en de vertakte zijketens op de naburige thiofeen-eenheden te plaatsen werd een sterke temperatuursafhankelijkheid van de aggregatie van de opgeloste polymeren verkregen. Drie polymeren met vier thiofenen tussen opeenvolgende DPP eenheden (PDPP4T), allen met verschillende zijketens, en één polymeer met drie thiofenen (PDPP3T) werden gesynthetiseerd. Alle polymeren vertoonden deze

temperatuursafhankelijke aggregatie. In eerder gepubliceerde materialen heeft dit geleid tot betere zonnecelefficiënties wanneer dunne films uit warme oplossingen van de materialen werden aangebracht, maar dit was niet het geval voor onze materialen. Wanneer onze materialen uit warme oplossingen werden afgezet werden bredere vezels gevormd in de morfologie, waardoor de ladingsgeneratie verminderde. Dit is te verklaren met het nucleatie-en-groei model voor polymeervezels dat in het verleden al is voorgesteld voor DPP polymeren. Het enige polymeer waar een betere efficiëntie werd bereikt met het warm depositie was in het geval waarin filmvorming uit koude oplossing onmogelijk was door een te geringe oplosbaarheid bij kamertemperatuur.

De zijketens kunnen ook aangepast worden door andere functionaliteiten te introduceren, zoals siloxanen. Door de hoeveelheid siloxaan-dragende ketens en alkylketens in het polymeer aan te passen kunnen we een reeks materialen verkrijgen waarin polymeren met een grotere hoeveelheid siloxaanketens een verminderde oplosbaarheid en een lager moleculair gewicht vertonen. Ondanks dat de mobiliteit van positieve gaten verbetert met hogere concentraties siloxanen vermindert de zonnecelefficiëntie sterk. Met kleine hoek Röntgen verstrooiing (GIWAXS) en transmissie elektronmicroscopie werd de morfologie onderzocht en een grotere vezelbreedte werd waargenomen met grotere siloxaanconcentraties, wat overeenkomt met de vermindering in J_{sc}. Dit is een verassend resultaat gezien de oplosbaarheid van deze polymeren: in het verleden is namelijk vastgesteld dat verminderde oplosbaarheid leidt tot kleinere vezelbreedtes. Dit suggereert dat de invloed van het moleculair gewicht op de morfologie complexer is dan voorheen gedacht en belangrijker kan zijn dan de algemene oplosbaarheid van het polymeer. Een andere reden voor de verminderde zonnecelefficiëntie bij hogere siloxaanconcentraties is een sterker niet-radiatief verval van aangeslagen toestanden in het zuivere polymeer.

Het terpolymeer motief is in het verleden al aangewend om de energieniveaus en fotovoltaïsche eigenschappen van polymeren te beïnvloeden. Door de opto-elektronische eigenschappen van zeven regioregulaire terpolymeren die in onze groep zijn gesynthetiseerd te analyseren blijkt het mogelijk om deze eigenschappen te voorspellen. Een directe correlatie tussen de eigenschappen van de terpolymeren en de corresponderende copolymeren kon namelijk worden gevonden. De optische bandkloof en de energieniveaus van de terpolymeren kan met een goede betrouwbaarheid worden voorspeld door het

wiskundig gemiddelde te nemen van de waarden van de corresponderende copolymeren. Ook de V_{oc} van deze materialen kan op dezelfde wijze worden voorspeld. Dit eenvoudig model werd verder bevestigd door 21 eerder gepubliceerde terpolymeren en hun copolymeren te analyseren.

In conclusie heeft het werk beschreven in dit proefschrift geleid tot een dieper begrip van de factoren die de morfologievorming in DPP polymeren beïnvloeden, zoals vertakkingen of nieuwe zijketens. Ook is een beter inzicht verkregen in de relatie tussen efficiëntie en oplosbaarheid, aggregatie en moleculair gewicht. Ten slotte werd het inzicht in de factoren die de energieniveaus beïnvloeden, zoals homokoppeling en het terpolymeer motief, verfijnd en een voorspellende theorie over terpolymeren werd ontwikkeld.

Curriculum Vitae

Gaël Heintges was born on the 6th of July 1991 in Sint-Truiden, Belgium. After finishing his secondary education at Koninklijk Atheneum Tongeren in 2008, he studied chemistry at Hasselt University, obtaining his bachelor degree in 2011. He then pursued a master degree in chemical engineering at Eindhoven University of Technology. His graduation project was carried out in the group of prof. dr. ir. René Janssen under the supervision of dr. Koen Hendriks, on the subject of conjugated terpolymers for photovoltaic applications. After receiving his master degree cum laude in 2013, he obtained a scholarship from the Agentschap voor Innovatie door Wetenschap en Technologie (IWT) in Belgium to continue his research on organic solar cells in the form of a joint PhD between Eindhoven University of Technology and Hasselt University. The results of this research are presented in this dissertation.

List of Publications

Publications in scientific journals

Impact of polymorphism of a low-bandgap semiconducting polymer on the optoelectronic properties in solution and thin films

M. Li, A. Hesham Balawi, P. J. Leenaers, L. Ning, G. H. L. Heintges, T. Marszalek, W. Pisula, M. M. Wienk, S. C. J. Meskers, Y. Yi, F. Laquai, R. A. J. Janssen, *Nat. Commun.*, 2019, **10**, 2867. DOI: 10.1038/s41467-019-10519-z

- Contributed to the synthesis of monomers and supervised the synthesis of polymers
- Measured DSC on pristine polymers and blends

On the homocoupling of trialkylstannyl monomers in the synthesis of diketopyrrolopyrrole polymers and its effect on performance of polymer-fullerene photovoltaic cells

G. H. L. Heintges, R. A. J. Janssen, *RSC Advances*, 2019, **9**, 15703-15714. DOI: 10.1039/c9ra02670c

- Conducted all stages of the research
- Wrote the article

Solution-processed tin oxide-PEDOT:PSS interconnecting layers for efficient inverted and conventional tandem polymer solar cells

D. Di Carlo Rasi, P. M. J. G. van Thiel, H. Bin, K. H. Hendriks, G. H. L. Heintges, M. M. Wienk, T. Becker, Y. Li, T. Riedl, R. A. J. Janssen, *Solar RRL*, 2019, **3**, 1800366. DOI: 10.1002/solr.201800366

- Synthesized PDPPTPT

The influence of siloxane bearing side-chains on the photovoltaic performance of DPP-based polymers

G. H. L. Heintges, K. H. Hendriks, F. J. M. Colberts, M. Li, J. Li, R. A. J. Janssen, *RSC Advances*, 2019, **9**, 8740-8747. DOI: 10.1039/C9RA00816K

- Synthesized the polymers
- Fabricated and analyzed the solar cells
- Analyzed TEM and GIWAXS data
- Wrote the article

Near-infrared tandem organic photodiodes for future application in artificial retinal implants

G. Simone, D. Di Carlo Rasi, X. de Vries, G. H. L. Heintges, S. C. J. Meskers, R. A. J. Janssen, G. H. Gelinck, *Adv. Mater.*, 2018, **30**, 1804678. DOI: 10.1002/adma.201804678

- Synthesized PDPPTPT

The impact of device polarity on the performance of Polymer-Fullerene solar cells
M. Li, J. Li, D. Di Carlo Rasi, F. J. M. Colberts, J. Wang, G. H. L. Heintges, B. Lin, W. Li, W. Li, W. Ma, M. M. Wienk, R. A. J. Janssen, *Adv. Energy Mater*., 2018, **8**, 1800550. DOI: 10.1002/aenm.201800550
- Synthesized PDPP(TPT-*alt*-3T)

A universal route to fabricate n-i-p multi-junction polymer solar cells via solution processing
D. Di Carlo Rasi, K. H. Hendriks, G. H. L. Heintges, G. Simone, G. H. Gelinck, V. S. Gevaerts, R. Andriessen, G. Pirotte, W. Maes, W. Li, M. M. Wienk, R. A. J. Janssen, *Solar RRL*, 2018, **2**, 1800018. DOI: 10.1002/solr.201800018
- Synthesized PDPPTPT

The effect of side-chain substitution and hot processing on diketopyrrolopyrrole-based polymers for organic solar cells
G. H. L. Heintges, P. J. Leenaers, R. A. J. Janssen, *J. of Mater. Chem. A*, 2017, **5**, 13748-13756. DOI: 10.1039/c7ta01740e
- Contributed to and supervised the synthesis of the materials and processing and analysis of the solar cells
- Wrote the article

Designing small molecule organic solar cells with high open-circuit voltage
J. Kudrjasova, M. Van Landeghem, T. Vangerven, J. Kesters, G. H. L. Heintges, I. Cardinaletti, R. Lenaerts, H. Penxten, P. Adriaensens, L. Lutsen, D. Vanderzande, J. Manca, E. Goovaerts, W. Maes, *Chemistryselect*, 2017, **2**, 1253-1261. DOI: 10.1002/slct.201601915
- Processed, analyzed and optimized solar cells

The effect of branching in a semiconducting polymer on the efficiency of organic photovoltaic cells
G. H. L. Heintges, J. J. van Franeker, M. M. Wienk, R. A. J. Janssen, *Chem. Commun*., 2016, **52**, 92-95. DOI: 10.1039/c5cc07185b
- Synthesized the polymers
- Fabricated and analyzed the solar cells
- Wrote the article

Conjugated polymer with ternary electron-deficient units for ambipolar nanowire field-effect transistors
Y. J. Ji, C. Y. Xiao, G. H. L. Heintges, Y. G. Wu, R. A. J. Janssen, D. Q. Zhang, W. P. Hu, Z. H. Wang, W. W. Li, *J. of Pol. Sci. Part A: Pol. Chem.*, 2016, 5**4**, 34-38. DOI: 10.1002/pola.27898
- Performed the GPC measurements
- Co-wrote the article

Polymer solar cells: solubility controls fiber network formation

J. J. van Franeker, G. H. L. Heintges, C. Schaefer, G. Portale, W. W. Li, M. M. Wienk, P. van der Schoot, R. A. J. Janssen, *J. Am. Chem. Soc.*, 2015, **137**, 11783-11794. DOI: 10.1021/jacs.5b07228

- Synthesized DT-PDPPTPT
- Fractionated the material

Ultrasonic spray coating as deposition technique for the light-emitting layer in polymer LEDs

K. Gilissen, J. Stryckers, P. Verstappen, J. Drijkoningen, G. H. L. Heintges, L. Lutsen, J. Manca, W. Maes, W. Deferme, *Org. Electron.*, 2015, **20**, 31-35. DOI: 10.1016/j.orgel.2015.01.015

- Performed the preliminary experiments spray-coating the material and fabricating and measuring the OLED's

Fluorination as an effective tool to increase the open-circuit voltage and charge carrier mobility of organic solar cells based on poly(cyclopenta[2,1-b:3,4-b']dithiophene-alt-quinoxaline) copolymers

P. Verstappen, J. Kesters, W. Vanormelingen, G. H. L. Heintges, J. Drijkoningen, T. Vangerven, L. Marin, S. Koudjina, B. Champagne, J. Manca, , L. Lutsen, D. Vanderzande, W. Maes, *J. Mater. Chem. A*, 2015, **3**, 2960-2970. DOI: 10.1039/c4ta06054g

- Processed, analyzed and optimized solar cells

Comparing random and regular diketopyrrolopyrrole–bithiophene–thienopyrrolodione terpolymers for organic photovoltaics

K. H. Hendriks , G. H. L. Heintges, M. M. Wienk, R. A. J. Janssen, *J. Mater. Chem. A*, 2014, **2**, 17899-17905. DOI: 10.1039/C4TA04118F

- Synthesized the polymers
- Fabricated and analyzed the solar cells

Homo-coupling defects in diketopyrrolopyrrole based co-polymers and their effect on photovoltaic performance

K. H. Hendriks, W. Li, G. H. L. Heintges, G. W. P. van Prijssen, M. M. Wienk, R. A. J. Janssen, *J. Am. Chem. Soc.*, 2014, **31**, 11128-11133. DOI: 10.1021/ja505574a

- Performed preliminary experiments synthesizing homocoupled polymers

High-Molecular-Weight Regular Alternating Diketopyrrolopyrrole-based Terpolymers for Efficient Organic Solar Cells

K. H. Hendriks, G. H. L. Heintges, V. S. Gevaerts, M. M. Wienk, R. A. J. Janssen, *Angew. Chem. Int. Ed.*, 2013, **52**, 8341-8344. DOI: 10.1002/anie.201302319

- Synthesized the polymers
- Fabricated and analyzed the solar cells

International conferences

The effects of siloxane bearing side-chains on the photovoltaic performance of conjugated polymers
G. H. L. Heintges, M. Li, K. H. Hendriks, F. J.M. Colberts, R. A. J. Janssen, *Hybrid and Organic Photovoltaics Conference*, 2018, Benidorm, Spain, **Poster presentation**.

The effects of siloxane bearing side-chains on the photovoltaic performance of conjugated polymers
G. H. L. Heintges, M. Li, K. H. Hendriks, R. A. J. Janssen, *Next-Gen III Conference*, 2017, Groningen, The Netherlands, **Poster presentation**.

The effect of branching in a semiconducting polymer on the efficiency of organic photovoltaic cells
G. H. L. Heintges, J. J. van Franeker, M. M. Wienk, R. A. J. Janssen, *International Fall School on Organic Electronics*, 2016, Moscow, Russia, **Oral contribution**.

Comparing random and regular terpolymers based on DPP and TPD
G. H. L. Heintges, K. H. Hendriks, M. M. Wienk, R. A. J. Janssen, *Hybrid and Organic Photovoltaics Conference*, 2015, Rome, Italy, **Poster presentation**.

Dankwoord

Having come to the end of this thesis and PhD, I can look back with satisfaction at my time in Eindhoven, during which I learned many things and had many interesting experiences. Research is never done in isolation, and many people have contributed directly and indirectly on a professional and personal front to the completion of this thesis.

Eerst en vooral wil ik graag René bedanken die mij de kans heeft gegeven om dit onderzoek te doen. Toen ik, later dan hij waarschijnlijk had verwacht, kwam aankloppen met de vraag of er plaats was in zijn groep heeft hij mij met open armen ontvangen en de vrijheid gegeven om nieuwe projecten voor te stellen. René, bedankt voor de begeleiding die ge mij al die jaren hebt gegeven. Ik apprecieer heel erg de manier waarop ik vrijheid kreeg wanneer het gepast was, en hoe ge meer raad en begeleiding gaf wanneer nodig. Vooral van uw manier om de belangrijkste punten in een discussie op te pikken en te behandelen, terwijl onbelangrijke dingen snel worden afgehandeld, heb ik veel geleerd. Wouter wil ik graag bedanken om de begeleiding die hij heeft gegeven in het behalen van mijn beurs, en omwille van de vrijheid die hij mij heeft gegeven in het zoeken naar een eigen pad in mijn PhD onderzoek.

Prof. Peter Skabara, prof. Rint Sijbesma, prof. Albert Schenning and prof. Jean Manca I would like to thank for reading and approving my thesis, and taking part in my defence.

On the professional front I owe my thanks to the co-authors without which my work could not be published. Hans van Franeker, Pieter Leenaers, Koen Hendriks, Fallon Colberts, Mengmeng Li, Junyu Li, and Andréanne Bolduc all made valuable contributions to the projects that are presented in this thesis. Furthermore I would like to especially thank Martijn en Stefan. Martijn, bedankt om altijd het lab draaiende te houden en om de kritische stem te zijn tijdens discussies: uw bijdrage aan de goede werking groep is groot. Stefan, bedankt voor altijd de interessante ingewikkelde vraag te vinden tijdens meetings, en bedankt voor het werk op de terpolymeren.

Tijdens mijn doctoraat heb ik meerdere studenten kunnen begeleiden bij hun afstudeerproject, en van elk van hun heb ik nieuwe dingen geleerd. Jasper was de eerste student die ik over langere termijn had en ik heb veel geleerd over hoe het best begeleiding

aan te pakken. Ik ben blij dat ge een goede job hebt gevonden kort na ons verlaten te hebben. Pieter, toen ik u voor het eerst ontmoette was ik onmiddellijk overdonderd door uw tomeloos enthousiasme. U begeleiden was op veel vlakken een plezier en uw hard werk heeft dan ook tot een mooie publicatie en hoofdstuk hier geleid. Met uw energie en werklust zal het dan ook geen probleem zijn om uw eigen doctoraat mooi af te ronden, en ik wens u daarmee het beste. Bedankt om mij ook te introduceren tot de mooie sport van het klimmen, hoewel voorzichtigheid hiermee altijd geboden is.

Over the years I had many colleagues, many of whom have become friends and provided great support both in the lab and outside. Alice, thank you for the many trips and dinners. Especially during my first year your presence really convinced me I had made the correct choices. Andréanne, as soon as we met in the office there was a sense that we would become good friends. Your enthusiastic and upbeat demeanour always brought life to the lab. Although you stayed for only one short year, I have a lot to be grateful for, chiefly your insistence for me to join the choir. It is thanks to you that I developed an entire new side to my musical life, which in turn connected me with many great people. I wish you all the best in Canada and lots of success with all your endeavours.

Ruurd, ik ben heel blij dat gij mijn collega waart en altijd goede muziek opzette in lab 1. We hebben gedurende onze PhD's vele leuke momenten gehad in het lab, op conferenties en op concerten. Het was een plezier om met u in de moshpit te staan. Bardo, bedankt voor mijn maatje te zijn gedurende mijn hele PhD, hoewel onze onderwerpen erg verschilden hebben we toch veel plezier beleefd op de conferenties die we samen bijwoonden. Robin, we hebben samen een leuke tijd gehad en in het bijzonder dank voor onze discussies over Belgische politiek. Matt, thank you for the interesting discussions about a variety of subjects, and a special thanks for our conversations about the state of English cricket and cricket in general. For this I also have to thank Kunal. Kunal, I really appreciate your sense of humour and general outlook on life, it was always a pleasure sharing coffee with you. On that subject, I would like to thank Dario for the strong coffee he provided me with during our time as officemates. Mike, Gijs, Weiwei, Chunhui, Miriam, Hans, Mengmeng, Junke, Bas, Tom, Nicolas, Benjamin, Serkan, Haijun, Bart, Olivera and Simone and all other colleagues I have met over the years I would like to thank for making the time during my PhD memorable and enjoyable.

Margot wil ik in het bijzonder bedanken om als een biechtmoeder te fungeren en voor het waken over het algemene welzijn van de hele groep. Bedankt voor de mentale steun die ge mij vaak hebt gegeven.

Koen, het is dankzij uw geweldige begeleiding tijdens mijn masterproject dat mijn ontwikkeling als onderzoeker echt is begonnen. Tijdens mijn doctoraat kon ik altijd bij u aankloppen met een of andere vraag waar we dan uitgebreid over konden discussiëren. Ook voor de steun die ge mij op persoonlijk vlak hebt gegeven en de fijne momenten die we buiten het werk hebben beleefd wil ik u graag bedanken. Ik wens u nog veel geluk in uw toekomstig onderzoek naar flowbatterijen, en bedankt om mijn paranimf te zijn.

Fallon, het was een plezier om met u te werken en muziek te maken. Uw enthousiasme om naar dit of dat concert te gaan, of het nu metal dan wel klassiek is, is altijd aanstekelijk. Samen Moskou verkennen na een week conferentie was heel leuk en zal mij altijd bijblijven. Bedankt voor mijn paranimf te zijn en veel succes in uw toekomstige carrière.

Over de jaren heb ik meerdere mensen leren kennen met wie ik gemusiceerd heb. Ik zou graag mijn medeleden van Vokollage, NSK en Quadrivium willen danken voor de vele leuke en inspirerende momenten, en in het bijzonder Renée, Beatrice, Emma, Jan-Pieter en Ruud. Beatrice, thank you for the support and many silly conversations we had. Emma, ik ben blij dat we zoveel goede ervaringen, zowel muzikaal als chemie-gerelateerd, hebben kunnen delen. Ruud, dankzij u heb ik mij muzikaal veel verder weten te ontwikkelen en heb ik een nieuwe appreciatie voor de muziek van Wagner gekregen, waarvoor dank.

De mentale steun van mijn vrienden is belangrijk geweest voor het afronden van dit werk. Daarom wil ik mijn oudste vrienden hier danken: Hans, Jonas, Sebastiaan en Kirsten. Ten slotte wil ik ook mijn ouders en grootouders bedanken voor de vele steun en blijken van interesse in mijn werk over de jaren.